Lighting The Way

A model-independent multilepton analysis to search for new physics with the ATLAS detector

Pepijn Johannes Cornelis Bakker

ISBN: 978-94-6416-573-9

Lighting The Way – A model-independent multilepton analysis to search for new physics with the ATLAS detector

Thesis, Radboud Universiteit Nijmegen

Cover design: Sandra Tukker

Printing: Ridderprint | www.ridderprint.nl

This work has been performed at the National Institute for Subatomic Physics (Nikhef) which is funded by the Dutch Research Council (NWO). The research was financially supported by the NWO Innovational Research Incentives Scheme (Vici).

Lighting The Way

A model-independent multilepton analysis to search
for new physics with the ATLAS detector

Proefschrift

ter verkrijging van de graad van doctor
aan de Radboud Universiteit Nijmegen
op gezag van de rector magnificus prof. dr. J.H.J.M. van Krieken,
volgens besluit van het college van decanen in het openbaar te verdedigen
op woensdag 2 juni 2021
om 14:30 uur precies

door

Pepijn Johannes Cornelis Bakker

geboren op 13 januari 1992
te Heemskerk

Promotor:	Dr. F. Filthaut
Copromotor:	Dr. S. Caron
Manuscriptcommissie:	Prof. dr. S.J. de Jong Prof. dr. R. Fleischer (Vrije Universiteit Amsterdam) Prof. dr. R.H.P. Kleiss Dr. M. Wu Dr. F. de Almeida Dias (Universiteit van Amsterdam)

Contents

Introduction **1**

I Particle Physics at the LHC 3

1 The Standard Model of Particle Physics 5
1.1 The Symmetries of Nature . . . 5
1.1.1 Local Gauge theories and Quantum Electrodynamics . . . 6
1.1.2 Quantum chromodynamics and the Strong Interaction . . . 8
1.1.3 The Brout-Englert-Higgs Mechanism . . . 10
1.1.4 The Electroweak Interaction . . . 12
1.2 Contents of the Standard Model . . . 16
1.2.1 Particles . . . 17
1.2.2 Parameters . . . 18
1.3 Physics Beyond the Standard Model . . . 19
1.3.1 Neutrino Oscillations . . . 19
1.3.2 Dark Matter . . . 20
1.3.3 Matter-antimatter asymmetry . . . 21
1.4 Model-independent searches for exotic physics . . . 22
1.4.1 The Type-III Seesaw Mechanism . . . 23
1.4.2 The doubly-charged Higgs Particle . . . 25
1.5 Event Generation . . . 26

2 The LHC and the ATLAS Detector 29
2.1 The Large Hadron Collider . . . 29
2.1.1 Data taking at the LHC . . . 31
2.2 The ATLAS detector . . . 34
2.2.1 Magnet System . . . 36
2.2.2 The Inner Detector . . . 36
2.2.3 Calorimeter System . . . 38
2.2.4 The Muon Spectrometer . . . 40
2.2.5 Trigger and Data Acquisition System . . . 42
2.2.6 Detector Simulation . . . 43

3 Event Reconstruction 45
3.1 Reconstruction of Tracks and Vertices . . . 45
3.1.1 From Hits to Tracks . . . 45
3.1.2 Vertex Reconstruction . . . 48

3.2 Physics Object Reconstruction . . . 51
3.2.1 Electrons . . . 51
3.2.2 Muons . . . 52
3.2.3 Lepton Efficiency Scale Factors . . . 55
3.2.4 Jets . . . 57
3.2.5 Missing Transverse Energy . . . 58

II Experiment Design 61

4 Region and Event Selection 63
4.1 Event Base Selection . . . 63
4.1.1 Event Quality Cuts . . . 63
4.1.2 Used Triggers . . . 64
4.1.3 Object Selection . . . 65
4.1.4 Trigger Matching . . . 67
4.1.5 Dilepton Mass Requirement . . . 67
4.2 Analysis Regions . . . 67
4.2.1 Choice of Signal Regions . . . 68
4.2.2 Control and Validation Regions . . . 70

5 Background Prediction 73
5.1 Used Event Generators . . . 73
5.1.1 Sherpa . . . 73
5.1.2 MadGraph5_aMC@NLO . . . 74
5.1.3 Powheg . . . 74
5.2 The Fake Factor Method . . . 75
5.2.1 Particle Classification . . . 75
5.2.2 The Fake Factor . . . 76
5.2.3 Using the Fake Factor . . . 76
5.2.4 Obtaining the Fake Factors: Estimation Regions . . . 79
5.2.5 Results . . . 83

III Interpretation 87

6 Statistical Analysis 89
6.1 Fitting and Limit Setting . . . 89
6.2 Systematic Uncertainties . . . 94
6.2.1 Theoretical Uncertainties . . . 94
6.2.2 Experimental Uncertainties . . . 96
6.2.3 Uncertainty Breakdown . . . 103

7 Results 109
7.1 Control Regions and Systematics . . . 109
7.2 Region Distribution Plots . . . 112
7.3 Fits . . . 120

7.4 Limits . . . 126
7.5 Model-specific comparison . . . 129
7.5.1 Type-III Seesaw model . . . 129
7.5.2 Doubly-Charged Higgs . . . 130
7.5.3 Obtaining cross-section limits . . . 131

Conclusion **135**

Appendices 137

A Fake Composition Plots **139**

B Four lepton, on-Z excess breakdown **143**

C Research Data Management **149**

Bibliography **151**

Summary **163**

Samenvatting **169**

Acknowledgments **175**

"Do nothing out of selfish ambition or vain conceit. Rather, in humility value others above yourselves, not looking to your own interests but each of you to the interests of the others."

— Philippians 2:3–4

Introduction

Over the past decades the particle physics community has dedicated itself to studying the forces of nature at the smallest measurable scale. This has led to the discovery of many new fundamental particles, whose behavior and properties are gathered under a theory known as the Standard Model of particle physics. With the discovery of the Higgs boson in 2012, the Standard Model is now considered complete. But while this framework seems to be a highly successful description, it is unable to account for gravitational force, nor can it explain the apparent presence of dark matter and the relative absence of anti-matter with respect to the amount of baryonic matter in the observable universe.

Many theories have been hypothesized to explain these anomalies. At the European Organization for Nuclear Research (CERN) facility in Geneva, members of the ATLAS collaboration perform experiments using data from the world's largest particle accelerator, the Large Hadron Collider (LHC). Data obtained from this collider offer unrivaled new insights into the energetic frontier of particle physics, allowing experimenters to either find evidence of physics beyond the Standard Model, or exclude them with ever-increasing precision. Many such models have now been tested. However, evidence thus far remains elusive, and the search continues.

In this thesis a search is presented that imposes fewer assumptions on the nature of potential new physics processes, but instead aims to be sensitive to large number of possible theories that might be observable from the ATLAS data. A large amount of data is studied in order to increase the probability of a serendipitous discovery in unexpected corners.

This analysis targets final states with 3 or 4 light leptons, and further separates these states into subsections to create multiple regions of interest. Each of these regions is to be tested for the possibility of new physics. Each region is further divided into multiple bins according to the particle mass reconstructed from all leptons in the event, each of which is tested individually using statistical techniques to fit and set limits on potential contributions due to exotic physics. Because these selections are model-independent, sensitivity to specific physics models is lower than it would be for a comparable dedicated search targeting the same model. Nevertheless, this analysis aims to be able to be a first indicator of potential signals.

In order to distinguish with precision whether measured events originate merely from Standard Model processes or also from additional yet-unknown sources, the behavior of Standard Model processes must be well-understood. It is also paramount to understand the ATLAS detector and its capability to reconstruct particles from the energy deposits it measures. In particular, the probability of the detector admitting an event containing less than 3 leptons due to an erroneous particle classification must be determined. This has been investigated for this thesis. Standard Model events are simulated using algorithmic event generators and compared to the observed data distributions, and a data-driven background estimation has been developed.

This thesis is divided into three parts:

- **Part I** is an overview of how physicists at the LHC procure high-quality particle collision data from the ATLAS detector. Chapter 1 provides an overview of the Standard Model, which includes all known particles and their interactions. This chapter also offers examples of observations currently unexplained by the theory, and potential extensions which have attempted to account for them. Chapter 2 discusses the ATLAS detector, describing its components and their purpose. Chapter 3 discusses how measured energy deposits can be reconstructed to derive the particles produced during collisions as well as their trajectories.
- **Part II** describes the setup of the analysis that was performed. Chapter 4 discusses the selection of collision events, as well as the criteria by which these were categorized into regions. Chapter 5 introduces the techniques which are used to predict the contributions of the various particle physics processes.
- **Part III** compares the Standard Model predictions for the regions in the analysis to the data measured by the ATLAS detector. Chapter 6 introduces the statistical toolbox that is needed to perform the comparison, and lists all the uncertainties that may impact its precision. In Chapter 7 the results obtained by the analysis are shown.

My personal contributions are contained within Part II and III of this thesis. Major contributions are the event selection and the choice of the analysis regions in Chapter 4 and the application of the fake factor method as a means of background estimation in Chapter 5.2. I have also performed the statistical analysis discussed in Chapter 6, apart from the establishment of the nuisance parameters, and produced the results given in Chapter 7.

Part I

Particle Physics at the LHC

Chapter 1

The Standard Model of Particle Physics

Over the years physicists have been incredibly successful at crafting an explanation for the machinations of nature down to its fundamental constituents. Three paradigms stand at the frontier of modern physics research: General relativity, the ΛCDM model and the Standard Model of Particle Physics. The latter of these three operates at the smallest possible scale, that of fundamental particles. It incorporates three of the four fundamental forces. These forces are the *electromagnetic force*, the *weak force* and *strong force*.

The goal of this chapter is to introduce the fundamental framework of particle physics, the Standard Model (SM). The chapter starts out with Section 1.1 introducing quantum field theory and how it can be used to derive the SM Lagrangian starting from the underlying symmetry group. Section 1.2 fills in the contents of the SM, describing the fundamental particles and the set of parameters by which the SM can be parameterized. In Section 1.3 a few phenomena are introduced which cannot be accounted for within the framework of the SM, requiring instead the existence of physics Beyond the Standard Model (BSM), also known as exotic physics. Section 1.4 provides a brief excursion into some current BSM theories to emphasize the vast amount of theories that can be probed through a model-independent search in three and four lepton final states. Finally, Section 1.5 discusses how knowledge of theory is leveraged in order to simulate particle physics processes using algorithmic event generators.

1.1 The Symmetries of Nature

The Standard Model is a *quantum field theory*: its fundamental constituents are quantum fields which are defined in all space-time coordinates. The eponymous particles of particle physics are the observable excitations of these quantum fields[1]. Multiple states of the underlying quantum fields may lead to the same state of the particle that is observed. A transformation which results in an identical observation it is called a *symmetry*.

The Standard Model is also a gauge theory: Its essence is a gauge group which reflects the symmetries within the fundamental forces of nature mentioned in the introduction. The gauge group that stands at the heart of the Standard Model is the non-abelian symmetry group given in Equation 1.1.

[1] A defining quality (and difficulty) of quantum mechanics is that fields can't be observed directly. Several interpretations exist to bridge the gap between mathematical formulation and observations.

$$SU(3)_C \otimes SU(2)_L \otimes U(1)_Y \tag{1.1}$$

This is the starting point for the formulation of the SM Lagrangian density function. It can be split into two parts: The *electroweak part* $SU(2)_L \otimes U(1)_Y$ representing the combination of weak and electromagnetic force (the reason they are treated together will become clear later in this chapter) and the group $SU(3)_C$ for the *strong interaction*.

The following sections discuss the formulation of the Standard Model Lagrangian density through the above symmetry groups. The Lagrangian of Quantum Electrodynamics (QED) is derived from local gauge symmetry $U(1)$. This is then repeated for the symmetry groups $SU(3)_C$ and the group $SU(2)_L \otimes U(1)_Y$. The Brout-Englert-Higgs (BEH) Mechanism is invoked which, through the process of spontaneous symmetry breaking, permits the massive vector bosons that are the observed carriers of the weak force in nature. The result will be a renormalizable, mathematically self-consistent theory with 18 parameters, 12 types of fermions and 5 types of bosons. It can be expressed as a Lagrangian density which in its most condensed and canonical form is written as in Equation 1.2.

$$\begin{aligned}\mathcal{L} = &-\frac{1}{4}F_{\mu\nu}F^{\mu\nu} \\ &+ i\overline{\psi}\not{D}\psi \\ &+ D_\mu\phi^\dagger D^\mu\phi - V(\Phi) \\ &+ \overline{\chi}_L\hat{Y}\Phi\psi_R + h.c.\end{aligned} \tag{1.2}$$

In this equation the top line contains the gauge terms describing the force carriers, the second line contains the interaction terms, the third line the Higgs particle, and the fourth line contains the mass terms in the form of Yukawa couplings. $h.c$ refers to the hermitian conjugates of the preceding terms. The next section will show how these terms arise naturally from a free Lagrangian, symmetries and a demand of invariance as per Noether's theorem.

1.1.1 Local Gauge theories and Quantum Electrodynamics

Equation 1.3 is the Dirac equation, the equation of motion for a free fermion, a spin-½ particle (Einstein sum notation[2] and natural units ($\hbar = c = 1$) are used throughout this thesis).

$$(i\gamma^\mu\partial_\mu - m)\psi = 0 \tag{1.3}$$

Here γ^μ are the Dirac matrices [1], ∂_μ is the partial derivative, m the particle mass, and ψ (actually $\psi(x)$ as it is dependent on its space-time coordinate) is the fermion field spinor.

[2]If the same index occurs both as raised and lowered in an equation, a summation over the indices is implied. That is, $A_iB^i = A_1B^1 + A_2B^2 + A_3B^3$. Roman indices iterate between 1-3, and Greek indices between 0-3 inclusive.

It can be confirmed that Equation 1.4 is a valid Lagrangian density which yields the above equation of motion when entered into the Euler-Lagrange equation.

$$\mathcal{L} = \overline{\psi}(i\gamma^\mu \partial_\mu - m)\psi \tag{1.4}$$

In the above equation $\overline{\psi}$ is the Dirac adjoint of the fermion field ψ. It is defined as $\overline{\psi} = \psi^\dagger \gamma^0$ and is useful due to the quantity $\overline{\psi}\psi$ being Lorentz invariant.

The absolute phase of a wave function cannot be measured. This fact of nature requires a theory with symmetry under transformations of the abelian[3] group $U(1) = e^i\alpha$, where α is an arbitrary phase. Proving global symmetry under this transformation is straightforward, since if $\psi \to \psi' = e^{i\alpha}\psi$ then $\partial_\mu\psi \to e^{i\alpha}\partial_\mu\psi$. But if local symmetry is desired, Lagrangian invariance is required under the fermion field transformation given in Equation 1.5.

$$\psi \to \psi' = e^{i\alpha(x)}\psi \tag{1.5}$$

where phase $\alpha(x)$ depends on space-time coordinate x. In this instance the partial derivative acting on ψ' leaves an extra term proportional to $\partial_\mu\alpha(x)$. In order to restore invariance of the Lagrangian, it is necessary to introduce an extra vector field which transforms to cancel the unwanted term. This can be done by substituting the partial derivative with the *covariant derivative* as formulated in Equation 1.6.

$$D_\mu = \partial_\mu - iqA_\mu \tag{1.6}$$

where A_μ is the newly introduced *gauge field*, in this case the photon field. q is the coupling constant by which this field couples to the fermion. This is shown through the term $q\overline{\psi}\gamma^\mu\psi A_\mu$ one obtains when replacing the partial derivative of Equation 1.4 with the covariant derivative. To cancel out the unwanted term from the transformation of Equation 1.5, it is required that the vector field transforms as $A_\mu \to A_\mu + \frac{1}{q}\partial_\mu\alpha(x)$.

What is left is to add a kinetic term for the photon field. This additional term must also leave the Lagrangian invariant under the above transformations, and therefore another term must be added: a kinetic term in the form of field strength tensors. Kinetic terms make up the first line in the SM Lagrangian of Equation 1.2. In this particular case, the addition results in the QED Lagrangian given in Equation 1.7.

$$\mathcal{L} = \overline{\psi}(i\gamma^\mu D_\mu - m)\psi - \frac{1}{4}F_{\mu\nu}F^{\mu\nu} \quad F_{\mu\nu} = \partial_\mu A_\nu - \partial_\nu A_\mu \tag{1.7}$$

This Lagrangian is one of the parts of the SM Lagrangian and consists of similar terms. They contain gauge terms (the Gauge term in Equation 1.2 is much more complicated, as will be revealed), interaction terms and mass terms.

[3]All elements of an abelian group are commutative.

1.1.2 Quantum chromodynamics and the Strong Interaction

The procedure followed in the preceding section can, with some adjustments, be leveraged to yield a similar expression for the structure of quantum chromodynamics (QCD). In this section this procedure is followed and additional steps that are required, and their implications, will be highlighted. As a starting point, consider the free Lagrangian given in Equation 1.8.

$$\mathcal{L} = \overline{q_j}(i\gamma^\mu \partial_\mu - m)q_j \tag{1.8}$$

Here q is a color field. There are three such fields in general (i.e. a complete formula would assign to the color fields an index q_j), but it will suffice to demonstrate gauge invariance for a single field. The $SU(3)_C$ (the subscript C stands for *color*) gauge symmetry requires invariance under the phase transformation displayed in Equation 1.9.

$$q(x) \to q'(x) = Uq(x) = e^{i\alpha_a(x)T_a}q(x) \tag{1.9}$$

In this equation U is an arbitrary 3×3 matrix expressed in terms of phase α_a and the generators of the $SU(3)$ group T_a. The index a runs from 1 through 8 as $SU(n)$ has $n^2 - 1$ generators.

A difference encountered when substituting the unitary group $U(1)$ with the special unitary one[4], is that the latter is non-abelian. This means that the generators T_a are non-commutative. Rather, they fulfill the commutation relations given in Equation 1.10

$$[T_a, T_b] = if_{abc}T_c \tag{1.10}$$

This is akin to saying that the commutator of any two generators is a linear combination of all generators. Here f_{abc} are real constants, the structure constants of the gauge group. This commutation relation gives rise to an additional difficulty. This becomes clear when the gauge fields G^a_μ for the strong interaction are considered. When the covariant derivative shown in Equation 1.11 is introduced, these fields must transform to restore gauge invariance.

$$D_\mu = \partial_\mu + igT_aG^a_\mu \tag{1.11}$$

Here g is another coupling constant. When substituting this covariant derivative into the free Lagrangian density the term $\overline{q}\gamma^\mu T_a q$ is not invariant under transformations. A term proportional to $i\alpha_b\overline{q}\gamma^\mu(T_aT_b - T_bT_a)q$ remains which due to the the relations in Equation 1.10 can be written as $f_{abc}\alpha_b(\overline{q}\gamma^\mu T_c q)$. Handling this additional term leads to the extended expression of the gauge fields' transformation properties:

[4]The members of a special unitary group all have determinant 1; this requirement is stricter than for an unitary group (e.g. the only member of $SU(1)$ is the constant 1).

$$G^a_\mu \to G^a_\mu - \frac{1}{g}\partial_\mu \alpha_a - f_{abc}\alpha_b G^c_\mu \tag{1.12}$$

Having obtained the expression for the eight gauge fields, it becomes possible to express the final QCD Lagrangian after adding again a kinetic term constructed from a field strength tensor $G^a_{\mu\nu}$. This Lagrangian is given in Equation 1.13. However, the field strength tensor is more complex than its QED counterpart owing to the additional terms discussed below. The exact expression is given in Equation 1.14

$$\mathcal{L} = \overline{q}(i(\gamma^\mu D_\mu) - m)q - \frac{1}{4}G^{\mu\nu}_a G^a_{\mu\nu} \tag{1.13}$$

$$G^a_{\mu\nu} = \partial_\mu G^a_\nu - \partial_\nu G^a_\mu - g f_{abc} G^b_\mu G^c_\nu \tag{1.14}$$

A consequence of the additional term in Equation 1.14 is that the field strength tensors added to the Lagrangian factor to produce terms that are cubic and quartic in G^a_μ. These terms are what allows for the self-coupling of three and four force-carrying particles, which we call gluons, with one another, with a relative strength g and g^2 respectively. The self-interaction of these gluons leads to several interesting phenomena, two of which are *asymptotic freedom* and *confinement*.

The coupling constants encountered so far are not actually constant, but differ at different length scales. Although both QCD and QED show divergence of the coupling strength, QCD distinguishes itself due to gluon-self coupling to exhibit *asymptotic freedom*. That is, the coupling strength decreases at lower distance scales (higher energy scales) and conversely increases at higher distances. This *ultraviolet divergence* sets a limit on the scales at which QCD can make predictions. The field of *perturbation theory* allows us to still make quantitative predictions down to a cutoff scale. An example of this is Equation 1.15, which predicts the value of the strong coupling constant $\alpha_s = g^2/4\pi$ at a certain energy scale for 1-loop diagrams.

$$\alpha_s\Big(\mu_R\Big) = \frac{12\pi}{(33 - 2n_f)\log\left(\frac{\mu_R}{\Lambda_{QCD}}\right)} \tag{1.15}$$

Here μ_R is the choice of *renormalization scale* Λ_{QCD} is the scale parameter. It signifies the energy where the strong coupling constant becomes infinite. Its value must be determined experimentally. Hence the value of α_s at a given μ_R must be determined experimentally too. It is usually quoted by its value at the scale of the mass of the Z-boson, which will be introduced later in this chapter.

Additionally, this increase of coupling strength at larger distances leads to phenomena of *confinement*. Because gluons self-interact, they must themselves carry a color charge. As a result, the gluon exchange of strongly interacting particles places a constraint on the color field by the exchanged particles, resulting in a color field between the aforementioned

particles that exerts a constant force. This force remains constant when the distance increases, leading to a linear increase of energy. At a certain distance, the field becomes stretched to the point that enough energy is available for an additional particle-antiparticle pair, which is promptly created. This is known as color confinement: particles that carry color charge aren't seen in isolation, but always in groups which together form a neutral (colorless) composite. Such particles are collectively known as *hadrons* and the confinement-driven process which creates them is *hadronization*. Collinear groups of particles formed through hadronization will be referred to as *jets* throughout this thesis.

1.1.3 The Brout-Englert-Higgs Mechanism

The gauge bosons encountered thus far have been massless. It is not possible to merely add a bare mass term $\frac{1}{2}mA_\mu A^\mu$ to the Lagrangian as such a term would not be invariant. However, massive gauge bosons have been observed in nature, specifically as carriers of the weak force. Therefore, before the electroweak symmetry group $SU(2)_L \otimes U(1)_Y$, another ingredient is required. This ingredient is the Brout-Englert-Higgs (BEH) mechanism [2, 3], which is the focus of this section.

First the concept of spontaneous symmetry breaking is introduced. It will then be shown how it can lead to gauge bosons through the addition of a complex scalar field known as the Higgs Field. The BEH mechanism applies this technique to the electroweak symmetry group so that it is broken into $U(1)_{EM}$ and $SU(2)$, giving rise to the physical fields of the weak and electromagnetic forces observed in nature.

Spontaneous symmetry breaking occurs when a physical system moves from a state which is symmetric to a vacuum ground state which is not. Whether this occurs or not depends on the shape of the potential of a given Lagrangian. Consider the Lagrangian in Equation 1.16. This Lagrangian has a global $U(1)$ gauge symmetry, which can be extended to a local symmetry if the same steps as in Section 1.1.1 were followed.

$$\mathcal{L}_H = (\partial_\mu \phi)^\dagger (\partial^\mu \phi) - \mu^2 \phi^\dagger \phi - \lambda(\phi^\dagger \phi)^2 \tag{1.16}$$

Here the field ϕ is a complex scalar field. It can be written in a Hermitian basis so that $\phi = \sqrt{\frac{1}{2}}(\phi_1 + i\phi_2)$. The potential term of this Lagrangian is $\mu^2\phi^\dagger\phi + \lambda(\phi^\dagger\phi)^2$. It has its minimum at $\phi = 0$ if both μ^2 and λ are positive. If, however, $\mu^2 < 0$, the potential has a circular set of minima given by $\phi^\dagger\phi = \frac{1}{2}(\phi_1^2 + \phi_2^2) = \mu^2/\lambda = v^2$, where v is introduced as the vacuum expectation value. This is also shown in Figure 1.1. It is now possible to pick a particular minimum in this set without loss of generality which satisfies these solutions, e.g $\phi_1 = v$ and $\phi_2 = 0$.

The next step is to expand the Lagrangian in terms of excitations around the new vacuum minimum by rewriting $\phi_1 = v + \eta$, $\phi_2 = \xi$, with η and ξ being the parallel and tangent components of the perturbation (see Figure 1.1). The new expression for ϕ is then shown in Equation 1.17.

$$\phi = \sqrt{\frac{1}{2}}(v + \eta + i\xi) \approx \sqrt{\frac{1}{2}}(v + \eta)e^{i\xi/v} \tag{1.17}$$

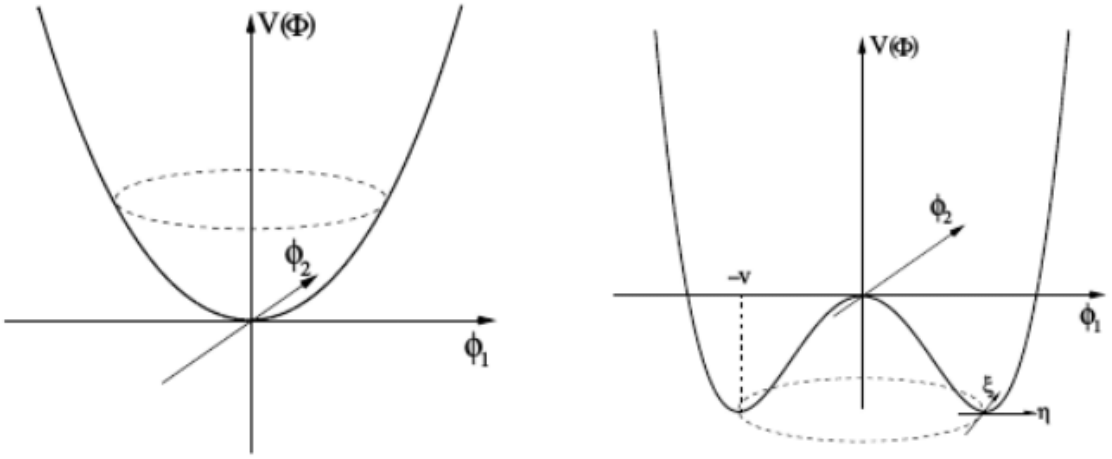

Figure 1.1: Schematic of the Higgs potential $V(\Phi)$ for $\mu^2 > 0$ (left) and $\mu^2 < 0$ (right). The rightmost image presents spontaneous symmetry breaking. ϕ_1 and ϕ_2 represent the real and imaginary part of a complex scalar field ϕ. The new minima in the right image are arranged in circular fashion so that $\phi_1^2 + \phi_2^2 = v^2$.

When this expression is substituted into Equation 1.16 a new Lagrangian is obtained which is described in terms of the fields η and ξ rather than ϕ. The real particles are expected to be described by these fields, in line with the observation that nature tends towards the lowest energy state of a given system. In the new Lagrangian the (real) mass terms of the fields are $m_\eta = \sqrt{2}\mu$ and $m_\xi = 0$. The second zero-mass particle is known as a Goldstone boson and is a result of the symmetry breaking that has just been performed [4].

The last step is the invocation of the BEH mechanism. If the same technique of symmetry breaking is applied to a Lagrangian that obeys a particular gauge symmetry, the following can be shown:

- An additional massive gauge particle is obtained with mass term proportional to the vacuum expectation value v.
- The real field η introduces a massive scalar particle to the Lagrangian. This is the Higgs particle.
- The massless Goldstone boson turns out to be just the longitudinal polarization of the massive gauge boson.

For example, if the Lagrangian in Equation 1.16 was invariant under $U(1)$ transformations, it would look like Equation 1.18, with the covariant derivative D_μ and field strength tensor $F_{\mu\nu}$ analogous to their definition in Section 1.1.1.

$$\mathcal{L}_H = (D_\mu\phi)^\dagger(D^\mu\phi) - \mu^2\phi^\dagger\phi - \lambda(\phi^\dagger\phi)^2 - \frac{1}{4}F_{\mu\nu}F^{\mu\nu} \tag{1.18}$$

Then, the substitution of equation 1.17 is performed using the first order approximation. The gauge field A_μ transforms in order to keep gauge invariance so that $A_\mu \to A_\mu + \frac{1}{gv}\partial_\mu \xi$. The resulting Lagrangian is given in Equation 1.19.

$$\begin{aligned}\mathcal{L}_H =& \frac{1}{2}(\partial_\mu \eta)^2 - \lambda v^2 \eta^2 + \frac{1}{2} q^2 v^2 A_\mu^2 - \lambda v \eta^3 - \frac{1}{4}\lambda \eta^4 \\ &+ \frac{1}{2} q^2 A_\mu^2 \eta^2 + v q^2 A_\mu^2 \eta - \frac{1}{4} F_{\mu\nu} F^{\mu\nu}\end{aligned} \tag{1.19}$$

Indeed, this equation includes a mass term for a scalar particle ($\lambda v^2 \eta^2$), for a massive gauge particle ($\frac{1}{2} q^2 v^2 A_\mu^2$), the Goldstone boson does not appear, and invariance under $U(1)$ is maintained[5]. This is the BEH mechanism in action. In the next section the principle will be applied to the electroweak sector, where such massive gauge bosons are needed.

1.1.4 The Electroweak Interaction

This section is dedicated to constructing a Lagrangian for the gauge symmetry $SU(2)_L \otimes U(1)_Y$. The starting point for this process will be the group $SU(2)$. Local gauge invariance with respect to this group can be enforced using the familiar procedure introduced earlier in this chapter. Consider the transformation:

$$\psi \to \psi' = e^{i\alpha_a J_a}\psi \tag{1.20}$$

Here α^a has arbitrary and coordinate-dependent values as gauge invariance is local. Summation over $a = 1...3$ is implied as $SU(2)$ has three generators. $J_a = \frac{1}{2}\sigma_a$ are the generators, with σ_a representing the Pauli matrices [6]. These generators belong to a non-abelian group and so have a commutation relation $[J_i, J_j] = i\epsilon_{ijk} J_k$, where ϵ_{ijk} is the Levi-Civita symbol[6]. The result is a gauge field W_μ^a with three elements which transforms as:

$$W_\mu^a \to W_\mu'^a = W_\mu^a + \partial_\mu \alpha_a - g\epsilon_{abc}\alpha^b W_\mu^c \tag{1.21}$$

This leads to a covariant derivative $D_\mu = \partial_\mu + \frac{1}{2} i g J_a W_\mu^a$ and the field strength tensor $W_{\mu\nu}^a = \partial_\mu W_\nu^a - \partial_\nu W_\mu^a - g W_\mu^a \times W_\nu^a$. A Lagrangian can be made $SU(2)$ invariant by substituting this covariant derivative and adding the kinetic term $-\frac{1}{4} W_{\mu\nu}^a W_a^{\mu\nu}$.

These gauge fields do not correspond to the gauge bosons seen in nature because the latter are massive. This is why the BEH mechanism must be invoked. In order to do this correctly, however, the electroweak group $SU(2)_L \otimes U(1)_Y$ must be constructed. These groups have been treated individually. Combined, however, there are some additional

[5] This is not trivial as the symmetry is hidden due to the choice of the ground state. It has however been proven that the theory can still be made renormalizable for the $SU(2) \otimes U(1)$ symmetry group [5].

[6] This follows from identities of the Pauli matrices. The Levi-Civita symbol is fully asymmetric under index exchange, zero on repeated indices, and $\epsilon_{123} = 1$

considerations to be taken into account. First, let us modify the $U(1)$ gauge transform from Equation 1.5 slightly to add the charge operator Q, as is done in Equation 1.22. It obeys the relation in Equation 1.23[7] needed to give charge to all quark and lepton fields instead of just the electron.

$$\psi \to \psi' = e^{i\alpha(x)Q}\psi \tag{1.22}$$

$$Q = J_3 + \frac{1}{2}Y \tag{1.23}$$

The term J_3 is the third component of the isospin, the third element of the weak generators J_a. Y is the hypercharge [7]. The physical gauge field A_μ that has been encountered is therefore a combination of the gauge fields W^3_μ and a gauge field related to the $U(1)_Y$ group that will be called B_μ, of which Y is the generator. This new gauge field also comes with a new coupling, which will be written as $g'Y/2$, where g' is distinct from the coupling constant g (which is associated with the weak force). With these ingredients, it becomes possible to write the $SU(2)_L \otimes U(1)_Y$ invariant Lagrangian. The covariant derivative for this group is given in Equation 1.24.

$$D_\mu = \partial_\mu + ig\frac{1}{2}\sigma_a W^a_\mu - ig'\frac{Y}{2}B_\mu \tag{1.24}$$

The kinetic term should look familiar. It is given in Equation 1.25

$$\mathcal{L}_{kin} = -\frac{1}{4}W^a_{\mu\nu}W^{\mu\nu}_a - \frac{1}{4}F_{\mu\nu}F^{\mu\nu} \tag{1.25}$$

Lastly, the fields ψ are the left-handed[8] isospin doublets $\chi_L = \binom{\nu_e}{e^-}_L$, and right-handed isosinglet $\psi_R = e^-_R$ for the leptons. For quarks these are $\chi_L = \binom{u}{d}_L$ and $\psi_R = u_R, d_R$. Note that $SU(2)_L$ couples exclusively to the weak force, meaning that for the right-handed fields the middle term of 1.24 drops out. These fermion fields have specific eigenvalues with regards to the operators J, Q and Y, which are their quantum numbers.

The couplings in this Lagrangian are fixed with respect to the EM coupling constant g and the *weak mixing angle* θ_W (also known as the Weinberg angle). The Weinberg angle is the angle by which spontaneous symmetry breaking rotates the B and W_3 field in order to generate the physical A and Z fields [8], as can be seen in Equation 1.26. This furthermore leads to the identities in Equation 1.27, which reveal the relation between the coupling constants of the involved fields, between the masses of the weak gauge bosons, and between

[7] This only follows upon application of the BEH mechanism

[8] Helicity or "handedness" refers to direction of the spin relative to the direction of motion. When they are opposite, the particle is said to be left-handed. Otherwise it is right-handed. When massive particles are overtaken their handedness flips for that observer. Massless particles cannot be overtaken, so their helicity is the same for all reference frames.

the $SU(2)$ fields W_1, W_2 and the physical massive gauge bosons $W^{\pm}$. These relations between fields due to spontaneous symmetry breaking are also shown in Figure 1.2.

$$\begin{pmatrix} \gamma \\ Z \end{pmatrix} = \begin{pmatrix} \cos\theta_W & \sin\theta_W \\ -\sin\theta_W & \cos\theta_W \end{pmatrix} \begin{pmatrix} B \\ W_3 \end{pmatrix} \tag{1.26}$$

$$q = g\sin\theta_W = g'\cos\theta_W, \quad M_Z = \frac{M_W}{\cos\theta_W}, \quad W^{\pm} = \frac{1}{\sqrt{2}}(W_1 \mp iW_2) \tag{1.27}$$

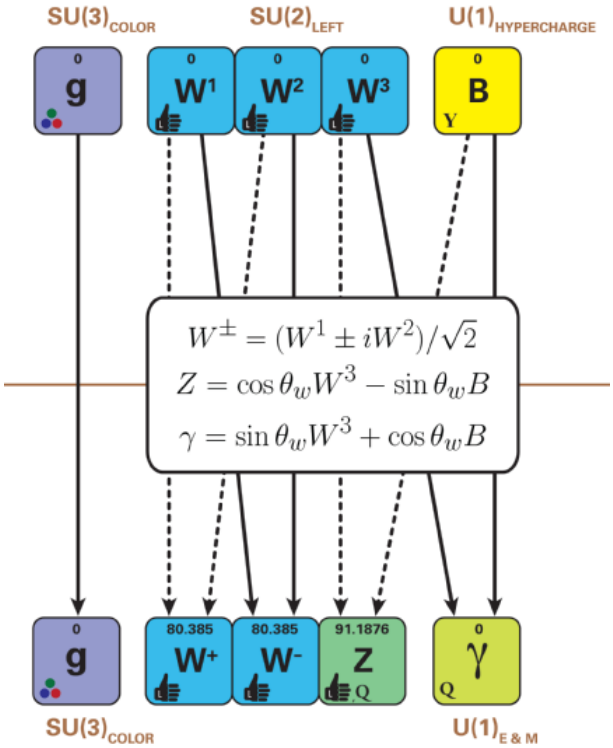

Figure 1.2: The gauge fields of the symmetry group $SU(3)_C \otimes SU(2)_L \otimes U(1)_Y$ before (top) and after (bottom) symmetry breaking, showing how the formulated fields mix to create the observed gauge bosons of nature, with their masses given in GeV. [9]

This by itself does not ensure the mass terms of the gauge bosons. For this, the BEH mechanism is required. Symmetry breaking can be achieved through the introduction of a complex scalar field $\phi = \begin{pmatrix} \phi^+ \\ \phi^0 \end{pmatrix}$, the Higgs field. This field is an isospin doublet with hypercharge $Y = 1$; it can be written in the Hermitian basis as a combination of four real fields $\phi_1 ... \phi_4$. A potential term $V_H = \mu^2(\phi^\dagger\phi) + \lambda(\phi^\dagger\phi)^2$ is also added, analogous to Section 1.1.3. This addition to the Lagrangian is, in essence, the third line in Equation 1.2.

Requiring $\mu^2 < 0$ and $\lambda > 0$ will lead to a hypersphere of minima with the vacuum expectation value v with $\phi^\dagger\phi = \mu^2/\lambda = v^2$. The complex field can then be rewritten as

excitations around a ground state in line with these minima. The conventional choice of parametrization of the field is given in Equation 1.28.

$$\phi = \begin{pmatrix} \phi^+ \\ \phi^0 \end{pmatrix} = \frac{1}{\sqrt{2}} \begin{pmatrix} \phi_1 + i\phi_2 \\ \phi_3 + i\phi_4 \end{pmatrix} = \frac{1}{\sqrt{2}} \begin{pmatrix} 0 \\ v + h \end{pmatrix} \tag{1.28}$$

This equation implies that the vacuum expectation value is $\phi_0 = \frac{1}{\sqrt{2}} \begin{pmatrix} 0 \\ v \end{pmatrix}$. h is the real part of the Higgs field representing excitations around the ground state. Additional terms in this field which correspond to the Goldstone bosons have been omitted as these are absorbed by the massive gauge bosons as part of the BEH mechanism. Indeed, the choice of ϕ_0 which has a third isospin term $J_3 = -\frac{1}{2}$ breaks both $SU(2)$ and $SU(1)_Y$ symmetry, therefore generating mass terms for these gauge terms. However, ϕ_0 is neutral ($Q\phi_0 = 0$). Hence the $U(1)_{EM}$ symmetry is not broken and the associated gauge boson remains massless. Thus it can be inferred that the new scalar particle must be uncharged. This also explains the choice $\phi^+ = 0$.

The complex scalar field must now be inserted into the electroweak Lagrangian. The relevant term which yields the mass terms is the acting of the covariant derivative (Equation 1.24) acting on the vacuum expectation part $\begin{pmatrix} 0 \\ v \end{pmatrix}$ of the Higgs field. Since $\partial_\mu v = 0$ and recalling the Pauli matrices, the end result is Equation 1.29.

$$\begin{aligned} \left| \left(ig\frac{1}{2}\sigma_a W_\mu^a - ig'\frac{Y}{2}B_\mu \right) \frac{1}{\sqrt{2}} \begin{pmatrix} 0 \\ v \end{pmatrix} \right|^2 =& \frac{1}{8}v^2 g^2 \left[(W_\mu^1)^2 + (W_\mu^2)^2 \right] \\ &+ \frac{1}{8}v^2 \left(g'B_\mu - gW_\mu^3 \right) \left(g'B^\mu - gW^{\mu 3} \right) \end{aligned} \tag{1.29}$$

Combined with the relations in Equation 1.27 this leads to the mass terms $(\frac{1}{2}vg)^2 W^{+\mu} W_\mu^-$, $\frac{1}{4}v^2(g^2 + g'^2) Z_\mu Z^\mu$, and $0 A_\mu A^\mu$. These are the desired massive gauge bosons for the electroweak theory, W and Z, with masses $M_W = 80.38$ GeV and $M_Z = 91.12$ GeV. Meanwhile, the photon remains massless.

The same principle that lets the Higgs field give masses to the gauge bosons allows it to generate masses to the leptons and quarks. As an example, for the leptons this can be done by adding to the Lagrangian a gauge invariant term which couples the Higgs field to the left-handled isospin doublet and right-handed singlet, as shown in Equation 1.30, then performing symmetry breaking through the substitution in Equation 1.28.

$$-y_\ell \left(\overline{\chi}_L \phi \psi_R + \overline{\psi}_R \overline{\phi} \chi_L \right) \tag{1.30}$$

The introduced coupling y_ℓ is called a Yukawa coupling [10]. It relates to the mass of the lepton through $m_\ell = v y_\ell / \sqrt{2}$. This additional Yukawa term is contained in the fourth line of the Standard Model Lagrangian in Equation 1.2. This line also includes the mass terms for the quarks, although independent couplings and a different form of the Higgs doublet is required in order to compose these terms to generate their masses.

***

The parts of this section that have just been traversed circumscribe all the ingredients necessary in order to compose a Lagrangian density reflecting the Standard Model of particle physics. An explicit expression of this Lagrangian is lengthy, but can be found by consulting e.g. [11]. It is now time to look at the utility that the Standard Model provides in categorizing the fundamental particles of the universe, as well as the parameters that must be determined from experiment that give the SM its predictive power. This will be discussed in the following section.

1.2 Contents of the Standard Model

A model is only as useful as the predictive power it equips experiments with. It is time to look at the physics that the SM circumscribes. This will be done in two steps. The first is an exhibition of all the particles the model features as well as their behavior. The second is a discussion on the parameters from which, once their values have been determined, one can draft the rules that nature is expected to abide by on the most fundamental level.

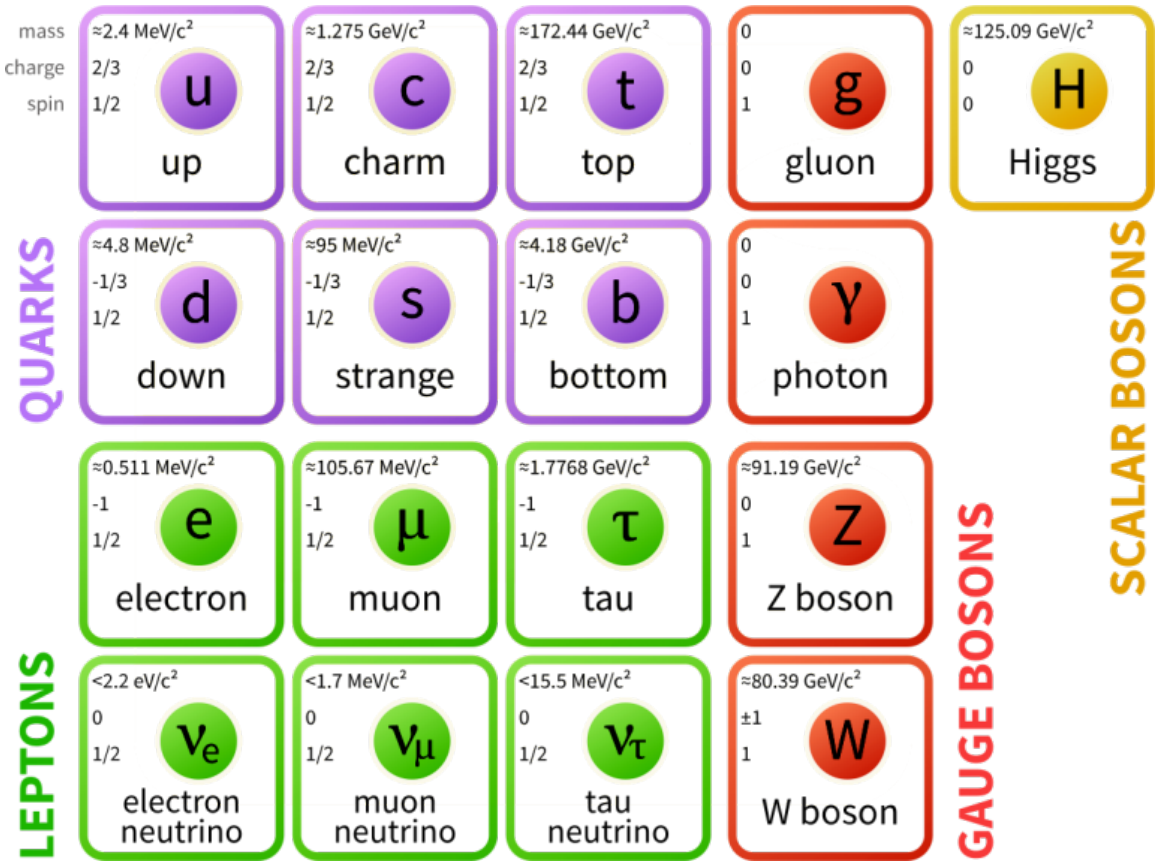

Figure 1.3: Chart of the Standard Model [12]. The top two lines (in purple) show the three generations of quarks, while the bottom lines (in green) show the three generations of leptons. Together these make up the elementary fermions. Charge-carrying bosons are given in the right column (in red) while the Higgs boson is given in yellow in the top right corner. Masses of each particle are also given in GeV/c^2 (expressed in natural units simply as GeV) or upper limits where the exact masses are not known (as is the case for the neutrinos.

1.2.1 Particles

The fundamental particles featured by the Standard Model are shown in Figure 1.3. They are sorted into categories already encountered in the previous section. These categories are the fermions, being the quarks and leptons, and the bosons, which are vector gauge bosons and the scalar Higgs boson. This section goes deeper into some of the properties of these particles.

The *fermions* of the Standard Model have spin 1/2 and come in three generations. These generations are ordered in increasing order of mass. The fermions are further subdivided into quarks and leptons.

The quarks carry non-zero color charge and fractional EM charge, either +2/3 or -1/3. The three generations of positively-charged quarks are, in order of increasing mass, up (u), charm (c), and top (t) quark. The negatively-charged quarks are the down (d), strange (s) and bottom (b). As mentioned in Section 1.1.2, these particles are exclusively observed in colorless composites called *hadrons*. They are formed from color-charged particles in a process called *hadronization*.

The leptons have integer charge and are either massive or massless in the Standard Model. The massive, charged leptons are the *electron* (e, often called *positron* when positively charged), the *muon* (μ) and *tau* (τ). The neutral leptons are called *neutrinos* referred to per generation by their charged counterpart (ν_e, ν_μ, ν_τ). Throughout this thesis, the term *lepton* indicates the charged leptons (and not neutrinos), and *light leptons* indicates the electron and muon.

Table 1.1 summarizes the fermions, their generations, quantum numbers and transformations under the SM gauge group.

Category	Content	$SU(3) \otimes SU(2) \otimes U(1)$	Charge	Particles
Quarks	$\binom{u}{d}_L$	$\mathbf{3} \otimes \mathbf{2} \otimes \frac{1}{6}$	$+2/3, -1/3$	$u_L, u_R = u, c, t$
	u_R	$\mathbf{3} \otimes \mathbf{1} \otimes \frac{2}{3}$	$+2/3$	$d_L, d_R = d, s, b$
	d_R	$\mathbf{3} \otimes \mathbf{1} \otimes -\frac{1}{3}$	$-1/3$	
Leptons	$\binom{\nu_e}{e^-}$	$\mathbf{1} \otimes \mathbf{2} \otimes -\frac{1}{2}$	$0, -1$	$e = e^-, \mu^-, \tau^-$
	e_R^-	$\mathbf{1} \otimes \mathbf{1} \otimes -1$	-1	$\nu = \nu_e, \nu_\mu, \nu_\tau$

Table 1.1: The SM fermions and their transformations under the gauge group $SU(3)_C \otimes SU(2)_L \otimes U(1)_Y$.

The *bosons* are the gauge particles that have been discussed extensively in the previous section. Bosons have integer spin and can be massive or massless, charged or uncharged. The amount of gauge bosons is equal to the total amount of generators in the SM symmetry group. They are the eight *gluons*, which each carry a superposition of color-anticolor states[9], the charged $W^\pm$ boson, the uncharged, massive Z-boson and the massless, chargeless *photon* (γ). The only spin-zero particle is the Higgs boson, an excitation of the Higgs

[9]The categories of color charge are divided into red, green, and blue. A combination of equal charge of each color creates a color-neutral composite, as does a combination of one color and its respective anticolor.

field whose discovery was crucial to the completion of the Standard Model theory [13, 14]. Table 1.2 summarizes the bosons' transformations under the SM gauge group.

Category	Content	$SU(3) \otimes SU(2) \otimes U(1)$	Spin	Particles
Gluons	$g^{1..8}$	$\mathbf{8} \otimes \mathbf{1} \otimes 0$	1	$g^{1..8}$
W bosons	$W_{1..3}$	$\mathbf{1} \otimes \mathbf{3} \otimes 0$	1	$W^{\pm}, Z^0, \gamma$
B boson	B	$\mathbf{1} \otimes \mathbf{1} \otimes 0$	1	
Higgs	$\binom{\phi^+}{\phi^0}$	$\mathbf{1} \otimes \mathbf{2} \otimes 1$	0	H^0

Table 1.2: The SM bosons and their transformations under the gauge group $SU(3)_C \otimes SU(2)_L \otimes U(1)_Y$.

Particles that carry non-zero values for quantum numbers that are conserved have an *antiparticle* of identical mass and similar properties but inverted quantum numbers such as charge. Particles in the SM that have antiparticles are quarks, leptons[10] and the $W^{\pm}$ boson. Antiparticles of the photon, the Z-boson and the Higgs are indistinguishable and therefore these are said to be their own antiparticle.

In accordance with nature's tendency towards the lowest possible energy state, heavier particles will decay into lower-mass combinations provided the quantum numbers of the system are conserved before and after the decay process. Only a few particles do not decay: the electron and positron, the neutrinos, the photon, and the proton, which is a baryon consisting of two up and one down quark. In experiments, particles are designated as *stable* if their mean decay time is larger than the time it takes for them to traverse the detector. Stable but decaying particles are the muon and, in the categories of jets, the charged *pions* (but not the neutral pion) and the *kaons*.

1.2.2 Parameters

The Standard Model is an effective field theory that is self-consistent and renormalizable. These properties are important because together they impose some prior assumptions on which particle physicists set up their experiments. Being qualified as an effective field theory means that the Standard Model is expected to be valid only up to certain energy scales. It is expected to be either a part of, a low-energy limit of, or an approximation of a larger unifying theory which is not yet known. Being self-consistent is a required quality of any mathematically motivated model. That the SM is renormalizable is not a trivial quality. Practically, it means that only a limited set of masses, couplings and wavefunctions need to be renormalized.

The conclusion drawn from the previous paragraph is that the Standard Model has a finite amount of parameters that can be determined and tested across different experiments. Initially, values for these parameters cannot be produced by purely mathematical means; they must be determined through experiment. Once these parameters are known they can be used, through renormalization, to supply predictions for experiments carried out at arbitrary energy scales (albeit limited by the validity scale of the Standard Model).

[10]The discovery of massive neutrinos opens the possibility of neutrinos being their own antiparticle.

Conducting experiments at new frontiers thus brings the eventuality of a result which runs counter to predictions. Results that thus invalidate the Standard Model simultaneously provide data from which a new, more complete model can be composed.

The free parameters that the Standard Model consists of are as follows:

- 3 gauge couplings;
- Yukawa Couplings: 6 for the quark masses and 3 for the lepton masses;
- Quark mixing terms: 3 angles and 1 CP-phase (together these allow for parametrization of the Cabibbo–Kobayashi–Maskawa (CKM) matrix [6];
- 1 Higgs mass term.

1.3 Physics Beyond the Standard Model

The Standard Model has proven to be extremely effective as a description of physics governed by the strong, weak and electromagnetic forces. However, no analogous description for the gravitational force has been incorporated so far (although theories for a force-carrying particle for the gravitational force, the hypothetical *graviton*, do exist). There are furthermore observations which run counter to expectations when attempting to explain physics using purely SM physics. Some of these phenomena will be discussed in this section.

1.3.1 Neutrino Oscillations

The discovery of neutrino oscillation was momentous as it implied the existence of massive neutrinos, which in turn opened up a window to various possible brands of exotic physics. Hints for neutrino oscillation came first from the Homestake experiment [15], which observed solar neutrinos. It was found that the measured electron neutrino and antineutrino flux was in discrepancy with the expected value. This is known as the Solar Neutrino problem. Neutrino oscillation was a proposed solution to the issue, although its predictions would go beyond only the disappearance of solar electron neutrinos. Later observations of muon neutrino disappearance [16] and atmospheric tau appearance [17] would come to undergird the nascent theory. Definitive observation of neutrino mixing came from researchers at Super-Kamiokande [18] and the Sudbury Neutrino Observatory [19]. The existence of two distinct eigenbases for the neutrino sector, one for the flavor states of the mass states, was confirmed.

Neutrino mixing was formalized in a way similar to the CKM matrix [20] in the quark sector. The Pontecorvo–Maki–Nakagawa–Sakata matrix (PMNS matrix) is the unitary 3×3 mixing matrix which connects the neutrino mass states $\nu_{1..3}$ to the neutrino flavor states ν_e, ν_μ, ν_τ. This is shown in Equation 1.31. Neutrino oscillation is encoded in the non-negligible values for the off-diagonal elements.

$$\begin{bmatrix} \nu_e \\ \nu_\mu \\ \nu_\tau \end{bmatrix} = \begin{bmatrix} U_{e1} & U_{e2} & U_{e3} \\ U_{\mu 1} & U_{\mu 2} & U_{\mu 3} \\ U_{\tau 1} & U_{\tau 2} & U_{\tau 3} \end{bmatrix} \begin{bmatrix} \nu_1 \\ \nu_2 \\ \nu_3 \end{bmatrix} \tag{1.31}$$

This unitary matrix has nine degrees of freedom. However, 5 of those real parameters can be absorbed as the phases of the lepton field. A possible but not unique parametrization is the expression of the PMNS matrix in three mixing angles θ_{ij} and a single complex CP-phase δ_{CP}. The matrix can then be written as the product of matrices describing the three potential oscillation modes. This is shown in Equation 1.32.

$$\begin{bmatrix} 1 & 0 & 0 \\ 0 & c_{23} & s_{23} \\ 0 & -s_{23} & c_{23} \end{bmatrix} \begin{bmatrix} c_{13} & 0 & s_{13}e^{-i\delta_{CP}} \\ 0 & 1 & 0 \\ -s_{13}e^{\delta_{CP}} & 0 & c_{13} \end{bmatrix} \begin{bmatrix} c_{12} & s_{12} & 0 \\ -s_{12} & c_{12} & 0 \\ 0 & 0 & 1 \end{bmatrix} =$$

$$\begin{bmatrix} c_{12}c_{13} & s_{12}c_{13} & s_{13}e^{-i\delta_{CP}} \\ -s_{12}c_{23} - c_{12}s_{23}s_{13}e^{i\delta_{CP}} & c_{12}c_{23} - s_{12}s_{23}s_{13}e^{i\delta_{CP}} & s_{23}c_{13} \\ s_{12}s_{23} - c_{12}c_{23}s_{13}e^{i\delta_{CP}} & -c_{12}s_{23} - s_{12}c_{23}s_{13}e^{i\delta_{CP}} & c_{23}c_{13} \end{bmatrix} \tag{1.32}$$

In this equation $s_{ij} = \sin\theta_{ij}$ and $c_{ij} = \cos\theta_{ij}$. Of these three mixing angles, θ_{12} is referred to as the solar angle and θ_{13} is called the atmospheric angle according to the sources from which they are derived [21]. The oscillation is dependent on both these angles and on the squared mass differences between the corresponding neutrinos, which are therefore known, even if the absolute masses are not[11]. This leaves open the possibility of two different hierarchies of the neutrino mass eigenstates $\nu_{1...3}$. This is the Neutrino Hierarchy Problem. By convention, $m_{\nu 1} > m_{\nu 2}$; the question is whether $m_{\nu 3}$ is heavier or lighter, respectively corresponding to the Normal mass Ordering and the Inverted mass Ordering. Recent experiments have provided more accurate measurements on the final mixing angle θ_{23} and the complex phase, which paves the way to the eventual solution to the ordering question.

The existence of massive neutrinos has opened up multiple possibilities for BSM physics. It has given rise to the question of neutrinos having Dirac or Majorana masses, the latter case indicating that neutrinos are their own antiparticle. Neutrinos would then be the only Majorana fermions of all particles in the Standard Model. Additionally it allows the inclusion of right-handed counterparts to the exclusively left-handed neutrinos (and left-handed counterparts to right-handed antineutrinos) that exist in the Standard Model. Given the absence of observations of these neutrinos, they would either have to be sterile, carrying additional quantum numbers that prevent their decay to or interaction with currently known particles, have only very small coupling to known particles, or be heavy enough to be out of reach of the current generation of particle accelerators.

1.3.2 Dark Matter

The proposition of dark matter is supported by a series of observations that seem to confirm matter- and gravitation-related effects requiring an undiscovered type of exotic, invisible matter. One of these observations is of the rotational spectrum of the interstellar gas of galaxies as a function of its distance from the galactic center. The measured rotational velocity is higher than expected when assuming only visible matter and the current formulation of gravity [23], suggesting the presence of additional matter within the

[11] constraints on the absolute masses come from cosmological sources measured by different experiments [22].

galactic halo[12]. Since this discovery was made, other phenomena have arisen that reinforce a belief in the existence of additional matter in the galaxy beyond what is currently visible. These phenomena include the curvature of light in gravitational lensing observations [24], the temperature non-uniformity in the present-day cosmic microwave background [25], and the large scale structure formation of the universe [26]. These later observations, coupled with the observation of accelerated inflation of the universe, has also led to hypothesis of Dark Energy, present in even greater abundance. Current measurements predict a universe of about 4.9% ordinary matter, 26.8% dark matter and 68.3% dark energy [25].

Although competing explanations exist that explain these phenomena individually without requiring additional types of matter, no alternative theory has been developed far enough to explain all these aberrations simultaneously. If dark matter were to exist, it would be in the form of a particle or particles which are mostly inert. Baryonic and electromagnetic interactions are forbidden due to the absence of observations that would be indicative of its presence in this scenario. Interaction through the weak force is neither required nor precluded. Most particle physics experiments however search for dark matter through couplings with the weak force or a new force mediated through Higgs bosons. Many different dark matter candidates are predicted by various theories and are captured under the umbrella term Weakly Interacting Massive Particles (WIMPs). Theories that predict additional, heavy neutrinos have become popular candidates for dark matter.

1.3.3 Matter-antimatter asymmetry

In the previous section antiparticles were introduced. Prevailing theories surrounding the Big Bang predict the production of an amount of antimatter equal to the amount of ordinary matter [27]. Given that these types of matter interact almost identically and particles colliding with their antiparticles annihilate, one would expect all matter to have either vanished through annihilation or remain in equal quantities. And while most matter did annihilate in this manner, the present-day universe, features a notable lack of any antimatter. A small amount of ordinary matter remained after the Big Bang whereas its antimatter counterpart did not.

The Standard Model does allow for the laws of nature coupling differently to matter and antimatter in the weak sector, and experiments have confirmed this happening. This asymmetry could lead to the current excess of ordinary matter. The underlying principle is called baryogenesis, the creation of baryonic matter out of energy. The criteria for baryogenesis to occur include B violation[13], charge and CP-violation, and a deviation from thermal equilibrium [28].

The Standard Model does provide processes that can satisfy the first two conditions (the third condition is provided through the expansion of the universe) [29]. The rates by which these processes can occur are dependent on two particular parameters in the Standard Model: the CP-phase term of the CKM matrix and the Yukawa coupling terms for the quarks [30]. Given that these parameters are measured, it can be tested if the Standard Model is sufficient for the production of the amount of matter that is present in the universe. It has been found that the Standard Model is insufficient [27]. Additional interactions that go beyond the SM are required.

[12]Or a modification of Newtonian dynamics, which is an alternative theory but which lies outside the realm of particle physics.

[13]Baryon number conservation is one of the accidental global symmetries in the Standard Model.

1.4 Model-independent searches for exotic physics

The previous section has demonstrated some of the shortcomings of the Standard Model. Attempts to address these outstanding issues by extending the Standard Model generally lead to a hypothesis of one or more new exotic particles. This provides experimenters with the motivation to pursue further experiments to seek evidence for the existence of such particles.

There's a large amount of exotic physics models that predict decays leading to three-lepton and four-lepton final states. Many, although not all, of these models include the production of heavy leptons, particularly neutrinos, in one way or another, as this class of particles is particularly well-suited to solve the shortcomings of the current Standard Model discussed in the previous sections. Such neutrinos would be WIMPs, making them valid Dark Matter candidates. They would also be required to be sterile to account for the lack of decays observed thus far. They would also fill the slot that has opened up for an extension to the Standard Model due to the discovery of massive neutrinos. Finally, they provide a gateway to potential Lepton Flavor Violation (LFV) phenomena through which the baryon asymmetry of the universe can be explained [31].

Examples of theories featuring the desired final state include SUSY neutralino and chargino production [32], SUSY di-Higgs production [33], and through multiple types of seesaw models [34]. Two examples of such theory models which shall serve as benchmark comparisons for the wider model-independent search later in this thesis will be given. Before this, however, a quick diversion is needed to motivate the choice of using the final state of three or more charged leptons to detect these BSM signatures.

The choice of using specifically the light charge leptons is due to the relatively clean signature that these particles will produce in detector experiments. Both the electron and muon are stable particles[14], meaning they can be observed directly, rather than their presence being implied by the detection of their decay product. Conversely, many heavier particles, including postulated BSM particles, can be expected to partake in decay chains with these leptons as the final product.

The heaviest lepton, the τ, is expected to be produced in equal quantity as a light lepton in decay chains, assuming that lepton universality holds[15]. Because of this, an analysis that focuses exclusively on final states with light leptons does not miss out on its ability to detect any BSM theories. While it does lose some sensitivity by not studying the hadronic decay mode of τ leptons, the search is still offered some sensitivity to τ lepton through its leptonic decay channels: The τ lepton is expected to decay into either an electron or muon about $^1/_3$rd of the time [20]. This means sensitivity to the τ is maintained without the need for inferring a τ progenitor particle from hadronic decay products, a process which requires significant additional effort.

Understanding the value of this particular set of final states, the rest of this section discusses examples of exotic physics the analysis regions would be sensitive to.

[14]The muon lifetime is actually 2.2×10^{-6} seconds, but this is considered stable in high energy physics.
[15]Not all BSM theories assume this.

1.4.1 The Type-III Seesaw Mechanism

The discovery of neutrino oscillations has mandated the addition of massive neutrinos to the existing Standard Model. With this addition, one would have to explain the smallness of these masses compared to those of quarks and leptons. The most straightforward way to do this is to construct an effective field theory on top of the SM, valid at some energy scale Λ [35]. This effective field theory consists of one additional dimension-five operator invariant under $SU(3) \times SU(2) \times U(1)$ that generates neutrino Majorana masses through Yukawa couplings. The operator is given in Equation 1.33

$$\lambda_{ij}\Lambda^{-1}\phi^0\phi^0\nu_i\nu_j \tag{1.33}$$

In this equation λ_{ij} is a (possibly energy-dependent) Wilson coefficient [36], Λ is the cutoff scale, ϕ^0 is the second component of the Higgs doublet, and ν_i the neutrino part of the $SU(2)_L$ lepton doublet, both of which have been introduced in Section 1.1.3. Indeed, all models of neutrino mass and mixing, assuming no additional light particles beyond what is available in the SM were added, will include this operator for the generation of light neutrino masses [37].

Obtaining this operator at tree-level using only renormalizable interactions can be realized through three distinguishable models, called the seesaw models [37]. Neutrino masses arise from the eigenvalues of a 2×2 matrix, the most general mass matrix allowed by gauge invariance of the SM action, and the corresponding charges of the lepton and neutrino fields. For one of these eigenvalues to be small, corresponding to the small neutrino masses, assuming no excessively deviant values of the Yukawa coupling, the other eigenvalue must be significantly large, invoking the image of a seesaw. Since information on neutrino masses is limited to upper bounds and relative mass differences between eigenstates, there is no theoretical guidance for the expected mass of these heavy leptons beyond the argument of naturalness preferring a Yukawa coupling constant close to unity.

The lepton multiplets that are allowed are limited by what can be formed through the combination of the lepton doublet and the Higgs doublet that currently exist in the SM. Three possibilities exist, corresponding to the types of seesaw: Type-I [38] requires a fermion singlet. The mediator leading to Equation 1.33 is a heavy neutrino N. For each of the three light neutrinos to be massive one heavy neutrino is required, hence this type of seesaw model usually introduces three fermion singlets. Type-II [39] introduces a scalar triplet. It does not need any heavy right-handed neutrinos to be introduced as its mediator, but instead introduces three scalar particles with total absolute charges of 0, 1 and 2. Only one such triplet is required to generate masses for each generation of neutrinos. The Type-III [40] seesaw introduces a fermion triplet. The new particles generated by this theory include heavy neutrinos and heavy charged leptons. Three such triplets would lead to three non-vanishing neutrino masses, although strictly speaking only two triplets are required to fit the current observations of the neutrino mass differences. These triplets of the Type-III seesaw model would be produced mainly in pairs in the proton-proton collisions at the LHC through gauge coupling [41].

Each of the seesaw models can lead to three- or four-lepton final states. Type-III models additionally can lead to final states with five or more leptons [34]. For the purposes of this analysis, the Type-III model will be considered in cases where three or four lepton

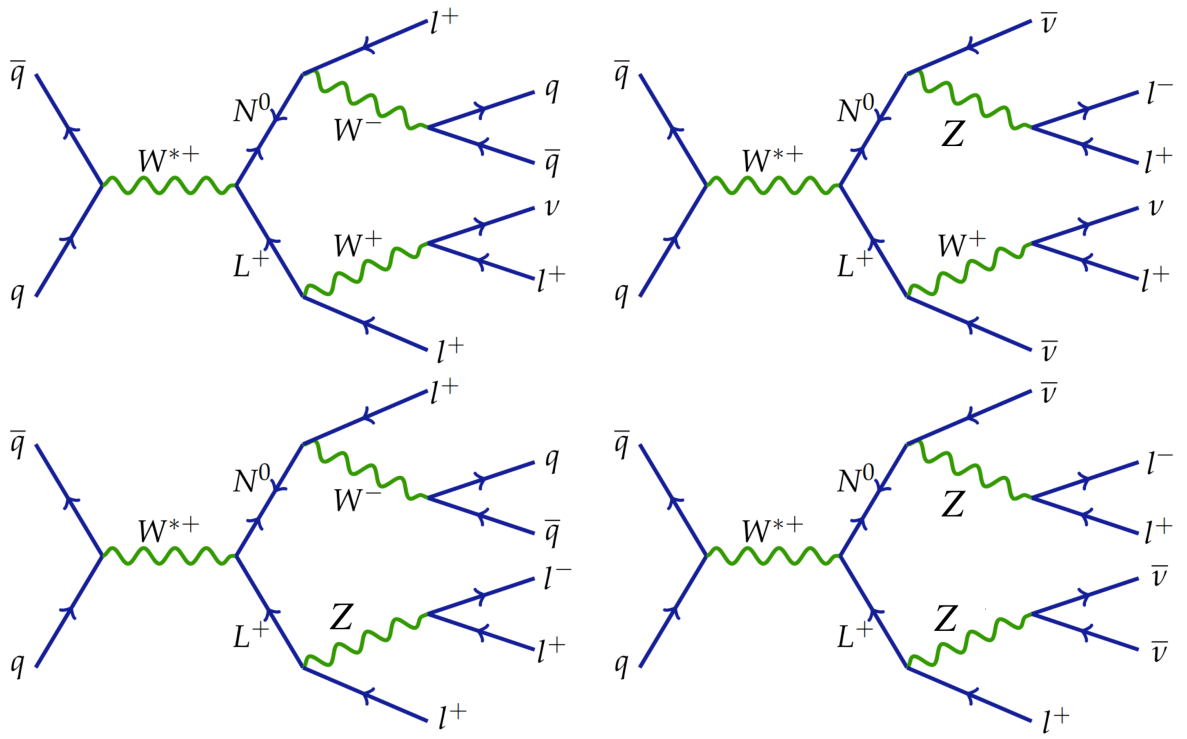

Figure 1.4: Feynman diagrams demonstrating how the Type-III seesaw mechanism can lead to final states containing three or four charged leptons through the heavy W-like boson production process $W^{\pm} \to L^{\pm} N^0$.

final states are produced. For this, it is necessary to understand the allowed decay modes of the heavy leptons, which are given in Equation 1.34.

$$\begin{aligned} L^{\pm} &\to \ell^{\pm} H \\ L^{\pm} &\to \ell^{\pm} Z \\ L^{\pm} &\to \nu W^{\pm} \\ N^0 &\to \nu H \\ N^0 &\to \nu Z \\ N^0 &\to \ell^{\pm} W^{\mp} \end{aligned} \tag{1.34}$$

The bosons thus produced have decay chains resulting in light leptons [20] which can therefore lead to higher lepton multiplicities. Nearly all production modes also include at least one neutrino in their final state. Heavy lepton pairs can be produced in the LHC either through the Drell-Yan process $q\bar{q} \to Z \to L^+ L^-$ or via W-boson production (including W-like heavy bosons introduced by various BSM theories, such as the Wino in SUSY [42]) facilitated through $q\bar{q} \to W^{\pm} \to L^{\pm} N^0$. Example Feynman diagrams by which the Type-III seesaw produces three- and four-lepton final states are shown in Figure 1.4.

1.4.2 The doubly-charged Higgs Particle

As discussed in the previous section, the Type-II seesaw model predicts as a new particle a doubly-charged scalar [43], but there are many other models in which the doubly-charged Higgs is a requirement. These include the left-right symmetric (LRS) models [44] (as well as supersymmetric left-right models [45]) or, scalar singlet dark matter [46] or the Zee-Babu model [47]. A common feature of these theories is that they introduce at least one Higgs triplet to extend the Standard Model [48, 49].

For this section, the doubly-charged Higgs is considered in the context of the LRS model[16]. This model is a unified gauge theory, providing full lepton-quark symmetry of the weak interaction [50]. In these models, parity is an exact symmetry of the Lagrangian, only broken spontaneously due to the form of the scalar field potential.

The LRS model introduces a left-handed and a right-handed $SU(2)$ triplet. The neutral component of the right-handed triplet acquires a vacuum expectation value, breaking the $SU(2)_R$ symmetry and generating large Majorana masses for the right-handed neutrinos, which in turn explains the smallness of neutrino masses.

Two doubly-charged scalar particles arise from these triplets: $H_R^{\pm\pm}$, a $SU(2)_L$ singlet coupling to *right-handed* leptons, and $H_L^{\pm\pm}$, contained by the $SU(2)_L$ triplet which couples to the *left-handed* leptons. They may also couple to W-bosons, allowing for an additional production mode apart from Drell-Yan pair production and an additional decay mode. The ability to detect doubly-charged Higgs decays in charged lepton final states is dependent on the vacuum expectation value v_Δ of the neutral members of the triplet [51]. The decay channels are given in Equation 1.35. The doubly-charged Higgs has (lepton-flavor violating) leptonic decay modes, both same-flavor and mixed-flavor. It can also decay to a pair of W-bosons.

$$\begin{aligned} H^{\pm\pm} &\to \ell_1^\pm \ell_1^\pm \\ H^{\pm\pm} &\to \ell_1^\pm \ell_2^\pm \\ H^{\pm\pm} &\to W^\pm W^\pm \end{aligned} \tag{1.35}$$

The value of v_∂ determines the coupling of the $H^{\pm\pm}$ to W-bosons. If v_∂ vanishes, the decay modes of $H^{\pm\pm}$ are entirely leptonic and the branching fraction $\Gamma(H^{\pm\pm} \to W^\pm W^\pm) = 0$. Additionally in this case, production of the particle at the LHC from quark-antiquark collisions is then in the form of pair production predominantly mediated through the Drell-Yan process.

The cross-section of this process is a function of only the electroweak quantum numbers and the mass of the particle. However, the ratio of cross sections between the left-handed and right-handed triplets is different due to different couplings to the Z-boson: The left-handed boson $H_L^{\pm\pm}$ is produced 2.3 times as often.

The partial decay width of $H^{\pm\pm}$ to lepton pairs is then determined from Equation 1.36 [52]. Here $k = 1$ for same-flavor, 2 for mixed-flavor lepton combinations, $h_{\ell\ell'}$ is the relative strength of the Yukawa coupling per flavor combination which must be determined [53,

[16] This is strictly in the context of producing a comparison model for the analysis. Properties of the theorized triplet fields are model-independent.

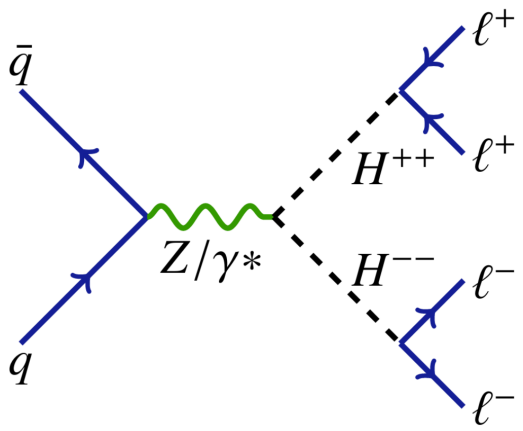

Figure 1.5: Feynman diagram of a four charged lepton final state through the production of a doubly-charged Higgs pair accommodated by the Drell-Yan process.

54], and M is the particle mass. Current experimental upper limits on $h^2_{\ell\ell'}$ do not indicate a preference for decays into τ-leptons over the lighter flavors [53].

$$\Gamma(H^{\pm\pm} \to \ell^{\pm}\ell'^{\pm}) = k\frac{h^2_{\ell\ell'}}{8\pi}M \tag{1.36}$$

Figure 1.5 shows the Feynman diagram of doubly-charged Higgs pair production through the Drell-Yan process as it might occur from proton-antiproton collisions at the LHC. Theoretical calculations have predicted that this process is the dominant production channel for the production of this new particle [44, 55].

1.5 Event Generation

In order to predict the consequences of SM and BSM processes inside the ATLAS detector, we need a way to provide a detailed description of their properties and behavior. This can be accomplished through a combination of *event generation* and *detector simulation*. This section describes how features of a particle physics process are simulated. The aspects of simulating an *event*, a single particle collision and the associated secondary interactions, are discussed. The concepts of event generators and the simulation of the ATLAS detector environment are also introduced.

The most important components of event generation are the hard scattering (HS) process and the parton shower (PS). One must also consider the additional interactions within a proton-proton collision producing additional objects that together make up the underlying event, and how a generated HS is matched to a PS and scaled to the interaction cross-sections. A schematic representation of a fully generated event is shown in Figure 1.6. The paragraphs below discuss the aspects of event generation.

Of the multiple partons contained within a proton, one parton pair of the pp-collision is responsible for the largest transfer of momentum. This is the hard scatter, and due to its potential to create the heavier particles of the SM (and the potentially even heavier particles of BSM models), it is the most important part of an event. Computing the hard

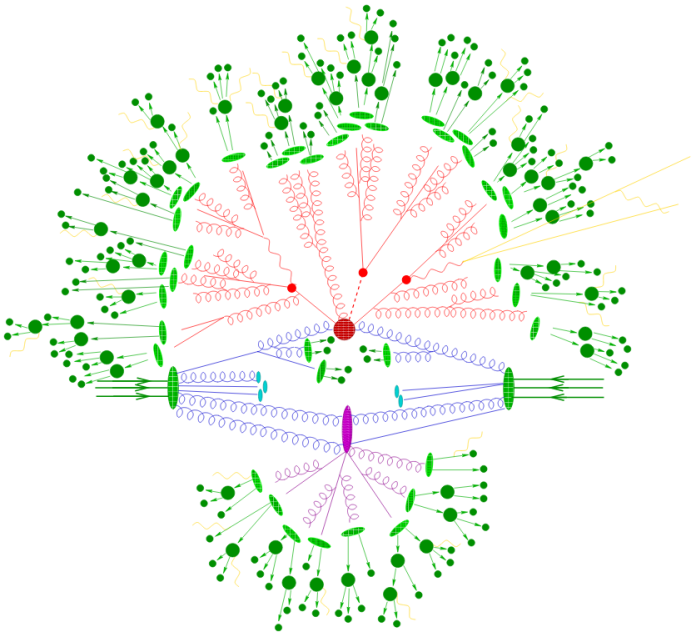

Figure 1.6: Representation of an event simulated by a generator. The central red blob represents the hard scattering, while the resulting decay chains are shown the red lines and secondary blobs. Secondary event interactions taking place in the underlying event are shown in purple. Light green ovals represent the hadronisation of colored particles, while dark green lines are the resulting hadrons undergoing additional decays. Yellow lines are the particles created due to photon radiation [56].

scatter requires calculation of the matrix element (ME), the Lorentz invariant amplitude. The internal parton structure of the proton is also needed, but due to infrared divergence (Section 1.1.2) cannot be calculated perturbatively. Instead, this information is provided through precision measurements, the outcome of which is a set of parton distribution functions [57]. Sets of parton distribution functions, computed by means of the factorisation theorem [58], give the probability of finding partons inside the proton with a given four-momentum fraction at a particular energy scale, thus quantifying the relative occurrence of particular interactions. PDFs at different energy scales can then be obtained through extrapolation.

Parton showers are created by colored particles which undergo radiation, expending their initial energy. Colored particles are initially radiated off the particles that enter into or exit from the HS, processes being called initial state radiation (ISR) and final state radiation (FSR) respectively. Showering is a recursive process, propagating and creating new colored particles as long as the available energy allows it. The final products of a parton shower are colorless particles owing to color confinement. Therefore, the final step of simulating a parton shower involves a computation of the hadronization products.

If both these components are simulated, a calculated ME for a HS interaction must be combined with an appropriate PS model. For this, one must take into consideration potential double-counting of higher-order corrections affecting the final jet multiplicity due to the creation of additional partons. Other interacting partons of the underlying event (UE) must also be taken into account, which despite being of lower momentum can nevertheless lead to additional showers and contribute to the particles in the final state. The processes which can facilitate this step are referred to as matching and merging [59, 60].

Each of these steps can be accomplished by applying developed software algorithms known as *event generators* based on Monte Carlo (MC) simulation. MC simulation refers to the repeated application of random sampling of a particular process to obtain a distribution, henceforth referred to as a sample. When provided with accurate physics model parameters based on precision measurements, generated samples become an excellent way to model the expected contribution of known physics process in observed data. Samples can also be created using hypothetical model parameters to simulate a potential contribution of currently undetected BSM physics. Either way, MC generators are well-equipped to handle the simulation of particle physics processes, with a proven track record as a tool for precise predictions of scattering cross sections and event topology.

Delivering the simulation steps described above is a joint effort performed by a combination of algorithms [61–64]. Algorithms used for this analysis, which particle physics processes and event aspects they simulate, are the focus of Section 5.1.

Chapter 2

The LHC and the ATLAS Detector

The Standard Model described in the previous chapter is a comprehensive review of the current understanding of particle physics. As has been established however, it as of yet fails to account for certain experimental results. Modern experimental particle physics is focused both on testing Standard Model processes to ever greater precision as well as searching for signatures of physics that fall outside of what is currently explained by the Standard Model. In order to facilitate such endeavours, experiments are designed and constructed. The Large Hadron Collider [65–68] is one such experiment.

This chapter delves into the Large Hadron Collider and the detector that is to be used in the analysis described in this thesis: the ATLAS detector [69–71]. First, the purpose and capabilities of the LHC itself will be explained in Section 2.1. The ATLAS detector and its components will be described in Section 2.2.

2.1 The Large Hadron Collider

The Large Hadron Collider or LHC is a circular collider with a circumference of 27 kilometers. It was constructed for the purpose of accelerating and colliding protons or atomic nuclei with each other. It is situated in a tunnel between 45 and 170 meters underground at the CERN facility, situated in the Geneva region near the French-Swiss border. The LHC saw its first run between the years of 2010 and 2012. After a shutdown in order to to improve and enhance its capabilities the accelerator then started run 2 which lasted from 2015 to 2018. It is the particle collisions measured during this second run that will be studied by this analysis.

The collisions of interest for this analysis are between protons. Protons are obtained from hydrogen gas: Molecular hydrogen in the gas is split into hydrogen atoms and stripped of its electrons to obtain protons. Prior to collision they are accelerated to a velocity over 99.99% of the speed of light.

The protons undergo multiple preparatory steps prior to their injection into the main tunnel of the LHC which contains the main experiments [68]. First, the protons are accelerated in the LINAC 2, a linear accelerator, where they reach a momentum of 50 MeV. Subsequently the protons reach the PS Booster where they are accelerated to 1.5 GeV. After the PS booster the particles reach the Proton Synchotron (PS) and the Super Proton Synchotron (SPS), circular accelerators where the protons reach energies of respectively 26 GeV and 450 GeV. Reaching this energy, the particles are introduced into the main tunnel. This series of accelerators can also be seen schematically in Figure 2.1.

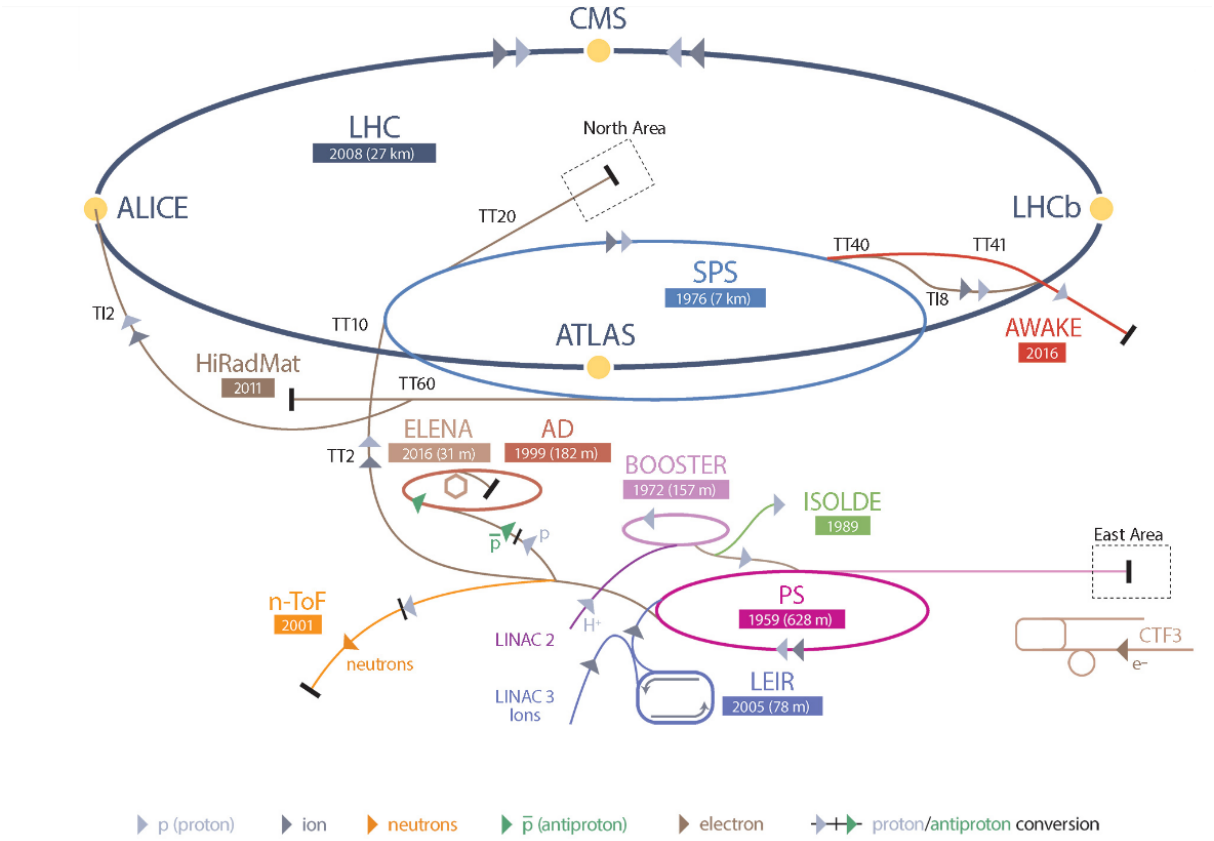

Figure 2.1: Schematic view of the components that make up and contribute to the Large Hadron collider, showing the 27 km main tunnel, the experiments attached to it, and the various accelerator components. Image from [72].

Furthermore, a 400 Mhz superconducting radio frequency (RF) cavity system allows for storage of the particles and separates them into distinct groups called bunches. These bunches are intended to separate the time between collisions to 25 ns, equivalent to a bunch crossing frequency of 40 MHz.

The LHC is designed to operate at a center-of-mass energy of $\sqrt{s} = 14$ TeV. However, in run 2 of the LHC the actual operating center-of-mass energy has been $\sqrt{s} = 13$ TeV. Thus, protons in the main tunnel of the LHC need to be accelerated to an energy of 6.5 TeV. In order to facilitate this acceleration within the available circumference a series of 1232 superconducting dipole magnets is required which can bend the particles' trajectories in the tunnel at high energy [66, 73]. These magnets are each 15 meters long, use a current of 11 kA and operate at a temperature of 1.9 K. This allows the magnets to achieve a peak magnetic field strength of 8.3 T. The dipole magnets actually feature two separate beam bores, with opposite magnetic fields, which allows counter-rotating positively charged particles to be accelerated simultaneously.

Data-taking is divided into distinct periods called runs which begin at the injection of the proton beam. Throughout a single run the collimated beam must be guarded against injection errors and against effects like Coulomb repulsion, synchrotron radiation and intra-beam-scattering. A variety of systems exist to ensure beam stability. Longitudinal injection errors are prevented by the RF cavity system mentioned above, while transverse injection errors are prevented by a separate system of electrostatic deflectors. Furthermore,

a system of 392 quadrupole magnets exist to stabilize the magnetic field and continuously focus the particle beams.

The LHC tunnel has four straight sections. These are the designated particle collision points and house the major experiments of the LHC. These four major experiments are ATLAS, CMS [74], LHCb [75] and ALICE [76]. The locations of these detectors in the LHC tunnel are also shown in Figure 2.1. Of these, the ATLAS detector is the focus of this analysis and will be further described in Section 2.2.

2.1.1 Data taking at the LHC

Experiments connected to the LHC are interested in measuring the decay products of individual collisions between accelerated particles. A single collision measurement is called an *event*. To explain how the LHC delivers events to be recorded, two additional terms need to be explained first: *Luminosity* and *pileup*. The subsequent sections will be dedicated to defining these terms, concluding with a description of the values of these quantities during operation.

Luminosity

Luminosity is a good quantification of the amount of particles that are brought together for collision over a given unit of time, thus being a measure of the expected event rate [77, 78]. The total amount of events delivered by the LHC can be expressed as a function of its integrated luminosity, which itself is a function of the instantaneous luminosity over time, as given in Equation 2.1.

$$N_{event} = \mathcal{L}\sigma_{event} \text{ where } \mathcal{L} = \int L dt \tag{2.1}$$

Here the number of events is expressed as a product of $\mathcal{L}$, the integrated luminosity over a data taking period, and the interaction cross-section σ_{event}. The integrated luminosity is computed from the instantaneous luminosity, which is dependent on the properties of the LHC beam. Its design criteria specify the instantaneous luminosity to be $10^{-34}\text{cm}^{-2}\text{s}^{-1}$, but its actual operating luminosity will have to be determined explicitly. At ATLAS the LUCID-2 [79] detector has the function of measuring the luminosity. The formulaic determination given here is adapted from [80] and assumes Gaussian shaped beams colliding head-on, with an additional corrective term applied for the actual crossing angle. The computation of instantaneous luminosity is shown in Equation 2.2.

$$L = \frac{f_{rev} N_b^2 n_b \gamma_r}{4\pi(\sigma^T)^2} S \text{ where } S = \left(1 + \left(\frac{\theta_c \sigma_z}{2\sigma^T}\right)^2\right)^{-0.5} \tag{2.2}$$

Here N_b is the amount of protons per bunch, which is squared because two bunches each containing N_b particles collide when beams cross; n_b is the amount of bunches per beam; f_{rev} is the revolution frequency of the beams (11.2455 kHz); γ_r is the Lorentz factor known from special relativity and is another way of expressing the beam energy (7 TeV by design, 6.5 TeV during operation in run 2); σ_T is the transverse RMS beam size at the interaction

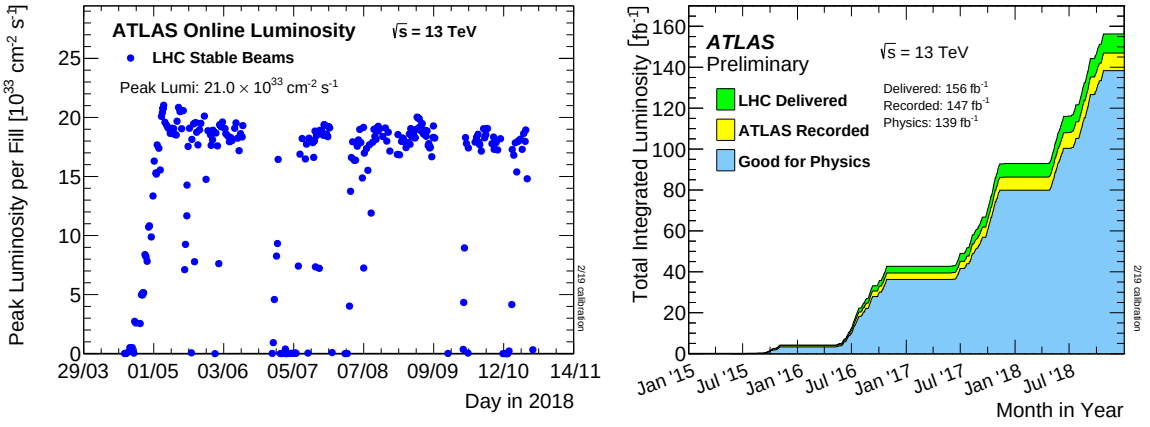

(a) (b)

Figure 2.2: Plots describing the luminosity throughout run 2 at the LHC, showing (a) the peak instantaneous luminosity of the LHC beams over time throughout run 2 and (b) the total amount of integrated luminosity delivered by the LHC, recorded by ATLAS and useful for physics. Images taken from [81].

point. Additionally, the corrective factor S represents the loss of luminosity of the beams due to the crossing angle (θ_c) at the interaction point, again assuming identical Gaussian bunches, where σ_z is the RMS bunch length.

Figure 2.2 shows the operating instantaneous luminosity of the LHC throughout the duration of run 2 and the total amount of integrated luminosity captured. Integrated luminosity is typically given in inverse femtobarn (fb^{-1}) owing to cross-sections in particle physics being typically expressed in units of barn ($1\text{b} = 10^{-24}\text{cm}^2$).

Pileup

A bunch crossing at the LHC can have independent collisions between particles occurring simultaneously. The overlap of the products of such interactions can be a factor in the reconstruction of the events measured by a detector. As such, a new term is required to quantify the multiple of inelastic interactions occurring per bunch crossing. This term is the *pileup* (μ) and it is computed by Equation 2.3 [82]:

$$\mu = \frac{\sigma_I \, L}{n_b f_{rev}} = \frac{\sigma_I N_b^2 \gamma_r}{4\pi(\sigma^T)^2} S \tag{2.3}$$

Here n_b and f_{rev} are the amount of bunches per beam and revolution frequency, as introduced earlier; σ_I is the proton-proton inelastic cross section. This cross section can be estimated for a particular center-of-mass energy. For ATLAS it was determined to be 78.1 ± 2.9 mb using rings of plastic scintillators in the forward region of the detector, which was then extrapolated to the full phase space [83]. The time dependence of the pileup can be inferred due to its dependence on the instantaneous luminosity. Protons inside each bunch gradually deplete over the duration of a single run, causing a reduction of luminosity and therefore the average rate of collisions during a single bunch crossing. Although collisions of protons within the same bunch would otherwise act independently,

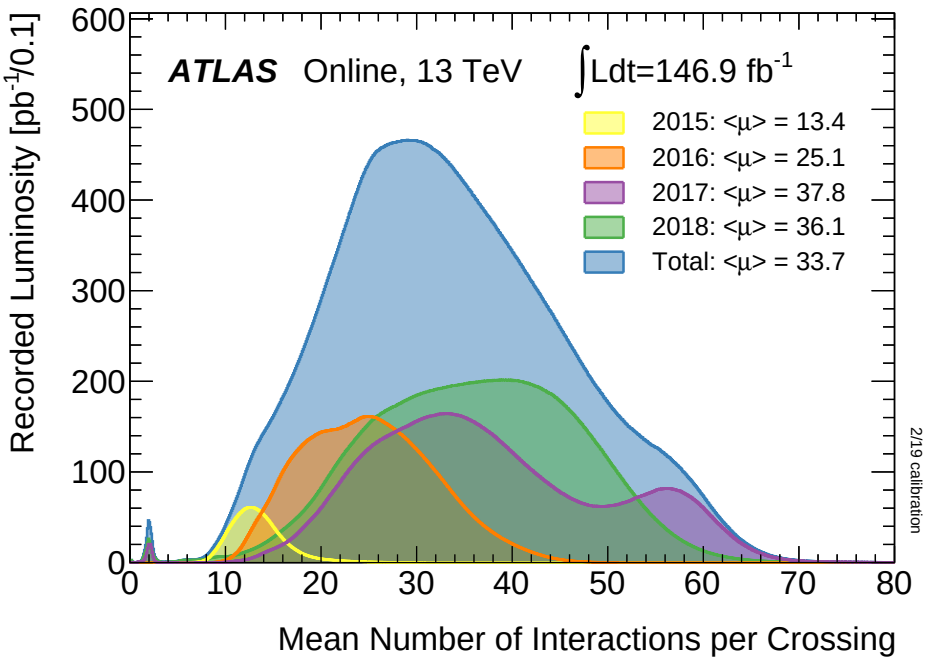

Figure 2.3: Plots describing the recorded luminosity for different amounts of pileup throughout run 2. The mean pileup ($\langle\mu\rangle$) distribution is given both per data-taking year and in total throughout run 2. Image taken from [81].

this difference in pileup over time must nevertheless be taken into consideration as a property of an event as it affects the efficiency of reconstructing the event from its decay products.

Figure 2.3 shows the pileup profile of the ATLAS detector. The profile is different for each data-taking year because the instantaneous luminosity changed over the course of run 2. The mean pileup $\langle\mu\rangle$ is also given in this plot, both for each data-taking year and in total. The total mean pileup is established to be $\langle\mu\rangle = 33.7$.

In measured data, pileup is a continuous variable related on the instantaneous luminosity. However, Monte Carlo events are simulated under a discrete pileup value. The pileup of an event can influence the efficiency of several reconstruction algorithms and as such the pileup distribution of an event set should match between observed data and generated Monte Carlo distribution. However, differences between these pileup distributions are observed. To rectify this, each Monte Carlo event is scaled by an associated weight that reflects the ratio between data and background at a particular pileup value [84].

***

The definitions of luminosity and pileup have now been established. Table 2.1 gives an overview of the parameters during operation of the LHC. The number of bunches per beam (n_b), the protons per bunch (N_b), peak instantaneous (L) and integrated ($\mathcal{L}$) luminosity, and the average pileup ($\langle\mu\rangle$) are given for each data-taken year and then contrasted with their design values. Together, these values make up a quantitative description of the proton beams used in the LHC during run 2.

Parameter	design	2015	2016	2017	2018
Maximum number of filled bunches	2808	1380	2232	2208	2556
Protons per bunch [10^{-11}]	1.15	1.2	1.18	1.3	1.1
Peak Luminosity [10^{34} cm^{-2} s^{-1}]	10.0	5.02	13.8	20.9	21.0
Delivered integrated Luminosity [fb^{-1}]	80-120	4.2	38.5	50.2	63.3
Recorded integrated Luminosity [fb^{-1}]	n/a	3.9	36.1	46.9	60.6
Average interactions per bunch crossing (pileup)	25.0	13.4	25.1	37.8	36.1

Table 2.1: parameters of the LHC beam throughout run 2 given per year, contrasted with the provided design parameters. Given values are taken from [85] while design values come from [66].

2.2 The ATLAS detector

The ATLAS detector [69–71] is a multi-purpose detector designed for the (successful) experimental discovery of the Higgs boson, performing unparalleled precision measurements on known Standard Model processes, and the search for signatures indicating potential exotic physical processes. A schematic overview of the detector is given in Figure 2.4.

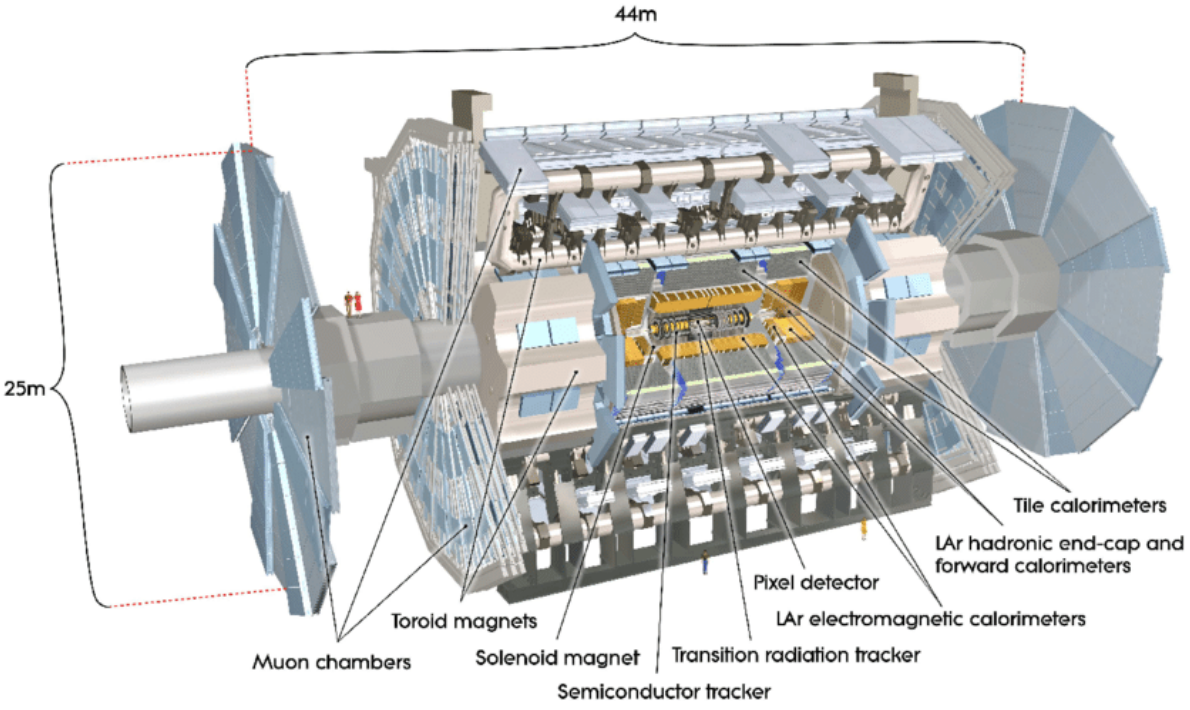

Figure 2.4: Schematic depiction of the ATLAS detector revealing and labeling the sub-detectors it contains [86].

The detector features almost full coverage of the 4π solid angle around the interaction point, down to a few degrees from the beam direction. It is transverse and forward-backwards symmetric and would be cylindrically symmetric but for one of the sub-detectors (the Muon Spectrometer). Layers of the detector are oriented in different ways with respect to the beam pipe: cylindrical around the beam, referred to as the *barrel*, or transverse to it, in which case it is called either the *end-cap* or *forward* depending on the component being respectively far or near the incoming beam.

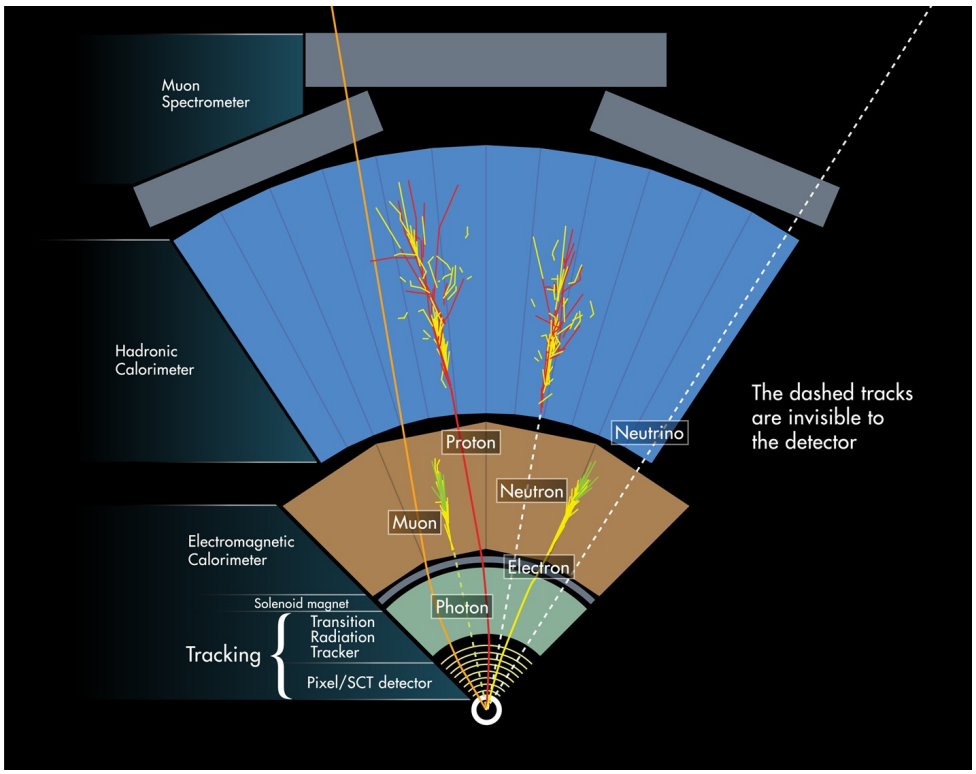

Figure 2.5: Schematic view of the different types of particles that traverse the ATLAS detector, showing their interactions with the detector subsystems and the tracks they leave [87].

Because the trajectory of detected particles is crucial information a coordinate system around the beam interaction point is defined. The z-axis is the longitudinal axis, defined to be collinear to the proton beams, while the x and y axis point towards the LHC center and upwards respectively. More prominent, however, is the use of polar coordinates: θ being the polar angle and ϕ being the azimuthal angle. Often-used quantities derived from these are the *pseudorapidity* η and the relative angular distance ΔR, expressed in Equation 2.4. These quantities provide useful angular information for particles: From the pseudorapidity one can determine which parts of the detector the particle intersects with, which is of consequence to the ability to reconstruct the particle later. From relative angular distance one can determine if particles are either collinear or *back-to-back*, suggesting the possibility of a common origin.

$$\eta = -\ln\tan(\theta/2),\ \Delta R = \sqrt{\Delta\eta^2 + \Delta\phi^2} \tag{2.4}$$

A closer look at the ATLAS detector reveals multiple constituent layers concentric around each other and the beam interaction point. The detectors that make up ATLAS are sensitive to properties of different types of particles. From the inside out, the sub-detectors are the Inner Detector, the Calorimetry system, and the Muon Spectrometer. ATLAS furthermore includes a magnet system and a trigger system. Each of these components and its purpose will be explained in the sections that follow. The different particle flavors and their tracks as observed or invisible by components inside ATLAS are shown in Figure 2.5.

2.2.1 Magnet System

The Magnet System [88] provides the bending power required to curve the trajectory of charged particles, which is required for the momentum and charge measurements by the ATLAS sub-detectors. The degree of deflection is indicative of a particle's momentum while the direction of the curvature can be used to determine the particle's charge. For its purposes ATLAS has opted for an arrangement of multiple magnets, a central solenoid surrounding the Inner Detector and three toroid magnets located inside the Muon Spectrometer.

Solenoid Magnet

The solenoid magnet [89] is composed of 9 km of superconducting wire which generates a magnetic field of 2T oriented along the z-direction within the volume of the Inner Detector. Due to it being located in front of the calorimeter system the coil must be designed to be as thin as possible to minimize interference of the material with detector operations, yet without sacrificing its operational stability.

Toroid Magnet

There are three toroid magnets [90, 91], one in the barrel region and one in each end-cap, all located around the outer parts of ATLAS. This outer location lets the toroid magnets exercise a field over the outermost detector component, which is the Muon Spectrometer (MS). This makes muon momentum measurement in the MS possible based on track curvature. The toroid magnet features over 100 km of superconducting wire designed to operate at a temperature of 4.5K (actual temperature during operation is 4.7K). In total these magnets are capable of generating a magnetic field of 4T.

2.2.2 The Inner Detector

The Inner Detector (ID) reconstructs the trajectories of charged particles from the beam interaction point to the calorimeters [92, 93]. It is sensitive to the direction, momentum and charge of the decay products of proton-proton interactions. Being the system closest to the beam, it is the most compact and most sensitive sub-detector, but is also the most afflicted by degradation due to radiation. The Inner Detector is shown in Figure 2.6.

The ID itself is made up of four components. Starting closest to the beam, these are the Insertable b-layer (IBL), the Pixel Detector, the Semiconductor Tracker (SCT) and the Transition Radiation tracker (TRT). Each of these will be discussed in the following paragraphs.

Insertable b-layer

The IBL [95–98] is the new innermost component of the ID. It was installed in 2014 at a radius of 3.325 cm from the beam, taking advantage of a new smaller radius of the beam pipe. The IBL maintains or improves ATLAS tracking performance close to the beam pipe which is especially important for the identification of decay products originating from the unstable b-quark. It consists of 14 carbon fiber staves 64 cm long and 2 cm across each containing 20 silicon pixel modules [99], of which 12 are two-chip planar modules and 8

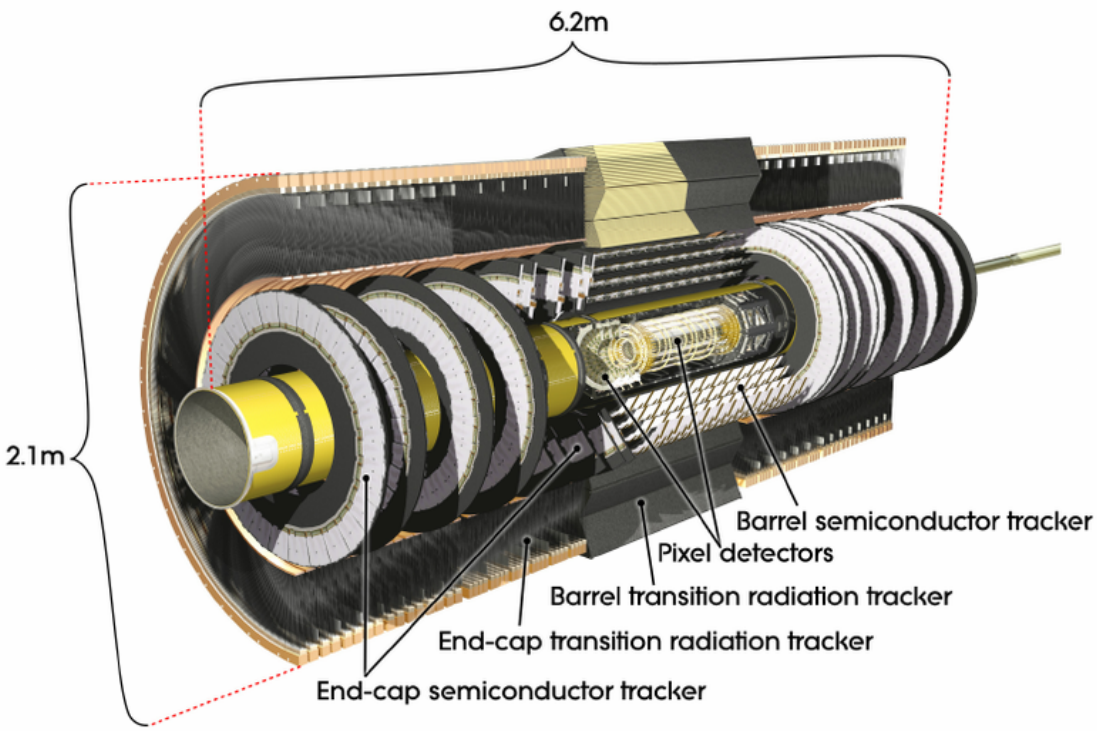

Figure 2.6: Cut-away rendition of the ATLAS Inner Detector [94].

are single-chip modules with 3D sensors. This means that each stave is instrumented with 32 chips which each contain 26880 pixels 50×250 µm^2 in size [97]. This gives the IBL a transverse and longitudinal resolution of 8.5 µm and 47 µm respectively.

Pixel Detector

The pixel detector [92, 98, 100] offers a high-granularity, high-precision set of measurements as close to the interaction point as possible. It is located at the radius between 5.1 to 12.3 cm around the beam. Its proximity makes it pivotal for distinguishing primary from secondary vertices, revealing if detected particles originate directly from collision or arise due to secondary decay processes. For this purpose it consists of 1744 modules spread over three barrel layers (1456 modules) and three disks in each end-cap (288 modules). Each module contains over 46000 readout channels which each services one pixel 50×400 µm^2 in size. In total, the Pixel Detector features 80 million pixels over an area of 1.7 m^2. This detector has a resolution of 10 µm and 115 µm in the transverse and longitudinal direction [99].

Semiconductor Tracker

The SCT [101] is a silicon microstrip detector that provides precision measurements in the intermediate radial range. It consists of 4 barrel layers which are located at radii between 30 and 52 cm away from the beam, and 18 planar end-cap disks. As its sensors silicon wafers are used, divided into 4088 modules, 2112 in the barrel layers and 988 per end-cap [101]. Each barrel or disk provides two strip measurements from two sensor pairs glued back-to-back at a stereo angle of 40 mrad. These strip measurements are combined to build space-points. A total of 6.3 million readout strips are interspersed across the

silicon with a separation of 80 µm. The silicon detector achieves an intrinsic resolution of 17 µm.

Transition Radiation Tracker

The TRT [102] is the outermost component of the ID, being situated at a distance between 55 and 108 cm from the interaction point. The TRT is a straw tracker consisting of a collection of tubes filled with gas to detect crossing particles. It is made up of 350848 gas-filled straw tubes that are 4 mm in diameter. These tubes are divided among 96 modules in 3 barrel layers, and among 40 modules for each of the four end-cap disk (160 modules total, 80 on each side). Each straw's wall is made out of kapton and reinforced with carbon fibre for rigidity, leading to a thickness of 71 µm. At its center there is a gold-plated tungsten wire with a diameter of 31 µm.

The walls and central wire are held at a relative potential difference of 1530V so that each straw functions as a drift chamber. When a charged, relativistic particle such as an electron traverses the boundary of media with differing dielectric constants, it radiates energy proportional to its Lorentz factor in the form of photons. Photons ionize the gas through the photoelectric effect, at which point the freed electron drifts towards the anode (the wire) due to the potential difference. Readout equipment at both ends captures the conducted signal and determines the location of the ionization based on the time difference between detection at both ends. The measurement precision of this detector is 0.17 mm.

2.2.3 Calorimeter System

The purpose of a calorimeter is to measure energy deposits due to incident particles. To be most effective, such a measurement must be destructive, meaning the absorbing power of a calorimeter must be greater than the energy spectrum of particles it intends to study. Calorimeters typically consist of a high-density passive material, meant to absorb the energy of traversing particles, and an sensitive active material with which the measurement is performed. The active and passive material are placed in alternating layers orthogonal to incoming particles.

The ATLAS calorimeter system [103, 104] exists out of multiple calorimeters which target different classes of particles. It is depicted in Figure 2.7. The calorimeter system provides coverage in a pseudorapidity range of $|\eta| < 4.9$. The sub-components are the electromagnetic (ECal) and hadronic (HCal) calorimeters. They will be described individually in the oncoming paragraphs.

Electromagnetic Calorimeter

The electron and photon are particles which are capable of creating electromagnetic (EM) showers. In such a shower incident particles create more electromagnetic products which diverge in a branching structure. The driving processes behind electromagnetic showers are bremsstrahlung and e^+e^- pair production which will continue as long as the energy of the shower components is sufficient.

The ECal is designed with the purpose of triggering such showers and absorbing their contents with the intent of measuring the incident particle energy. The active material used for this purpose is liquid argon (LAr) kept at a temperature of 90 K, while the passive

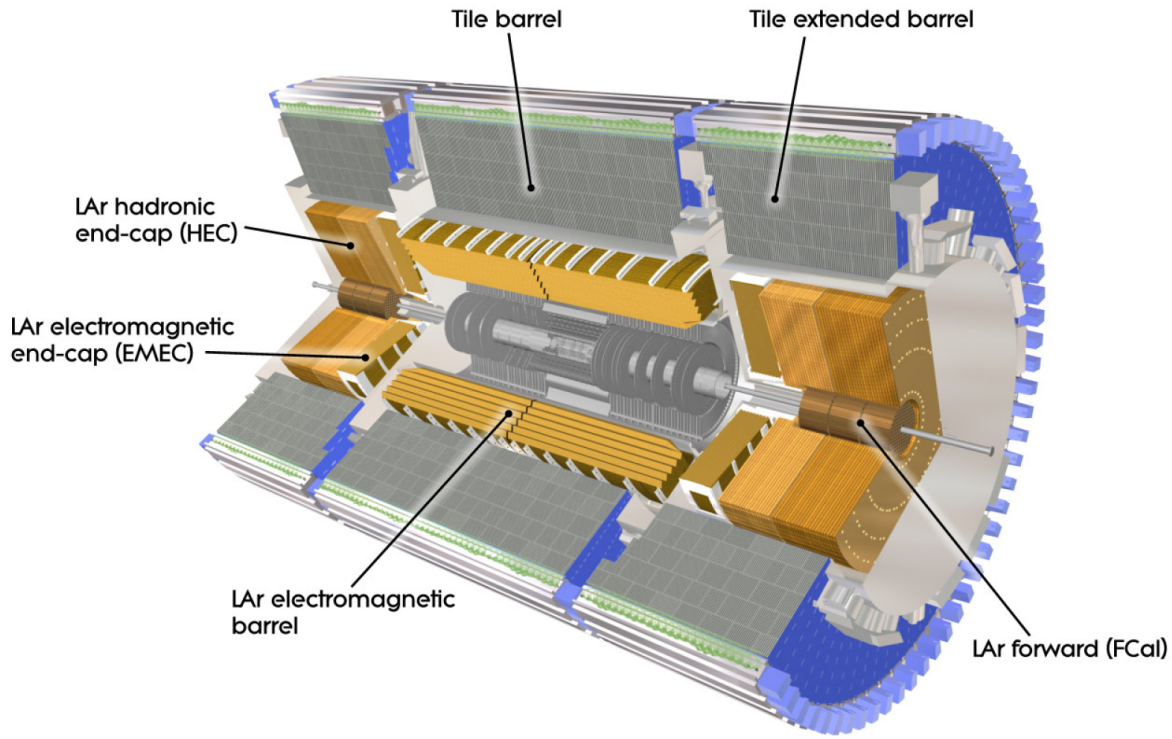

Figure 2.7: Cut-away rendition of the ATLAS calorimeter system [94].

material is lead. The calorimeter has a single 6.4 m long, 53 cm thick barrel providing a coverage of $|\eta| < 1.475$ and two 2.08 m long, 63 cm thick end-cap disks which cover pseudorapidity range $1.375 < |\eta| < 3.2$.

The ECal consists of three layers of differing thickness, each of which is made up of cells with cell sizes differing between layers. The thickness of each layer is best described in radiation lengths, a feature of EM showers. The first layer is 4.3 radiation lengths in thickness with cell sizes of $\Delta\eta \times \Delta\phi = 0.003 \times 0.1$. This layer is finely segmented in the η direction to allow for precise measurement of e.g. photon direction, equipping the ECal to separate overlapping photon pairs originating from the decay of energetic π^0 hadrons. The second layer spans 16 radiation lengths with cells $\Delta\eta \times \Delta\phi = 0.025 \times 0.025$ in size, being the largest layer thus meant to absorb the bulk of an EM shower's energy. The third layer is only 2 radiation lengths with cell sizes $\Delta\eta \times \Delta\phi = 0.05 \times 0.025$. Due to its placement, this layer allows distinguishing an EM shower from its hadronic counterpart, which is to be absorbed by the hadronic calorimeter described below.

Hadronic Calorimeter

Placed on the outside of the ECal are the components that makes up the hadronic calorimeter [105]. Indeed, its purpose is to measure energy deposits from hadronic showers which are expected to penetrate past the ECal. It is made up of multiple components: A tile calorimeter and a LAr end-cap, and a forward calorimeter (FCal).

The tile calorimeter consists of a central and two extended barrels which are made out of multiple wedges. The passive material used in this calorimeter is steel while plastic scintillator tiles make up the active material. 64 wedges occupy the central barrel, each of

them 5.6 m long, for a coverage of $|\eta| < 1.0$. The extended barrels each contain another 64 wedges 2.6 m in length which together cover the pseudorapidity range $0.8 < |\eta| < 1.7$. These barrels are also separated into three layers: The central barrel has layer thicknesses of 1.5, 4.1 and 1.8 nuclear interaction lengths, and the extended barrel thickness is 1.5, 2.6 and 3.3 interaction lengths. Photomultipliers reading out the scintillator data provide an effective cell size of $\Delta\eta \times \Delta\phi = 0.1 \times 0.1$.

The end-cap region for the hadronic calorimeter features a LAr calorimeter where copper is used as the passive material. Two wheels with a radius of 2.09m and thicknesses of 0.8m and 1.0m on each side are placed directly after the EM end-caps. This results in a total depth of about 10 nuclear interaction lengths. There is also a calorimeter in the forward region very close to the beam pipe. This forward calorimeter uses both copper and tungsten because it serves to absorb both hadronic and electromagnetic interactions.

2.2.4 The Muon Spectrometer

Although the calorimeter system, due to its thickness and full coverage, stops most incident particles, all but the lowest-energy muons are able to traverse it. In order to detect muons, the outermost and most voluminous sub-detector of ATLAS is the Muon Spectrometer [106, 107] (MS). The magnetic field from the toroid magnet system allows it to derive direction, momentum and charge of muons from measuring bent trajectories. The MS is shown in Figure 2.8.

A total of 4000 individual muon chambers leveraging four different technologies makes up the volume of the MS. These four technologies make up the two different subsystems which serve distinct purposes: The *Precision Chambers*, which emphasize high-precision spatial measurements of incident muons, and the *trigger Chambers*, emphasizing fast response times.

Precision Chambers

The precision chambers perform the high-sensitivity measurements of muon tracks from which charge and momentum are determined. The dominant technology used in most of the muon spectrometer are Monitored Drift Tubes (MDT). These are drift chambers formed by aluminum tubes 3 cm across and between 0.85 to 6.5 m long. These tubes are filled by a gas mixture kept at a pressure of 3 bar, which is ionized by traversing muons. From the drift time of the electrons thus liberated the location of the muon crossing point can be pinpointed with a precision of 80 µm. The drift tubes are mounted as three chamber layers in the barrel region (located 5 m, 7.5 m and 10 m from the interaction point), and on four large wheels in the end-cap region (at distances of 7.4 m, 10.8 m, 14 m and 21.5 m). They provide a coverage of $|\eta| < 1.0$ and $1.05 < |\eta| < 2.7$ in the barrel and end-caps respectively.

The pseudorapidity region $2.0 < |\eta| < 2.7$ has significant background flux (neutrons and photons) which warrants a precision detector with higher granularity. For this purpose the Cathode Strip Chambers [108] (CSC) features alongside the MDTs on the innermost wheel in the end-cap region. CSCs are multi-wire proportional chambers featuring central anode wires surrounded by two layers of orthogonal layers of cathode strips. When compared to MDTs, the CSCs have a lower sensitivity to neutrons and photons but have a better spatial resolution of 60 µm.

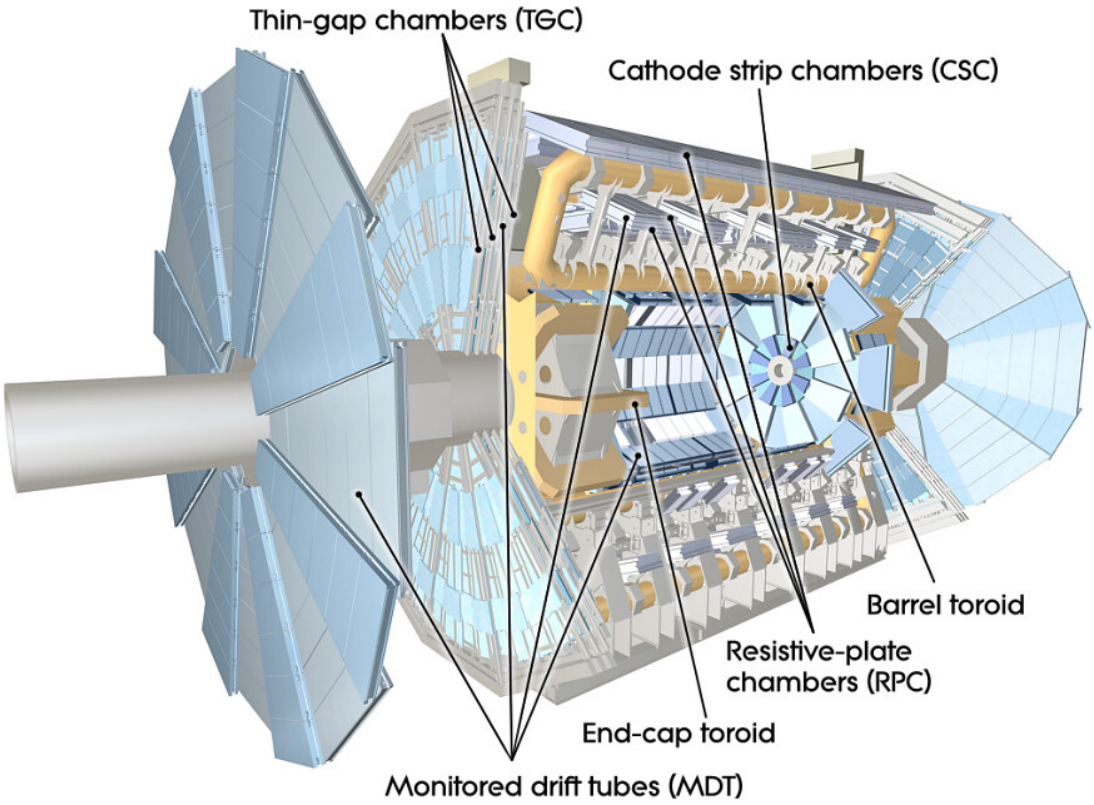

Figure 2.8: Cut-away rendition of the ATLAS muon spectrometer [94].

Although precise, the response time of the precision chambers is insufficient for triggering purposes, with drift times upwards of 800 ns for certain detections [109]. For this reason, the MS features a second set of chambers, explained in the next section.

Trigger Chambers

Different chamber types are used in the barrel and the end-cap region due to the expectation of different particle rates in these regions. Both are characterized by the fast response times needed to handle background and associate tracks to a particular bunch crossing at the interaction point.

Resistive Plate Chambers (RPC) are used in the barrel. They provide a coverage of $|\eta| < 1.05$. Each chamber uses gas gaps 2mm across. Muons ionizing the gas in this volume trigger an avalanche, a self-perpetuating multiplication of photons, under the influence of a 5000 V/mm electric field. Resistive bakelite plates on either end of this volume are then connected by this ionized gas. The resulting localized charge is collected and read by one of the four planes of copper read-out strips. This whole process provides a time resolution lower than 2 ns.

In the end-cap the Thin Gap Chambers (TGC) are used. These are multi-wire proportional chambers which provide a coverage of $1.05 < |\eta| < 2.4$. The titular thin gap refers to the 1.4 mm space between its anode and cathode plates which is such that it provides a time resolution of 4 ns and a spatial resolution between 2 and 7 mm depending on the muon direction.

2.2.5 Trigger and Data Acquisition System

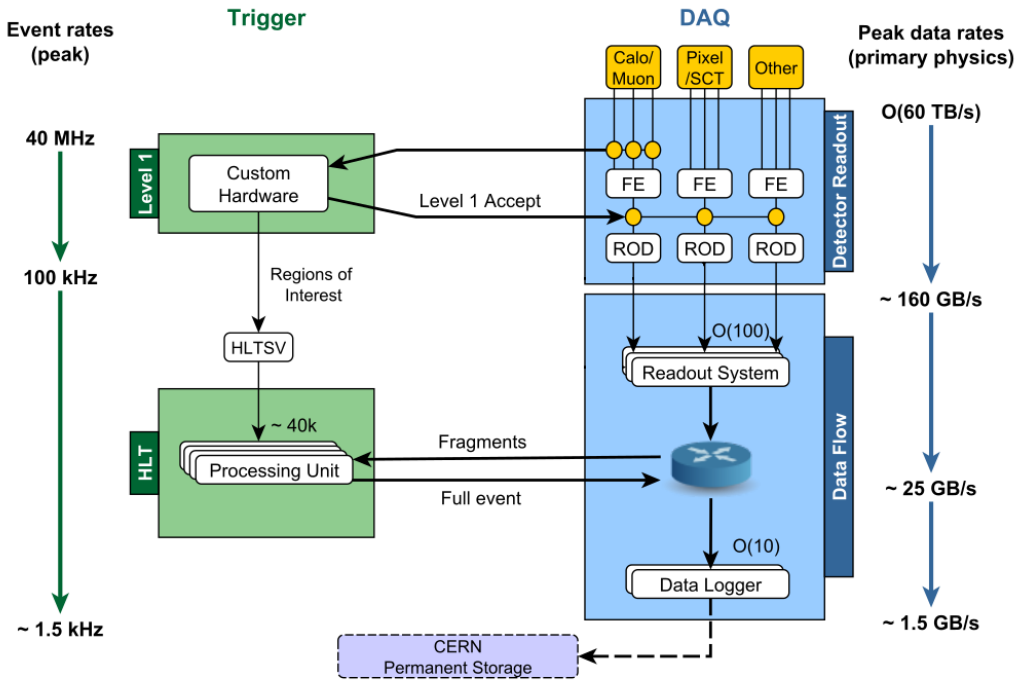

Figure 2.9: Flowchart diagram of the ATLAS Trigger and Data Acquisition system in Run 2 showing expected peak rates and bandwidths through each component. Image taken from [110].

The trigger system [111–113] is crucial to data acquisition in the ATLAS experiment due to its ability to limit recording of data only to events of interest. Given the high occupancy of the detector during operation and the bandwidth limitations of the transmission and recording infrastructure, the design of a system to filter and select events based on preset parameters of interests is warranted.

The trigger system sets lower thresholds on the energy and momentum of captured particles, rejecting events that do not pass at least one of its requirements. Furthermore, there is the possibility of accepting only one out of a set number of particular events and discard others. This is referred to as *prescaling* and is usually done for events with particles in the lower energy ranges in order to throttle their demand on the available bandwidth. Prescaling is flexible and can be tweaked based on the instantaneous luminosity (which decreases over the duration of a run, thus permitting a lower prescale over time).

The workflow of the ATLAS trigger and data acquisition system is schematically drawn in Figure 2.9. As can be seen in the figure, there are two distinct components that make up the trigger: the Level-1 and the High-Level Trigger. These will be described in the sections that follow.

Level-1 Trigger

The task of the Level-1 trigger (L1) is to reduce the event rate from the LHC bunch crossing rate of 40 MHz down to 100 KHz. Furthermore, it defines Regions of Interest

(RoI), which are the starting point for software algorithms to base a decision to pass or fail the event on. To accomplish this the L1 uses reduced granularity information from the calorimeters to select particular photon, electron, and hadron energy deposits. Muon L1 trigger information comes from the Trigger Chambers discussed previously in Section 2.2.4.

In addition to selecting on particle energies, a new system allows for the usage of kinematic variables to make more efficient trigger decisions at this level. This system is the Level-1 Topological Trigger [114] (L1Topo). The inputs for the L1Topo are the information received from the L1Calo and muon systems, both of which are forwarded by the output merger systems. The L1Topo is then able to combine these pieces of information. In doing so, additional properties to select on are facilitated, such as the angular separation between particles or the sum of all particle momenta.

High-Level Trigger

Receiving L1 information from the central trigger processor, the High Level Trigger (HLT) has the task of further reducing event rates down to about 1.5 kHz. The HLT is a computer farm where many cached events can be processed in parallel using full-granularity information. The detector components on which it bases its decisions are defined through the RoIs that have been declared by the L1 system. Trigger objects are reconstructed at this level using algorithms that closely match those maintained in the offline reconstruction software. This allows the HLT to predict as accurately as possible the properties of objects in the event, judging whether or not they are of interest to analyses performed by the ATLAS collaboration.

2.2.6 Detector Simulation

In order to ascertain the response of produced particles within the ATLAS detector, the detector environment has also been simulated computationally. This simulation is used with MC generated events (see Section 1.5) in order to observe and calibrate the detector response. For this, the `Geant4` toolkit is used [115]. `Geant4` is able to simulate different materials and the physics processes instigated by particles traversing these materials. A simulation of the ATLAS detector has been produced with this toolkit in order to measure the response of MC events [116]. This simulation includes a thorough study of how emanated particles from a collision process interact with the detector to produce signals that can be compared with what is measured experimentally.

Use of MC generated events in this analysis mandates that the light leptons in which we are interested, electrons and muons, are well simulated. This includes their response to the detector material (tested through `Geant4`), as well as their efficiencies under application of the same reconstruction and identification algorithms as are used on recorded data. Despite best efforts of the ATLAS collaboration in simulating the detector response, slight differences in response between real and simulated events remain (as can be seen in the plots in Section 3.2). Rectifying these differences requires the use of *scale factors*. The derivation of scale factors by comparing measured data to MC generated processes is a topic of discussion throughout Chapter 3.

Chapter 3

Event Reconstruction

The intent of this chapter is to bridge the gap between the measurements made by the ATLAS detector and the fundamental particles to be studied. Particles created by the LHC leave traces of their interaction with the tracking components called *hits* as well as *energy deposits* in the calorimeter system. The process by which these deposits are combined into events and their constituent objects is known as *event reconstruction*.

The first part of this chapter discusses how hits in the detector are combined into *tracks*. Variables by which these tracks can be parameterized are introduced, and the process by which tracks are reconstructed is discussed. These tracks are furthermore extrapolated to their interaction vertices, classifying them as the primary and secondary products of a particular particle interaction. The second part discusses the process by which tracks are combined with energy deposits to construct objects. Objects of interest for this analysis and the criteria by which they are identified are presented. Both parts also highlight the reconstruction efficiency, the leading causes of imperfect reconstruction and their consequences.

3.1 Reconstruction of Tracks and Vertices

3.1.1 From Hits to Tracks

Interactions of particles with the Inner Detector and Muon Spectrometer components leave behind *hits* in the detector layers. Hits are combined to reveal the trajectory of a charged particle traversing the detector. Thus, hits form the basis of the track reconstruction [117, 118].

The algorithm that produces tracks from these hits is the New Tracker (NEWT) algorithm [119]. NEWT is a consolidation of previously competing and disconnected reconstruction algorithms, brought together into a modular design to be able to reconstruct tracks from individual hits for both the ID and MS (discussed in Sections 2.2.2 and 2.2.4). Tracking is organized into three distinct steps: combining clusters of hits from adjacent layers into *seeds*, extrapolation of seeds with further hits inside the ID by means of a Kalman filter [120], and the resolution of ambiguities [121].

The formation of seeds employs an inside-out tracking algorithm which is tasked with combining a cluster of three hits from three distinct layers of the IBL and Pixel[1] detector, and the SCT. From these seeds, initial values of the track parameters are extracted.

[1]The IBL and Pixel detector are considered a component for the purpose of track reconstruction.

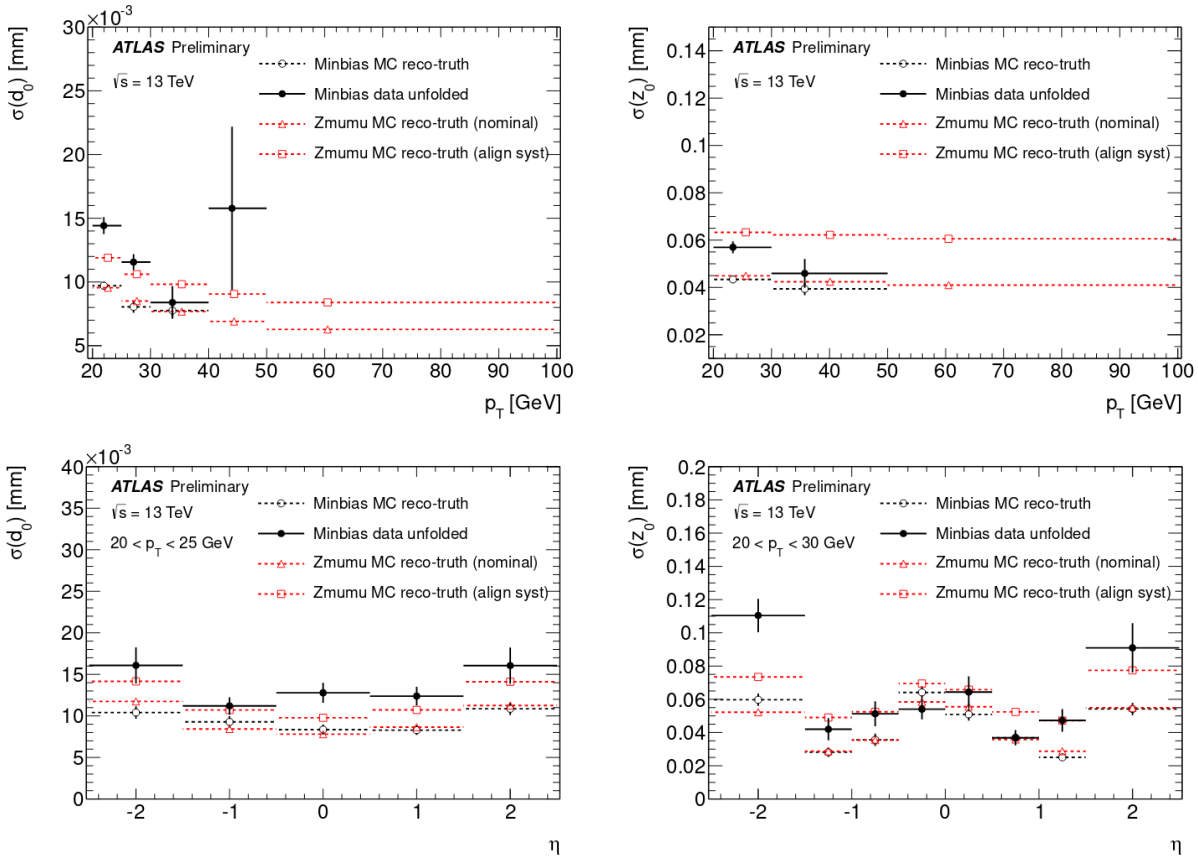

Figure 3.1: Unfolded resolution of the transverse (left) and longitudinal (right) impact parameters plotted as a function of transverse momentum (top) and as a function of pseudorapidity (bottom). Values are shown for both measured minimum bias data and $Z \to \mu\mu$ simulation. For simulation, the resolution is taken as the difference between the truth and reconstructed quantities, while for data the resolution is derived using an iterative deconvolution procedure [122].

Tracks are parameterized locally as helices, reflecting the curved nature of charged particle trajectories under the influence of the magnetic field. The full set of variables which parameterize a track are:

- d_0: the transverse impact parameter. This is the distance of the track from the beam line at the Position of Closest Approach (PCA) in the plane perpendicular to the beam line;
- z_0: the longitudinal impact parameter. It corresponds to the axial coordinate of the PCA where d_0 is measured, defined along the beam line;
- ϕ_0: the azimuthal angle of the track at the PCA;
- θ: the polar angle of the track at the PCA;
- q/p: particle charge divided by momentum. This is an effective proxy of track curvature because the impact of the magnetic field is dependent on these variables.

Since these parameters are important to unambiguously distinguish different tracks originating from different but nearby vertices, the ability to perform precise resolution measurements is mandated. Tests have been performed to extract these resolutions for both measured data and simulation as a function of p_{T} and η [122]. The outcome is presented in Figure 3.1.

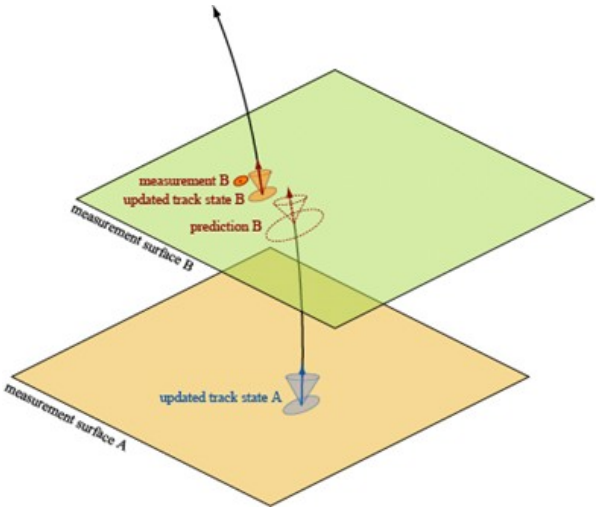

Figure 3.2: Representation of the incremental extrapolation of the discovered tracks by means of integration of additional measurements in adjacent detector layers. Measurements are scored for integration into an existing track by a Kalman filter [123].

When track parameters are determined, additional hits from other layers may be added based on their compatibility. Each additional hit admitted to the track updates (with decreasing impact) the values of these parameters. A Kalman filter is employed to judge the addition of a measurement. This process is shown schematically in Figure 3.2.

Resolving ambiguities means checking for *shared hits*: hits assigned to more than one track in the previous steps. The presence of shared hits within a particular module implies a *shared module* for a track. A Pixel (SCT) module is considered shared if it features at least 1 (2) shared hits. The ambiguity solver also scores tracks negatively based on the presence of holes, defined as intermediate layers that had no hit to be assigned to the scored track. In this step tracks erroneously constructed from an incorrect combination of hits are vetoed.

Two categories are considered for a track to be accepted: *Loose* and *Tight Primary*. The latter set is a strict subset of the former and is designed and optimized for selecting *primary tracks*[2] [122]. The selection criteria of the Loose selection are as follows:

- $p_T > 400$ MeV;
- $|\eta| < 2.5$;
- ≥ 7 Pixel and SCT hits;
- ≤ 1 shared module;
- ≤ 2 holes in total, and ≤ 1 hole in the Pixel.

The Tight Primary selection furthermore imposes the following criteria:

- Pixel and SCT hits at least 9 (11) for tracks with $|\eta| < 1.65$ ($|\eta| > 1.65$);
- At least 1 IBL hit;
- No Pixel holes.

[2]primary tracks are defined as tracks of charged particles with a mean lifetime $\tau > 300$ ps.

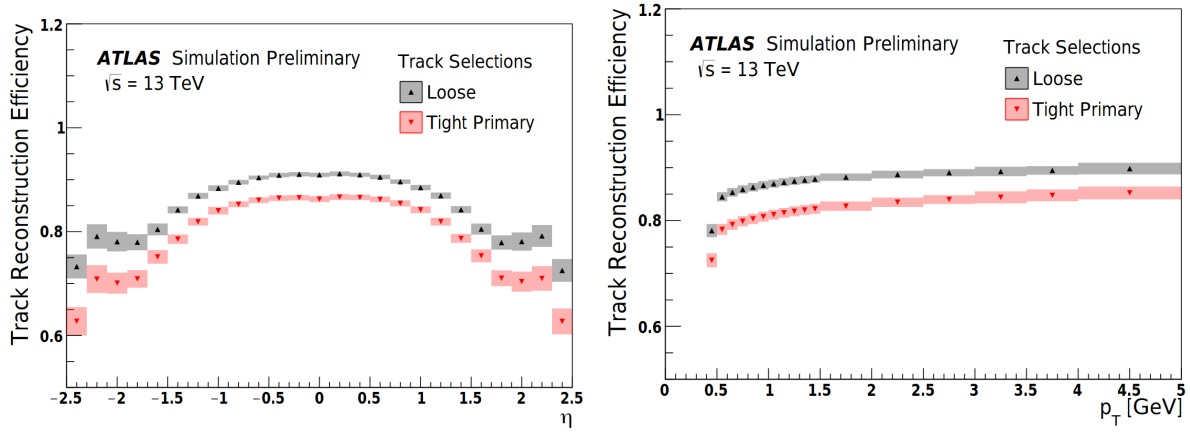

Figure 3.3: Track reconstruction efficiency with uncertainty bands, computed using minimum bias simulated events for Loose and Tight Primary selection criteria. Efficiencies are binned according to truth pseudorapidity (left) and transverse momentum (right) [122].

The efficiencies of these categories are shown in Figure 3.3. The figure shows that the track reconstruction efficiency increases is lower at the lowest transverse momenta and eventually becomes flat with increasing p_T, while for pseudorapidity the efficiency is mostly flat for values of $|\eta| < 1.05$, after which it decreases.

3.1.2 Vertex Reconstruction

Vertex reconstruction [124, 125] is the discovery of a common origin point of identified tracks. Assigning tracks to a vertex is an involved process because multiple proton-proton collisions are expected to occur simultaneously in a single bunch crossing (known as pileup, Section 2.1.1). This step also distinguishes between the primary vertex, the location of a hard-scattering collision, and secondary vertices, which instead indicate the decay location of an unstable particle.

The Iterative Vertex Fitter (IVF) handles the reconstruction of primary vertices in the ATLAS detector for run 2 [118, 126]. The process features three parts: vertex finding, track assignment and fitting. These parts involve multiple steps, a flowchart of which is shown in Figure 3.4. These steps are executed as follows:

- Tracks are selected based on the criteria given in the previous section, creating the *seed pool* from which vertices are composed.
- A vertex seed is created. The location of the seed is a position along the z-axis, whose value is initially determined from the longitudinal impact parameters (z_0) of all tracks in the seed pool.
- An iterative approach is used to find the most likely z coordinate [127]. To associate tracks with the vertex an iteratively-weighted Kalman filter is used, assigning to each track a weight which represents its degree of compatibility with the vertex. The weighted set of tracks is becomes the input of the next iteration of the fitting procedure. Annealing is used to avoid local minima in the optimization.
- Tracks which are incompatible are discarded from the found vertex. Compatible tracks are removed from the seed pool.
- The process repeats using a seed pool containing the remaining tracks.

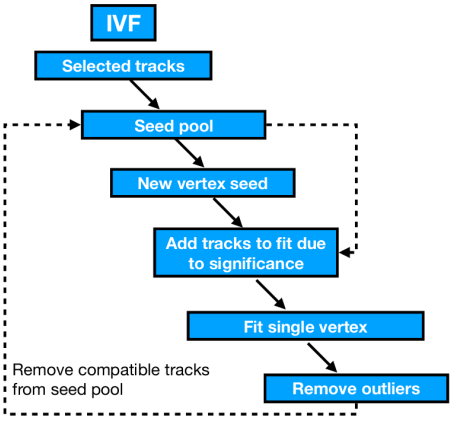

Figure 3.4: Flowchart of the IVF algorithm by which tracks from a seed pool are sequentially assigned to vertices through an iterative vertex fit [128].

The algorithm is robust against incorrectly splitting the actual vertex into two reconstructions, although the iterative approach struggles when facing higher pileup as it risks combining multiple vertices into a single reconstruction [128]. The reconstruction efficiency is positively correlated with a vertex' track multiplicity. These effects are shown in Figure 3.5, which shows the increase in vertex reconstruction efficiency when the number of tracks increases, and Figure 3.6, showing how the selection efficiency and vertex reconstruction efficiency decrease as the pileup (μ) increases.

An uncertainty on the vertex position can occur due to hit cluster errors, ionization energy losses due to material in the detector or the residual misalignment. These uncertainties have been quantified by producing resolution measurements for both measured data and simulation [125]. The values of these two measurements may differ, so scale factors are introduced to reconcile these differences based on the Split-Vertex method [129].

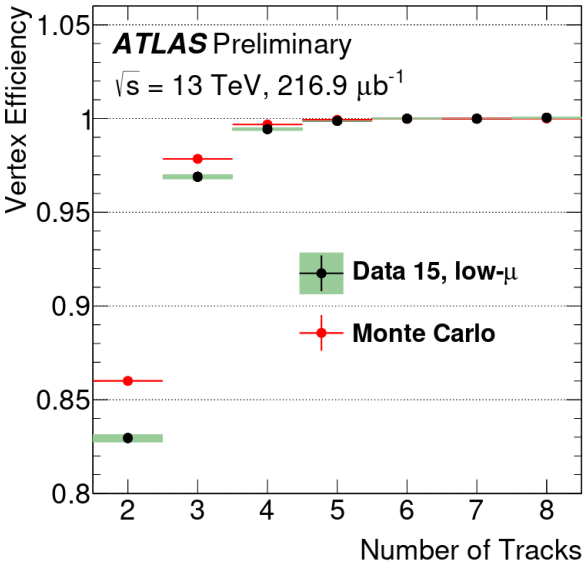

Figure 3.5: Efficiency of vertex reconstruction as a function of the number of tracks in low pileup data [125].

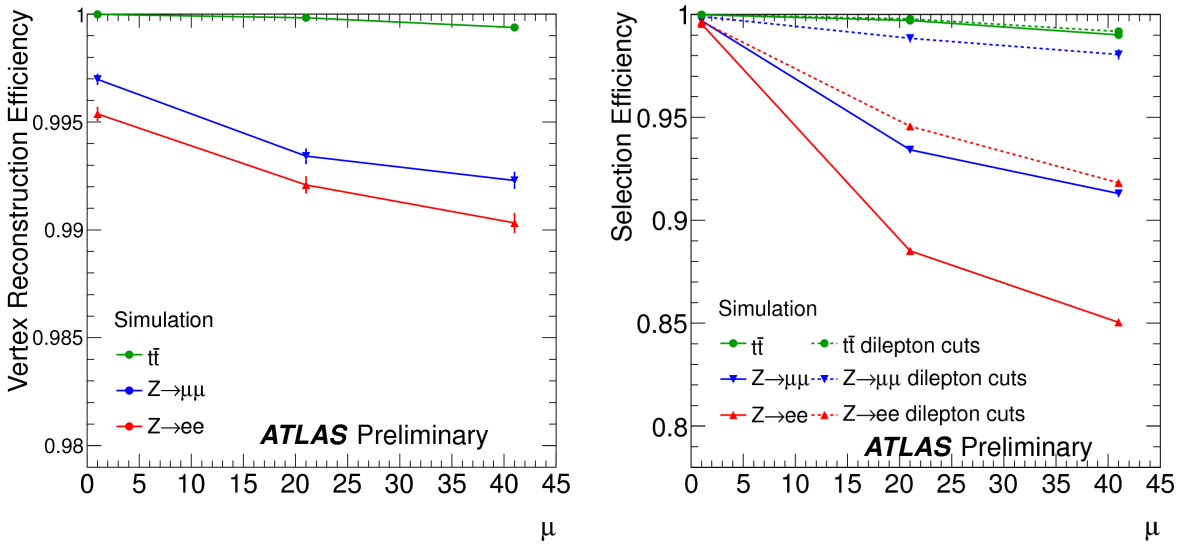

Figure 3.6: Efficiency to reconstruct (left) and to select *and* reconstruct (right) the hard-scatter interaction vertex as a function of average pileup for three distinct physics signatures. Selection criteria of the right plots includes the JVT requirements introduced in Section 3.2.4. Image taken from [130].

3.2 Physics Object Reconstruction

With reconstructed tracks and vertices available, combining this with information on energy deposits from the calorimeters, it is now possible to build the physics objects of interest. Chief among these are the light leptons, electrons and muons, being the primary focus of the analysis. However, there is also vested interest in jets, collimated bundles of hadrons, and the missing transverse energy, which is calculated from the apparent momentum imbalance that remains after all other objects have been reconstructed and is a proxy for the vectorially summed transverse momenta of objects that could not be measured by the detector. This section discusses each of these objects in turn.

3.2.1 Electrons

Section 2.2.3 states that both electrons and photons leave energy deposits in the electromagnetic calorimeter by producing particle showers. This is a destructive measurement, allowing the ECal to absorb all energy of these particles and making it excellently suitable to measure particle energy. Furthermore, hits left by electrons in the ID can be used for the measurement of direction. The photon is invisible in the ID[3] as it is uncharged, and one relies on the finely segmented first ECal layer for its directional measurement. As a consequence, associating a track with an ECal energy deposit is how electrons can be identified [131–133].

To find an ECal energy deposit related to an electron, cluster seeds are first constructed using a sliding-window algorithm [134] across available calorimeter towers within the pseudorapidity coverage. The towers are organized in a grid of 200×256 elements of size $\Delta\eta \times \Delta\phi = 0.025 \times 0.025$. The sliding-window considers an area of 3×5 towers looking for localised energy deposits exceeding 2.5 GeV. Such a deposit becomes the seed of a potential electron candidate. The algorithm iterates in steps of 0.025 in either the η or ϕ direction. Two cluster seeds close in distance are considered conflicting, which is resolved by discarding the seed with the lowest total transverse energy deposit.

Then, the energy deposit is matched to an ID track. Tracks are extrapolated using their determined parameters and matched to cluster deposits in the ECal. For this a Gaussian Sum Filter [135] is used, which is based on a generalisation of the Kalman filter introduced previously. The location of the track must match that of the cluster such that $|\eta_{track} - \eta_{cluster}| < 0.05$ and $-0.2 < q \times (\phi_{track} - \phi_{cluster}) < 0.05$, where q is the reconstructed charge of the track[4]. If multiple tracks can be associated with a single energy deposit, the most compatible track is chosen based on the momentum differences between track and cluster. Because both ID and ECal information is required the pseudorapidity range of electron reconstruction is limited to $|\eta| < 2.5$ and excludes the transition region of barrel to endcap, $1.37 < |\eta| < 1.52$. If no track can be associated with an energy deposit, the particle is classified as a photon instead.

Efficiency of the electron reconstruction is judged through the $Z \to ee$ decay, which is a well-understood process with variables such as cross-section and decay widths having been accurately determined. The efficiency depends on the transverse momentum of the

[3] Unless it converts into an e^+e^- pair due to interaction with detector material.

[4] Another ϕ requirement is applied if the reconstructed momenta of the track and cluster differ [131]. This requirement is asymmetric to account for the momentum loss due to Bremsstrahlung.

electron, with higher p_T values being more efficiently reconstructed, and its pseudorapidity. This is shown in Figure 3.7.

Once the electron candidate is found, it needs to be identified as a prompt electron, differentiating it from misidentified hadrons (which can also leave tracks and ECal energy deposits), electrons from photon conversion or from semileptonic hadron decay[5]. For this, the steps of *identification* and *isolation* are employed. When considering these criteria one must be mindful of the trade-off between correctly accepting real electrons (*real efficiency)* and erroneously accepting fake electrons (*fake efficiency*). Different sets of selection criteria called *working points* are provided to cater to differing needs of analyses.

The identification algorithm is a multivariate analysis which uses likelihood-based scoring of the electron candidate using variables such as the shower shape observed by the ECal, penetration of the particle into the hadronic calorimeter, track properties, quality of track-cluster matching and Bremsstrahlung effects. Several sets of scoring thresholds are provided in the form of working points, called *Loose*, *Medium* and *Tight*. Tighter working points reject electron candidates more aggressively, lowering both real and fake efficiency rates. Tighter working points are strict subsets of their looser counterparts, meaning all electrons passing *Tight* selection necessarily pass *Medium* selection, which in turn necessarily pass the *Loose* selection. The efficiencies of each of these identification working points plotted as a function of p_T and η is shown in Figure 3.8.

Electron isolation measures the total transverse energy of particles collinear to the electron candidate (E_T^{cone}) and compares it to the transverse energy of the candidate ($E_T^{electron}$). Isolation of the electron is useful in distinguishing prompt electrons from those created inside jets. The isolation algorithm can use information both from tracks and from energy deposits in the calorimeter. Working points are established here which vary the threshold of ratio $E_T^{cone}/E_T^{electron}$, the width of the cone (expressed in ΔR), which can either be fixed or gradual based on the energy signature, or which sub-detectors information is drawn from. Isolation working points available during run 2 include `FCLoose`, `FCTight` and `Gradient` [137]. The efficiencies of each of the `FCTight` isolation working point plotted as a function of p_T and η are shown in Figure 3.9.

The curvature of the electron track under the influence of the magnetic field is used to measure its charge (from the direction of curvature). However, it is possible for an electron's charge to incorrectly assigned by the detector, in which case it becomes a *charge-flipped* electron. To understand the frequency of incorrect assignment of electron charge, scale factors have been calculated based on $Z \to ee$ charge measurements in both data and Monte Carlo events.

3.2.2 Muons

The reconstruction of muons [138] starts out from track candidates identified by the NEWT algorithm. It differs from electron reconstruction by the detector components that are involved in the process, which for muons are the ID and the Muon Spectrometer (MS) (the calorimeters have a limited role in certain fringe cases). As it happens, the NEWT algorithm is capable of track reconstruction using inputs from both these sub-detectors [119]. The first step of muon reconstruction is performed in both of these components independently.

[5]Electrons from leptonic τ decay are also considered prompt for our purposes.

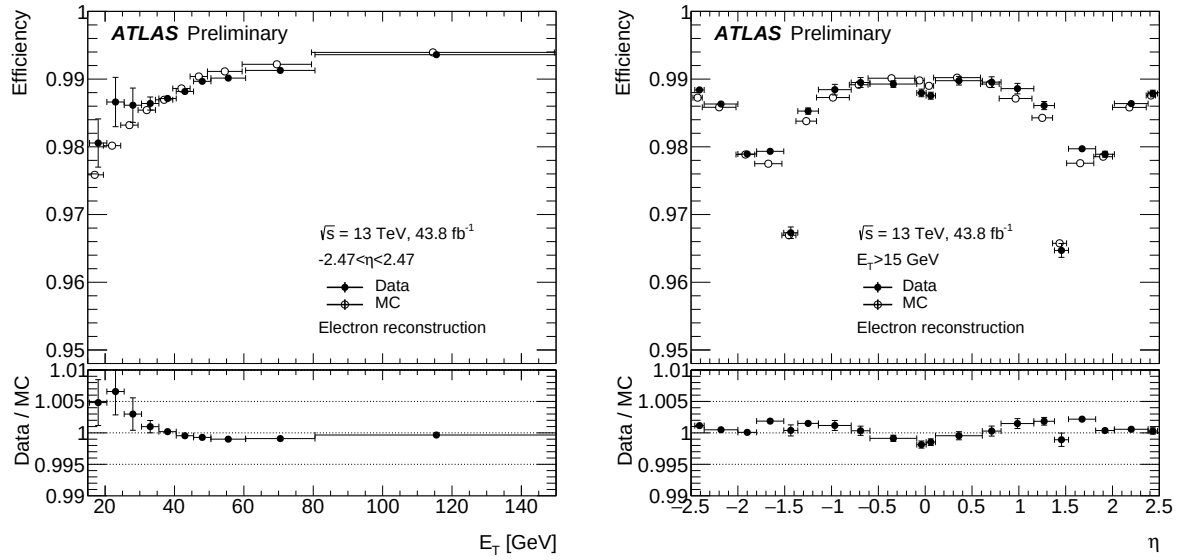

Figure 3.7: The reconstruction efficiency relative to reconstructed clusters as a function of electron transverse momentum (left) and pseudorapidity (right). Detected electrons originate from the $Z \to ee$ process, measured for both real data and simulated events [136].

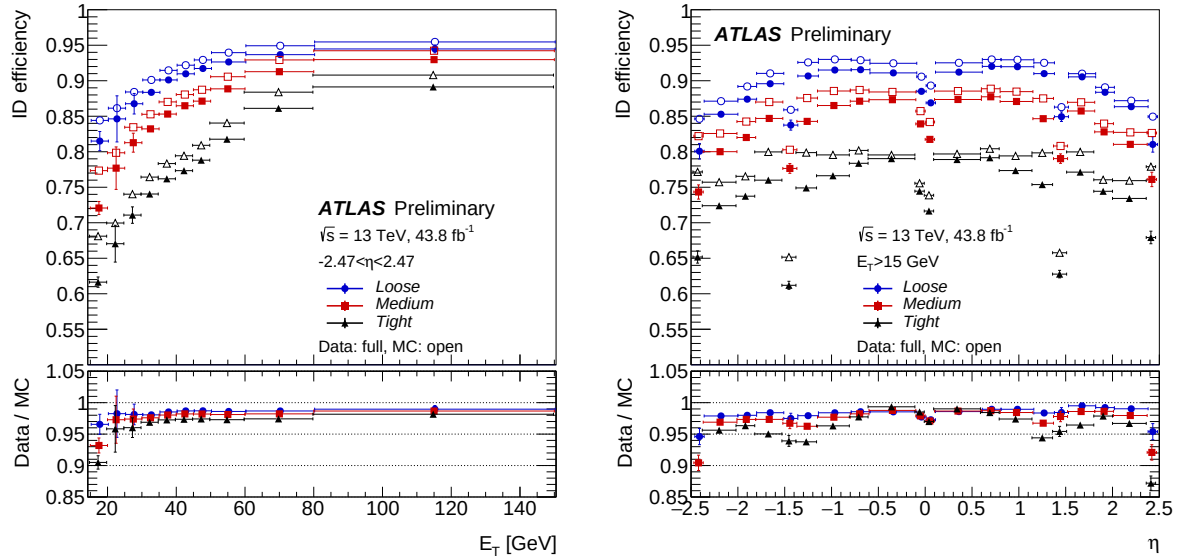

Figure 3.8: The electron identification efficiency as a function of electron transverse momentum (left) and pseudorapidity (right) shown for all identification working points. Detected electrons originate from the $Z \to ee$ process, measured for both real data and simulated events [136].

Muon reconstruction in the MS begins by grouping hits in each muon chamber into segments. Collecting related hits is done using a Hough transform [139, 140] which scans for a trajectory of hits aligned in the bending plane of the detector. For the precision chambers, MDT segments are created using a straight-line fit through the hits found in each later, while a separate combinatorial search is used in the η and ϕ detector planes for CSC segments. For trigger chamber hits (TGC and RPC), hits are fitted using the coordinate orthogonal to the bending plane. Muon track candidates are then constructed by combining found segments, starting out with seeds found in the middle layers of the MS, then extending outwards by matching segments from the inner and outer layers using their relative positions and angles, judging them for compatibility based on hit multiplicity and fit quality. Ambiguity solving is performed on segments which were assigned to two separate tracks simultaneously. A track candidate is accepted by imposing a chi-square test criteria on the total track with scoring based on each of the hits. Failing tracks may be refitted after having hits with the highest χ^2 contribution removed until they are accepted or fall below minimum segment requirements.

Muon tracks in the MS are then combined with track information obtained from the ID and energy deposits from the calorimeters. This can lead to four classes of muons:

- *Combined* muons, having processed information from both the ID and MS. This is the most reliable class of muon candidates and is favored over other classes in the case of conflicting segment assignment.
- *Segment-Tagged* muons, which have a reconstructed ID track but only one segment in the precision chambers, generally caused by muons with low p_{T} or tracks crossing MS regions with lower sensitivity.
- *Calorimeter-Tagged* muons. These muons are constructed from an ID track and an energy deposit in the calorimeters compatible with a minimum ionizing particle[6]. This muon class is relevant for the pseudorapidity range $|\eta| < 0.1$, which is not covered by MS chambers.
- *Extrapolated* muons are reconstructed from only a MS track and certain track criteria based on compatibility with the beam interaction point. This muon type is useful for the extended pseudorapidity range $2.5 < |\eta| < 2.7$, which is not covered by ID instrumentation.

A unique property of muons is their ability to penetrate the calorimeter to reach the muon spectrometer. This feature motivates the placement of the MS on the outside of ATLAS, and as a consequence muons do not share the MS volume with other particles that could be misidentified. However, the production of non-prompt muons through hadronic decays must still be considered. For this identification and isolation procedures are applied, analogous to the treatment for electrons.

Muon identification seeks to distinguish prompt muons from those created by the in-flight decay of hadrons. As for the electron, a multivariate analysis is used, scoring based on variables such as the q/p ratio, the difference in p_{T} measured by the ID and MS, and the χ^2 of the combined track fit. Four working points are provided: `Loose`, `Medium`, `Tight` and `HighPt`. The first three of these working points provide increasingly better non-prompt reduction with the drawback of potentially rejecting a true muon. The `HighPt` working

[6]Minimum ionizing particles (MIPs) lose energy only from radiative effects. Muons are effectively MIPs at ATLAS production energies due to their mass.

point has lower efficiency than other working points (even at the transverse energy range for which it is designed), but it has significantly improved rejection capabilities and greatly improved momentum resolution at the transverse momentum region for which it is designed. Use of this working point is therefore recommended for use by analyses when considering muons of about $p_T > 300$ GeV [141].

A set of quality cuts is performed on muons independent of identification which assure accurate momentum measurement of the muon is possible. These quality cuts are lower limits on the amount of Pixel, SCT and TRT hits and upper limits on the allowed amount of Pixel and SCT holes [138]. Furthermore, muons may be discarded if the found q/p value differs strongly when considering a combined muon versus the overlapping extrapolated counterpart. This is known as the *bad muon veto*.

Muons can furthermore be required to be isolated, further reducing the acceptance of muons which originate from in-flight decays of heavy hadrons. Here, too both calorimeter and track information can be used. Cone size and the threshold of the ratio $p_{\mathrm{T}}^{cone}/p_{\mathrm{T}}^{muon}$ are used as inputs to produce working points. For muons, the working points include `FCLoose`, `FCTight`, `FCTightTrackOnly` and `TightTrackOnly_FixedRad`.

Reconstruction and isolation efficiencies are gauged using the well-understood $Z \to \mu\mu$ process and checked for both measured data and Monte Carlo generated events. This is shown in Figures 3.10 and 3.11 for the `Medium` identification and `FCTightTrackOnly` isolation working points respectively. Here it becomes clear that the reconstruction efficiency is poor in the $|\eta| < 0.1$ range where MS instrumentation is sparse. The `Loose` WP is also shown in the figure to highlight the change in efficiency in this region when calorimeter-tagged muons are included, as is the case for that working point. What can be learned from the isolation figure is that the efficiency is poor for low-energetic muons of $p_{\mathrm{T}} < 20$ GeV, after which it rapidly increases to become close to unity for muons of $p_{\mathrm{T}} > 100$ GeV.

3.2.3 Lepton Efficiency Scale Factors

For the observed efficiencies for both electrons (Figures 3.7, 3.8 and 3.9) and muons (Figures 3.10 and 3.11) it can be seen that a discrepancy between data and MC simulation remains. This discrepancy is solved by means of *scale factors*, which are computed as the ratio of data and simulated efficiencies [132, 138]. These scale factors depend on the lepton's kinematics: their transverse momentum and pseudorapidity. The steps of reconstruction, identification and isolation each have their own scale factors. Furthermore, an efficiency scale factor exists to measure the difference in response of the used triggers between data and Monte Carlo [143, 144].

Because these scale factors themselves also rely on measured data, there remains on these scale factors a degree of uncertainty which limits their precision. This uncertainty must be propagated to the experimental uncertainty present in the analysis. These uncertainties consist of a set of uncorrelated per-bin uncertainties due to the limited statistics available in a bin where the scale factor is measured, and a set of systematic uncertainties originating from a variety of instrumental sources, correlated across bins but uncorrelated from each other. These uncertainties have been provided by ATLAS performance groups after dedicated studies, as well as correlation models which can be used [145, 146]. Systematic uncertainties are discussed in Section 6.2.

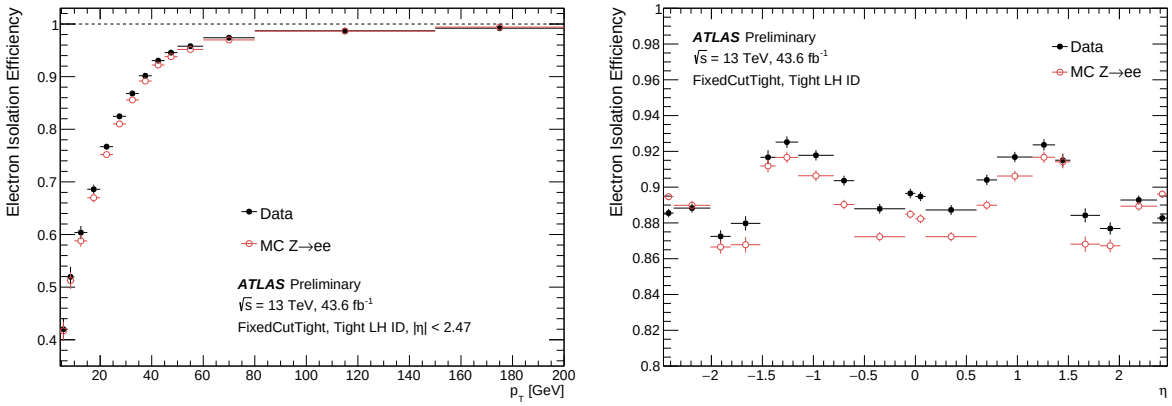

Figure 3.9: The electron isolation efficiency as a function of electron transverse momentum (left) and pseudorapidity (right) shown for the `FCTight` isolation working point. Detected electrons originate from the $Z \to ee$ process, measured for both real data and simulated events [136].

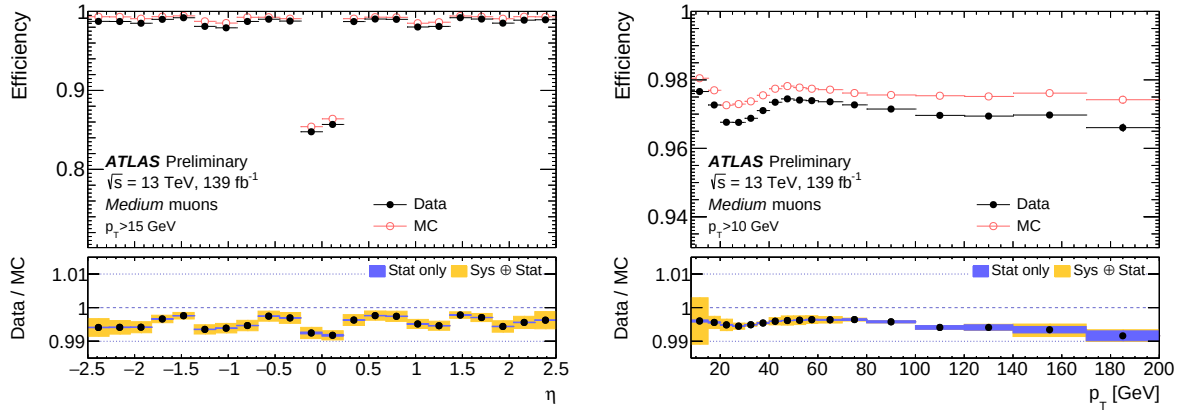

Figure 3.10: Muon reconstruction efficiencies using the `Medium` identification working point as a function of pseudorapidity (left) and transverse momentum (right). $Z \to \mu\mu$ processes are used to measure the efficiencies given here both in simulation and data [138].

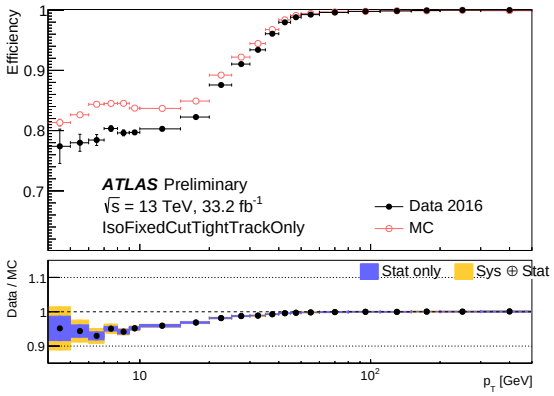

Figure 3.11: Muon isolation efficiencies using the `FixedCutTightTrackOnly` isolation working point as a function of transverse momentum for. $Z \to \mu\mu$ processes are used to measure the efficiencies given here in both simulation and data [142].

3.2.4 Jets

Color confinement and the resulting hadronization resulting from strong interactions were discussed in Chapter 1.2. Collimated bundles of hadronic particles are referred to as *jets* [147]. The colored quarks and gluons are furthermore capable of *initial* and *final state radiation* (ISR and FSR), creating more colored particles which hadronize.

The first step of jet reconstruction is the formation of *topo-clusters* [148]. Topo-cluster seeds are initially formed from calorimeter cells whose energy deposits exceed by four standard deviations the expected noise. The seed cluster is then expanded by including adjacent cells whose signal exceeds expected noise by two standard deviations. In the last step, direct neighbors of cells selected so far are indiscriminately accepted. If two local energy maxima occupy the same cluster, it is split.

The next step combines disparate topo-clusters into jets. This is done by the anti-k_t clustering algorithm [149], implemented through the FastJet reconstruction package [150]. The algorithm bundles closely collinear particles within a cone of predefined aperture into a jet. Neighboring clusters are combined based on their relative distance d_{ij}, which is expressed in Equation 3.1.

$$d_{ij} = min\Big(\frac{1}{p_{T,i}^2}, \frac{1}{p_{T,j}^2}\Big)\frac{\Delta R_{ij}^2}{R^2} \tag{3.1}$$

In this equation $p_{T,i}$ is the transverse momentum of cluster i, ΔR_{ij}, is the geometric distance and $R = 0.4$ the jet cone radius, similar to the way a cone is defined around a lepton to check its isolation. Clusters are combined until no two clusters have relative distance smaller than the distance between the cluster and the beam spot, i.e. $d_{ij} > d_{i,beam}$ $(= p_{T,i}^{-2}\Delta R_{i,beam}^2 R^{-2})$ for all j, at which point the grouping is promoted to the status of jet. This process is repeated for all topo-clusters.

Pileup is a particularly problematic issue for the reconstruction of jets due to high multiplicity in the detector environment. Jet pileup can be categorized into in-time and out-of-time pileup, corresponding to objects from other interactions within the same and of neighboring bunch crossings respectively. Several techniques are employed to counteract the negative impact of pileup on reconstruction efficiency:

- The energy threshold for forming topo-clusters is dynamic based on the expected noise in the detector. Pileup noise is included into the formulation of expected noise, and the fact that pileup can change between runs and over the course of a single run is taken into consideration.
- The *particle flow* algorithm [151] modifies the inputs provided to the anti-k_t algorithm. Specifically, it removes from consideration energy deposits from the calorimeter caused by charged hadrons. Charged hadrons have been shown to have superior momentum measurements provided by the ID, which are used instead. Foregoing the usage of topo-clusters in this manner is shown to achieve pileup stability as well as improved energy resolution.
- Jets can be identified as having originated from the primary vertex by applying *jet-vertex tagging* (JVT) [152, 153]. JVT is a multivariate analysis scoring jets which is based on three variables, most prominent of which is the jet vertex fraction

(JVF) [154], the ratio of the p_{T} sum of matched ID tracks originating from the primary vertex to the sum of tracks overall. Combined with the other two variables[7], a JVT score can be assigned to a particular jet, where JVT = 0 indicates a pileup-like, and 1 indicates a hard-scatter-like jet. Because the JVT requires ID information, this technique is only usable for $|\eta| < 2.4$

- Reconstructed jets are recalibrated using the jet energy scale (JES) [155], which leads to a series of four-momentum corrections intended to calibrate the reconstructed jet according to the jet response derived from Z/γ + jets simulation samples. This generally leads to lower transverse momenta measurements of pileup jets, allowing an increased rejection for analyses imposing a minimum p_{T} requirement on jets.

3.2.5 Missing Transverse Energy

Momentum conservation insists that the sum of all transverse momenta vanishes, i.e. $\sum \overrightarrow{p_T} = 0$. Should this not be the case, the deficit is classified as "missing". This leads to the pseudo-object Missing Transverse Energy ($E_{\mathrm{T}}^{\mathrm{miss}}$) [156–158], defined as the vector sum $E_{\mathrm{T}}^{\mathrm{miss}} = -\sum \overrightarrow{p_T}$. $E_{\mathrm{T}}^{\mathrm{miss}}$ is an event-level quantity but can be assigned a momentum similar to other objects.

Reconstruction of the $E_{\mathrm{T}}^{\mathrm{miss}}$ can be performed using either ID (track) or calorimeter information [159]. Ideally, the $E_{\mathrm{T}}^{\mathrm{miss}}$ is a perfect reflection of the four-momentum of invisible particles such as neutrinos having been produced during a *pp*-collision. In practice, momentum resolution limitations, miscalibrations, and particles going through un-instrumented regions all contribute to the $E_{\mathrm{T}}^{\mathrm{miss}}$ reconstruction. The result is a reconstructed $E_{\mathrm{T}}^{\mathrm{miss}}$ from a combination of invisible particle momentum and fake $E_{\mathrm{T}}^{\mathrm{miss}}$ contributions, affecting performance.

The $E_{\mathrm{T}}^{\mathrm{miss}}$ can be divided into a *hard* and *soft* term. For the hard term specifically reconstructed objects, electrons, muons, tau leptons, photons and jets, are considered. These objects each have their own reconstruction, rejections and corrections, as well as a selection process which qualifies them for use for a particular analysis. Once this process is fully performed, the objects enter into consideration for the computation of the hard $E_{\mathrm{T}}^{\mathrm{miss}}$ term, where the reconstruction algorithm imposes additional criteria on each object independent of the requirements already imposed by previous object selection. This selection includes an internal overlap removal process which removes objects from consideration if their tracks overlap based on a certain priority scheme.

The soft $E_{\mathrm{T}}^{\mathrm{miss}}$ term is more challenging to calculate, being comprised of all detector signals not associated with any of the aforementioned hard objects. Such contributions may include soft products from the hard scattering interaction as well as pileup-related contamination. The current generation of soft $E_{\mathrm{T}}^{\mathrm{miss}}$ reconstruction algorithms used during run 2 calculates a track-based soft term, which incorporates contributions of all identified tracks not explicitly associated to hard objects. Tracks must, however, be able to be related back to the identified primary vertex. This is assured due to cuts on the longitudinal and transverse track parameters, d_0 and z_0. For jets reconstructed by the particle flow (PFlow) algorithm, these requirements are as follows:

[7] The other two variables are the pileup-corrected JVF and R_{pT}, the scalar p_{T} sum of the tracks that are associated with the jet and originate from the hard-scatter vertex, divided by the fully calibrated jet p_{T}. The exact definitions of these variables can be found in Ref. [152].

- $p_{\mathrm{T}} > 0.5$ GeV;
- $|\eta| < 2.5$;
- $|d_0/\sigma_{d_0}| < 2$;
- $|z_0 \sin\theta| < 2.0$ mm.

The track-based calculation of the soft $E_{\mathrm{T}}^{\mathrm{miss}}$ term is unable to take into account contributions from neutral particles. However, this turns out to be an advantage as it suppresses contamination due to out-of-time pileup[8].

The performance of the reconstruction algorithm is be studied with derived quantities such as the mean, the width and the integral of the tail of the $E_{\mathrm{T}}^{\mathrm{miss}}$ distribution. This has for example been done by performing a data to MC comparison for $Z \to \ell\ell$ selections, where $\ell = e, \mu$. Since no $E_{\mathrm{T}}^{\mathrm{miss}}$ is expected for these events, the actual obtained distribution of the $E_{\mathrm{T}}^{\mathrm{miss}}$ provides information on the impact of resolution and miscalibration effects. The plots are furthermore indicative of the ability to model the distribution of $E_{\mathrm{T}}^{\mathrm{miss}}$ obtained in data with Monte Carlo generated events. The comparison is shown in Figure 3.12.

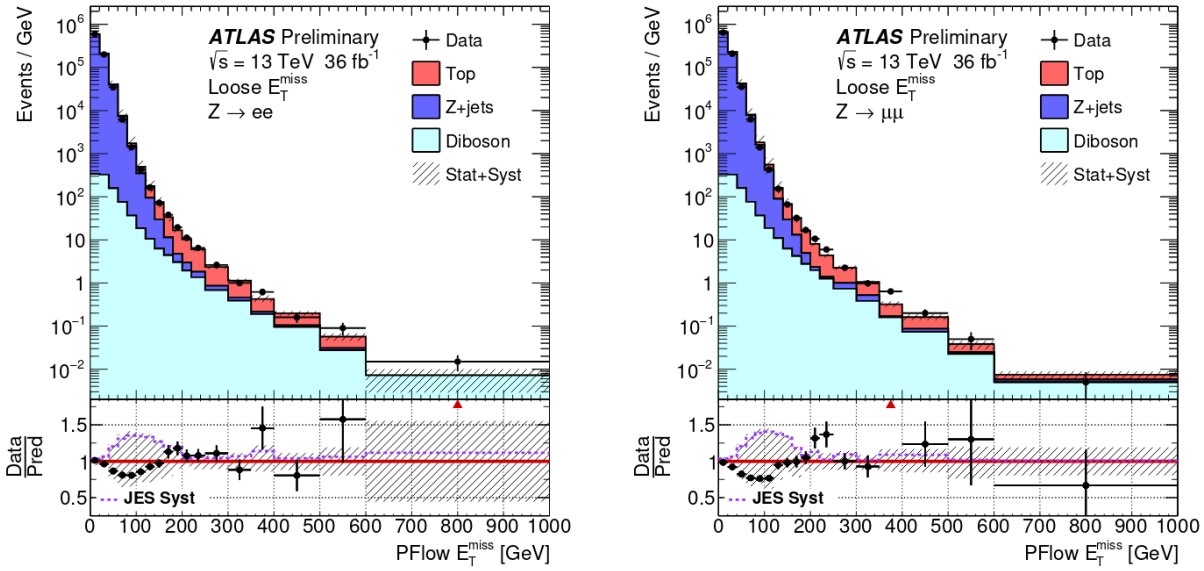

Figure 3.12: Distributions of the $E_{\mathrm{T}}^{\mathrm{miss}}$ using PFlow jets for $Z \to ee$ (left) and $Z \to \mu\mu$ (right) selections. Included are the ratio of data to MC per bin and the total statistical and systematic uncertainties. The rightmost bin includes all events with a $E_{\mathrm{T}}^{\mathrm{miss}}$ above 600 GeV [159]. The Loose $E_{\mathrm{T}}^{\mathrm{miss}}$ working point is pictured, which is also the working point used for this analysis.

[8]Neutral contributions are not used in the current iteration of the soft $E_{\mathrm{T}}^{\mathrm{miss}}$ construction algorithm.

Part II

Experiment Design

Chapter 4

Region and Event Selection

In order to perform the analysis the desired subsets of the total available physics data must be chosen. Data selected must be suitable for the analysis' purposes, which in this case means that it must contain light leptons (electrons and muons) of sufficient quality with a momentum above a specific threshold. The selected data can then be divided into categories according to their role in the analysis.

This chapter is divided into two sections: Section 4.1 establishes the base selection, a set of criteria which is common to all events. It discusses the used triggers, selection working points, and thresholds which are needed to obtain a selection consisting mostly of unambiguous light leptons. Section 4.2 then describes four different purposes for which the data is to be used, and imposes additional cuts to create corresponding regions for each of these purposes.

4.1 Event Base Selection

These are the selection criteria that every event taken by the ATLAS detector must satisfy in order to be considered for this analysis. These cuts are applied in the order as it is written here: First, an event must pass the *quality cuts* and have fired at least one of the listed *triggers*. Then, objects of interest for this analysis are selected. Objects that remain after this selection are re-checked for compatibility with the criteria of the fired trigger in a process called *trigger matching*. Finally, a veto of low dilepton masses for same-flavor, opposite-charge lepton pairs is applied.

4.1.1 Event Quality Cuts

A set of cuts relating to event quality are made early in the selection. These event quality cuts are the result of investigations by the ATLAS Data Preparation Group [160]. The cuts made are as follows:

- Events from luminosity blocks not featured on the *Good Runs List* (GRL) are vetoed. Occasionally parts of a data taking run in the ATLAS detector are considered unsuitable for use by analyses due to errors that may have occurred during data taking. The Good Run List is a collection of those runs that are confirmed to be suitable. There are multiple lists used by the ATLAS collaboration alongside instructions and recommendations on which list to use for a certain kind of analysis [161].
- Cleaning of data events affected by liquid argon calorimeter (LAr) noise bursts or that otherwise have their integrity corrupted.

- Similarly, a small amount of corrupted events with causes originating from the HCal should be rejected.
- Events need to be rejected if they are affected by the recovery procedure for single event upsets in the SCT.

4.1.2 Used Triggers

For the nominal selection the lowest-unprescaled dilepton triggers available for each year of data taking are used, except when choosing a lower-p_{T} trigger would not capture additional events that pass the object selection. These triggers are given in Table 4.1.

	2015	2016	2017-2018
ee	`2e17_lhvloose_nod0`	`2e17_lhvloose_nod0`	`2e24_lhvloose_nod0`
$e\mu$	`e17_lhloose_nod0_mu14`	`e17_lhloose_nod0_mu14`	`e17_lhloose_nod0_mu14`
$\mu\mu$	`mu18_mu8noL1`	`mu22_mu8noL1`	`mu22_mu8noL1`

Table 4.1: The dilepton triggers used for the analysis validation and signal regions.

The name of each trigger provides information about the associated requirements that go along with it. The name consists of a combination of tags that can be interpreted. The tag `eXX` requires with a transverse momentum of at least XX GeV. Preceding the letter with another integer, such as `2e17`, instead requires multiple electrons to pass this p_T requirement (in this example one would require 2 electrons of at least 17 GeV to fire the trigger). The same naming scheme holds for muons, which are indicated by `mu` instead. The tags `lhloose` and `lhvloose` succeeding a lepton requirement indicate an additional demand at the offline reconstruction level of loose and very loose identification criteria respectively. The tag `nod0` for the electron triggers simply indicates that d_0 information is not used for said reconstruction.
For the muon triggers, the tag `noL1` indicates that the preceding muon is not required to be identified at Level 1. This relaxed requirement was imposed because the Level 1 muon trigger is known to have low efficiency. This is why the dimuon trigger `mu22_mu8noL1` is preferred over the other muon trigger `HLT_2mu14`: Although both are unprescaled, the latter requires two Level 1 muons, decreasing efficiency.
Other trigger tags include the isolation requirements, e.g. `ivarloose` and `ivarmedium`, or at L1 indicated by the `I` in `L1EM15VHI`. Due to the nature of the fake factor analysis triggers with such tags are not usable due to the bias they would introduce in the baseline lepton object selection, which is required to be unisolated.

For all the single-lepton regions, which includes all regions for the extraction of fake factors and the W+jets validation region, single-lepton triggers are used instead. The triggers used for this analysis are given in Table 4.2.

Triggers at low transverse momentum without further requirements on isolation and loose offline reconstruction requirements are in general prescaled. The prescale of a trigger is the ratio between the number of events that the trigger has recorded and the amount of events that fired the trigger. Prescaling becomes necessary when the firing rate of a trigger

Trigger	Data Period	Lower p_T threshold	Average Prescale
`e17_lhvloose_nod0`	2015-2018	-	1475
`e26_lhvloose_nod0_L1EM20VH`	2015-2017	28 GeV	184
`e26_lhvloose_nod0_L1EM22VH`	2018	28 GeV	499
`e60_lhvloose_nod0`	2015-2018	64 GeV	32.11
`e140_lhvloose_nod0`	2016-2018	145 GeV	2.14
`e160_lhvloose_nod0`	2017-2018	165 GeV	1.62
`mu24`	2015-2018	-	50 (32 in 2015)
`mu50`	2015-0218	52 GeV	1

Table 4.2: Loose triggers used for the electron and muon fake factor estimation regions. At most a single trigger can be associated with a momentum range: the lower p_{T} threshold for a trigger is simultaneously the upper p_{T} threshold for the preceding trigger.

exceeds the maximum bandwidth available to record events, as is the case in triggers with lower p_{T}, looser identification criteria or the lack of an isolation requirement. Trigger prescales might vary between years or runs. Trigger prescales may also be lowered as an individual run progresses and the beam luminosity decreases.

When dealing with analyses that require loose or unisolated particles to be used, as is the case here, the prescaling of the trigger will have to be taken into account. This can be done by either attaching a weight to the Monte Carlo events that models the data falling under a prescaled trigger's regime, or by attaching the inverse of that weight to the associated data events. The latter option is chosen for this analysis. The choice to use prescaled triggers means a large fraction of admissible data is discarded, but ensures the recorded data featuring lower-p_{T} objects are free from bias that would occur due to imposing tighter requirements at the trigger level.

4.1.3 Object Selection

Light Leptons

The electron and muon criteria of the analysis are given in Table 4.3 and 4.4. Given in both of these tables are the choices of the identification and isolation working points (introduced in Chapter 3), a set of track to vertex association criteria to ensure that leptons selected come from the primary event vertex. Requirements on the transverse momentum and pseudorapidity are also imposed to remove forward and low-energy leptons, as these carry a higher rate of misidentified leptons or leptons from uninteresting standard model background processes. For electrons, the crack region of $1.37 < |\eta| < 1.52$, where calorimeter instrumentation is sparse, is also excluded.

Two classes of light leptons are distinguished: *baseline* and *signal*. The baseline lepton selection is the minimum set of requirements for a lepton to be admitted into the analysis. Baseline leptons are considered for all subsequent cuts, such as overlap removal, and are used as a component of the for the fake factor method discussed in Section 5.2. The *signal* selection is used in the nominal analysis and is a strict subset of the baseline selection.

Variable	Baseline Electron	Signal Electron
Transverse Momentum	$p_{\mathrm{T}} > 25$ GeV	
Pseudorapidity	$\lvert\eta\rvert < 1.37$ **or** $1.52 < \lvert\eta\rvert < 2.47$	
Track to vertex association	$\lvert d_0^{BL}(\sigma)\rvert < 3$ mm $\lvert\Delta z_0^{BL} \sin\theta\rvert < 0.5$ mm	
PID Quality	`LHLoose`	`LHTight`
Isolation	none	`FCTight`

Table 4.3: Object selection for electrons. The signal selection requirements are imposed in addition to the baseline selection for nominal electrons.

Variable	Baseline Muon	Signal Muon
Transverse Momentum	$p_{\mathrm{T}} > 25$ GeV	
Pseudorapidity	$\lvert\eta\rvert < 2.47$	
Track to vertex association	$\lvert d_0(\sigma)\rvert < 3$ mm $\lvert\Delta z_0 \sin\theta\rvert < 0.5$ mm	
PID Quality	`HighPt` if $p_{\mathrm{T}} > 300$ GeV, else `Medium`	
Isolation	none	`FCTightTrackOnly_FixedRad`

Table 4.4: Object selection for muons. The signal selection requirements are imposed in addition to the baseline selection for nominal muons.

Jets

For this analysis, jets are reconstructed using the anti-k_t algorithm [149] using the particle flow (PFlow) input constituents [151] (see Section 3.2.4). Jets are furthermore required to have $p_T > 20$ GeV and $|\eta| < 2.5$. The Jet Vertex Tagger (JVT) is used to reject jets resulting from pileup events [162]. Specifically, a JVT score > 0.59 for jets with $p_T < 60$ GeV and $|\eta| < 2.4$ is required.

Overlap Removal

Occasionally energy deposits within a component of the detector can be reconstructed as different objects by different algorithms. To prevent double-counting a set of rules has been established to choose a single prevailing object while discarding the alternative reconstructions. This process is known as *overlap removal*. The collaboration provides a set of software tools for this purpose. Criteria for the removal of overlapping objects for this analysis use the standard overlap removal tools `AssociationUtils` [163]. All electrons, muons and jet passing the *baseline* selections described above are entered into consideration for the overlap removal process. The imposed overlap removal requirements are shown in Table 4.5.

Reject	Against	Criteria
Electron	Electron	shared track, $p_{\mathrm{T},1} < p_{\mathrm{T},2}$
Muon	Electron	is Calo-Muon and shared ID track
Electron	Muon	shared ID track
Photon	Electron	$\Delta R < 0.4$
Photon	Muon	$\Delta R < 0.4$
Jet	Electron	$\Delta R < 0.2$
Electron	Jet	$\Delta R < 0.4$
Jet	Muon	Fewer than 3 tracks and $\Delta R < 0.2$
Muon	Jet	$\Delta R < 0.4$
Photon	Jet	$\Delta R < 0.4$

Table 4.5: Criteria for the removal of overlapping particle reconstructions of energy deposits in the ATLAS detector. Overlap removal criteria are applied in the order that they appear in the table (top criteria first), with only particles remaining from the previous selection being considered in each subsequent step.

4.1.4 Trigger Matching

After object selection is completed, an event's remaining objects are required to still match at least one of the triggers that fired the event. This requirement is referred to as *Trigger Matching*. Trigger matching is necessary because the object selection criteria are not a strict subset of the trigger firing criteria [164] (or vice-versa); the leptons responsible for initially firing the trigger for an event may be discarded during the object selections outlined above.

In the trigger matching procedure, each of the remaining electrons and muons is compared to each of the individual particle criteria of the fired trigger(s) to see if they would be sufficient for its firing. The transverse momentum required for the matching is 1 GeV higher than the trigger threshold to account for trigger activation inefficiencies. If no combination of leptons can be found in the event that matches any of the triggers, the event is discarded.

4.1.5 Dilepton Mass Requirement

On events with at least 2 leptons passing all of the above selection criteria, an additional cut is imposed. For all lepton pairs which have *same* flavor and *opposite* charge, a lower bound on the dilepton mass of 12 GeV is demanded. This prevents contamination from events where two leptons come from the decay from charmonium and bottomonium mesons. These particles have rest masses below 12 GeV but may decay to a lepton pair where each lepton has $p_{\mathrm{T}} > 25$ GeV in rare cases. Imposing a dilepton mass cut eliminates this contribution.

4.2 Analysis Regions

There are several categories of regions which fulfill different purposes. One of these categories *signal regions*, to be analyzed for the presence of new physics. Other categories are the *control regions*, *fake estimation regions* and the *validation regions*. They will be

explained in this section, with the exception of the regions related to the computation of the fake factor, which are explained in Chapter 5 instead.

The regions used in this analysis and their definitions are given in Table 4.6. The definition of these regions is based on various selection criteria that are used to either qualify or disqualify events. These criteria are imposed on top of the selection that has been discussed in the previous section. An inclusive list of variables on which selection criteria are based follows.

- **SFOS**: Same-flavor, opposite sign. Refers to a pair of leptons which are of the same flavor but opposite charge.
- **On-Z**: In this category, at least 2 light leptons (of any combination) are required to originate from a leptonic Z-boson decay. This is any lepton pair that is SFOS which additionally has a reconstructed dilepton mass falling within 10 GeV of the Z mass of 91.2 GeV. Thus, $81.2 < M_{\ell\ell} < 101.2$ GeV.
- **Off-Z**: This cut is the complement of the cut above. This event has no same flavor, oppositely charged lepton pair with a dilepton mass of $81.2 < M_{\ell\ell} < 101.2$ GeV (failing any of these three requirements qualifies the lepton pair as being off-Z).
- ***eee***, ***eeμ***, ***e$\mu\mu$***, ***$\mu\mu\mu$***: Categories where an exact amount of specific flavors of light leptons are required.
- **Missing Energy** ($E_{\mathrm{T}}^{\mathrm{miss}}$): Transverse energy that could not be attributed to any identified objects in the event after the transverse energy of all these objects is combined (discussed in Section 3.2.5).
- **Transverse Mass** (m_T): Combination of the object's transverse momentum, the missing energy, and the angle between the two according to $m_T^2 = 2p_T E_{\mathrm{T}}^{\mathrm{miss}}(1 - \cos\phi)$ (ϕ is the angle between the lepton and $E_{\mathrm{T}}^{\mathrm{miss}}$ momentum components in the plane perpendicular to the beam direction).
- **Lepton Multiplicity**: Total amount of light leptons that must be present in the event. For signal and control regions, the lepton multiplicity requirement is either three (3ℓ) or four (4ℓ).
- **Jet Multiplicity**: the total amount of jets present in the event that pass the selection criteria from the previous section.

4.2.1 Choice of Signal Regions

The selection of signal regions, which is presented in Table 4.6, is based on the following considerations:

- Areas of the phase space which contain a low rate of expected background events.
- Properties of potential BSM physics models that might separate them from the backgrounds that can be leveraged without over-committing to one particular model.

The Standard Model production of WZ, ZZ, as well as the Z+jets processes, share these topological features: they are **on-Z** events which contain one (or two for the ZZ contribution) lepton pair originating from a Z boson. Events from these processes also tend towards lower missing transverse energy. These properties have been leveraged for

Region	Particles	$E_{\mathrm{T}}^{\mathrm{miss}}$	Z-pairs	Other
		Fake Estimation Regions		
e-fakes	$1e$	< 25 GeV	-	jets ≥ 1
μ-fakes	1μ	< 40 GeV	-	jets ≥ 2, at least 1 jet $p_{\mathrm{T}} > 35$ GeV, $\lvert\Delta\phi(\mu, j)\rvert > 2.7$
		Validation Regions		
$W \to e\nu$	$1e$	> 25 GeV	-	
$W \to \mu\nu$	1μ	> 40 GeV	-	
3ℓ Fakes	$ee\mu + e\mu\mu$	-	1	off-flavor ℓ: $M_T(\ell, MET) < 40$ GeV
3ℓ Off-Z	$ee\mu + e\mu\mu$	-	0	2 SFOS leptons. off-flavor ℓ: $M_T(\ell, MET) < 40$ GeV
		Control Regions		
WZ	3ℓ	-	1	off-Z ℓ: $40 < M_T(\ell, MET) < 80$ GeV
ZZ	4ℓ	-	2	
		Events that fulfill either CR or VR requirements are vetoed from use in signal regions		
		Signal Regions		
3 leptons	3ℓ	< 50 GeV	1	**veto** off-Z ℓ if $M_T(\ell, MET) < 80$ GeV
	3ℓ	> 50 GeV	1	**veto** off-Z ℓ if $M_T(\ell, MET) < 80$ GeV
	3ℓ	< 50 GeV	0	**veto** off-flavor ℓ if $M_T(\ell, MET) < 40$ GeV
	3ℓ	> 50 GeV	0	**veto** off-flavor ℓ if $M_T(\ell, MET) < 40$ GeV
4 leptons	4ℓ	< 50 GeV	1	-
	4ℓ	> 50 GeV	1	-
	4ℓ	-	0	-

Table 4.6: Overview of the regions defined for this analysis. Blank cells indicate no requirements being made on the variable for that particular region. n_ℓ,n_μ,n_e indicates the amount of leptons required for the event and their flavor composition (ℓ implying either an electron or muon). All of these regions are orthogonal. Additional cuts on signal regions described in the *Other* column will veto events that are used in the control or validation regions from entering into the signal regions. $E_{\mathrm{T}}^{\mathrm{miss}}$ indicates the total missing transverse energy. The Z-pairs column asks for the amount of non-overlapping lepton pairs that are same-flavor, oppositely charged and reconstruct to a dilepton mass within 10 GeV of the Z-boson mass of 91.19 GeV. `SFOS` stands for same-flavor, opposite-sign, and requires that the two same-flavor leptons in the event have opposite charge, but do not have a dilepton mass within 10 GeV of the Z-mass. All 3+ lepton regions include a cut on dilepton mass of SFOS lepton pairs of $m_{\ell\ell} > 12$ GeV.

the creation of the control regions, but they can also be considered for the purposes of defining signal regions which separate events which contain leptons that likely originate from an on-shell Z lepton from events which do not contain such leptons.

A large group of contemporary hypotheses are predicated on the existence of at least one additional heavy lepton, either charged or uncharged (examples include the Seesaw models, which have been discussed in Section 1.4). Such models often feature final states with one or more neutrinos, which translates into a missing energy deposit in the detector. This motivates a selection of signal regions separated by a $E_{\mathrm{T}}^{\mathrm{miss}}$ cut, separating such signals from the diboson background. A dividing threshold of $E_{\mathrm{T}}^{\mathrm{miss}} = 50$ GeV was chosen. This separates the combined expected background event yields into two parts of approximately equal size. That is, taking the sum of all expected background events in all signal regions, about half will have $E_{\mathrm{T}}^{\mathrm{miss}} < 50$ GeV, and half will have $E_{\mathrm{T}}^{\mathrm{miss}} > 50$ GeV. However, since no prior assumptions are made about the signal model to be detected, there remains a degree of arbitrariness in choosing an exact value of the $E_{\mathrm{T}}^{\mathrm{miss}}$ cut.

Signal Region Set	Mass Bins			
3-lepton	0 - 200 GeV	200 - 400 GeV	400 - 600 GeV	600+ GeV
4-lepton	0 - 400 GeV		400+ GeV	

Table 4.7: Mass binning used for each of the signal regions in the analysis. Each mass bin is performed as an independent experiment for the purposes of fitting and limit setting.

We also create signal regions for events which do not contain any combination of leptons which combine to form an on-Z lepton pair. These **off-Z** signal regions are expected to be relatively low in the primary background contributions discussed above, while being sensitive to BSM particles which do not decay to Z bosons to produce leptonic final states (such particles might instead produce multilepton final states through intermediate W bosons or decay directly to lepton pairs).

The four lepton phase space is subdivided in a similar way, but the region separation is coarser. Since the expected background yield is lower, originating mainly from the ZZ diboson background (which can be constrained through the ZZ control region) with only minor contributions from $H \to ZZ$ and associated top quark contributions, there is less of a need to separate the four lepton region as finely as the three lepton region.

After these categories have been established, each individual category is then binned according to its distribution in a single kinematic variable. In this analysis, the *invariant mass* has been chosen as the variable. All leptons in the event are used to compute this invariant mass, but jets are not. These kinematic bins are given in Table 4.7. Invariant mass of all leptons in an event is referred to as M_{inv}. The mass bins are kept sufficiently wide to diminish the effect of bin migration of a possible signal. No correlation is initially assumed between the signals probed in each mass bin. This method is chosen to honor the signal-independent nature of the analysis. The analysis performs a set of independent cut-and-count experiments. Each of these experiments considers a single mass bin within a single signal region.

4.2.2 Control and Validation Regions

The control regions are used to set or constrain the values of the nuisance parameters that enter into the analysis (the exact process by which systematics are constrained is explained in Chapter 6). Two control regions have been established for the WZ and ZZ diboson processes where each boson decays leptonically, leading to 3ℓ and 4ℓ final states respectively. Definitions of these control regions are based on the flavor, charge and kinematic properties which leptons originating from diboson pairs are expected to have. Because of these criteria, the relevant diboson processes are expected to make up the vast majority of the expected events, with a low contribution from fakes, other SM processes or exotic physics.

Control regions being free from the contamination of new physics signals is crucial for them to serve their purpose while keeping the analysis sensitive to potential new signals. While it is impossible to guarantee this for every possible new physics model in a model-independent search, it can be contended that the abundance of SM background events and the particular selections used for these regions leads to an insensitivity to exotic physics

contamination. Furthermore, the selections used for these control regions and the processes have been studied by the ATLAS Standard Model group [165, 166].

The WZ diboson region is similar but orthogonal to the three-lepton signal regions of the model-independent multilepton search and is used as a control region of the dominant SM background in the three lepton regions. Requirements for this region, apart from the base object selection, are as follows: Two leptons must be on-Z, while the third lepton in the event must be off-Z and have a transverse mass of $40 < m_T(\ell, E_{\mathrm{T}}^{\mathrm{miss}}) < 80$ GeV, which allows it to serve as a proxy for the W boson decaying leptonically.

In the four lepton regions the primary contributor to the background estimation is the leptonic decay of two Z-bosons produced by either $q\bar{q} \to ZZ$ or $gg \to ZZ$ processes. The ZZ control region is established to validate these processes and ensure they are correctly modeled. The ZZ control region is defined as requiring exactly four leptons, either electrons or muons, which combine to form exactly two on-Z pairs.

The validation regions are three lepton regions containing any mixed-flavor event ($ee\mu$ and $e\mu\mu$) where the same-flavor lepton pair must be of opposite sign, and the third lepton has transverse mass $m_T(\ell, E_{\mathrm{T}}^{\mathrm{miss}}) < 40$ GeV. This selection is split into two distinct validation regions: an on-Z region, which requires the same-flavor lepton pair to additionally have dilepton mass $m_{\ell\ell}$ within 10 GeV of the Z mass, and the off-Z region, which requires the dilepton mass to fall outside of this range.

The on-Z region is the fakes validation region: It validates the accuracy of the fake factor method in determining the fake background. Its selection criteria are designed to expose the region to Z+jets processes with a fake lepton being the third lepton in the event. The off-Z validation region exists to check the modeling of the WZ background when the Z-boson is produced off-shell. It also confirms proper prediction of the fake background in off-Z events (which will have relatively fewer fakes from Z+jets processes and more from $t\bar{t}$). It furthermore proves that the lower $m_{\ell,\ell}$ spectrum does not suffer from a mismodeling due to an additional quarkonium contribution.

Chapter 5

Background Prediction

Two different methods of background estimation are used concurrently in this analysis. One method relies entirely on event generators, using Monte Carlo techniques to simulate all aspects of the event based on knowledge of theory. The processes estimated in this way and the algorithms used to simulate them are given in Section 5.1. The other method is a data-driven technique called the fake factor method, relying on measuring an event ratio in a dedicated region which is then extrapolated to other regions. Section 5.2 describes the specifics of the fake factor method and the motivation for using it for certain processes.

5.1 Used Event Generators

Three ATLAS baseline generators are used to produce many samples for this analysis. Information is given on what algorithms are used to compute the ME and PS, what PDF set is used and how matching is performed, including references to more detailed descriptions of each. These descriptions are common to all processes. Alongside descriptions of each generator the Standard Model processes for which they have been used are also given. This information is additionally summarized in Table 5.1.

5.1.1 Sherpa

SHERPA [167] is a general purpose generator featuring both a ME generator and a parton showering algorithm. It is furthermore capable of simulating additional hard parton emissions [168]. It is suitable for simulating each of the previously mentioned event aspects, but is limited in its description of processes to $2 \to 2$ particles.

Generated events are matched to a parton shower based on Catani-Seymour dipoles [169]. The authors of the algorithm natively provide a tuned set of parton shower parameters. The NLO+PS matching [170] is employed for the different multiplicities of jets emitted (higher jet multiplicities may be limited to leading-order computations), which are then merged into an inclusive sample using an improved CKKW matching procedure [60, 171]. This is extended to NLO accuracy using the MEPS@NLO prescription [172]. In the software versions applied in this thesis, SHERPA uses the `NNPDF3.0nnlo` set [173] of parton density functions (PDFs).

All heavy boson processes used as backgrounds in this analysis are simulated by SHERPA. This includes the diboson processes which make up the most prominent background, $WZ \to \ell\ell\ell\nu$ and $ZZ \to 4\ell$. Loop-induced Higgs and VH processes are included into the diboson processes as a single inclusive sample. For triboson processes, only the on-shell contribution is generated; the off-shell component is considered a negligible contribution

Process	Event Generator	Parton Shower	Order	PDF Set	Usage
WZ,ZZ,WW	Sherpa 2.2.2	Sherpa	NLO	NNPDF3.0nnlo	both
VVV (V=W,Z)	Sherpa 2.2.2	Sherpa	NLO	NNPDF3.0nnlo	nominal
ggH, VBF, VH,	Sherpa 2.2.2	Sherpa	LO	NNPDF3.0nnlo	nominal
t	PowhegBox v2	Pythia8	NLO	NNPDF3.0nnlo	fakes
$t\bar{t}$	PowhegBox v2	Pythia8	NLO	NNPDF3.0nnlo	both
$t\bar{t}$ + W,Z	MadGraph5_aMC@NLO	Pythia8	NLO	MEN30NLO	nominal
$t\bar{t}$ + H	PowhegBox v2	Pythia8	NLO	NNPDF30ME	nominal
$t\bar{t}$ + WW	MadGraph5_aMC@NLO	Pythia8	LO	NNPDF3.0nnlo	nominal
tZ	MadGraph5_aMC@NLO	Pythia8	LO	NNPDF3.0nnlo	nominal
$3t, 4t$	MadGraph5_aMC@NLO	Pythia8	LO	NNPDF2.3lo	nominal
$Z/\gamma \to \ell\ell$	Sherpa 2.2.1	Sherpa	NNLO	NNPDF3.0nnlo	fakes
$W \to \ell\nu$	Sherpa 2.2.1	Sherpa	NNLO	NNPDF3.0nnlo	fakes
Type-III SS	MadGraph5_aMC@NLO	Pythia8	LO	NNPDF3.0nnlo	signal
$H^{\pm\pm}$	Pythia8	Pythia8	LO	NNPDF3.0nnlo	signal

Table 5.1: All the physics processes estimated through Monte Carlo generation and the generators used to create them. Order values are "LO" for leading order and "NLO" (NNLO) for subsequent (next-to) next-to leading order cross-section normalization. Values refer to the simulation order of the *dominant* diagrams contributing to the process: additional sub-dominant contributions (as well as processes with additional parton emissions) may have been produced at lower orders. Detailed information on these orders is provided in the accompanying text in this chapter. Usage column values "fakes" for samples that are used for estimation of the fake factor (explained in Chapter 5), "nominal" for samples used in 3/4 lepton control and signal regions, or "both" if the samples enter into both regions. The term "signal" is used if the sample is meant as a benchmark for BSM physics the analysis is potentially sensitive to.

to the background estimation for this analysis. Single vector boson processes $W \to \ell\nu$ and $Z \to \ell\ell$ are also simulated by Sherpa for use in single-lepton regions.

5.1.2 MadGraph5_aMC@NLO

This algorithm is exclusively an MC generator, capable of HS cross section ME calculations at leading order and can do so for processes of $2 \to n$ particles. It is interfaced with Pythia8 [174] for the modeling of the parton shower and underlying event. To remove overlap between the matrix element and the parton shower the CKKW-L merging procedure [175, 176] is applied. The A14 tune [177] of Pythia8 is used with the NNPDF2.3lo PDF set [178] with $\alpha_S = 0.13$. The EvtGenv1.2.0 program [179] is used to simulate bottom and charm hadron decays.

MadGraph5_aMC@NLO is used for the simulation of most of the rare top processes which can lead to three or more leptons: $t\bar{t} + V$ (V=W,Z), $t\bar{t} + WW$ and tZ, as well as 3 top and 4 top production.

5.1.3 Powheg

PowhegBox [180–182] provides a general framework for implementing NLO QCD calculations with shower Monte Carlo programs. Like MadGraph, PowhegBox is interfaced to PYTHIA 8.212 [183] for the purposes of generating parton showers, using also the A14 tune. The samples were generated in the G_μ scheme [184], ensuring an optimal description of pure electroweak interactions at the electroweak scale. This algorithm uses the NNPDF3.0nnlo set of PDFs. The EvtGenv1.2.0 program [179] is used to simulate bottom and charm hadron decays.

POWHEG is used for the simulation of top samples which are prominent in single-lepton regions, these being single-top (all production channels: s, t, Wt) and $t\bar{t}$ production. It is also used for a single background process that can produce a 3+ lepton final state: $t\bar{t}H$. However, the contribution of this sample is tiny.

5.2 The Fake Factor Method

Although the majority of background events can be simulated through Monte Carlo (MC) methods, there remains a class of events where at least one of the recorded leptons does not originate from a particular physics process, but is instead caused by detector measurement errors or secondary in-flight decays of heavy hadrons. This limitation of Monte Carlo simulation is addressed in this chapter, and a data-driven alternative is introduced: The *Fake Factor method*. The process and associated machinery required to obtain a fake background estimation will be outlined step by step.

Section 5.2.1 will introduce several classifications of particles to make clear what is meant by the term *fake*. Section 5.2.2 will then define the meaning of the term *fake factor*, its physical meaning and the compounds that go into its computation. Section 5.2.3 will explain how the fake factor can be used to create estimations for a background that is expected to partially consist of events with at least 1 fake lepton. Section 5.2.4 will then explain the process behind setting up a fake-enriched region, clarifying some of the assumptions and requirements that go into setting up such a region. Separate sections will be dedicated to the construction of such fake-enriched regions for the electron and the muon separately. Finally, in Section 5.2.5, the resulting fake factors that have been obtained and used for this analysis will be shown.

5.2.1 Particle Classification

Prior to discussing how to estimate the fake background, it is helpful to clarify exactly what types of particles are encompassed by the term *fake* leptons. Broadly, there are two groups of reconstructed leptons which are referred to as fakes:

The first group of fakes is due to the reconstruction algorithms wrongfully classifying hadrons as leptons. These objects are genuinely fake, as the reconstructed object was never an actual lepton, but merely a misidentification of the object that was detected.

In the second group of fakes, the detected object is an actual lepton, but the lepton is not classified as *prompt*. A prompt lepton is a lepton that was produced at the primary vertex (or from short-lived particles whose decay vertex is indistinguishable from the primary vertex due to its short lifetime). Conversely, a non-prompt lepton is one that was produced through the decay of a long-lived hadron. This includes semileptonic decays of hadrons containing b-quarks or c-quarks. It also includes leptons produced due to the conversion of photons from hadrons decaying electromagnetically, (e.g. $\pi^0 \to \gamma\gamma$).

However, if a prompt τ is produced, and this τ decays to lighter leptons (e.g. $\tau \to \mu\nu_\tau\bar{\nu}_\mu$), the resulting lepton is also considered prompt. Furthermore, conversion of photons radiated off other leptons[1] are also prompt.

[1] Overlap removal usually discards these leptons as they are generally collinear with the lepton they radiated off.

5.2.2 The Fake Factor

The *fake factor* is the ratio in which a fake particle will pass a certain set of selection criteria (the *ID* or *nominal* selection) relative to another closely related, but different set of selection criteria (the *anti-ID* selection). Mathematically, the fake factors f_i are a set of unitless quantities, which is calculated by taking a division of two regions with similar topology but slightly different lepton object definitions. These regions will be called the *ID* and *anti-ID* regions.

$$f_i = \frac{N_{N,i}}{N_{D,i}} \tag{5.1}$$

Here $N_{N,i}$ and $N_{D,i}$ are the estimated number of non-prompt leptons in respectively the ID and anti-ID selection for a particular subselection i. These quantities are defined as $N = n_{data} - n_{MC}$, the amount of data events minus the amount of events expected from prompt sources, which is estimated using Monte Carlo techniques. The difference between the prompt prediction and the total observed by data is assumed to be due to an additional source of events containing non-prompt leptons.

The fake factor is determined as a function of two kinematic variables of the lepton: transverse momentum and pseudorapidity. For brevity's sake these dimensions are folded into the single index i. Electron and muon fake factors are computed separately, reflecting that sources of fake leptons will affect the total amount of each lepton flavor to different degrees. It is assumed that these fake factors solely depend on the aforementioned object properties, and not on any other properties in the event.

5.2.3 Using the Fake Factor

Consider a signal region that features 3 leptons. Each of the leptons in the signal region is required to pass the nominal selection, and therefore each of them will be an ID lepton. We express a three-lepton event where all leptons pass the ID selection as $\ell_1^N \ell_2^N \ell_3^N$. ℓ_i^N indicates the presence of an ID lepton in the event. Each of the leptons is an object indexed with 1, 2 and 3. The numerical ordering of these leptons is arbitrary (it describes no particular ordering of p_{T} or any other variable).

Each of these leptons can be either a real lepton or a fake one. An event with three real leptons can be expressed as $\ell_1^R \ell_2^R \ell_3^R$. The probability of any ID lepton being fake is assumed to be independent of the properties of the *other* leptons in the event. Therefore, this composition of an event with three ID leptons can be separated into eight different combinations of real and fake leptons. This is shown in Equation 5.2.

$$\begin{aligned} \ell_1^N \ell_2^N \ell_3^N =& \ell_1^R \ell_2^R \ell_3^R + \ell_1^R \ell_2^R \ell_3^F + \ell_1^R \ell_2^F \ell_3^R + \ell_1^F \ell_2^R \ell_3^R \\ &+ \ell_1^R \ell_2^F \ell_3^F + \ell_1^F \ell_2^R \ell_3^F + \ell_1^F \ell_2^F \ell_3^R + \ell_1^F \ell_2^F \ell_3^F \end{aligned} \tag{5.2}$$

One term of Equation 5.2 can be estimated accurately with Monte Carlo generated events: An event that consists entirely out of real leptons: $\ell_1^R \ell_2^R \ell_3^R$. The other 7 terms each contain

one or more fake leptons, the rate of which can be derived from the anti-ID regions. For this purpose, regions containing at least one anti-ID lepton are set up. Let ℓ_i^D be a anti-ID lepton. Examples of such regions can then be written as $\ell_1^D \ell_2^N \ell_3^N$ and $\ell_1^D \ell_2^D \ell_3^D$. In total, 7 such combinations exist. These regions can also be expressed as a combination of real and fake leptons, as is demonstrated in Equations 5.3, 5.4 and 5.5. In these equations, take special notice of the fake factor terms f_i, which are introduced through $\ell_i^N = \ell_i^D f_i$.

$$\left.\begin{aligned} \ell_1^D \ell_2^N \ell_3^N f_1 &= \ell_1^F \ell_2^R \ell_3^R + \ell_1^F \ell_2^F \ell_3^R + \ell_1^F \ell_2^R \ell_3^F + \ell_1^F \ell_2^F \ell_3^F \\ \ell_1^N \ell_2^D \ell_3^N f_2 &= \ell_1^R \ell_2^F \ell_3^R + \ell_1^F \ell_2^F \ell_3^R + \ell_1^R \ell_2^F \ell_3^F + \ell_1^F \ell_2^F \ell_3^F \\ \ell_1^N \ell_2^N \ell_3^D f_3 &= \ell_1^R \ell_2^R \ell_3^F + \ell_1^F \ell_2^R \ell_3^F + \ell_1^R \ell_2^F \ell_3^F + \ell_1^F \ell_2^F \ell_3^F \end{aligned}\right\} F_1 \tag{5.3}$$

$$\left.\begin{aligned} \ell_1^D \ell_2^D \ell_3^N f_1 f_2 &= \ell_1^F \ell_2^F \ell_3^R + \ell_1^F \ell_2^F \ell_3^F \\ \ell_1^D \ell_2^N \ell_3^D f_1 f_3 &= \ell_1^F \ell_2^R \ell_3^F + \ell_1^F \ell_2^F \ell_3^F \\ \ell_1^N \ell_2^D \ell_3^D f_2 f_3 &= \ell_1^R \ell_2^F \ell_3^F + \ell_1^F \ell_2^F \ell_3^F \end{aligned}\right\} F_2 \tag{5.4}$$

$$\left.\ell_1^D \ell_2^D \ell_3^D f_1 f_2 f_3 = \ell_1^F \ell_2^F \ell_3^F \right\} F_3 \tag{5.5}$$

An object fulfilling the anti-ID selection is not necessarily a fake object. The equations above simply use the fact that, given N_N objects satisfying the nominal selection and the requirements for a particular fake factor bin i, there are expected to $N_D = N_N / f_i$ objects passing the anti-ID selection, f_i being the fake factor associated to bin i.

We can sum the terms in Equations 5.3, 5.4 and 5.8 as follows, introducing F_1, F_2 and F_3 as shorthand to indicate lepton combinations with exactly one, two and three anti-ID leptons respectively:

$$\begin{aligned} F_1 &= \ell_1^D \ell_2^N \ell_3^N f_1 + \ell_1^N \ell_2^D \ell_3^N f_2 + \ell_1^N \ell_2^N \ell_3^D f_3 \\ &= \ell_1^F \ell_2^R \ell_3^R + \ell_1^R \ell_2^F \ell_3^R + \ell_1^R \ell_2^R \ell_3^F \\ &+ 2\Big(\ell_1^F \ell_2^F \ell_3^R + \ell_1^F \ell_2^R \ell_3^F + \ell_1^R \ell_2^F \ell_3^F\Big) \\ &+ 3(\ell_1^F \ell_2^F \ell_3^F) \end{aligned} \tag{5.6}$$

$$\begin{aligned} F_2 &= \ell_1^D \ell_2^D \ell_3^N f_1 f_2 + \ell_1^D \ell_2^N \ell_3^D f_1 f_3 + \ell_1^N \ell_2^D \ell_3^D f_2 f_3 \\ &= \ell_1^F \ell_2^F \ell_3^R + \ell_1^F \ell_2^R \ell_3^F + \ell_1^R \ell_2^F \ell_3^F + 3(\ell_1^F \ell_2^F \ell_3^F) \end{aligned} \tag{5.7}$$

$$F_3 = \ell_1^D \ell_2^D \ell_3^D f_1 f_2 f_3 \tag{5.8}$$

Combining this result with Equations 5.2 and 5.5 (let $F_3 = \ell_1^D \ell_2^D \ell_3^D f_1 f_2 f_3$ to emphasize the symmetry of equation 5.5 with 5.3 and 5.4) yields Equation 5.9.

$$F_1 - F_2 + F_3 = \ell_1^N \ell_2^N \ell_3^N - \ell_1^R \ell_2^R \ell_3^R \tag{5.9}$$

From here it becomes evident how the event rate of a region containing 3 ID leptons can be estimated from the combination of a region with 3 real leptons (estimated with MC generated events that allow only truth-matched particles) and the various combined ID/anti-ID object regions multiplied with (compounded) fake factors. This is detailed in Equation 5.10. Of special note is the third row of the equation, a negative contribution that is needed to prevent double counting of events with exactly 2 fakes and 1 real lepton.

$$\begin{aligned}
\ell_1^N \ell_2^N \ell_3^N &= \ell_1^R \ell_2^R \ell_3^R \\
&+ \ell_1^D \ell_2^N \ell_3^N f_1 + \ell_1^N \ell_2^D \ell_3^N f_2 + \ell_1^N \ell_2^N \ell_3^D f_3 \\
&- \left(\ell_1^D \ell_2^D \ell_3^N f_1 f_2 + \ell_1^D \ell_2^N \ell_3^D f_1 f_3 + \ell_1^N \ell_2^D \ell_3^D f_2 f_3 \right) \\
&+ \ell_1^D \ell_2^D \ell_3^D f_1 f_2 f_3
\end{aligned} \tag{5.10}$$

The explanation given here is for a 3 lepton final state, but a similar derivation will hold for regions with 4 or more leptons. The only difference is the introduction of additional permutations in the composition of fake objects in the event. It is again assumed that ID region is composed of contributions consisting of fake and real events, as shown in Equation 5.11.

$$\begin{aligned}
\ell_1^N \ell_2^N \ell_3^N \ell_4^N = {} & \ell_1^R \ell_2^R \ell_3^R \ell_4^R + \ell_1^R \ell_2^R \ell_3^R \ell_4^F + \ell_1^R \ell_2^R \ell_3^F \ell_4^R + \ell_1^R \ell_2^F \ell_3^R \ell_4^R + \ell_1^F \ell_2^R \ell_3^R \ell_4^R \\
& + \ell_1^R \ell_2^R \ell_3^F \ell_4^F + \ell_1^R \ell_2^F \ell_3^R \ell_4^F + \ell_1^F \ell_2^R \ell_3^R \ell_4^F + \ell_1^R \ell_2^F \ell_3^F \ell_4^R + \ell_1^F \ell_2^R \ell_3^F \ell_4^R + \ell_1^F \ell_2^F \ell_3^R \ell_4^R \\
& + \ell_1^R \ell_2^F \ell_3^F \ell_4^F + \ell_1^F \ell_2^R \ell_3^F \ell_4^F + \ell_1^R \ell_2^F \ell_3^R \ell_4^F + \ell_1^F \ell_2^F \ell_3^R \ell_4^F + \ell_1^F \ell_2^F \ell_3^F \ell_4^R + \ell_1^F \ell_2^F \ell_3^F \ell_4^F
\end{aligned} \tag{5.11}$$

Following a similar line of reasoning as for the 3 lepton scenario, an expression arises to estimate the fake contribution from events with at least one fake lepton to the four-lepton signal region. This is given in Equation 5.12.

$$\begin{aligned}
\ell_1^N \ell_2^N \ell_3^N \ell_4^N &= \ell_1^R \ell_2^R \ell_3^R \ell_4^R \\
&+ \ell_1^D \ell_2^N \ell_3^N \ell_4^N f_1 + \ell_1^N \ell_2^D \ell_3^N \ell_4^N f_2 + \ell_1^N \ell_2^N \ell_3^D \ell_4^N f_3 + \ell_1^N \ell_2^N \ell_3^N \ell_4^D f_4 \\
&- \Big(\ell_1^D \ell_2^D \ell_3^N \ell_4^N f_1 f_2 + \ell_1^D \ell_2^N \ell_3^D \ell_4^N f_1 f_3 + \ell_1^D \ell_2^D \ell_3^N \ell_4^D f_1 f_4 \\
&+ \ell_1^N \ell_2^D \ell_3^D \ell_4^N f_2 f_3 + \ell_1^N \ell_2^D \ell_3^N \ell_4^D f_2 f_4 + \ell_1^N \ell_2^N \ell_3^D \ell_4^D f_3 f_4 \Big) \\
&+ \ell_1^D \ell_2^D \ell_3^N \ell_4^N f_1 f_2 f_3 + \ell_1^D \ell_2^D \ell_3^N \ell_4^D f_1 f_2 f_4 + \ell_1^D \ell_2^N \ell_3^D \ell_4^D f_1 f_3 f_4 \\
&+ \ell_1^N \ell_2^D \ell_3^D \ell_4^D f_2 f_3 f_4 - \ell_1^D \ell_2^D \ell_3^D \ell_2^D f_1 f_2 f_3 f_4
\end{aligned} \tag{5.12}$$

5.2.4 Obtaining the Fake Factors: Estimation Regions

We now turn to the fake estimation regions, already defined in Table 4.6 in Section 4.2. Electrons and muons are treated separately due to their differing fake composition. In both cases, a region is established using loose, prescaled triggers and requiring exactly one lepton to pass the baseline selection (see Section 4.1). Events containing more than one lepton of any flavor are vetoed.

Electrons

Electron fakes are expected to originate from two sources: *semileptonic heavy flavor decays* and *misidentified light hadrons*. An estimate for these fake contributions can be obtained from a single-electron region. For this, a set of prescaled single electron triggers are used. This has been explained more in-depth in Section 4.1.2. The used triggers and the data taking year they are used in are given in Table 4.2. Furthermore, to obtain a better ratio of fake leptons compared to non-fake leptons in these regions, we require at least 1 jet (with selection criteria given in Section 4.1.3) in each event. Furthermore, the $W \to e\nu$ contribution is partially suppressed by imposing a missing energy cut of $E_{\mathrm{T}}^{\mathrm{miss}} < 25$ GeV.

Table 5.2 outlines the requirements for electrons to be admitted into the fake-enriched region as either ID or anti-ID electrons. There are two criteria, each of which aims to capture one of the two main sources of electron fakes. The PID quality selection seeks to include misidentified light hadrons, while the isolation criteria aims to select those electrons that originate from semileptonic heavy flavor decays.

Criteria	ID	anti-ID
PID Quality	`Tight`	`Loose` and **fail** `Tight`
Isolation	`FCTight`	**fail** `FCTight`

Table 5.2: Criteria that when taken in addition to the baseline electron selection describe a ID (signal) and anti-ID electron respectively. anti-ID electrons are required to pass exactly one of the two anti-ID criteria and pass exactly one of the two ID criteria. Electrons passing both anti-ID criteria (i.e. failing both ID criteria) are discarded instead.

Plots for this region are given in Figure 5.1. The difference between the data and the MC prediction in these figures is the estimated contribution coming from events with fake electrons. More granular plots that also split the regions according to the pseudorapidity separation of fake factors are given in Appendix A.

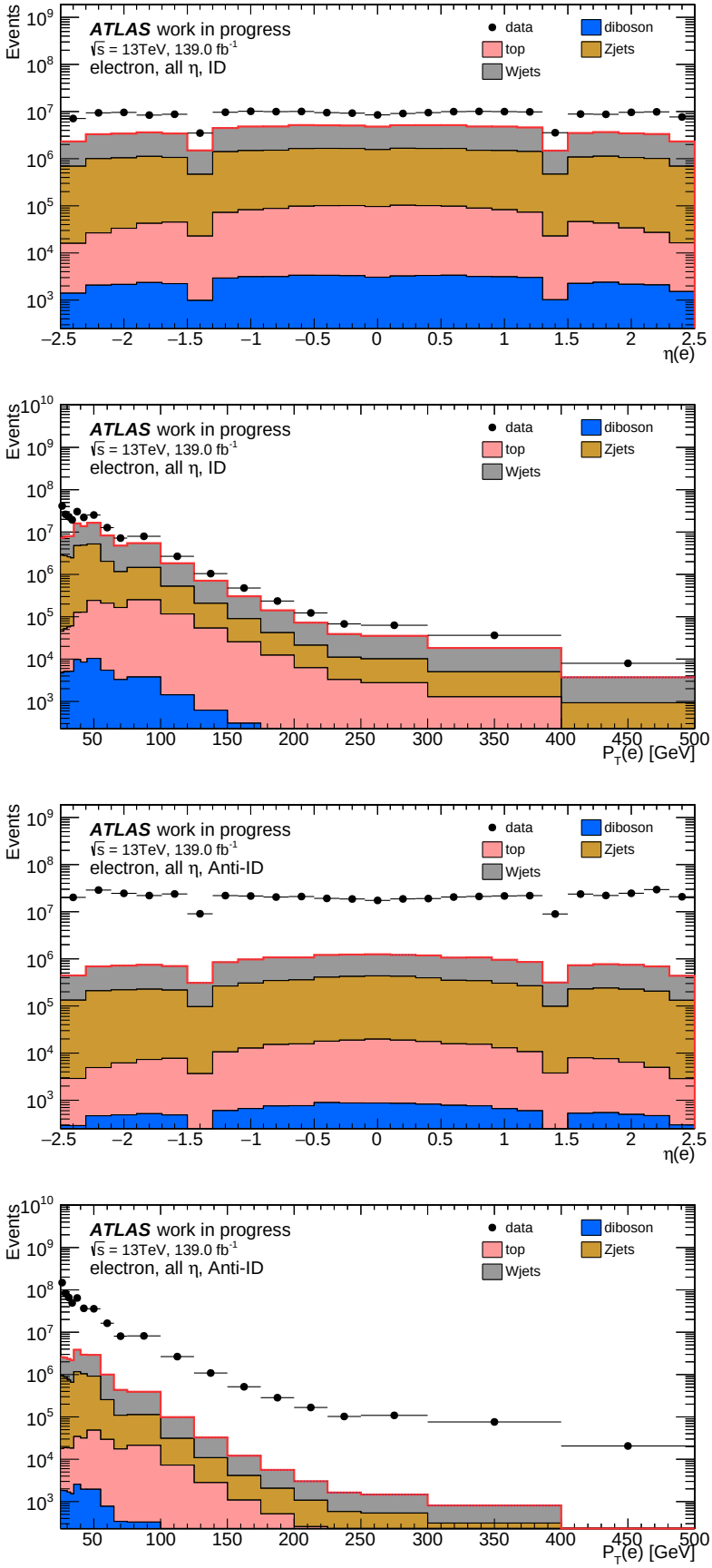

Figure 5.1: Distributions of the electron fake-enriched-region for the ID (top two images) and anti-ID (bottom two images) selections.

Muons

The main source of muon fakes is assumed to be the in-flight decays of bottom and charm hadrons inside jets [185]. Misidentified light hadrons, which are considered as a fake source for the electron fake factor, are negligible because intermediate photon conversion rarely leads to the detection of muons by the muon spectrometer, which is located on the outside of the ATLAS detector. Because of this difference with respect to the electron, different selection criteria on the amount of jets and missing energy are used. These selection criteria reflect the overall lower fake rate and the fake sources of interest for these leptons.

The single muon is selected using a tag-and-probe method in order to obtain a good fraction of fake leptons [185]. For this method there is the requirement of exactly one jet (the *tag*) in the event which has $p_{\mathrm{T}} > 35$ GeV and lies back-to-back with the muon (the *probe*). Specifically, we require an azimuthal angle $\Delta\phi(\mu, \mathrm{jet}) > 2.7$ and at least 2 jets (including the tag jet) are required. This method is shown schematically in Figure 5.2 A $E_{\mathrm{T}}^{\mathrm{miss}}$ cut of $MET < 40$ GeV is imposed in order to exclude $W \to \mu\nu$ events.

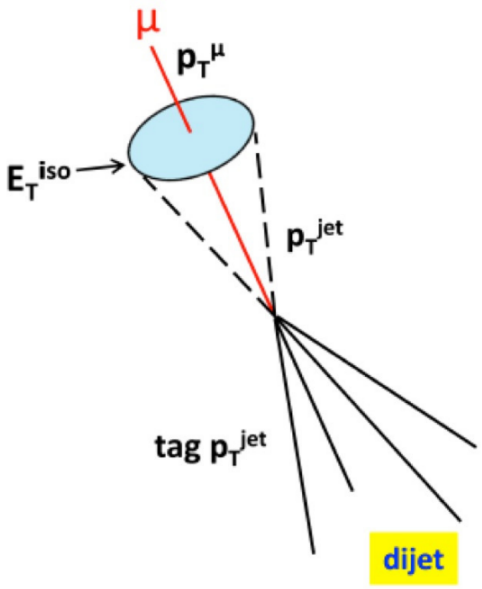

Figure 5.2: Schematic figure of the tag and probe method by which muons are selected from dijet events based on the azimuthal muon-jet angle. Image taken from [185].

Given that semileptonic heavy flavor decays are the main source of fakes, it is sufficient to invert the isolation criteria on the muon object selection to capture the orthogonal region where such objects are more prominent. Therefore, the baseline muon selection given in Table 4.4 suffices as the anti-ID object selection.

Plots for this region are given in Figure 5.3. The difference between the data and the MC estimation in these figures is the estimated contribution coming from events with fake muons. More granular plots that also split the regions according to the pseudorapidity separation of fake factors are given in Appendix A.

The fake-enriched region plots for muons demonstrate that the rate of muon fakes is negligible above a transverse momentum of 100 GeV. The potential muon fake contribution in this region is smaller than the uncertainty on the Monte Carlo estimation, which makes the fake factor method unsuitable for providing an estimate. Therefore, muons above this transverse momentum are not included for the computation of fake factors.

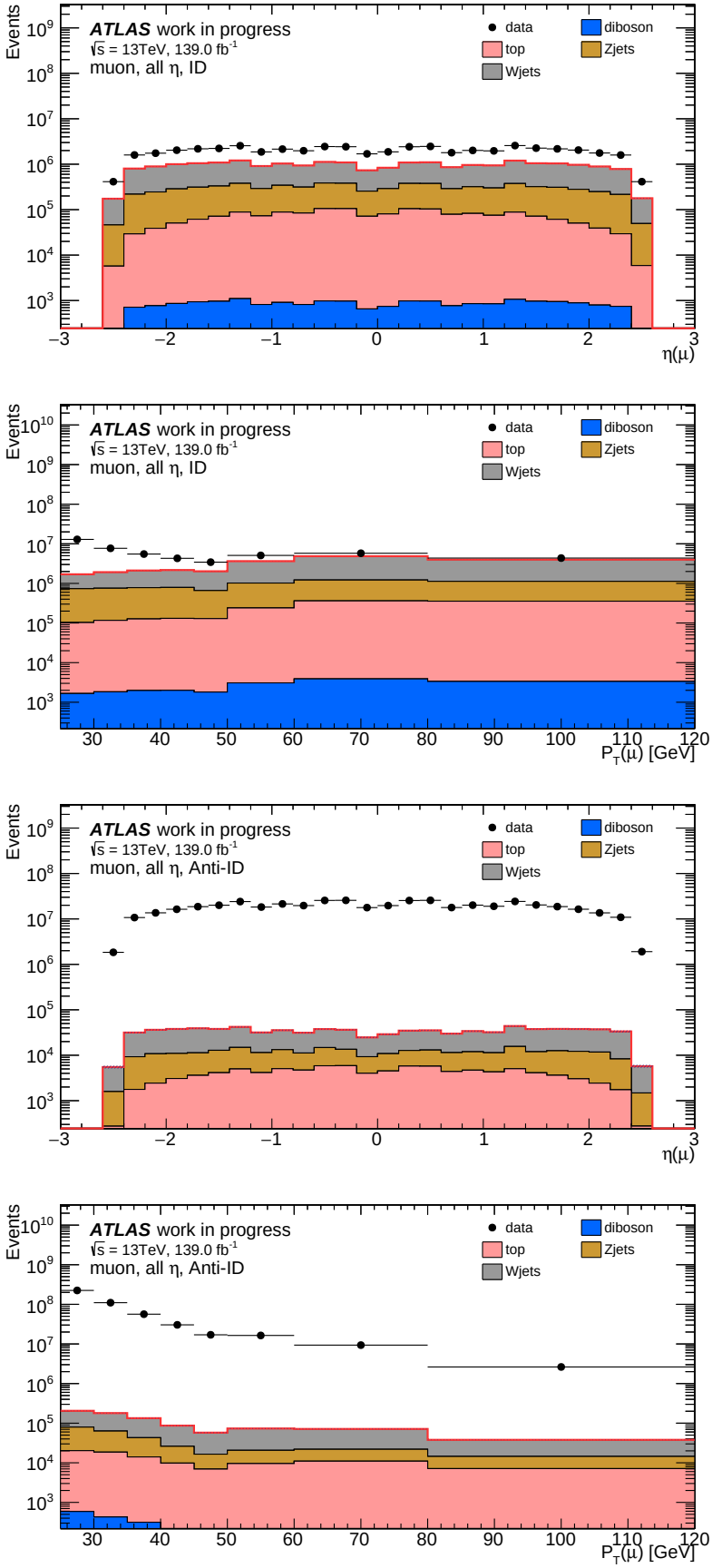

Figure 5.3: Distributions of the muon fake-enriched-region for the ID (top two images) and anti-ID (bottom two images) selections.

5.2.5 Results

Figure 5.4 shows the fake factors for electrons and muons as they have been measured for this analysis. These results demonstrate the dependence of the fake factors on the transverse momentum and pseudorapidity region. There is a significant difference between the electron fake factors and muon fake factors. As mentioned earlier in this Chapter, this is because electrons have an additional source of fakes arising from misidentified light hadrons, while muons only have fakes from semileptonic flavor decays.

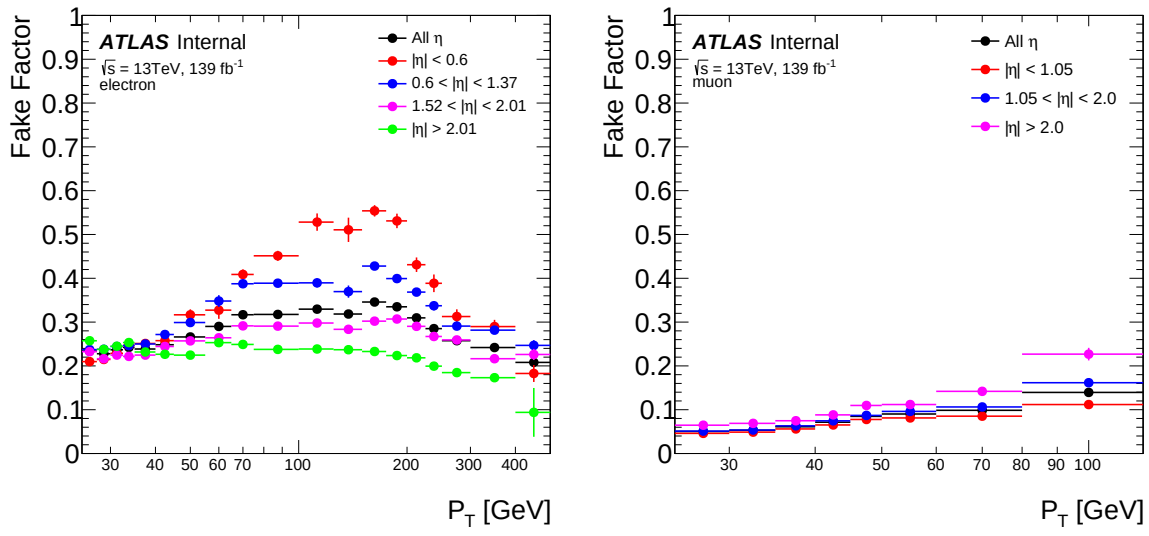

(a) electron **(b)** muon

Figure 5.4: fake factors measured in p_{T} and η for events with (a) electrons and (b) muons.

Through single-lepton validation regions it is checked that these computed fake factors with the used binning are applicable and can be transferred to compute a fake background[2]. These validations regions are kinematically close (but orthogonal) to the electron fake computation region and are used as an initial test for the fake factor estimates, exposing and identifying any binning effects. There are two regions: the $W \to e\nu$ and the $W \to \mu\nu$ region, which require exactly one electron (and zero muons) and exactly one muon (and zero electrons). The missing energy requirement for events is inverted with respect to the fake selection regions to become orthogonal to these regions. That is, cuts are imposed of $E_{\mathrm{T}}^{\mathrm{miss}} > 25$ GeV for the $W \to e\nu$ region and $E_{\mathrm{T}}^{\mathrm{miss}} > 40$ GeV for the $W \to \mu\nu$ region. No jet-based criteria such as a minimum jet multiplicity or angular distances are imposed.

Plots of the momentum and pseudorapidity are given in Figure 5.5 for the $W \to e\nu$ region and in Figure 5.6 for the $W \to \mu\nu$ region. Although the fake background is a relatively small contribution in these regions, no major mismodeling effects stand out. A slight trend can be observed in the lower p_{T} range for both the electron and the muon at $p_{\mathrm{T}} < 60$ GeV. These effects are the result of the transfer of the fake background between the low and the high-MET region and are addressed by systematic uncertainties (discussed in Section 6.2.2). Slight trends are also noticeable in the pseudorapidity range $|\eta| > 2.0$. However, this fake estimate, when averaged out over the entire bin, is still compatible.

[2]Three lepton validation regions to check that the fake background is correctly modelled also exist, and are shown in Chapter 7.

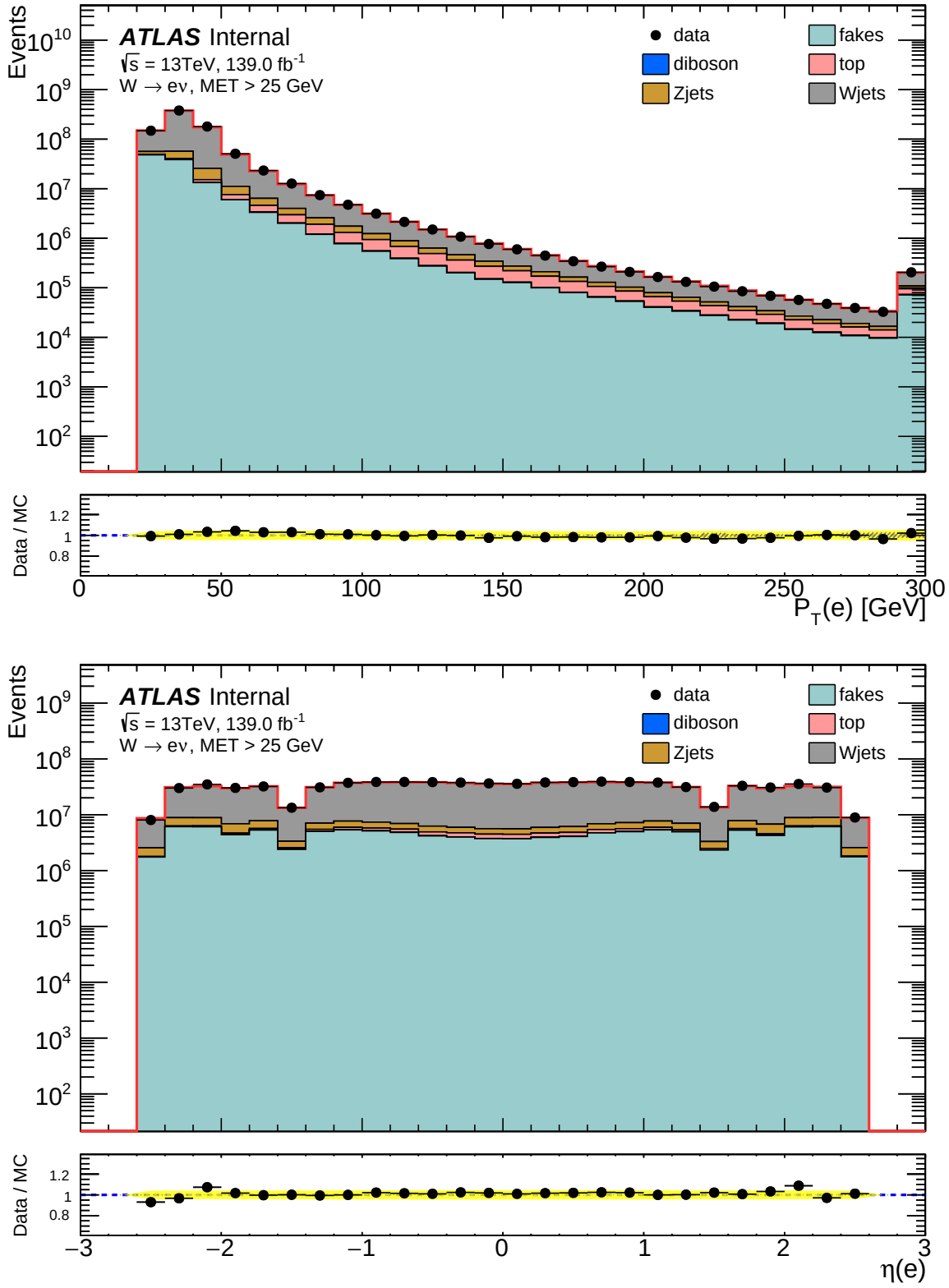

Figure 5.5: Variables for the electron in the $W \to e\nu$ validation region, showing the transverse momentum (top) and pseudorapidity (bottom). Uncertainties given are the statistical uncertainties on data and Monte Carlo events, the fake systematic uncertainties and theoretical uncertainties on MC contributions.

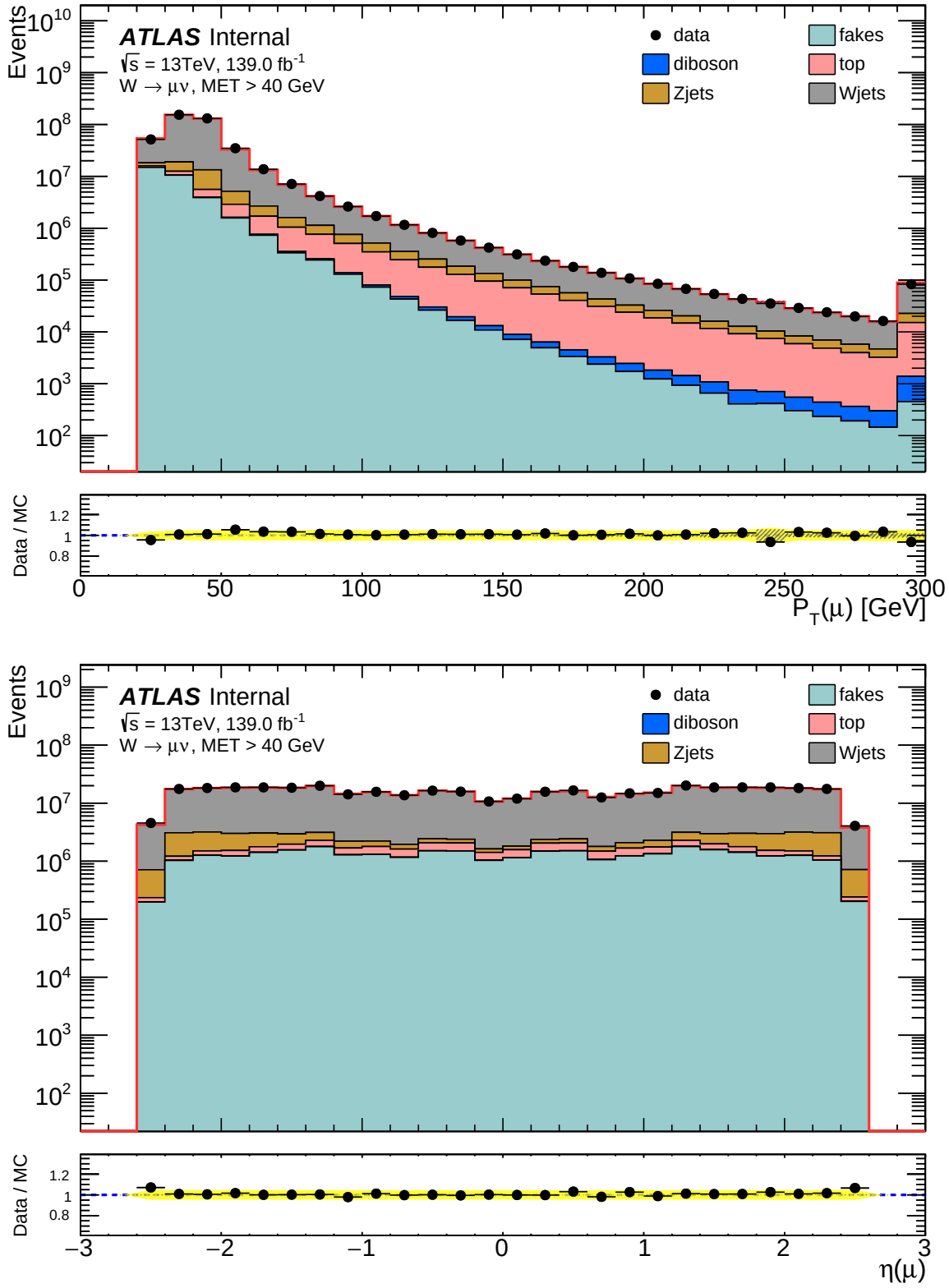

Figure 5.6: Variables for the muon in the $W \to \mu\nu$ validation region, showing the transverse momentum (top) and pseudorapidity (bottom). Uncertainties given are the statistical uncertainties on data and Monte Carlo events, the fake systematic uncertainties and theoretical uncertainties on MC contributions.

Part III

Interpretation

Chapter 6

Statistical Analysis

The previous chapters established the regions of interest, and how we have managed to quantify our background expectation for these regions. Now it will be explained how this expectation and measured data are to be compared, and how the extracted results can be interpreted. First, the statistical toolbox is introduced. Then, a complete explanation is provided for the treatment of all of the relevant uncertainties.

6.1 Fitting and Limit Setting

This analysis uses the Profile Likelihood Ratio technique [186–188] to infer the likelihood of the presence of new physics against the likelihood of a Standard Model-only hypothesis. A *likelihood*[1] is a function to measures the goodness of fit of a statistical model to a data sample for specific model parameter values. Profiling is a technique used to find the maximum likelihood of a statistical model by adjusting the model's parameters in a continuous way. Through profiling, one can find a new optimal set of model parameters when shifting the value of one of those parameters, effectively reducing the dimensionality of the likelihood formulation For this analysis, the likelihood formula is reduced to a one-dimensional dependence.

The following section guides the reader through the motivation of the statistical tools used, and the means by which they are applied.

To understand the motivation for the use of a likelihood ratio, consider the type of errors that can be made when choosing to reject a null hypothesis in favor of an alternative hypothesis. These types of errors can be classified into false positives (Type-I, rejecting a valid null hypothesis) and false negatives (Type-II, failing to reject an invalid null hypothesis).

The Neyman-Pearson lemma [189] introduces the likelihood ratio test as the most powerful test when comparing simple hypotheses. That is, it establishes the lowest possible Type-II error once an acceptable Type-I error has been chosen. This lemma ceases to be valid for composite hypotheses containing also one or more nuisance parameters, as is the case for this analysis. Even so, the likelihood ratio test displays good properties in many situations, and is the preferred starting point of ATLAS analyses that have a large number of observations.

Competing hypotheses will have discernible probability distribution functions (PDF). The basis of the likelihood formulation for this analysis is a set of single-bin Poisson distributions.

[1] Frequentist definitions are used throughout this chapter.

For each individual signal region one expects a particular amount of background events N_B and an unknown (due to model-independence) amount of signal events N_S. The likelihood for a given experiment where n_{obs} events are observed in a signal region is then given by

$$L_{SR} = e^{-(N_S+N_{B,SR})} \frac{(N_S + N_{B,SR})^{n_{obs}}}{n_{obs}!}. \tag{6.1}$$

For each signal region we have the null hypothesis $H_0 : N_S = 0$ and the alternative hypothesis $H_1 : N_S \neq 0$. The amount of signal events, N_S, is the *parameter of interest* (PoI). This parameter is unbounded and unconstrained, and in case of this analysis is allowed to be negative[2]. Other undetermined parameters also enter into the model. These *nuisance parameters* (NPs) represent the quantified ignorance of the assumptions that have entered into the model. These must also be accounted for. Nonzero values indicate the potential presence of a deviation, hinting at the possibility of an additional exotic physics contribution, or potentially destructive BSM interference with Standard Model processes (if $N_S < 0$).

The control regions incorporated in this analysis use binned distributions, which should increase the experiment's power to constrain the values of the nuisance parameters. It is assumed no signal is present in the control region, as it is defined to be dominated by a large amount of Standard Model events so that any additional signal contribution is negligible. The likelihood function of a control region is a multi-bin Poisson distribution where $N_S = 0$, shown in Equation 6.2. In this equation N_B, i refers to the total background yield of an individual bin in the control region.

$$L_{CR} = \prod_{i=1}^{n_{bins}} e^{N_{B,i}} \frac{(N_{B,i})^{n_i}}{n_i!} \tag{6.2}$$

The background contributions $N_{B,i}$ are a composition of multiple contributions: WZ, ZZ, triboson, top processes and fake processes. Predictions of these processes are themselves functions of two sets of nuisance parameters which can be categorized as *normalization factors* (NF) and *systematic uncertainties*.

NFs are unbounded nuisance parameters that scale the total prediction of a single SM process, but do not affect the distribution shape. Processes with dedicated control regions, WZ and ZZ, have free-floating normalization factors. We indicate these normalization factors with ϕ_{WZ} and ϕ_{ZZ}. For other background processes the value is fixed to their MC[3] predictions. Thus, the background yield in a single bin can be written as

$$N_{B,i} = \phi_{WZ} N_{WZ,i} + \phi_{ZZ} N_{ZZ,i} + N_{triboson,i} + N_{top,i} + N_{fakes,i}. \tag{6.3}$$

Two control regions are defined in this analysis two determine these NFs, and the choice of these control regions is unchanged: they are used for every individual signal region. A

[2] as long as $N_{B,SR} + N_S \geq 0$. For all regions of this analysis, $N_B > 0$.
[3] Except for the fake background, which is determined from data.

combined likelihood formula for a single signal region and two binned control regions can be composed using the product of individual likelihood formulas:

$$\begin{aligned} L_{CRSR}(N_S, \phi_{WZ}, \phi_{ZZ}) = e^{-(N_S+N_{B,SR})} \frac{(N_S + N_{B,SR})^{n_{SR}}}{n_{SR}!} \\ \cdot \prod_{i}^{n_{bins,WZ}} e^{-N_{B,i}} \frac{(N_{B,i})^{n_i}}{n_i!} \\ \cdot \prod_{j}^{n_{bins,ZZ}} e^{-N_{B,j}} \frac{(N_{B,j})^{n_j}}{n_j!} \end{aligned} \tag{6.4}$$

In this equation, $N_{B,SR}$ is the predicted background in the signal region, while $N_{B,i}$ and $N_{B,j}$ are predicted background yields in bins of the WZ and ZZ control regions respectively. Each of these terms is dependent on a common ϕ_{WZ} and ϕ_{ZZ} and can be written as a sum of individual background contributions using Equation 6.3. n_{SR} is the amount of data events observed in the signal region, while n_i and n_j are the amount of data events observed in the bins of the WZ and ZZ control regions respectively.

Systematic uncertainties are the remaining set of uncertainties on the various parameters that have been used to produce a total background predictions. A full list of systematic uncertainties is given in Section 6.2. Systematic uncertainties affect the total background estimation N_B, and unlike NFs have a *shape effect*[4] so they might differently affect individual background yields $N_{B,i}$. The set of systematic uncertainties is indicated with θ_j. Alternatively, they can be expressed as a normalized, dimensionless quantity Θ_j, given as

$$\Theta_j = (\hat{\theta}_j - \theta_{j,0})/\Delta\theta_j. \tag{6.5}$$

Here, $\theta_{j,0}$ is the nominal value of the systematic uncertainty, $\hat{\theta}_j$ is the found best-fit value of the NP. $\Delta\theta_j$ is the *average* of the $\sigma = \pm 1$ deviations of the parameter compared to the nominal.

Through profiling, the PoI and NPs are simultaneously adjusted in an effort to find the maximum likelihood values of an hypothesis. With each iteration these values are updated to reflect the changes found in the previous iteration. This continues until the fitted value remains stable[5]. Systematic uncertainties (but not NFs) handled in this way each add a constraint term to L_{CRSR}. The total likelihood formulation then becomes

$$L(N_S, \phi, \theta) = L_{CRSR} \prod_{j=1}^{n_{NP}} C(\Theta_j). \tag{6.6}$$

[4] Although NFs have a shape effect insofar they affect only one of multiple backgrounds, the relative contribution of which can vary between bins. Thus the normalization factor affects these bins differently.

[5] It is possible in some cases that no stable values are found regardless of the amount of iterations. In these cases it can be helpful to update the initial fit values, the allowed range of values, or to question the assumptions that go into the fitting function.

The dependence of the likelihood on N_B has been rewritten as a dependence on the nuisance parameters ϕ and θ. $C(\Theta_j)$ are the constraint terms[6], a set of standard Gaussian PDFs, each a function of a single NP. There is no explicit formula to describe these $\sigma_{\pm}1$ deviations of the nuisance parameters, which are instead given through two additional input histograms representing the background distributions for the upwards and downwards deviations of the NP[7]. Intermediate values of θ_j are interpolated from these histograms and the nominal prescription ($\theta_{j,0}$) to find a best-fit value $\hat{\theta}_j$. Nonzero values of Θ_j are called *pulls*, having the following properties:

- $\Theta_j = +1$: morph to *up* histogram of systematic (provided);
- $\Theta_j = -1$: morph to *down* histogram of systematic (provided);
- $\Theta_j = 0$: no change to nominal histogram(s).

Values beyond $\pm$ 1 are possible, but due to the provided up and down histograms this might lead into nonphysical territory (i.e. negative event estimates). If large pulls occur, they must be more closely investigated to assure their accuracy and the continued trustworthiness of the model. In practice, the chosen binning for the control regions of this analysis does not lead to large pulls. If very granular binning is used, the lack of statistics in some bins can lead to input histograms with large per-bin differences, causing issues of this nature.

Finding the maximum of the full likelihood formula in Equation 6.6 leads to finding the best-fit values of the nuisance parameters, denoted as $\hat{\phi}$ and $\hat{\theta}$, and the best-fit value on the amount of signal events, $\hat{N}_S$, with an uncertainty $\sigma_{\hat{N}_S}$. From these best-fit values the *significance* Z of the result can be defined as $Z = \hat{N}_S/\sigma_{\hat{N}_S}$. The chosen definition quantifies the strength of the deviation from the background-only hypothesis and furthermore allows for negative significance values in case of $\hat{N}_S < 0$. The (two-sided) p-value is calculated from the significance as $p_0 = 1 - \Phi(|\hat{\mu}/\sigma_{\mu}|)$, where Φ is the Gaussian CDF.

In order to set exclusion limits, the likelihood formula thus established can be transformed into a profile likelihood ratio, leading to the test statistic [189] t_μ given in Equation 6.7. $\hat{\hat{\theta}}$ and $\hat{\hat{\phi}}$ are the best-fit values of the NPs as a function of N_S, while and $\hat{\theta}$ and $\hat{\phi}$ are the *global* best-fit values (when $N_S = \hat{N}_S$). Because of profiling, ϕ and θ are functions that depend only on N_S.

$$t_\mu = -2 \ln \frac{L(N_S, \hat{\hat{\theta}}(N_S), \hat{\hat{\phi}}(N_S))}{L(\hat{N}_S, \hat{\theta}, \hat{\phi})} \tag{6.7}$$

This test statistic can be used to compute a confidence interval for N_S. To do this, one first settles on a Type-I error and chooses whether a central, upper or lower limit is desired. This analysis is interested in one-sided 95% upper limits, corresponding to a Type-I error $\alpha = 0.05$. An expression for this limit requires us to define the PDF of the test statistic. Assumptions on the the test statistic can be made based on the work of Wilks [186] and Wald [187]. According to these results, the probability distribution of

[6] alternatively known as the *prior* or *penalty term*.

[7] For an example of this, see Figures 6.4 or 6.6, which show the nominal distribution of theory systematic uncertainties alongside their $\pm$1 uncertainty bands.

the test statistic, $f(t_\mu|N_S = n)$, where n is the hypothesized amount of signal events, asymptotically approaches a χ^2-distribution with one degree of freedom for a large number of events [190, 191]. This theorem holds true for as few as $\sim \mathcal{O}(10)$ events and can be used to save time by forgoing the need to run computationally expensive pseudo-experiments. Furthermore, because we are only interested in the upper limits, we define for negative values $\hat{N_S} < 0$ an alternative test statistic:

$$t_\mu = \begin{cases} -2\ln\frac{L(N_S,\hat{\hat{\theta}}(N_S),\hat{\hat{\phi}}(N_S))}{L(\hat{N_S},\hat{\theta},\hat{\phi})}, & \hat{N_S} \geq 0 \\ -2\ln\frac{L(N_S,\hat{\hat{\theta}}(N_S),\hat{\hat{\phi}}(N_S))}{L(0,\hat{\theta}(0),\hat{\phi}(0)}, & \hat{N_S} < 0 \end{cases} \tag{6.8}$$

The CL_s method [192] is used to ascertain upper limits on the signal regions. It is computed from the p-values of the alternative hypothesis (p_s) and null hypothesis (p_0). The confidence level by which the signal plus background hypothesis can be excluded is dependent on the observed value of the test statistic and the degree of overlap between the two hypotheses. If there were no overlap, it would suffice to solve the inequality $p_s < \alpha$ (called the CL_{s+b} procedure) for the signal plus background hypothesis alone. For a one-sided upper limit, we are only interested in excluding $N_S > 0$ values, so this p-value can be given as $p_s = \int_{t_{\mu,obs}}^{\infty} f(t_\mu|N_S = n)dt_\mu$.

However, there is usually significant overlap between hypotheses. Furthermore, if the amount of signal events in a region is small compared to background[8], a downward fluctuation in data can lead to an unreasonably strong rejection of the alternative hypothesis [192]. We therefore modify this inequality with the p-value of the null hypothesis, given as $p_0 = \int_{-\infty}^{t^{\mu,obs}} f(t_\mu|N_S = n)dt_\mu$. The combination of these expressions leads to the inequality for the CL_s method, given as

$$CL_s = \frac{p_s}{(1-p_0)} < \alpha \tag{6.9}$$

The above inequality is solved using the asymptotic approximation and the Type-I error $\alpha_s = 0.05$, allowing for the computation of 95% CL upper limits. Both expected and observed limits are computed for each signal region of the analysis, with the results presented in Section 7.3.

[8]Currently undiscovered BSM models in many regions would have small signal strength compared to background; they would have been already observed otherwise.

6.2 Systematic Uncertainties

Aside from the statistical uncertainties on the data and Monte Carlo simulation, there are other uncertainties which influence the distinguishing power of the analysis. These uncertainties can be divided into *theoretical* and *experimental* uncertainties. The treatment of theoretical uncertainties will be described in Section 6.2.1, the experimental uncertainties in Section 6.2.2

6.2.1 Theoretical Uncertainties

Theoretical uncertainties considered for this analysis originate from the *missing higher orders* in the perturbative expansion of the partonic cross-section, from *PDF uncertainties*, and from the *uncertainty on the strong coupling constant*. Each of these can cause a difference between the assumed and the actual cross-section of a physics process.

We first describe a recipe by which the theoretical uncertainties on the SHERPA predictions are computed. These samples are used for multiboson processes in the nominal ($3\ell+$) regions. Top samples included in the $3\ell+$ regions include $t\bar{t}W$, $t\bar{t}Z$ and certain rare top processes. Top backgrounds that enter into the fake factor estimation (due to MC background subtraction) are the single top and $t\bar{t}$ processes. These are estimated using a different approach, to be discussed at the end of this section.

Diboson and triboson predictions

Two techniques are used to estimate a set of uncertainties [193]: *Variation of the choice of the QCD renormalization and factorization scale* and *varying the choice of PDF*, which includes cross-comparing with central values of different PDF sets and varying the strong coupling constant α_s. The recipes put forward for these estimations are described below.

- **Choice of QCD Scales**: The choice of the QCD renormalization scale μ_r and factorization scale μ_f is taken as an uncertainty. The conventional approach is to vary these scales upwards and downwards by a factor of two [194], both individually and simultaneously, except variations where one term is scaled upwards and the other downwards. This leads to a 7-point variation of the QCD scales of which one is the nominal choice, as shown in Table 6.1. For each bin, the largest of these uncertainties is taken, following a technique called enveloping. This theoretical uncertainty is decorrelated between the WZ, ZZ and triboson backgrounds, leading to three sets of uncertainties.

μ_r:		0.5	1.0	2.0
μ_f	0.5	*	*	*
	1	*	*	*
	2	*	*	*

Table 6.1: List of QCD scale variations at different renormalization (μ_r) and factorization (μ_f) scales that are used as theoretical uncertainties. Variations marked in green are taken as uncertainties, while off-diagonal variations marked in red are not. The cell $\mu_r = 1$, $\mu_f = 1$ is the nominal choice of renormalization and factorization scales.

- **Choice of PDF**: For the uncertainty in choice of PDF the analysis follows the PDF4LHC recommendations [195]. Different PDFs are used to recompute the event weights which are then compared to the nominal event weights. To estimate the effect of the computation of the strong coupling constant α_s of 0.118 the event weights are recomputed using PDFs where α_s is set as 0.119 and 0.117. For cross-checking, the results are also compared using the central values of the `CT14nnlo` [196] and `MMHT2014 NNLO` [197] PDF sets. The uncertainty on the strong coupling constant is averaged according to Equation 6.10.

$$\delta^{\alpha_s}\sigma = \frac{1}{2}\Big(\sigma(\alpha_s^{down}) - \sigma(\alpha_s^{up})\Big) \tag{6.10}$$

Top predictions

Backgrounds containing the decay products from at least one top quark are a secondary background for this analysis. As with the multiboson samples, uncertainties due to the choice of scale, the choice of PDF and the strong coupling constant affect the total accuracy on the provided cross sections of these processes. However, these uncertainties are treated somewhat differently, employing the measured values of these uncertainties that were previously determined [198–201]. Although it is possible that these measured values and the associated uncertainties are not universally applicable across the signal regions in this analysis, the impact of the top backgrounds is small enough compared to the diboson backgrounds that these uncertainties are sub-leading and that a more thorough examination of these uncertainties is not necessary.

Uncertainty values on the various top processes are known and given in Table 6.2. These values are used to scale the associated processes upwards and downwards. Two theoretical uncertainties are constructed, a scale uncertainty and a combined PDF/α_s uncertainty. Theoretical uncertainties are not provided for a few rare top processes, but these processes yield a negligible contribution to the background estimates of all signal regions.

Process	Cross Section [pb]	Scale unc.	PDF unc.	α_s unc.
ttW	0.601	+ 12.9% -11.5%	±2.0%	±2.7%
ttZ	0.840	+ 9.6% -11.3%	±2.8%	±2.8%
ttWW	0.00810	+10.9% -11.8%	±2.1%	
tttt	0.0120	+18% -21%		
$t\bar{t}$	831	+2.4% -3.5%	±4.2%	
t-chan	217	+3.1% -2.1%	±2.8%	
tW-chan	71.7	±2.5%	±4.7%	
s-chan	10.3	+2.8% -2.3%	±2.6%	

Table 6.2: Theoretical uncertainties on the cross section of top quark processes due to various sources [198, 199].

6.2.2 Experimental Uncertainties

All of the experimental uncertainties that are considered for this analysis are listed in Table 6.3. Each uncertainty has an upward and downward component and may be asymmetric. The rest of this section will explain the nature of each systematic included in this analysis.

General

- `Lumi`: The uncertainty on the total integrated luminosity recorded in the run 2 data taking period from 2015 to 2018. It is determined to be 1.7% [202].
- `PRW_DATASF`: Uncertainty due to pileup reweighting. Pileup reweighting is explained in Section 2.1.1. This systematic comes from the scale factor that is used to control the μ value by which the data is scaled (given as 1/1.03 [84]) prior to the assignment of pileup weights.

Electrons

- `EG_RESOLUTION_ALL` and `EG_SCALE_ALL` account for uncertainties in the electron momentum resolution and scale respectively, resulting in a total of 2×2 variations
- The efficiency scale factors (discussed in Section 3.2.3) which are calculated for the electron trigger, reconstruction, and isolation steps each have an associated uncertainty provided from dedicated analyses [132]. These uncertainties are: `EL_EFF_[Iso/Reco/Trigger]_TOTAL`.
- For the efficiency scale factors of the identification step an expanded correlation scheme of uncertainties is used [145]. This correlation scheme uses 16 systematic uncertainties, correlated between efficiency bins (`EL_EFF_ID_CorrNP[0-15]`), as well as uncorrelated uncertainties due to limited statistics on groups of efficiency bins. These uncertainties are binned in electron p_{T} and η. Only uncertainties on bins with $p_{\mathrm{T}} > 25$ are needed, leading to an additional 8 uncertainties (`EL_EFF_ID_UncorrNP[0-7]`).

Muons

- `MUON_ID` and `MUON_MS` are the uncertainties on the momentum measurements of the muon as measured by the Inner Detector and Muon Spectrometer respectively. These uncertainties are found through calibrating the MC momentum resolution to match data for measurements of both subdetectors.
- Analogous to the electrons, a set of uncertainties on the efficiency scale factors of the muon exists. In case of the muon, these uncertainties are folded into two nuisance parameter per scale factor, one to summarize all systematic effects and one to account for the limited statistics available in the bins where the scale factor was obtained. An additional. The names for these uncertainties are `MUON_EFF_[RECO/ISO]_[SYS/STAT]` and `MUON_EFF_Trig[Syst/Stat]Uncertainty`. An additional two nuisance parameters exist to account for the efficiency corrections between data and MC when muon track-to-vertex association (TTVA, see muon object selection, specifically Table 4.4) is performed: `MUON_EFF_[TTVA]_[SYS/STAT]`.

Category	Systematic	Name
Incoming Data	Luminosity	`Lumi`
	Pileup	`PRW_DATASF`
Electron Calibration	Resolution	`EG_RESOLUTION_ALL`
	Momentum Scale	`EG_SCALE_ALL`
Electron Efficiencies	ID	`EL_EFF_ID_CorrNP[0-15]`
		`EL_EFF_ID_UncorrNP[0-7]`
	Reconstruction	`EL_EFF_Reco_TOTAL`
	Isolation	`EL_EFF_Iso_TOTAL`
	Trigger	`EL_EFF_Trigger_TOTAL`
Muon Calibration	ID Track Smearing	`MUON_ID`
	MS Track Smearing	`MUON_MS`
	Momentum Scale	`MUON_SCALE`
	Sagitta Correction	`MUON_SAGITTA_RESBIAS`
Muon Efficiencies	Reconstruction	`MUON_EFF_RECO_SYS`
		`MUON_EFF_RECO_STAT`
	Isolation	`MUON_EFF_ISO_SYS`
		`MUON_EFF_ISO_STAT`
	TTVA	`MUON_EFF_TTVA_SYS`
		`MUON_EFF_TTVA_STAT`
	Trigger	`MUON_EFF_TrigSystUncertainty`
		`MUON_EFF_TrigStatUncertainty`
$E_{\mathrm{T}}^{\mathrm{miss}}$ soft track	Offset	`MET_SoftTrk_Scale`
	Resolution	`MET_SoftTrk_ResoPara`
		`MET_SoftTrk_ResoPerp`
Jet Calibration	Jet Energy Scale	`JET_EtaIntercalibration_NonClosure_highE`
		`JET_EtaIntercalibration_NonClosure_negEta`
		`JET_EtaIntercalibration_NonClosure_posEta`
		`JET_GroupedNP_[1-3]`
	Jet Energy Resolution	`JET_JER_DataVsMC_MC16`
		`JET_JER_EffectiveNP_[1-6]`
		`JET_JER_EffectiveNP_7restTerm`
JVT Efficiency		`JET_JvtEfficiency`
Fake Factors		`FAKEBKG_STAT_VAR`
		`FAKEBKG_SYST_VAR[0-2]`

Table 6.3: List of systematic uncertainties used. Values between brackets (e.g. [1-4]) indicate a numbered group of systematic uncertainties which are treated separately.

- Variations in the scale of the momentum on the muon account for two systematics: Uncertainty on the muon momentum scale (`MUON_SCALE`), and the residual charge-dependent bias in the scale of the momentum based after performing the muon track sagitta correction (`MUON_SAGITTA_RESBIAS`).

Missing Transverse Energy / $E_{\mathrm{T}}^{\mathrm{miss}}$

These are uncertainties on the MET Track Soft Term (TST), which are parameterized as components parallel and perpendicular to the hard term (which are signals associated to reconstructed objects, as opposed to the *soft* term, which are signals not associated to such objects, see also Section 3.2.5) [159]. The direction of momentum of all hard objects that go into MET reconstruction is called the hard axis, and the soft term is parameterized as components parallel and perpendicular to this axis. The systematic components are:

- `MET_SoftTrk_Scale`: the offset (up and down) along the hard axis;
- `MET_SoftTrk_ResoPara`: smearing by resolution uncertainty parallel to the hard axis;
- `MET_SoftTrk_ResoPerp`: smearing by resolution uncertainty perpendicular to the hard axis.

Jets

Jet-related uncertainties consist of uncertainties on the reconstruction steps that have been highlighted in Section 3.2.4. Three categories of uncertainties are considered [203]: uncertainties on the jet energy scale (JES) calibration, on the Jet Vertex Tagger (JVT), and on the determination of the jet energy resolution (JER).

On the JES calibration [155] a uncertainty scheme has been provided from dedicated analyses by the ATLAS collaboration [204]. These consist of six uncertainties in total. There are the uncertainties of the pseudorapidity (η) inter-calibration, accounting for three uncertainties in total:

- `JET_EtaIntercalibration_NonClosure_HighE`;
- `JET_EtaIntercalibration_NonClosure_negEta`;
- `JET_EtaIntercalibration_NonClosure_posEta`.

The remaining three systematics, given as `JET_GroupedNP`, are a combination of the uncertainties on over 100 parameters which are involved in the stages of the JES calibration.

The JER uncertainties [204] are a combination of uncertainties that result from the MC-only smearing according to the standard deviation of the energy resolution. Smearing by a $\pm\sigma$ factor has, regardless of sign, an identical result. The MC would in both cases be smeared by the same factor. Because of this, these uncertainties don't have upwards and downwards components, and manual symmetrization of the uncertainty is performed instead.

A single uncertainty `JET_JvtEfficiency` encodes the efficiency of the Jet Vertex Tagger algorithm.

Fake Factors

The computation of Fake Factors has been discussed in Section 5.2. The methods described in this Chapter mention uncertainties both statistical and systematic in nature.

The amount of data and MC events available for each fake factor is limited. This limitation introduces an statistical uncertainty to each individual fake factor bin. This introduces a set of uncertainties proportional to the granularity of the binning. These uncertainties are uncorrelated, but because they are individually extremely small, they are combined into a single uncertainty through a sum in quadrature (`FAKEBKG_STAT_VAR`).

Two additional sources introduce an uncertainty in translating the fake factor measured in the single-lepton estimation region to the final fake rate estimated in the signal regions. These sources are the *theoretical uncertainties on the subtracted Monte Carlo samples* and the *transfer uncertainty from translating between kinematically separated regions*. These uncertainties are handled as follows:

- `FAKEBKG_SYS_VAR0`: The cross section uncertainties on the prompt backgrounds to be subtracted. These are the Z+jets, W+jets, single-top and $t\bar{t}$ contribution. For the W+jets process, a recommended conservative 5% uncertainty on the k-factor [205, 206](a correction factor to scale the cross-section to higher orders which were not computed explicitly), is applied, as the fake background is expected to be small compared to the prompt diboson backgrounds in regions where these fake backgrounds are used. For the top processes, the values from Table 6.2 are used.
- Transferring the fake factors from the region in which they are determined to the signal region introduces uncertainties because these regions are kinematically different. In the fake-enriched region, cuts are imposed to obtain a high fraction of fake events as opposed to prompt background events. These cuts introduce kinematic biases in the selection. This effect is accounted for by varying the quantities used for these fake-enriching cuts upwards and downwards[9], and taking the associated changes in the fake factor as the systematic uncertainty, performed as follows:
  - `FAKEBKG_SYS_VAR1`: Shifting the MET cutoff point upwards and downwards by 10 GeV.
  - `FAKEBKG_SYS_VAR2`: For the muon fake factor, where the tag-and-probe method is used, Shifting the required transverse momentum of the tagging jet, $\Delta\phi(\mu, jet)$, upwards and downwards by 10 GeV (muon fake factor only).

Plots showing the impact of these systematics are given in Figures 6.1, 6.2 and 6.3.

[9]The momentum value by which these quantities are scaled is to some degree arbitrary. The uncertainties reveal a limitation of the fake factor method to accurately determine fake rates in region where this rate is expected to be small. However, in the absence of a more accurate prescription, varying of kinematic cuts is a good way to estimate in what regime the fake rate may be especially sensitive to underlying assumptions, providing guidance in the event that it is found that a particular signal region becomes particularly sensitive to fake backgrounds.

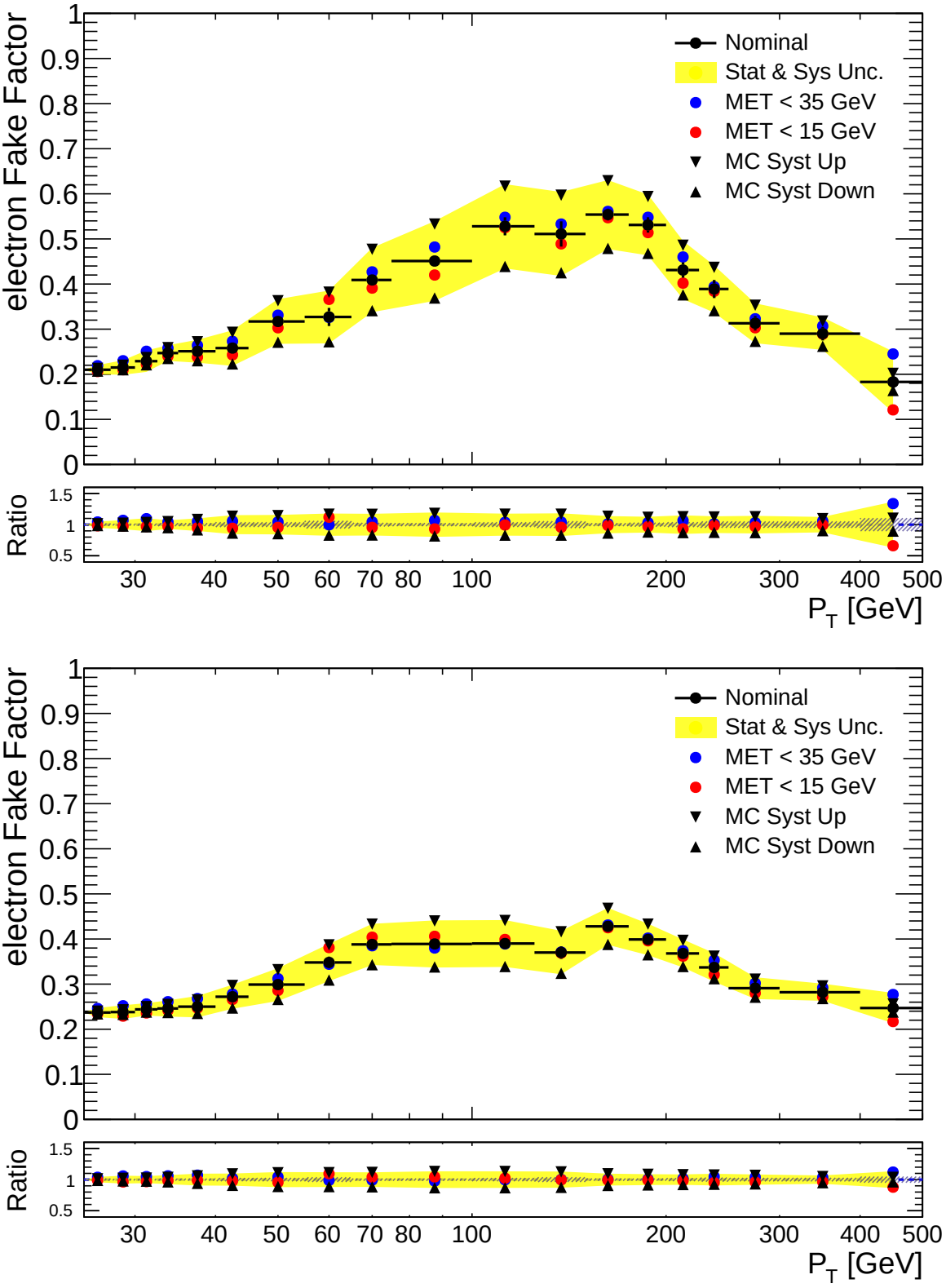

Figure 6.1: Plots showing the fluctuations in fake factors with respect to the systematic uncertainties for the electron with $|\eta| > 1.37$. The combined impact of statistical and systematic uncertainties added in quadrature is given as the shaded yellow area.

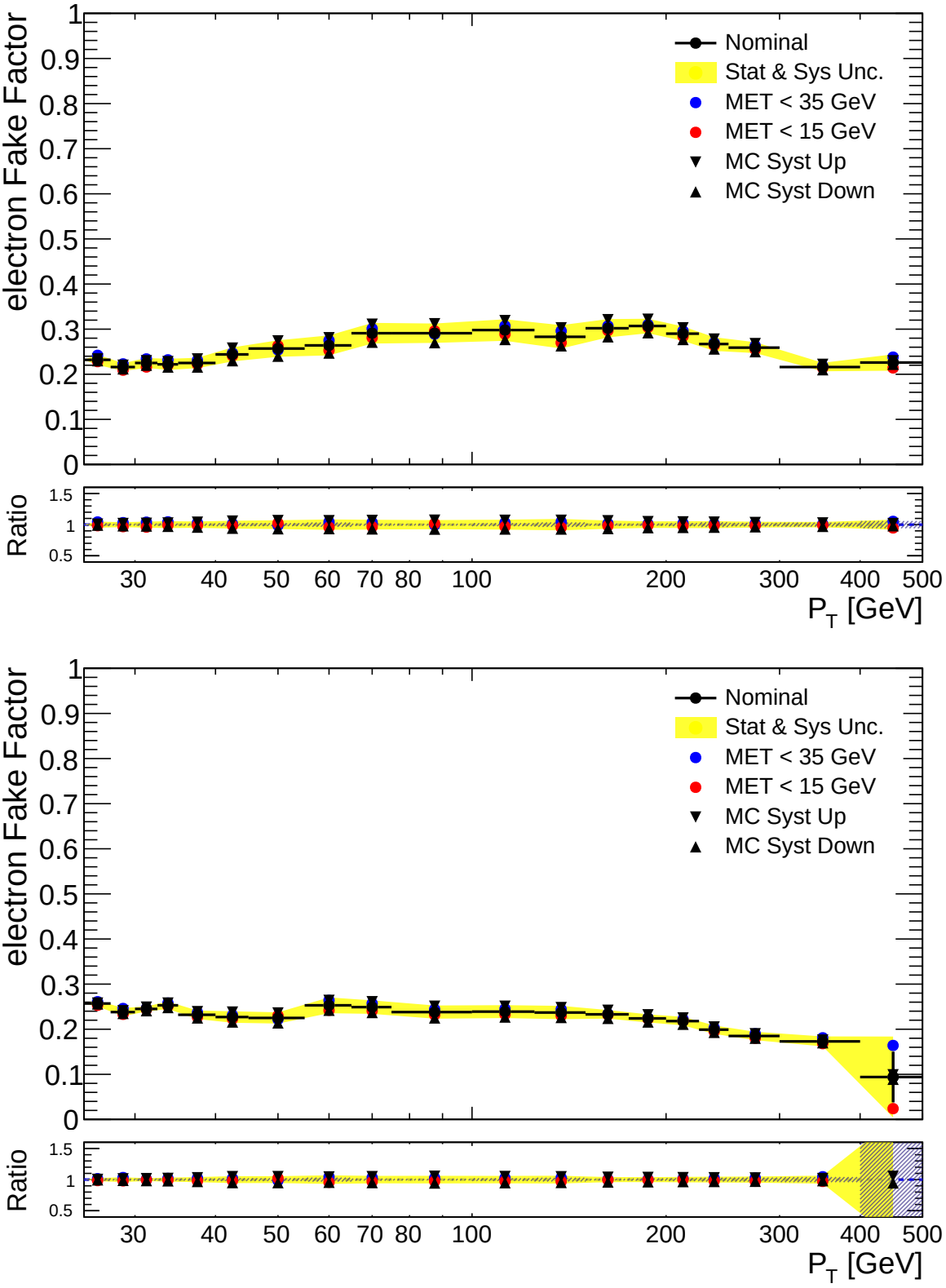

Figure 6.2: Plots showing the fluctuations in fake factors with respect to the systematic uncertainties for the electron with $|\eta| > 1.52$. The combined impact of statistical and systematic uncertainties added in quadrature is given as the shaded yellow area.

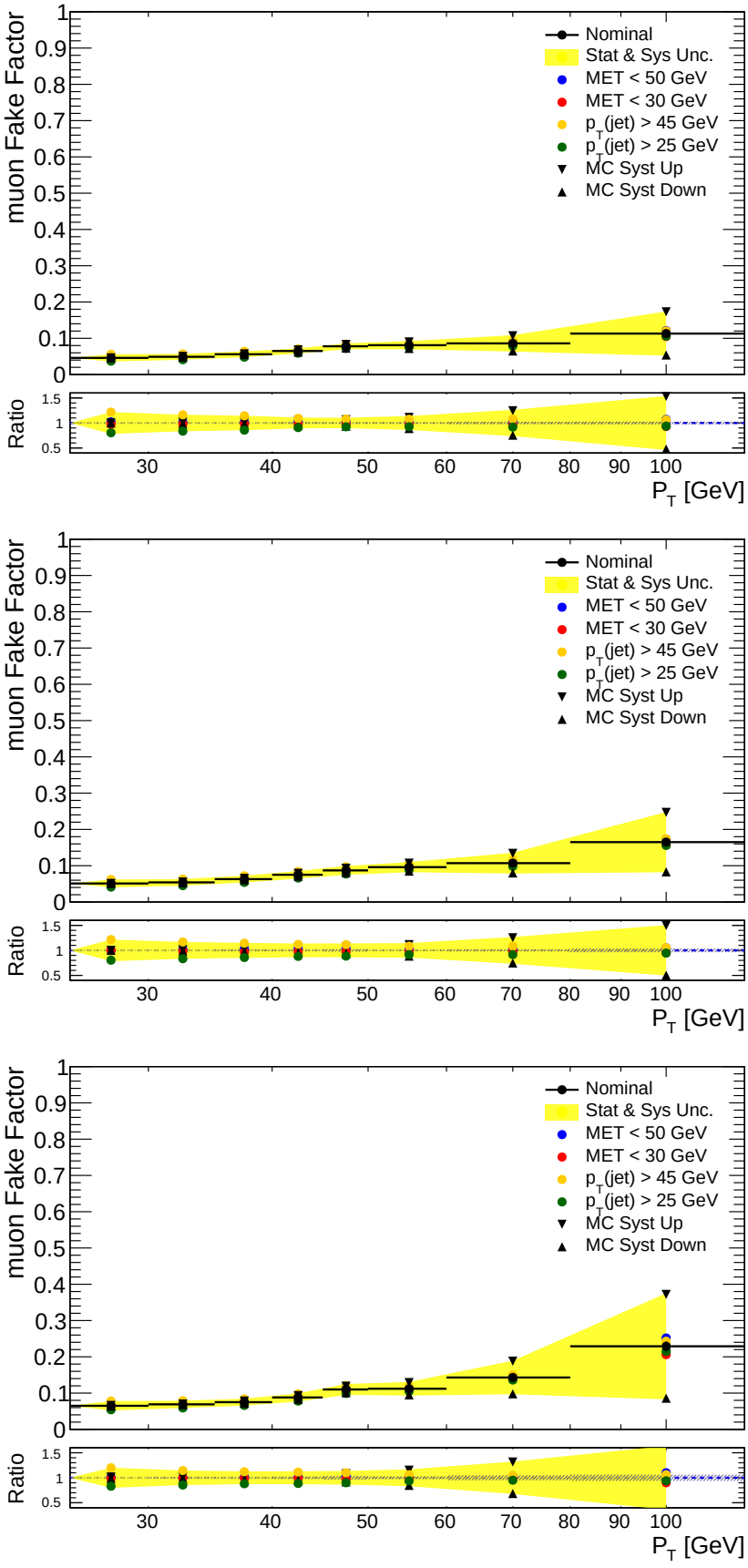

Figure 6.3: Plots showing the fluctuations in fake factors with respect to the systematic uncertainties for the muon. The combined impact of statistical and systematic uncertainties added in quadrature is given as the shaded yellow area.

6.2.3 Uncertainty Breakdown

The total impact of categories of systematic uncertainties is given in Table 6.4 for the control and validation regions, and in Tables 6.5 and 6.6 for the signal regions containing three and four leptons respectively. Categories shown in these tables are consistent with the categorization shown in Table 6.3. The uncertainties for the signal regions are computed by incorporating the entire mass range rather than from any specific mass bin.

Uncertainties whose impact on the total background prediction is negligible (defined as its $\pm 1\sigma$ variations being less than 0.5% of the total background distribution) are *pruned*. The pruning process offers insight into what uncertainties are worth paying attention to. An overview of remaining uncertainties after pruning is given in Table 6.7. This table indicates also in which regions certain systematic uncertainties are relevant. Systematics which are relevant in at least one control region can be pulled and constrained. Some systematics are small in both of the control regions, but are relevant to least one signal region.

Theoretical uncertainties on the diboson backgrounds are the dominant source of systematic uncertainty. Plots have been provided to show the effect of these uncertainties on the WZ background in the WZ control region and on the ZZ background in the ZZ control region. These plots are given in Figures 6.4, 6.5 and 6.6, showing the three groupings of theoretical uncertainty sources. The triboson contribution, which does not have its own control region and is furthermore small in all signal regions, is omitted.

Systematic Source	WZ CR	Fakes Validation	ZZ CR	Off-Z Validation
Lumi & PRW	1.81%	1.51%	1.97%	1.22%
Electron Calibration	0.09%	0.16%	0.15%	0.41%
Electron Efficiencies	0.25%	0.26%	0.34%	0.26%
Muon Calibration	0.09%	0.11%	0.20%	0.37%
Muon Efficiencies	0.88%	0.64%	1.21%	0.54%
MET Soft Track	1.58%	0.85%	0.00%	0.84%
Jet Calibration	0.07%	0.30%	0.20%	0.37%
Jet Efficiencies	0.17%	0.16%	0.22%	0.09%
Diboson Theory Scale	6.81%	6.49%	7.88%	5.07%
Diboson Theory PDF/α_s	2.06%	1.76%	2.64%	1.35%
Top Theory Scale	0.21%	0.31%	0.04%	0.63%
Top Theory PDF/α_s	0.05%	0.08%	0.01%	0.23%
Fakes	0.39%	1.29%	0.18%	2.06%
Total Experimental	2.61%	2.31%	2.38%	2.69%
Total Theory	7.12%	6.73%	8.31%	5.29%
Total	7.59%	7.15%	8.67%	6.11%

Table 6.4: Estimation of the systematic uncertainties from different sources for the control and validation regions, expressed in percent uncertainties on the total background sum. the 'Total Experimental' uncertainty indicates the combination of all non-statistical, non-theoretical uncertainties. 'Total Theory' includes all theoretical uncertainties from the diboson and top background processes.

Systematic Source	3ℓ On-Z $E_{\mathrm{T}}^{\mathrm{miss}} < 50$ GeV	3ℓ On-Z $E_{\mathrm{T}}^{\mathrm{miss}} > 50$ GeV	3ℓ Off-Z $E_{\mathrm{T}}^{\mathrm{miss}} < 50$ GeV	3ℓ Off-Z $E_{\mathrm{T}}^{\mathrm{miss}} > 50$ GeV
Lumi & PRW	1.77%	1.76%	1.45%	1.46%
Electron Calibration	0.20%	0.39%	0.26%	0.37%
Electron Efficiencies	0.24%	0.35%	0.24%	0.35%
Muon Calibration	0.15%	0.24%	0.25%	0.21%
Muon Efficiencies	0.83%	0.81%	0.78%	0.65%
MET Soft Track	1.92%	3.40%	1.76%	2.04%
Jet Calibration	0.20%	0.50%	0.19%	0.29%
Jet Efficiencies	0.17%	0.18%	0.12%	0.11%
Diboson Theory Scale	8.00%	15.80%	5.39%	10.09%
Diboson Theory PDF/α_s	2.19%	2.31%	1.70%	1.59%
Top Theory Scale	0.15%	0.65%	0.50%	1.45%
Top Theory PDF/α_s	0.04%	0.17%	0.20%	0.53%
Fakes	0.40%	0.31%	1.28%	1.64%
Total Experimental	2.81%	4.00%	2.77%	3.12%
Total Theory	8.30%	15.98%	5.68%	10.33%
Total	8.77%	16.47%	6.38%	10.81%

Table 6.5: Systematic uncertainties from different sources for the three lepton signal regions, expressed in percent uncertainties on the total background sum. the 'Total Experimental' uncertainty indicates the combination of all non-statistical, non-theoretical uncertainties. 'Total Theory' includes all theoretical uncertainties from the diboson and top background processes.

Systematic Source	4ℓ On-Z $E_{\mathrm{T}}^{\mathrm{miss}} < 50$ GeV	4ℓ On-Z $E_{\mathrm{T}}^{\mathrm{miss}} > 50$ GeV	4ℓ Off-Z
Lumi & PRW	1.90%	1.74%	1.64%
Electron Calibration	0.21%	0.44%	0.52%
Electron Efficiencies	0.35%	0.55%	0.46%
Muon Calibration	0.28%	0.38%	0.32%
Muon Efficiencies	1.19%	1.02%	1.03%
MET Soft Track	1.93%	4.13%	0.00%
Jet Calibration	0.51%	0.70%	0.31%
Jet Efficiencies	0.09%	0.20%	0.32%
Diboson Theory Scale	5.06%	11.45%	4.61%
Diboson Theory PDF/α_s	2.30%	1.59%	1.70%
Top Theory Scale	0.44%	4.09%	2.01%
Top Theory PDF/α_s	0.11%	1.01%	0.49%
Fakes	0.05%	0.59%	0.54%
Total Experimental	3.04%	4.75%	2.20%
Total Theory	5.58%	12.30%	5.33%
Total	6.50%	13.37%	6.82%

Table 6.6: Systematic uncertainties from different sources for the four lepton signal regions, expressed in percent uncertainties on the total background sum. the 'Total Experimental' uncertainty indicates the combination of all non-statistical, non-theoretical uncertainties. 'Total Theory' includes all theoretical uncertainties from the diboson and top background processes.

Fitted in both control regions	
Luminosity	
Diboson Scale: ZZ	
PRW_DATASF	
MUON_EFF_ISO_SYS	
Fitted in WZ control region	**Fitted in ZZ control region**
Diboson Scale: WZ	
Diboson PDF: WZ	Diboson PDF: ZZ
EG_RESOLUTION_ALL	EG_SCALE_ALL
MUON_SAGITTA_RESBIAS	MUON_SCALE
JET_GroupedNP_2	EL_EFF_ID_UncorrNP3
MET_SoftTrk_ResoPara	
MET_SoftTrk_ResoPerp	
MET_SoftTrk_Scale	
Significant in at least 1 signal region	
All other theory uncertainties	
MUON_ID	
MUON_EFF_RECO_SYS	
JET_GroupedNP_2	
JET_JER_EffectiveNP_1	
JET_JER_EffectiveNP_2	
JET_JER_EffectiveNP_3	
JET_JER_EffectiveNP_5	
JET_JER_EffectiveNP_6	
JET_JER_EffectiveNP_7restTerm	
EL_EFF_ID_CorrNP11	
EL_EFF_ID_CorrNP12	
EL_EFF_ID_CorrNP13	
EL_EFF_ID_CorrNP14	
FAKEBKG_SYST_VAR0	
FAKEBKG_SYST_VAR1	
FAKEBKG_STAT_VAR	

Table 6.7: Systematic uncertainties which remain after the pruning process, ordered according to which control regions are used to fit them, if any. Furthermore, systematics that are not fitted in either of the control regions but are still relevant for one or more signal regions are shown here as well.

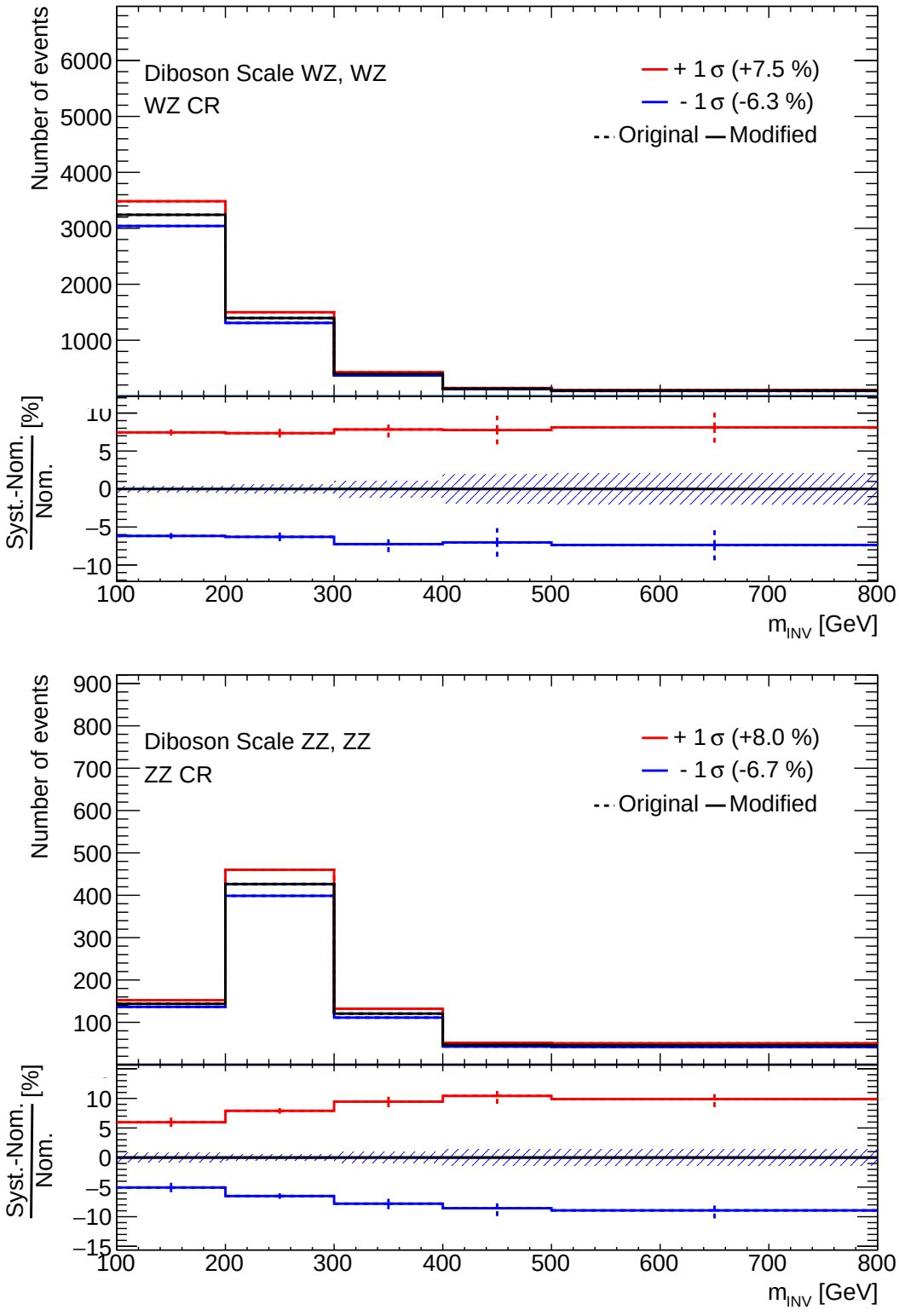

Figure 6.4: Plots showing the impact of the diboson theory renormalization and factorization uncertainties for the WZ background in the WZ control region (left) and the ZZ background in the ZZ control region. The Original and Modified line designation in the legend indicates the change of systematic distribution as a result of smoothing, which is not performed here. Dashed lines are the per-bin statistical uncertainties.

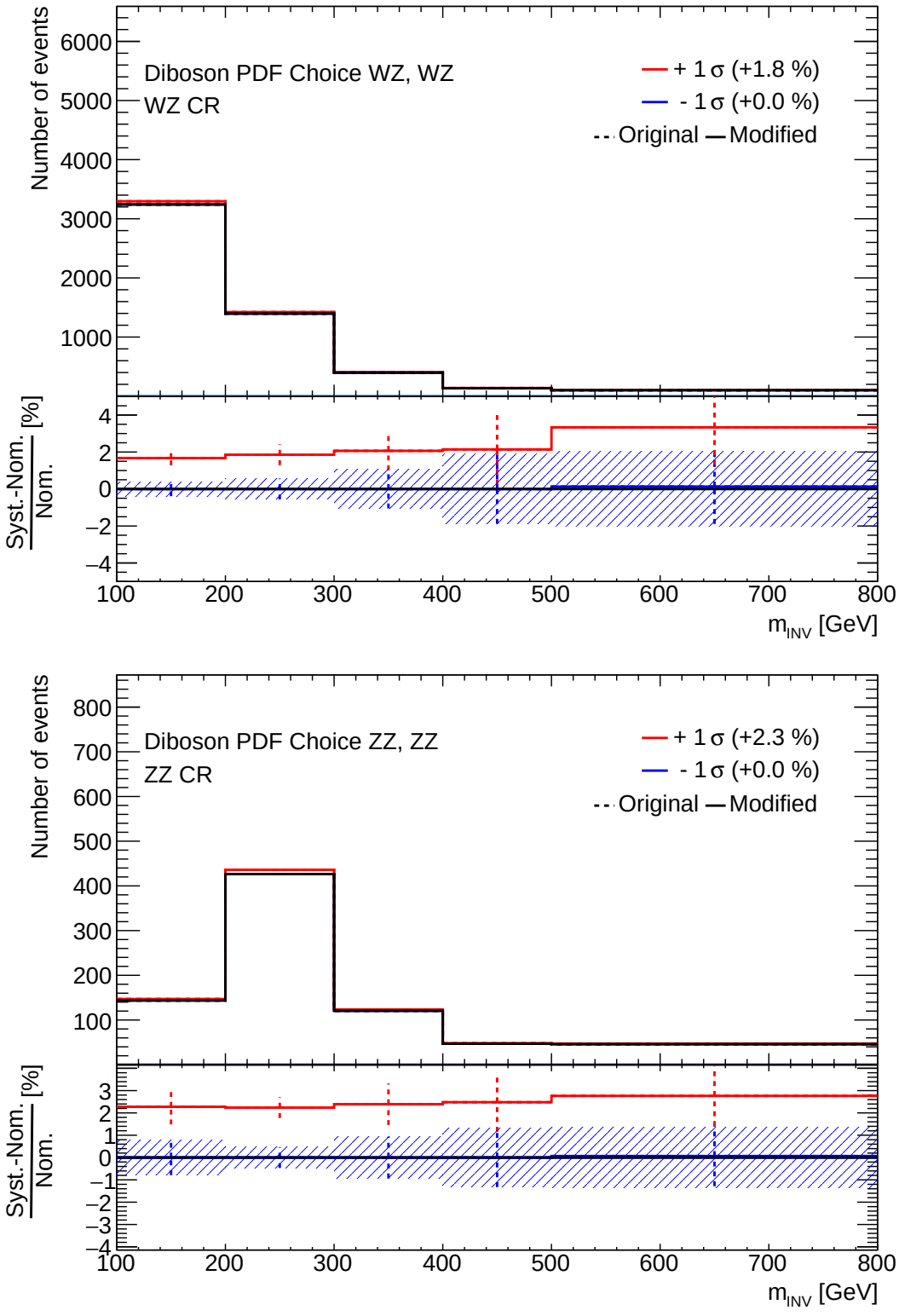

Figure 6.5: Plots showing the impact of the diboson theory PDF choice uncertainties for the WZ background in the WZ control region (left) and the ZZ background in the ZZ control region. Original and Modified line designation in the legend indicates the change of systematic distribution as a result of smoothing, which is not performed here. Dashed lines are the per-bin statistical uncertainties.

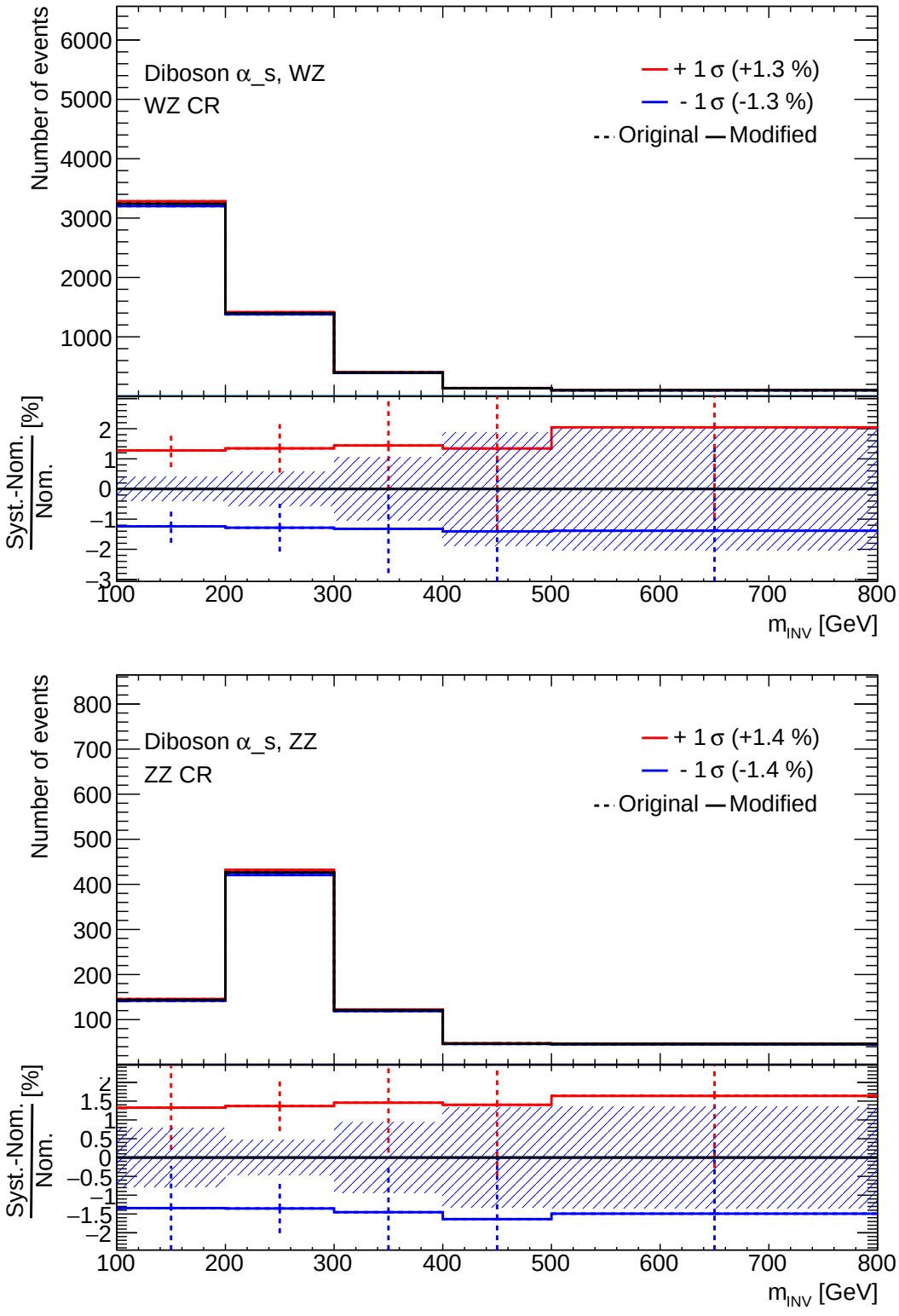

Figure 6.6: Plots showing the impact of the diboson theory strong coupling constant uncertainty for the WZ background in the WZ control region (left) and the ZZ background in the ZZ control region. Original and Modified line designation in the legend indicates the change of systematic distribution as a result of smoothing, which is not performed here. Dashed lines are the per-bin statistical uncertainties.

Chapter 7

Results

Now that the analysis strategy, the regions and the event selection for those regions, the parameters of interest and all the possible nuisance parameters (NPs) have been defined, we are ready to present the results of the analysis. In Section 7.1, the control regions and the nuisance parameters that have been fitted are displayed. Distributions of choice variables for the control and validation regions are given in Section 7.2. Sections 7.3 and 7.4 provide the results on the fitting and the limit-setting procedures in each of the signal regions. Results of these limit-setting and fitting studies are provided both as plots and tables and are interpreted in the context of a model-independent search.

In Section 7.5 analyses are performed on specific exotic physics theories, the Type-III seesaw mechanism and the Doubly-charged Higgs model, both introduced in Section 1.4. The present analysis is used to probe a few specific parameter settings of these models, and the sensitivity obtained is compared with that of specifically designed analyses.

7.1 Control Regions and Systematics

Prior to selecting a particular signal region it is possible to perform a CR-only fit. Such a procedure reveals the normalization factors as well as the pulls and constraints of the various nuisance parameters and is instructive regarding the health of the fitting setup prior to testing the data in the signal regions.

The fit has been performed with the results shown for the WZ and ZZ control regions in Figure 7.1. The binning of the control regions shown in these plots is chosen so that that shape information can be used to more accurately fit nuisance parameters that have variable impact across the invariant mass spectrum. The choice of binning is a trade-off between being narrow enough to maximize the ability to exploit shape effects in the systematics, but not so narrow that the fitting algorithm might be misled by statistical effects, leading to false pulls or underconstraints. Post-fit plots of the validation regions are provided in Figure 7.2, showing good agreement between the data and the background expectation and validating that the data-driven fake estimation is accurate, although it is to be noted that these regions do not influence the fit itself.

The normalization factors for the WZ and ZZ diboson backgrounds that are extracted from the control regions are $\mathbf{0.99 \pm 0.07}$ for the WZ background, and $\mathbf{1.05 \pm 0.09}$ for the ZZ background.

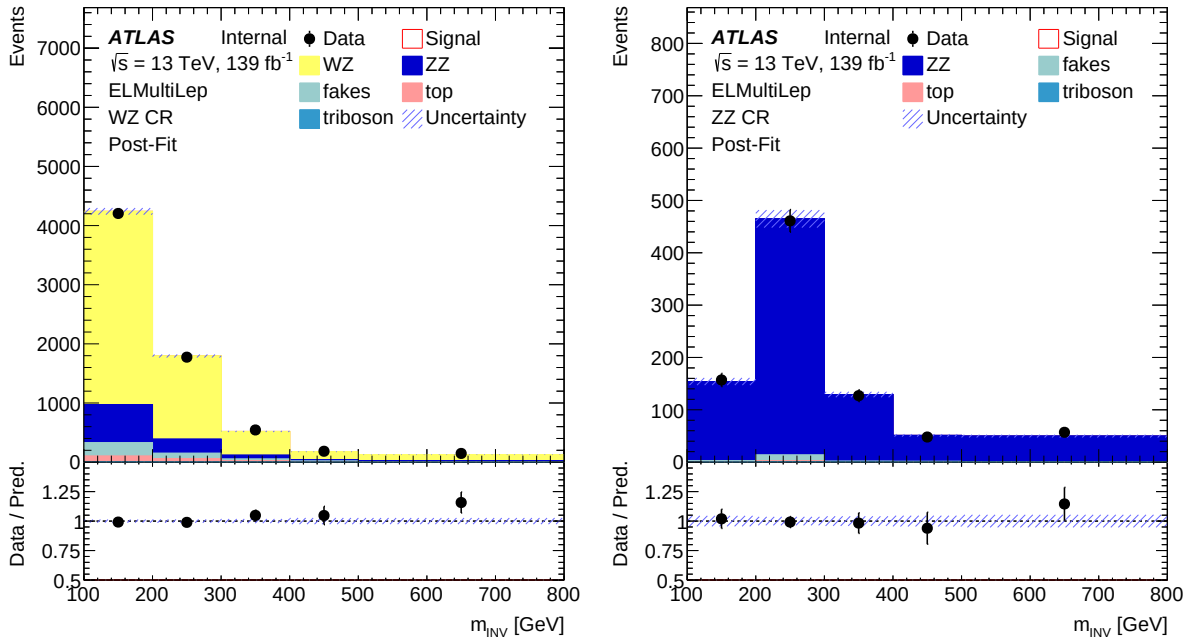

Figure 7.1: M_{inv} distributions comparing data and background expectation of the WZ (left) and ZZ (right) control region after fitting the normalization factors for the diboson backgrounds and systematic uncertainties.

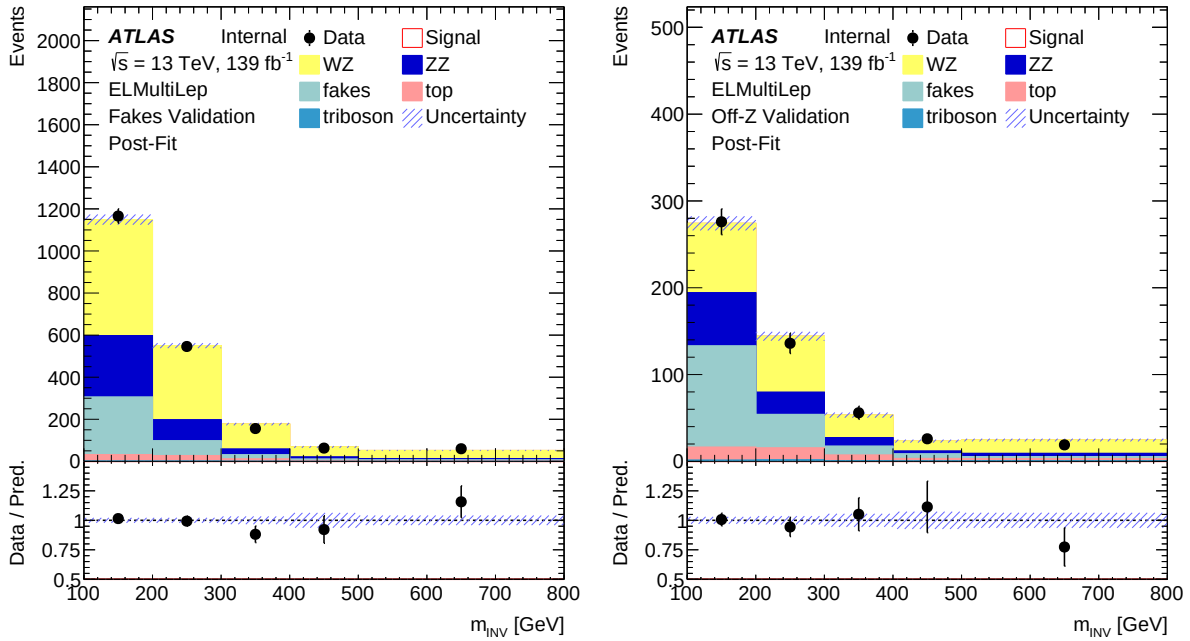

Figure 7.2: M_{inv} distributions comparing data and background expectation of the fakes (left) and off-Z (right) validation regions after fitting the normalization factors for the diboson backgrounds and systematic uncertainties.

Nuisance parameter pull and constraint plots per uncertainty category are given in Figure 7.3. The pre- and post-fit event yields are given for the control and validation regions are given in Table 7.1.

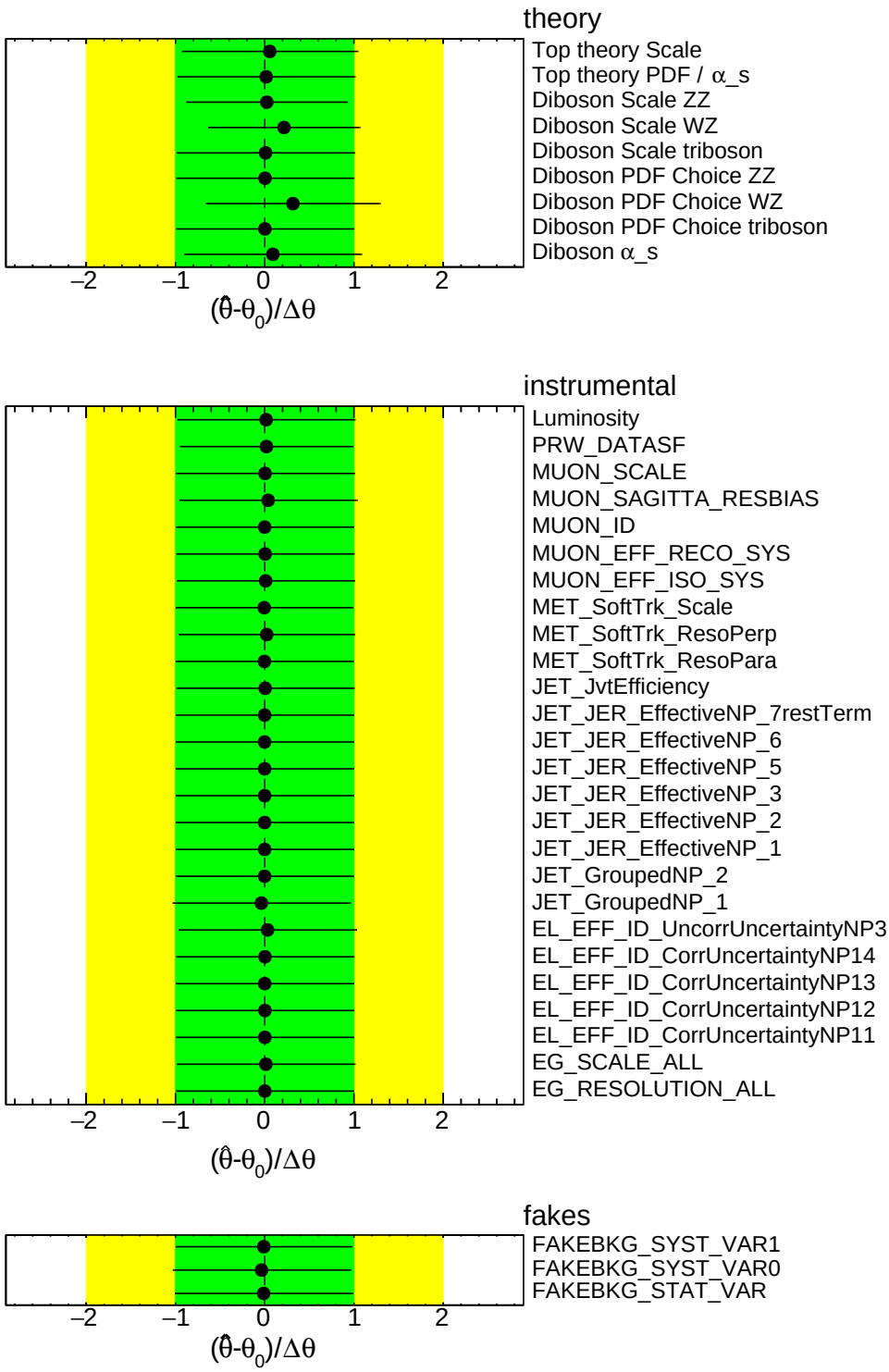

Figure 7.3: Nuisance parameter pull and constraint plots for the systematic uncertainties in the CR-only fit. The figure shows for each unpruned nuisance parameter the best-fit value of and the uncertainty on this value with respect to the initial value and standard deviation. The definitions the experimental uncertainties can be found in Table 6.3.

	Fakes VR	Off-Z VR	WZ CR	ZZ CR	Fakes VR	Off-Z VR	WZ CR	ZZ CR
top	74.4 ± 6.1	39.7 ± 3.5	186 ± 14	2.7 ± 0.3	74.7 ± 6.0	39.9 ± 3.5	187 ± 14	2.7 ± 0.3
triboson	3.0 ± 0.4	5.0 ± 0.6	8.9 ± 1.0	1.8 ± 0.2	3.0 ± 0.4	5.0 ± 0.6	9.0 ± 1.0	1.8 ± 0.2
WZ	1093 ± 99	195 ± 18	5272 ± 394	-	1106 ± 33	197 ± 6	5314 ± 102	-
ZZ	412 ± 26	97.7 ± 7.7	935 ± 67	783 ± 62	435 ± 22	103 ± 5	989 ± 44	828 ± 29
fakes	372 ± 26	174 ± 11	358 ± 29	15.6 ± 4.7	371 ± 25	174 ± 11	357 ± 28	15.6 ± 4.7
Total	1956 ± 109	512 ± 23	6760 ± 413	803 ± 62	1991 ± 35	519 ± 12	6856 ± 88	848 ± 30
Data	1991	513	6855	850	1991	513	6855	850

Table 7.1: Expected background event yields with total uncertainty (statistical and systematic) of the validation region and the WZ and ZZ control regions. Event counts are given per background contribution before (left) and after (right) fitting. Also provided is the total background expectation in the region and the amount of observed data events.

7.2 Region Distribution Plots

Variables pertaining to the diboson WZ region are displayed in Figure 7.4 and 7.5. Plots for the ZZ control region are shown in Figures 7.6 and 7.7. These plots (and subsequent plots in this section) are scaled with the found best-fit values of the WZ and ZZ NFs. These plots show that the predicted background agrees with observed data in the control regions. Furthermore, the desired diboson process is indeed the dominant background contribution for both the WZ and ZZ region. In these plots, MC. Stat uncertainties are given by the gray hatched area, while the total uncertainty (stat+syst) is given as the solid yellow area.

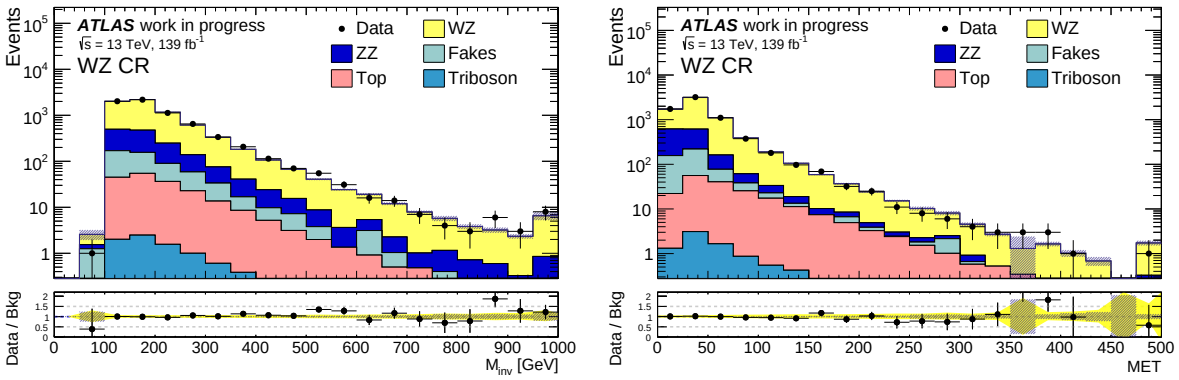

Figure 7.4: M_{inv} (left) and missing transverse energy (right) distributions in the diboson WZ control region. The rightmost bin of the M_{inv} plot is inclusive, including all events with $M_{inv} > 950$ GeV.

For the fakes validation region, distributions are shown in Figure 7.8, which gives the invariant mass and missing transverse energy distributions, and Figure 7.9 7.10, which give the invariant mass and off-flavor lepton transverse momenta of only $ee\mu$ and only $e\mu\mu$ events specifically. From these figures it can be concluded that there is a good agreement between the prompt SM backgrounds + fake rate event expectations and the observed data. It is also clear from Figures 7.9 and 7.10 in particular that fake electrons constitute the primary contribution to fake events, the rate of muon fakes being relatively small in comparison. Distributions for the off-Z validation region are shown in Figure 7.11, giving the M_{inv} and $E_{\mathrm{T}}^{\mathrm{miss}}$ distributions, Figures 7.12 and 7.13, giving the M_{inv} and lepton p_{T} distributions for $ee\mu$ and $e\mu\mu$ events respectively, and Figure 7.14, which gives the dilepton mass of the same-flavor lepton pair and the transverse mass of the off-flavor lepton. In these plots, MC. Stat uncertainties are given by the gray hatched area, while the total

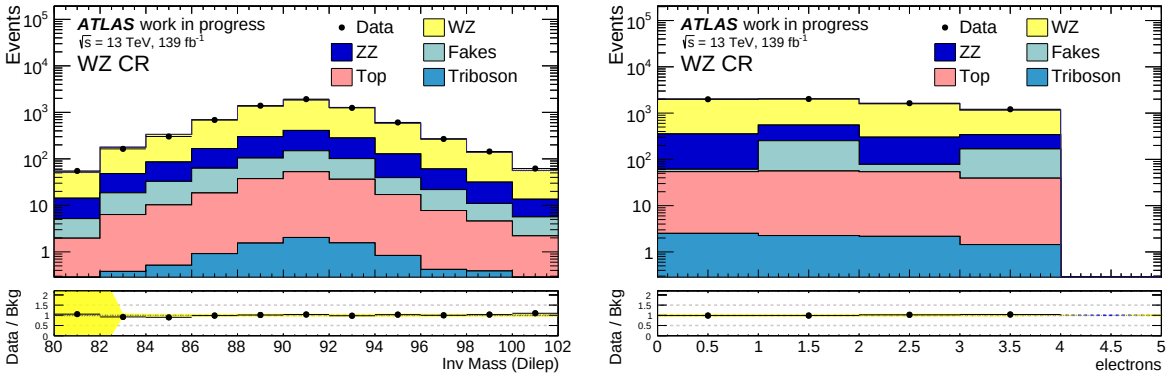

Figure 7.5: Distributions of the dilepton mass for the on-Z lepton pair (left) and the amount of electrons in the event (right) in the WZ control region. The muon multiplicity (n_μ) relates to the electron multiplicity (n_e) through $n_\mu = 3 - n_e$.

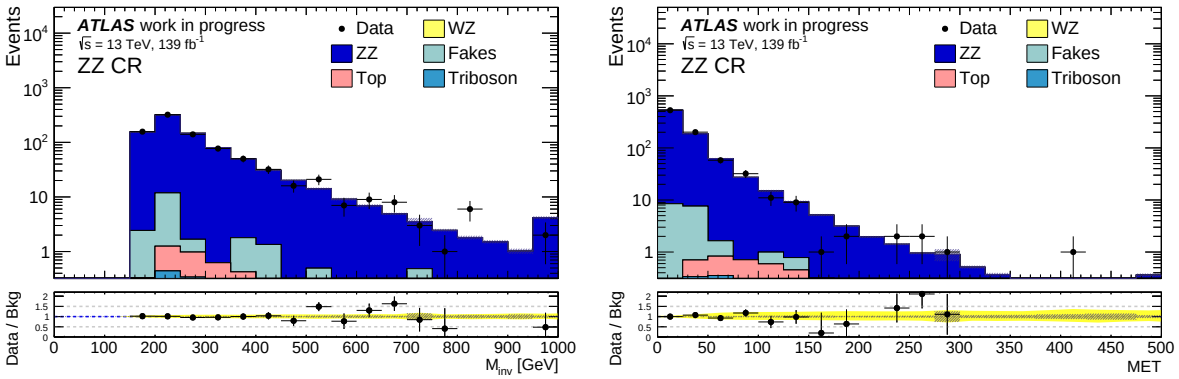

Figure 7.6: M_{inv} (left) and missing transverse energy (right) distributions in the diboson ZZ control region. The rightmost bin of the M_{inv} plot is inclusive, including all events with $M_{inv} > 950$ GeV or $E_{\mathrm{T}}^{\mathrm{miss}} > 475$ GeV.

uncertainty (stat+syst) is given as the solid yellow area. Here too we see good agreement between data and predicted background, with no sign of mismodelling at low dilepton masses or in bins where the fake background is large.

Figures 7.15-7.18 show invariant mass plots of each signal region individually. Missing transverse energy distributions for these signal regions are shown in Figure 7.19 and 7.20. Signal regions that are on-Z regions also have plots showing the dilepton mass of the lepton pair that qualifies the event as an on-Z event, and the transverse mass of the off-Z lepton(s). These plots are shown in Figures 7.21-7.24.

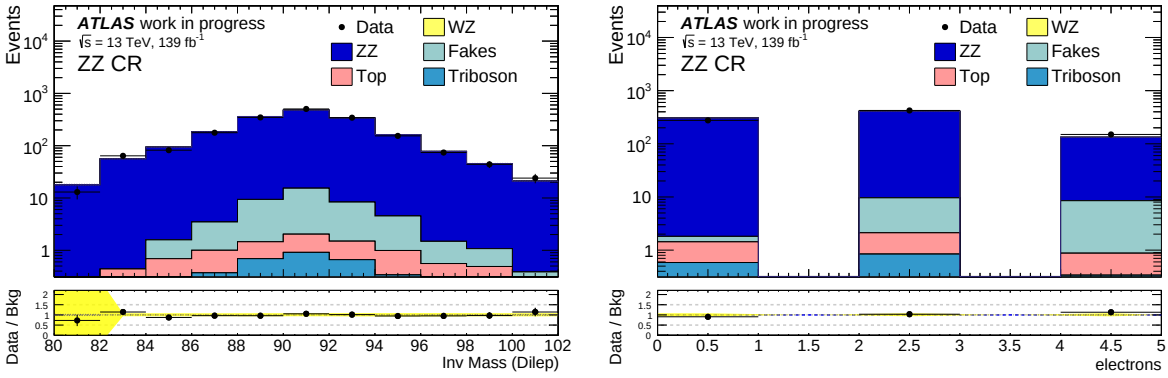

Figure 7.7: Distributions showing the dilepton masses for the two on-Z lepton pairs (2 entries per event) for the ZZ control region (left) and the amount of electrons in the event (right). The muon multiplicity (n_μ) relates to the electron multiplicity (n_e) through $n_\mu = 4 - n_e$.

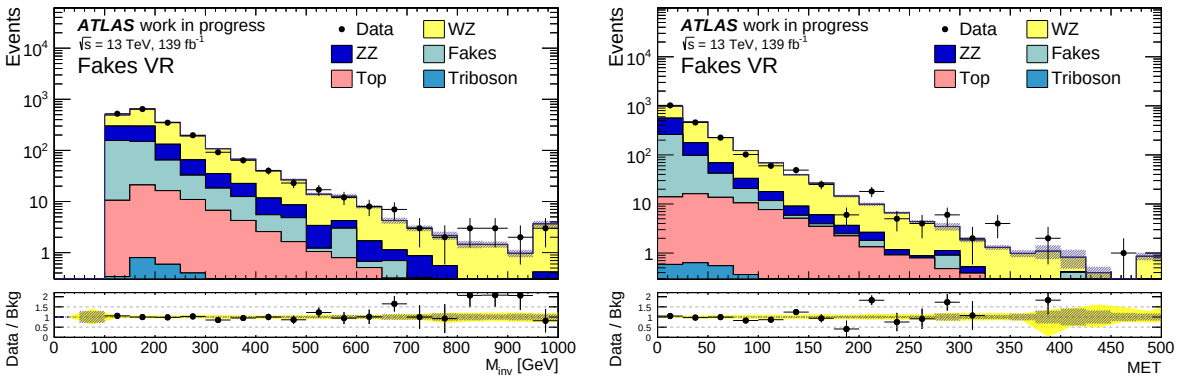

Figure 7.8: Distributions of the M_{inv} (left) and missing transverse energy (right) in the $ee\mu + e\mu\mu$ fake rate validation region. The rightmost bin is inclusive, including all events with $M_{inv} > 950$ GeV or $E_{\mathrm{T}}^{\mathrm{miss}} > 475$ GeV.

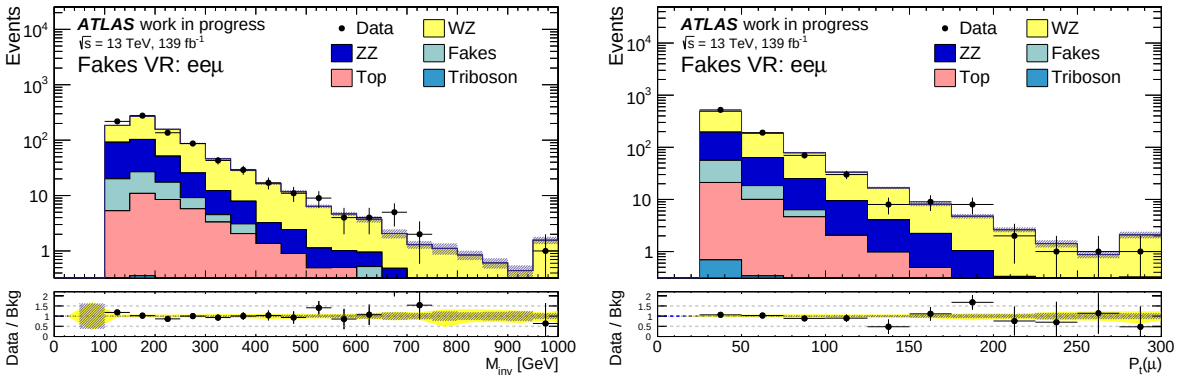

Figure 7.9: Distribution of the fake rate validation region filtered to only include $ee\mu$ events, showing the M_{inv} (left) and the transverse momentum of the muon (right).

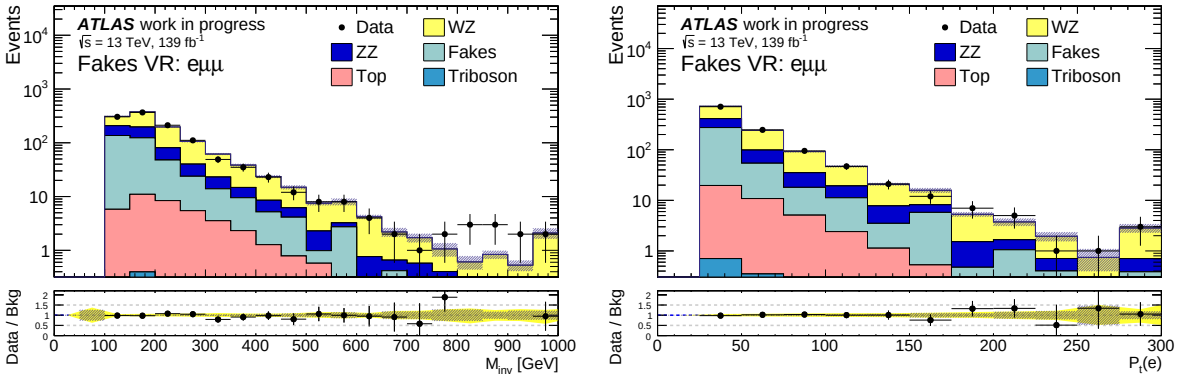

Figure 7.10: Distribution of the fake rate validation region filtered to only include $e\mu\mu$ events, showing the M_{inv} (left) and the transverse momentum of the electron (right).

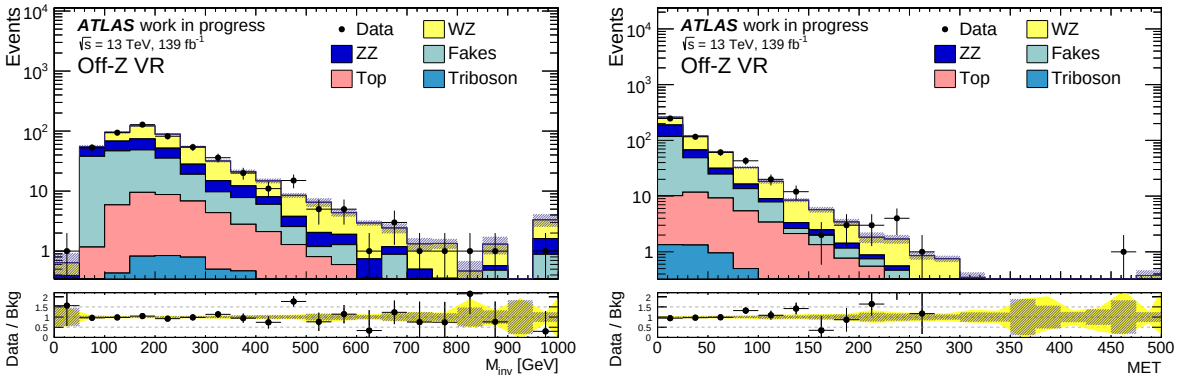

Figure 7.11: M_{inv} (left) and missing transverse energy (right) distributions in the $ee\mu + e\mu\mu$ off-Z validation region. The rightmost bin is inclusive, including all events with $M_{inv} > 950$ GeV or $E_{\mathrm{T}}^{\mathrm{miss}} > 475$ GeV.

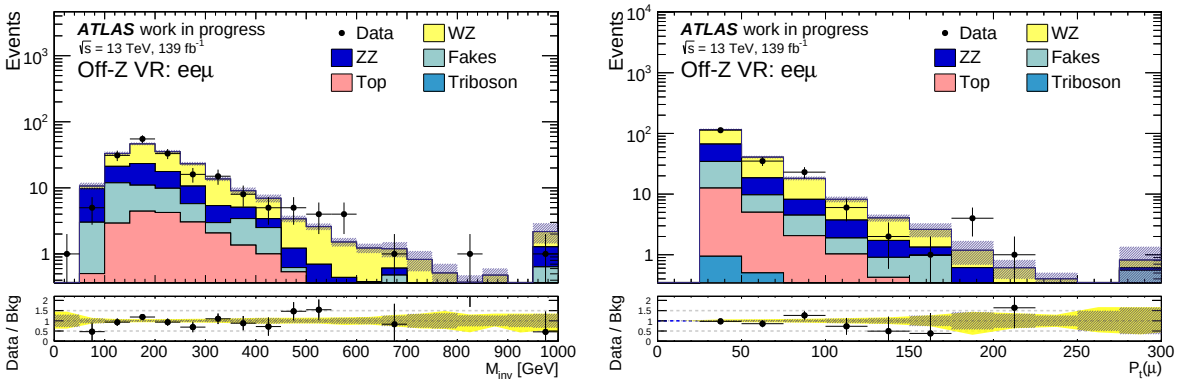

Figure 7.12: Distribution of the off-Z validation region filtered to only include $ee\mu$ events, showing the M_{inv} (left) and the transverse momentum of the muon (right).

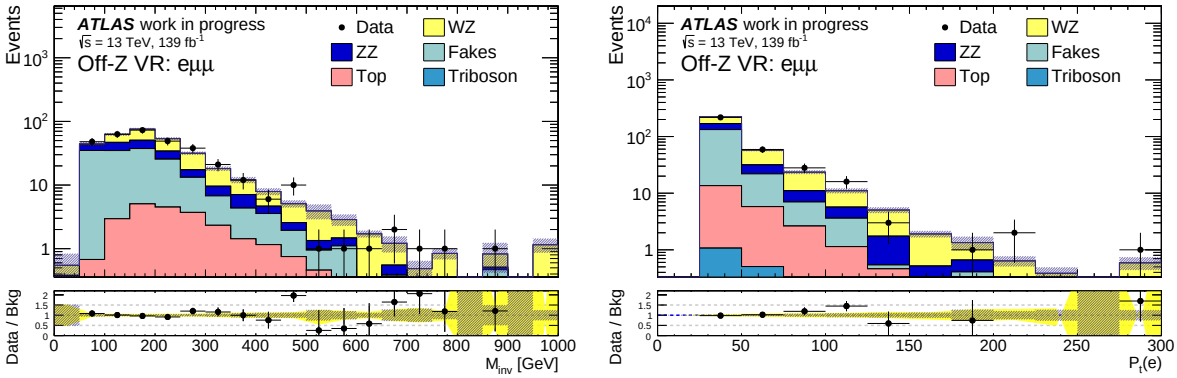

Figure 7.13: Distribution of the off-Z validation region filtered to only include $e\mu\mu$ events, showing the M_{inv} (left) and the transverse momentum of the electron (right).

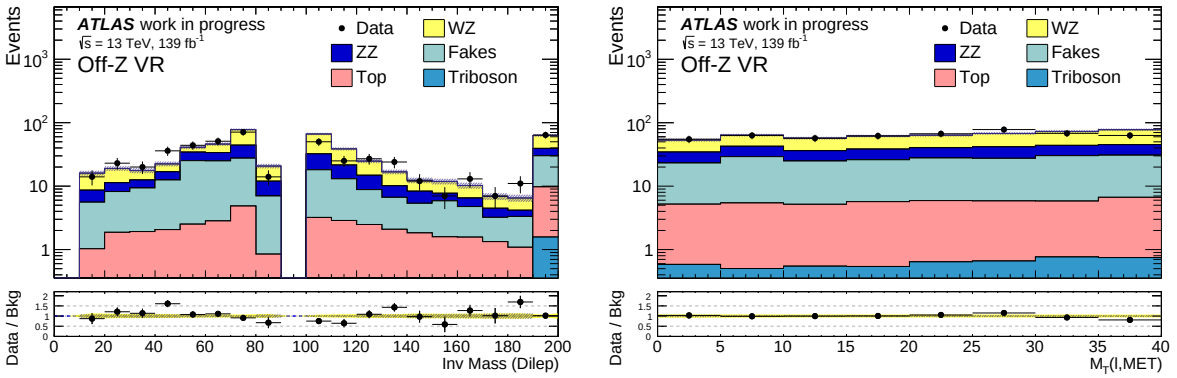

Figure 7.14: Distributions of the dilepton mass for the on-Z lepton pair (left) and the transverse mass for the off-flavor lepton (presumed fake or W lepton): $m_T\ell, MET$ (right) in the $ee\mu + e\mu\mu$ off-Z validation region

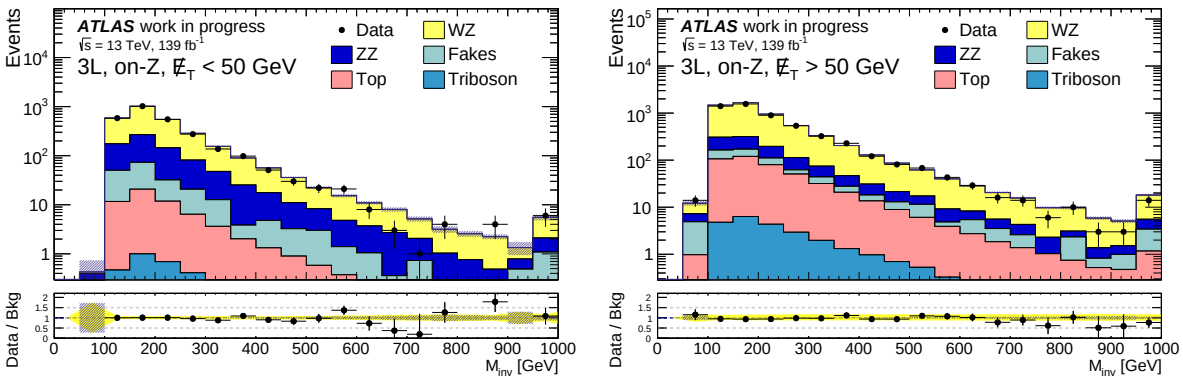

Figure 7.15: M_{inv} distributions for the three-lepton on-Z signal region with $E_{\mathrm{T}}^{\mathrm{miss}} < 50$ GeV (left) and $E_{\mathrm{T}}^{\mathrm{miss}} > 50$ GeV (right). The rightmost bin is inclusive, including all events with $M_{inv} > 950$ GeV.

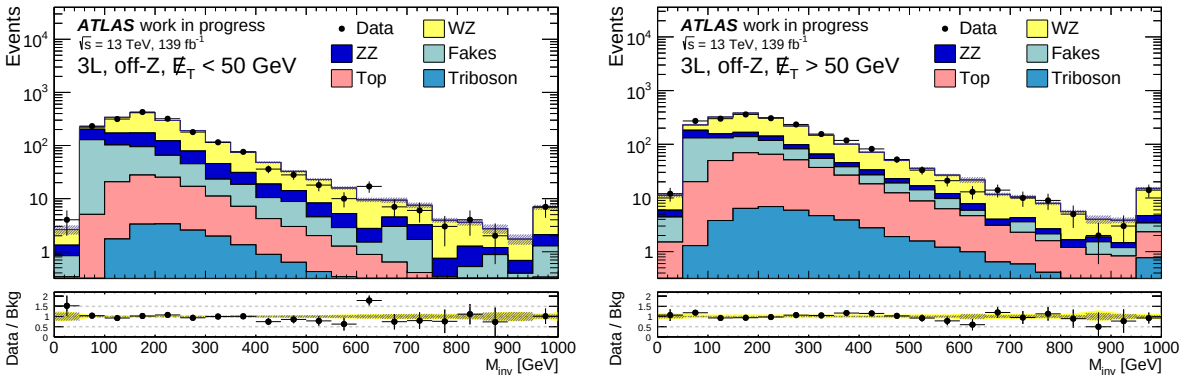

Figure 7.16: M_{inv} distributions for the three-lepton off-Z regions with $E_{\mathrm{T}}^{\mathrm{miss}} < 50$ GeV (left) and $E_{\mathrm{T}}^{\mathrm{miss}} > 50$ GeV (right). The rightmost bin is inclusive, including all events with $M_{inv} > 950$ GeV.

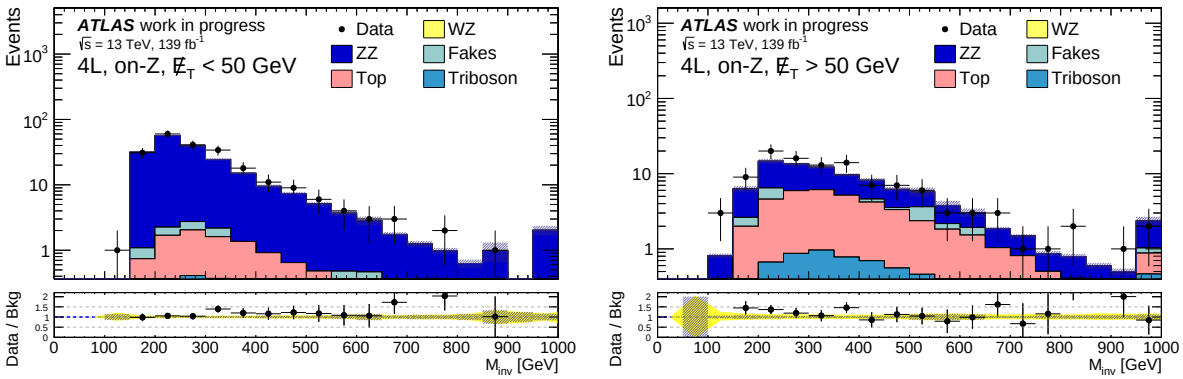

Figure 7.17: M_{inv} distributions for the 4 lepton on-Z regions with $E_{\mathrm{T}}^{\mathrm{miss}} < 50$ GeV (left) and $E_{\mathrm{T}}^{\mathrm{miss}} > 50$ GeV (right). The rightmost bin is inclusive, including all events with $M_{inv} > 950$ GeV.

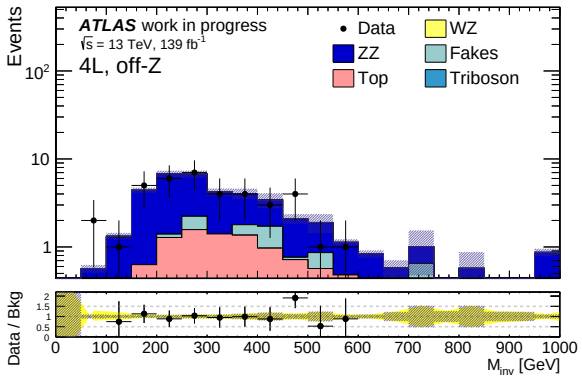

Figure 7.18: M_{inv} distributions for the four-lepton off-Z signal region. The rightmost bin is inclusive, including all events with $M_{inv} > 950$ GeV.

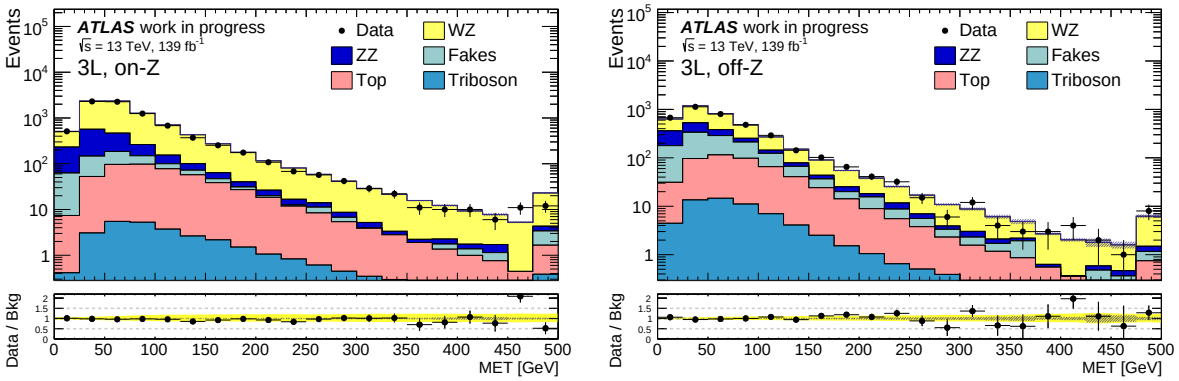

Figure 7.19: Distributions of for the missing transverse energy ($E_{\mathrm{T}}^{\mathrm{miss}}$) of the on-Z (left) and off-Z (right) three-lepton signal regions. The rightmost bin is inclusive, including all events with $E_{\mathrm{T}}^{\mathrm{miss}} > 475$ GeV.

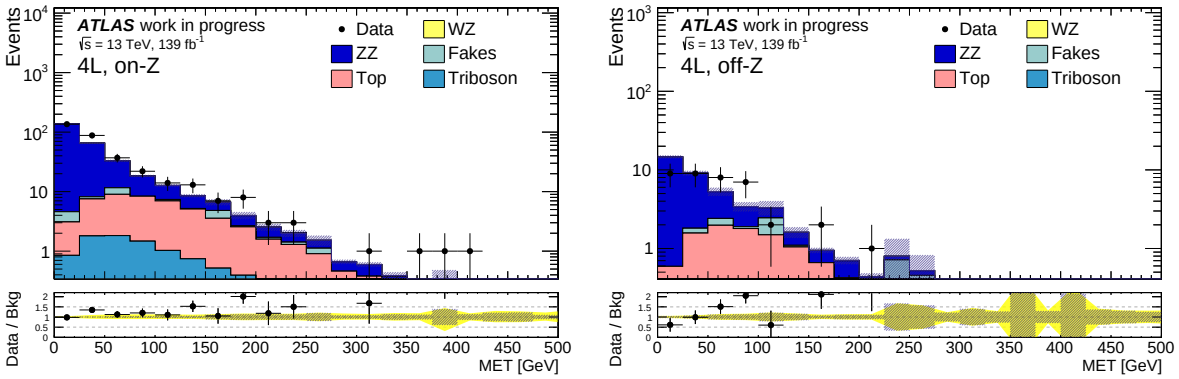

Figure 7.20: Distributions of for the missing transverse energy ($E_{\mathrm{T}}^{\mathrm{miss}}$) of the on-Z (left) and off-Z (right) four-lepton signal regions. The rightmost bin is inclusive, including all events with $E_{\mathrm{T}}^{\mathrm{miss}} > 475$ GeV.

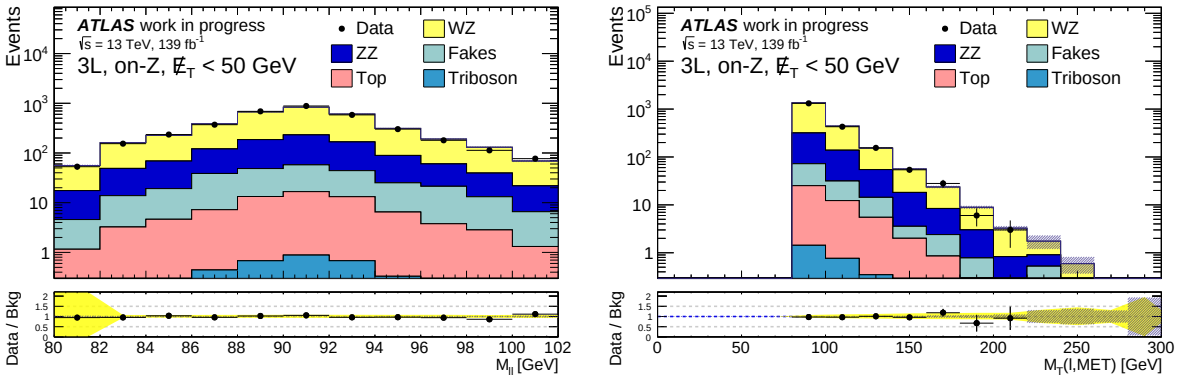

Figure 7.21: Distributions for the three-lepton on-Z region with $E_{\mathrm{T}}^{\mathrm{miss}} < 50$ GeV, showing the dilepton mass for the on-Z lepton pair (left) and the transverse mass off the off-Z lepton (right).

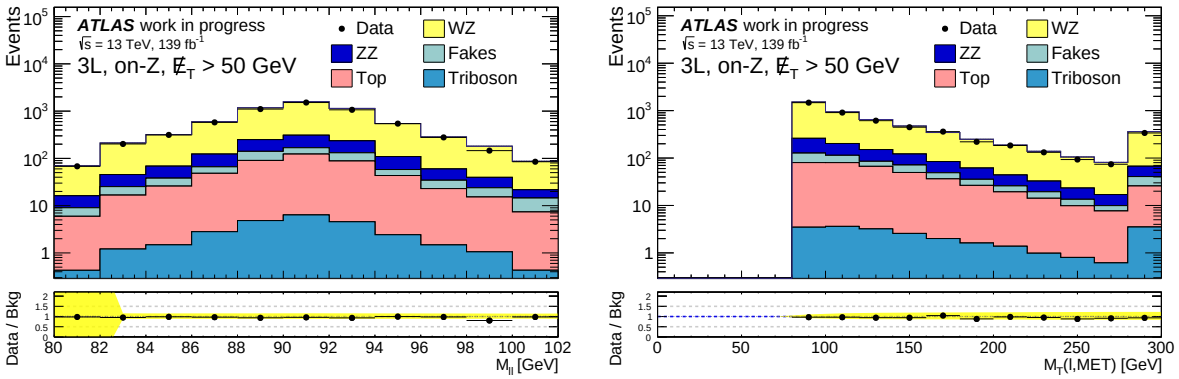

Figure 7.22: Distributions for the three-lepton on-Z region with $E_{\mathrm{T}}^{\mathrm{miss}} > 50$ GeV. Plots show the dilepton mass for the on-Z lepton pair (left) and the transverse mass off the off-Z lepton (right).

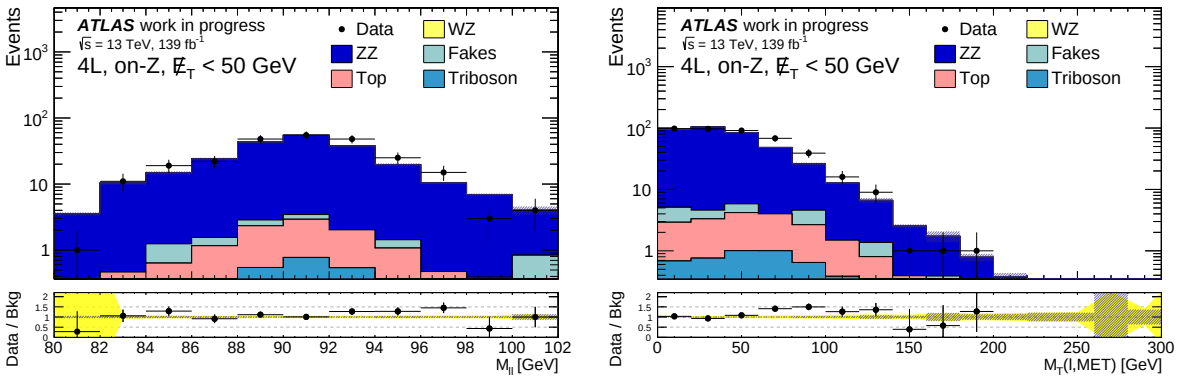

Figure 7.23: Distributions for the 4 lepton on-Z region with $E_{\mathrm{T}}^{\mathrm{miss}} < 50$ GeV, showing the dilepton mass for the on-Z lepton pair (left) and the transverse mass off the off-Z lepton (right).

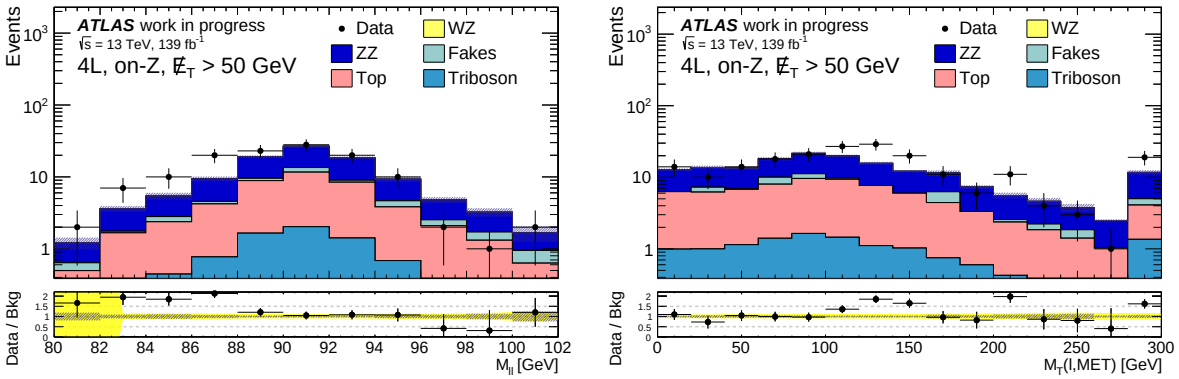

Figure 7.24: Distributions for the 4 lepton on-Z region with $E_{\mathrm{T}}^{\mathrm{miss}} > 50$ GeV, showing the dilepton mass for the on-Z lepton pair (left) and the transverse mass off the off-Z lepton (right).

7.3 Fits

This section shows the results of the fitting procedure explained in Chapter 6. The fits are carried out to the control regions plus a given signal region mass bin, where the PoI is the amount of events in the signal region. The PoI is shapeless, free-floating, allowed to be either positive or negative, independent between signal regions and between mass bins, and furthermore is assumed that the signal does not effect either of the control regions.

Invariant mass distributions before and after fitting of a (model-independent) signal are plotted for each signal region according to the mass binning used, showing the contribution of all processes as well as the observed data. These plots are shown in Figure 7.25 for the pre-fit yields and Figure 7.26 for the post-fit yields. All systematic uncertainties are included in these plots. Their total impact is shown as a solid yellow area in the ratio plots at the bottom of the figures. The total statistical uncertainty is additionally overlaid in the distribution and ratio plots as the hatched gray area. Statistical uncertainty of measured data, given as black bars on each data point, is presented as the square root of yield and is given alongside the data points.

An overview of the significance of each best-fit value is given in Table 7.2. An equivalent table that shows the p-values for each signal region mass bin is given in Table 7.3. The significance and p-value have been defined in Chapter 6.

No significance in any of these regions exceeds $|Z| > 3$, indicating no significant deviation from the Standard Model predictions. However, there are some results of note: The three-lepton, on-Z signal region with $M_{\text{inv}} > 600$ GeV shows a negative deviation of $|Z| > 1$ for both $E_{\text{T}}^{\text{miss}} < 50$ GeV and $E_{\text{T}}^{\text{miss}} > 50$ GeV (Figure 7.15). This is somewhat surprising, given that these regions are kinematically most similar to the WZ control region. Looking at the invariant mass plots of the WZ control region (or the fakes validation region) there is no such deviation of observed data compared to the background prediction for $M_{\text{inv}} > 600$ GeV. Furthermore, the four-lepton on-Z signal regions with $M_{\text{inv}} < 400$ GeV show the largest positive deviations, one that is observed in both the $E_{\text{T}}^{\text{miss}} < 50$ GeV and $E_{\text{T}}^{\text{miss}} > 50$ GeV signal regions (Figure 7.17). The nature of these deviations has been investigated in greater detail, but will require more thorough study before a definitive conclusion can be reached. The results of the investigation of this excess performed so far is shown in Appendix B. Lastly, the largest deviation of measured data from the Standard Model prediction is $Z = -2.72$. This result comes from the three-lepton, off-Z signal region with $E_{\text{T}}^{\text{miss}} < 50$ GeV and $400 < M_{\text{inv}} < 600$ GeV. This deviation has been investigated and seems congruent with being due to statistical effects[1]. The left plot in Figure 7.16 shows a downward fluctuation in M_{inv} bins between 400 and 600 GeV but a large upward fluctuation in the 600-650 GeV bin. This suggests the deviation observed in this region is enhanced due to the choice of binning.

The total event yields per background are given in Table 7.4 and 7.5 for the three-lepton signal regions, and in Table 7.6 for the four-lepton regions. Post-fit event yields include the best-fit value for the amount of signal events, which can be either a positive or a negative contribution.

[1]With 22 signal regions, one expects at least one region with a significance of at least $|Z| > 2.01$ due to statistical fluctuations alone.

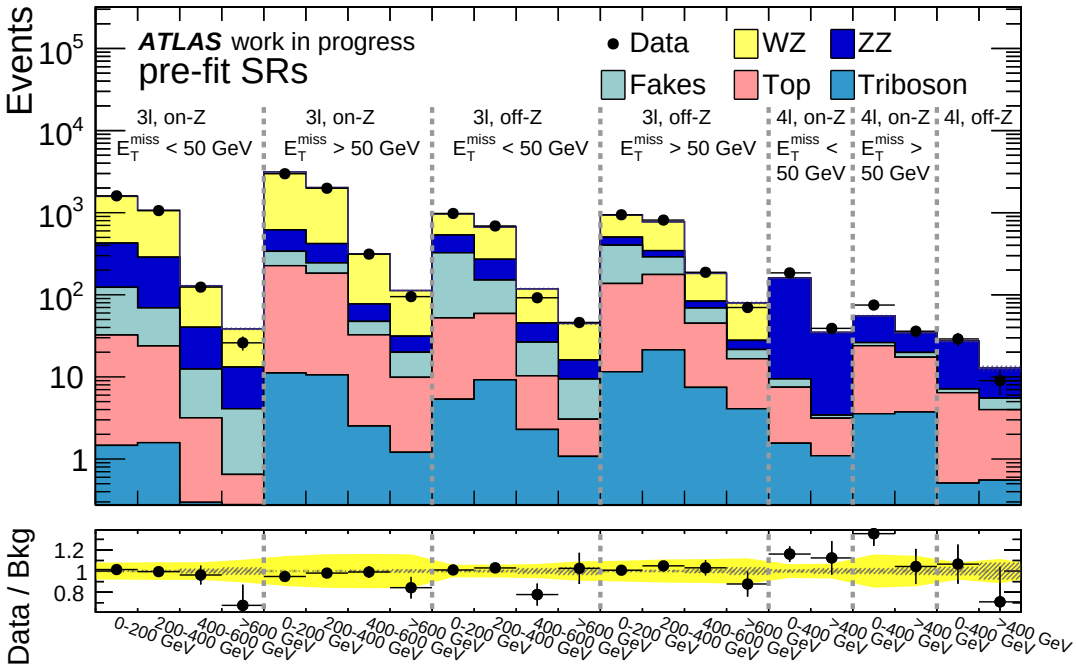

Figure 7.25: Fits comparing background expectation to measured data in each mass bin of each signal region of this analysis prior to performing a profile likelihood fit. Stat. uncertainties are given by the gray hatched area, while the total uncertainty (stat+syst) is given as the solid yellow area.

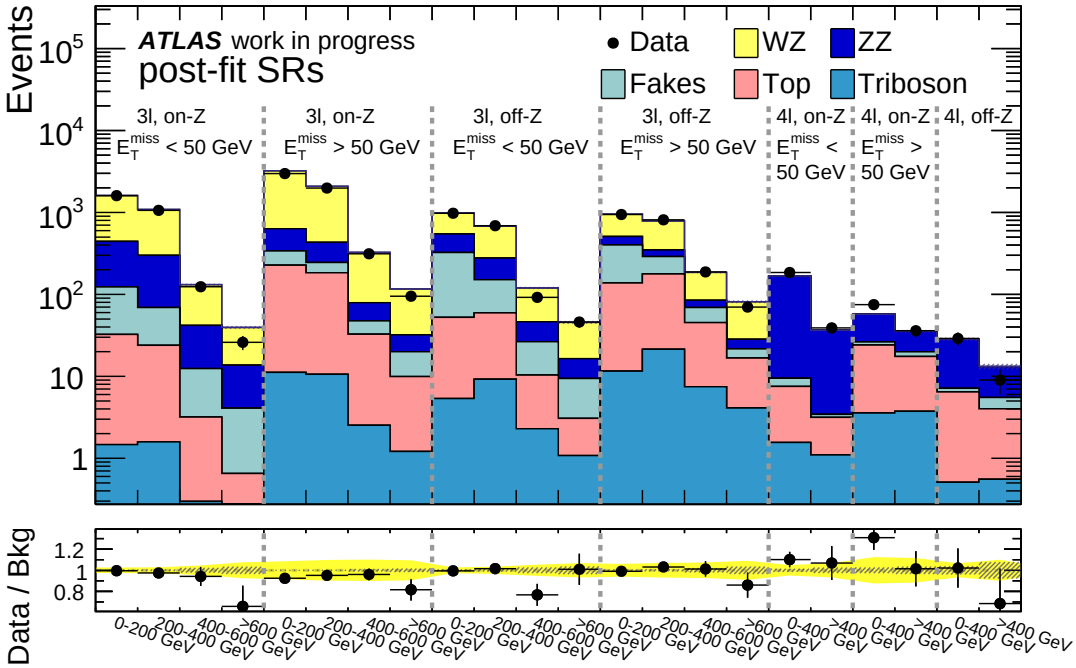

Figure 7.26: Fits comparing background expectation to measured data in each mass bin of each signal region of this analysis after performing a profile likelihood fit. Stat. uncertainties are given by the gray hatched area, while the total uncertainty (stat+syst) is given as the solid yellow area.

SR	0-200 GeV	200-400 GeV	400-600 GeV	>600 GeV
3ℓ, On-Z, $E_{\mathrm{T}}^{\mathrm{miss}} < 50$ GeV	-0.15	-0.72	-0.63	-2.47
3ℓ, On-Z, $E_{\mathrm{T}}^{\mathrm{miss}} > 50$ GeV	-0.97	-0.54	-0.38	-1.61
3ℓ, Off-Z, $E_{\mathrm{T}}^{\mathrm{miss}} < 50$ GeV	-0.15	0.35	-2.72	0.07
3ℓ, Off-Z, $E_{\mathrm{T}}^{\mathrm{miss}} > 50$ GeV	-0.15	0.56	0.16	-1.16
SR	0-400 GeV		>400 GeV	
4ℓ, On-Z, $E_{\mathrm{T}}^{\mathrm{miss}} < 50$ GeV	1.09		0.38	
4ℓ, On-Z, $E_{\mathrm{T}}^{\mathrm{miss}} > 50$ GeV	1.80		0.09	
4ℓ, Off-Z	0.11		-1.33	

Table 7.2: Significance values for each signal region mass bin of the best-found fit value for parameter of interest.

SR	0-200 GeV	200-400 GeV	400-600 GeV	>600 GeV
3ℓ, On-Z, $E_{\mathrm{T}}^{\mathrm{miss}} < 50$ GeV	0.44	0.24	0.26	0.0068
3ℓ, On-Z, $E_{\mathrm{T}}^{\mathrm{miss}} > 50$ GeV	0.17	0.29	0.35	0.053
3ℓ, Off-Z, $E_{\mathrm{T}}^{\mathrm{miss}} < 50$ GeV	0.44	0.36	0.0033	0.47
3ℓ, Off-Z, $E_{\mathrm{T}}^{\mathrm{miss}} > 50$ GeV	0.44	0.29	0.44	0.12
SR	0-400 GeV		>400 GeV	
4ℓ, On-Z, $E_{\mathrm{T}}^{\mathrm{miss}} < 50$ GeV	0.14		0.35	
4ℓ, On-Z, $E_{\mathrm{T}}^{\mathrm{miss}} > 50$ GeV	0.036		0.46	
4ℓ, Off-Z	0.45		0.091	

Table 7.3: p-values for each signal region mass bin of the best-found fit value for parameter of interest.

3ℓ, On-Z, $E_{\mathrm{T}}^{\mathrm{miss}} < 50$ GeV				
Sample	0-200 GeV	200-400 GeV	400-600 GeV	>600 GeV
top	30.8 ± 2.4	22.2 ± 1.9	2.9 ± 0.3	0.5 ± 0.1
triboson	1.5 ± 0.2	1.6 ± 0.2	0.3 ± 0.0	0.1 ± 0.0
WZ	1156 ± 101	780 ± 69	88.6 ± 7.9	25.4 ± 2.7
ZZ	302 ± 24	218 ± 18	27.8 ± 2.0	9.1 ± 1.1
fakes	91.0 ± 9.1	45.4 ± 7.3	9.3 ± 2.3	3.4 ± 0.9
Total	1581 ± 107	1067 ± 73	129 ± 9	38.5 ± 3.2
Data	1604	1061	124	26

3ℓ, On-Z, $E_{\mathrm{T}}^{\mathrm{miss}} > 50$ GeV				
Sample	0-200 GeV	200-400 GeV	400-600 GeV	>600 GeV
top	215.0 ± 17.7	172.1 ± 15.4	30.0 ± 2.8	8.7 ± 0.8
triboson	11.1 ± 1.4	10.6 ± 1.5	2.5 ± 0.4	1.2 ± 0.2
WZ	2528 ± 379	1604 ± 272	239 ± 42	81.4 ± 14.5
ZZ	277 ± 46	176 ± 33	29.9 ± 5.8	11.4 ± 2.3
fakes	112 ± 13	61.5 ± 9.3	14.9 ± 3.3	10.1 ± 1.8
Total	3144 ± 389	2024 ± 278	316 ± 43	113 ± 15
Data	2982	1985	313	95

3ℓ, Off-Z, $E_{\mathrm{T}}^{\mathrm{miss}} < 50$ GeV				
Sample	0-200 GeV	200-400 GeV	400-600 GeV	>600 GeV
top	46.9 ± 3.7	49.9 ± 4.7	8.0 ± 0.9	2.0 ± 0.3
triboson	5.3 ± 0.5	9.2 ± 1.0	2.3 ± 0.3	1.1 ± 0.2
WZ	434 ± 33	399 ± 27	73.1 ± 5.0	28.8 ± 2.5
ZZ	210 ± 19	119 ± 7	18.8 ± 1.1	6.6 ± 0.9
fakes	272 ± 16	91.9 ± 9.6	16.2 ± 3.0	6.4 ± 1.4
Total	968 ± 44	669 ± 32	118 ± 6	44.9 ± 3.1
Data	978	689	92	46

3ℓ, Off-Z, $E_{\mathrm{T}}^{\mathrm{miss}} > 50$ GeV				
Sample	0-200 GeV	200-400 GeV	400-600 GeV	>600 GeV
top	125 ± 10	155 ± 15	37.5 ± 4.0	12.5 ± 1.4
triboson	11.5 ± 1.4	21.3 ± 2.8	7.4 ± 1.1	4.1 ± 0.6
WZ	434 ± 63	430 ± 58	98.8 ± 12.8	51.9 ± 6.2
ZZ	102 ± 17	55.9 ± 8.6	14.7 ± 2.4	6.3 ± 1.0
fakes	264 ± 19	112 ± 12	24.0 ± 3.9	4.9 ± 1.2
Total	937 ± 71	775 ± 63	182 ± 15	79.8 ± 6.8
Data	944	813	188	70

Table 7.4: Predicted background and observed event yields per signal region, M_{inv} bin and background contribution for the signal regions containing three leptons with the total (statistical and systematic) uncertainty on the event rate.

3ℓ, On-Z, $E_{\mathrm{T}}^{\mathrm{miss}} < 50$ GeV				
Sample	0-200 GeV	200-400 GeV	400-600 GeV	>600 GeV
Signal	-7.0 ± 48.1	-27.5 ± 38.1	-7.6 ± 11.9	-13.5 ± 5.4
top	31.0 ± 2.8	22.3 ± 2.0	2.9 ± 0.3	0.5 ± 0.1
triboson	1.5 ± 0.2	1.6 ± 0.2	0.3 ± 0.0	0.1 ± 0.0
WZ	1168 ± 25	789 ± 18	89.8 ± 3.4	25.8 ± 1.7
ZZ	320 ± 13	230 ± 9	29.4 ± 1.5	9.6 ± 0.8
fakes	90.8 ± 9.0	45.2 ± 7.2	9.2 ± 2.3	3.4 ± 0.9
Total	1604 ± 43	1061 ± 35	124 ± 12	26.0 ± 5.4
Data	1604	1061	124	26

3ℓ, On-Z, $E_{\mathrm{T}}^{\mathrm{miss}} > 50$ GeV				
Sample	0-200 GeV	200-400 GeV	400-600 GeV	>600 GeV
Signal	-243 ± 256	-101 ± 186	-12.8 ± 33.1	-21.4 ± 13.3
top	216 ± 18	173 ± 15	30.1 ± 2.8	8.7 ± 0.8
triboson	11.2 ± 1.4	10.6 ± 1.5	2.5 ± 0.4	1.2 ± 0.2
WZ	2592 ± 216	1654 ± 163	247 ± 26	84.4 ± 8.3
ZZ	294 ± 40	187 ± 24	31.7 ± 4.0	12.1 ± 1.6
fakes	112 ± 13	61.3 ± 9.3	14.8 ± 3.3	10.0 ± 1.8
Total	2982 ± 59	1986 ± 47	313 ± 19	95.0 ± 10.1
Data	2982	1985	313	95

3ℓ, Off-Z, $E_{\mathrm{T}}^{\mathrm{miss}} < 50$ GeV				
Sample	0-200 GeV	200-400 GeV	400-600 GeV	>600 GeV
Signal	-5.5 ± 36.6	10.4 ± 30.0	-27.9 ± 10.2	0.4 ± 7.1
top	47.1 ± 3.7	50.2 ± 4.6	8.1 ± 0.9	2.0 ± 0.3
triboson	5.4 ± 0.5	9.2 ± 1.0	2.3 ± 0.3	1.1 ± 0.2
WZ	438 ± 9	401 ± 10	73.5 ± 2.8	29.1 ± 1.2
ZZ	222 ± 11	126 ± 7	19.9 ± 1.5	7.0 ± 0.9
fakes	271.9 ± 15.5	91.6 ± 9.5	16.1 ± 3.0	6.3 ± 1.4
Total	978 ± 34	689 ± 29	92.0 ± 10.4	46.0 ± 7.2
Data	978	689	92	46

3ℓ, Off-Z, $E_{\mathrm{T}}^{\mathrm{miss}} > 50$ GeV				
Sample	0-200 GeV	200-400 GeV	400-600 GeV	>600 GeV
Signal	-9.0 ± 55.2	24.5 ± 48.3	2.3 ± 16.5	-11.4 ± 9.5
top	126 ± 10	156 ± 15	37.8 ± 4.0	12.6 ± 1.4
triboson	11.6 ± 1.4	21.4 ± 2.9	7.5 ± 1.1	4.1 ± 0.7
WZ	444 ± 34	440 ± 31	101 ± 6	53.1 ± 3.9
ZZ	108 ± 13	59.3 ± 5.9	15.6 ± 1.7	6.7 ± 0.8
fakes	264 ± 19.2	112 ± 11.6	23.9 ± 3.8	4.9 ± 1.2
Total	944 ± 33	813 ± 31	188 ± 15	70.0 ± 9.2
Data	944	813	188	70

Table 7.5: Predicted background and observed event yields per signal region, M_{inv} bin and background contribution after fitting for the signal regions containing three leptons with the total (statistical and systematic) uncertainty on the event rate. The given *Signal* contribution shown in this table is the best-fit value of N_S (from Equation 6.4).

pre-fit

4ℓ, On-Z, $E_{\mathrm{T}}^{\mathrm{miss}} < 50$ GeV		
Sample	0-400 GeV	>400 GeV
Signal		
top	5.9 ± 0.7	2.0 ± 0.3
triboson	1.6 ± 0.2	1.1 ± 0.1
ZZ	150 ± 9	31.3 ± 1.9
fakes	1.9 ± 2.1	0.3 ± 0.7
Total	159 ± 10	34.7 ± 2.1
Data	185	39

4ℓ, On-Z, $E_{\mathrm{T}}^{\mathrm{miss}} > 50$ GeV		
Sample	0-400 GeV	>400 GeV
Signal		
top	20.4 ± 2.2	13.6 ± 1.5
triboson	3.6 ± 0.5	3.7 ± 0.6
ZZ	29.2 ± 5.9	14.7 ± 2.8
fakes	2.2 ± 1.5	2.5 ± 1.2
Total	55.4 ± 6.6	34.5 ± 3.5
Data	75	36

4ℓ, Off-Z		
Sample	0-400 GeV	>400 GeV
Signal		
top	5.9 ± 0.5	3.4 ± 0.4
triboson	0.5 ± 0.1	0.6 ± 0.1
ZZ	20.1 ± 1.3	7.2 ± 0.6
fakes	0.7 ± 1.0	1.5 ± 1.0
Total	27.2 ± 1.8	12.7 ± 1.2
Data	29	9

post-fit

4ℓ, On-Z, $E_{\mathrm{T}}^{\mathrm{miss}} < 50$ GeV		
Sample	0-400 GeV	>400 GeV
Signal	17.0 ± 15.6	2.5 ± 6.6
top	6.0 ± 0.7	2.1 ± 0.3
triboson	1.6 ± 0.2	1.1 ± 0.1
ZZ	159 ± 7	33.1 ± 1.9
fakes	1.9 ± 2.1	0.3 ± 0.7
Total	185 ± 14	39.0 ± 6.4
Data	185	39

4ℓ, On-Z, $E_{\mathrm{T}}^{\mathrm{miss}} > 50$ GeV		
Sample	0-400 GeV	>400 GeV
Signal	17.7 ± 10.2	0.5 ± 6.6
top	20.5 ± 2.2	13.7 ± 1.5
triboson	3.6 ± 0.5	3.7 ± 0.6
ZZ	31.0 ± 4.3	15.6 ± 1.8
fakes	2.2 ± 1.5	2.5 ± 1.2
Total	75.0 ± 9.0	36.0 ± 6.3
Data	75	36

4ℓ, Off-Z		
Sample	0-400 GeV	>400 GeV
Signal	0.6 ± 5.6	−4.1 ± 3.1
top	5.9 ± 0.5	3.5 ± 0.4
triboson	0.5 ± 0.1	0.6 ± 0.1
ZZ	21.3 ± 0.9	7.6 ± 0.4
fakes	0.7 ± 1.0	1.5 ± 1.0
Total	29.0 ± 5.6	9.0 ± 3.2
Data	29	9

Table 7.6: Predicted background and observed event yields per signal region, M_{inv} bin and background contribution for the signal regions containing four leptons prior to (left) and after (right) fitting with the total (statistical and systematic) uncertainty on the event rate. The given *Signal* contribution shown in this table is the best-fit value of N_S (from Equation 6.4).

7.4 Limits

Expected and observed limits on the event count above the SM prediction in each signal region (computed independently) are given in Table 7.7. In the absence of a specific physics theory, the strategy discussed in Section 6 can be used to set upper limits on the amount of additional events in a signal region at the 95% confidence level: N_{95}. Taking into consideration the amount of data collected during Run-2 at the ATLAS detector the same upper limit can also be given as the number of new physics events per inverse femtobarn of data: $\sigma_{\text{vis}} = N_{95}/\int \mathcal{L}dt$, known as the visible cross section limit. Limits expressed in σ_{vis} are also displayed in the plots in Figure 7.27.

The visible cross-section limit can be related to a limit on a specific model's cross-section. These two limits are related through the selection efficiency and acceptance of the signal model in a particular signal region, denoted as ϵ.

Consider a process which has a certain ϵ in a certain signal region, and a theoretical cross-section σ_i. One would expect, for a data sample of integrated luminosity λ, an event yield of $N = \lambda \times \epsilon \times \sigma_i$. An expected 95% CL upper limit on the event yield can be related to a cross-section limit as $N_{95} = \lambda \times \epsilon \times \sigma^{95}_{SIG}$. Visible cross-section limits given in this section can then be translated into model-specific limits, as long as the model's efficiency is known, according to

$$\sigma^{95}_{\text{vis}} = \frac{N_{95}}{\lambda} = \frac{\sigma^{95}_{\text{SIG}} \times \lambda \times \epsilon}{\lambda} \Rightarrow \sigma^{95}_{\text{SIG}} = \sigma^{95}_{\text{vis}}/\epsilon. \tag{7.1}$$

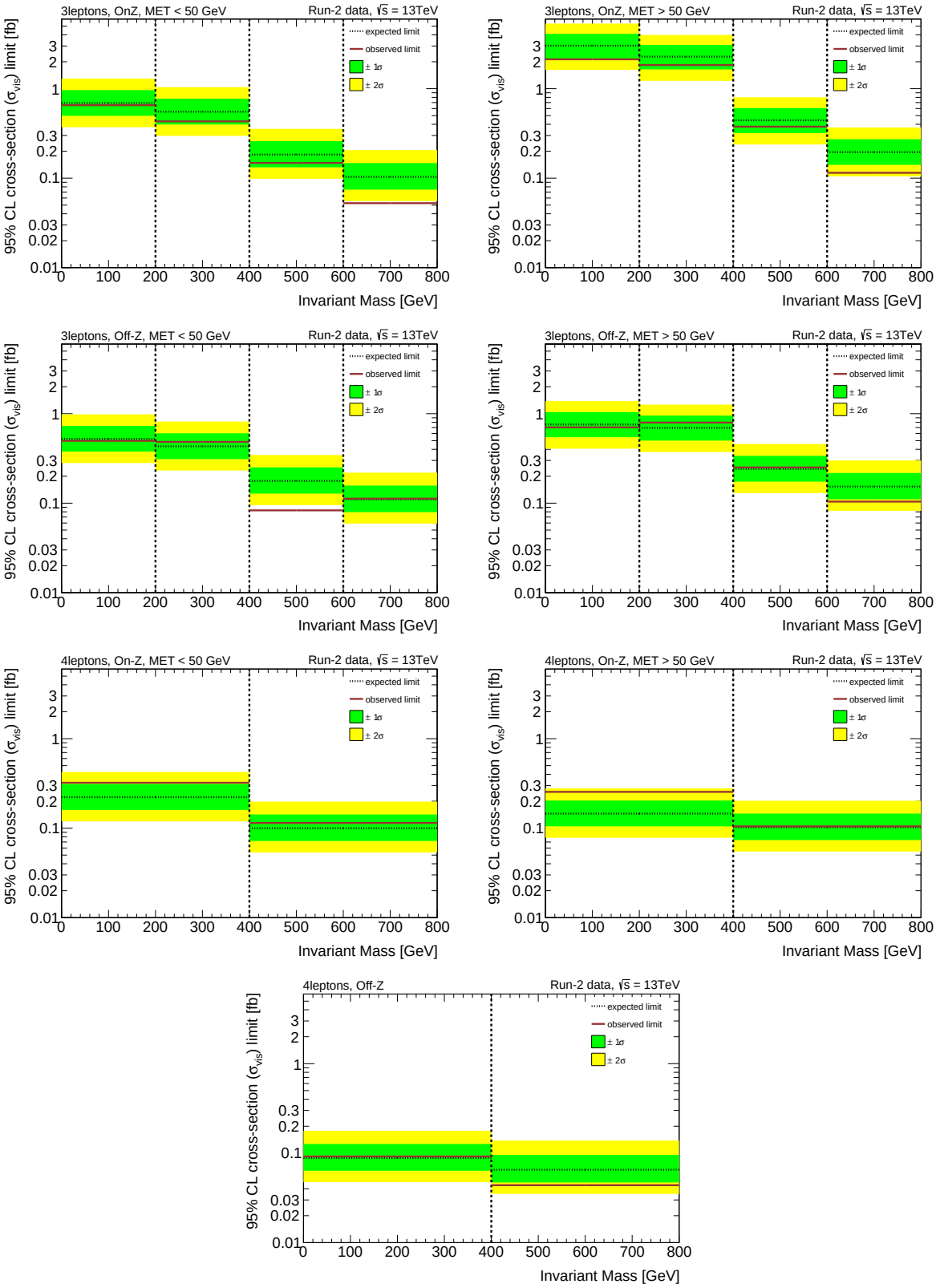

Figure 7.27: Plots of expected and observed upper limits per region and mass bin.

Mass Range	N_{95} (exp.)	$\pm 1\sigma$	$\pm 2\sigma$	σ_{vis} [fb] (exp.)	N_{95} (obs.)	σ_{vis} [fb] (obs.)
3ℓ, On-Z, $E_{\mathrm{T}}^{\mathrm{miss}} < 50$ GeV						
0-200 GeV	96.1	$^{+37.8}_{-26.9}$	$^{+84.1}_{-44.5}$	0.692	91.0	0.654
200-400 GeV	76.8	$^{+30.4}_{-21.5}$	$^{+67.7}_{-35.6}$	0.553	60.0	0.431
400-600 GeV	25.5	$^{+10.5}_{-7.1}$	$^{+23.9}_{-11.8}$	0.183	20.6	0.148
>600 GeV	14.4	$^{+6.1}_{-4.0}$	$^{+14.3}_{-6.7}$	0.103	7.3	0.053
3ℓ, On-Z, $E_{\mathrm{T}}^{\mathrm{miss}} > 50$ GeV						
0-200 GeV	420.0	$^{+149.8}_{-117.4}$	$^{+322.0}_{-194.6}$	3.021	296.2	2.131
200-400 GeV	316.7	$^{+111.2}_{-88.5}$	$^{+237.9}_{-146.7}$	2.279	255.6	1.839
400-600 GeV	61.6	$^{+22.8}_{-17.2}$	$^{+49.8}_{-28.5}$	0.443	52.3	0.376
>600 GeV	27.2	$^{+10.7}_{-7.6}$	$^{+24.1}_{-12.6}$	0.195	16.0	0.115
3ℓ, Off-Z, $E_{\mathrm{T}}^{\mathrm{miss}} < 50$ GeV						
0-200 GeV	72.7	$^{+28.7}_{-20.3}$	$^{+64.1}_{-33.7}$	0.523	69.1	0.497
200-400 GeV	60.0	$^{+24.0}_{-16.8}$	$^{+53.6}_{-27.8}$	0.432	67.3	0.484
400-600 GeV	24.6	$^{+10.2}_{-6.9}$	$^{+23.3}_{-11.4}$	0.177	11.6	0.083
>600 GeV	15.3	$^{+6.5}_{-4.3}$	$^{+15.2}_{-7.1}$	0.110	15.6	0.112
3ℓ, Off-Z, $E_{\mathrm{T}}^{\mathrm{miss}} > 50$ GeV						
0-200 GeV	105.3	$^{+39.5}_{-29.4}$	$^{+86.9}_{-48.8}$	0.757	97.7	0.703
200-400 GeV	96.5	$^{+35.7}_{-27.0}$	$^{+79.1}_{-44.7}$	0.694	110.5	0.795
400-600 GeV	33.5	$^{+13.4}_{-9.4}$	$^{+30.2}_{-15.5}$	0.241	34.9	0.251
>600 GeV	21.3	$^{+8.9}_{-6.0}$	$^{+20.4}_{-9.9}$	0.153	14.5	0.104
4ℓ, On-Z, $E_{\mathrm{T}}^{\mathrm{miss}} < 50$ GeV						
0-400 GeV	30.9	$^{+12.5}_{-8.6}$	$^{+28.1}_{-14.3}$	0.222	44.7	0.322
>400 GeV	13.9	$^{+5.9}_{-3.9}$	$^{+13.6}_{-6.4}$	0.100	15.9	0.114
4ℓ, On-Z, $E_{\mathrm{T}}^{\mathrm{miss}} > 50$ GeV						
0-400 GeV	20.2	$^{+8.1}_{-5.7}$	$^{+18.4}_{-9.4}$	0.145	35.4	0.254
>400 GeV	14.2	$^{+6.0}_{-4.0}$	$^{+14.0}_{-6.6}$	0.102	14.6	0.105
4ℓ, Off-Z						
0-400 GeV	12.3	$^{+5.3}_{-3.4}$	$^{+12.5}_{-5.7}$	0.088	12.8	0.092
>400 GeV	9.1	$^{+4.2}_{-2.5}$	$^{+10.2}_{-4.2}$	0.065	6.1	0.044

Table 7.7: Expected and observed upper limits per region and mass bin.

7.5 Model-specific comparison

It is useful to check if the results of the model-independent analysis are feasible, competitive, and lend themselves to reinterpretation for future searches of BSM physics. This can be tested by producing limits on model-specific signal samples and reflecting on the comparison of obtained results with those of model-specific analyses probing the same model. This is done for the search for Type-III seesaw heavy leptons [185, 207, 208] and for doubly-charged Higgs boson pair production [52, 209]. The implementation of these models' parameters, and the differences of the dedicated searches in relation to this analysis are discussed. Then, limits are presented using the machinery of the model-independent analysis on these particular models, which are then compared with the results reported by the aforementioned analyses.

The model parameters are set equal to those in the reference analyses. This ensures that the models with identical production channels, final states and branching fractions are studied and the obtained cross-section limits are directly comparable, even if the signal region selections to obtain these limits differ.

Since model-dependent searches have specific criteria and focus on a particular final state, their event selection is much more specific and different from what is used in the model-independent search. However, there are some similarities between the specific analyses compared in this section: In each analysis, the studied objects are light leptons, electrons and muons. Furthermore, each analysis considers the same set of event generators to produce the background prediction (although used background samples might differ, since different lepton multiplicity and event topology call for different backgrounds) and uses the Fake Factor method in order to determine their reducible background from non-prompt sources.

7.5.1 Type-III Seesaw model

The Type-III seesaw model is studied in both the three-lepton and the four-lepton final state[2]. Heavy-lepton decay is expected to produce multiple charged leptons and many possible final states will include also at least one neutrino, and potentially additional jets due to the hadronic decay modes of the bosons produced during the heavy lepton decay. The studied production channel is that of the heavy W-like boson decaying to a heavy charged lepton and heavy neutrino ($W^{*\pm} \to L^{\pm}N^{0}$), discussed in Section 1.4. The mixing matrix elements V_e, V_μ and V_τ determine the abundance of leptonic flavors among the decay products. For this analysis, the mixing element values are assumed to be equal to each other. Their values furthermore affect the relative leptonic branching fractions of the possible decay modes of the heavy leptons. The absolute value of the mixing matrix elements are set as $|V_\ell| = 0.063$. This is in line with existing upper bounds on these matrix elements [210–212]. The associated branching fractions are given in Figure 7.28.

For the demonstration in this analysis, two specific mass values for the heavy leptons are used. The masses of the $L^{\pm}$ and N^{0} are assumed to be identical. The tested masses are 400 GeV and 700 GeV.

[2]The reference analysis tests the same model, but targets decay modes which result in dilepton final states.

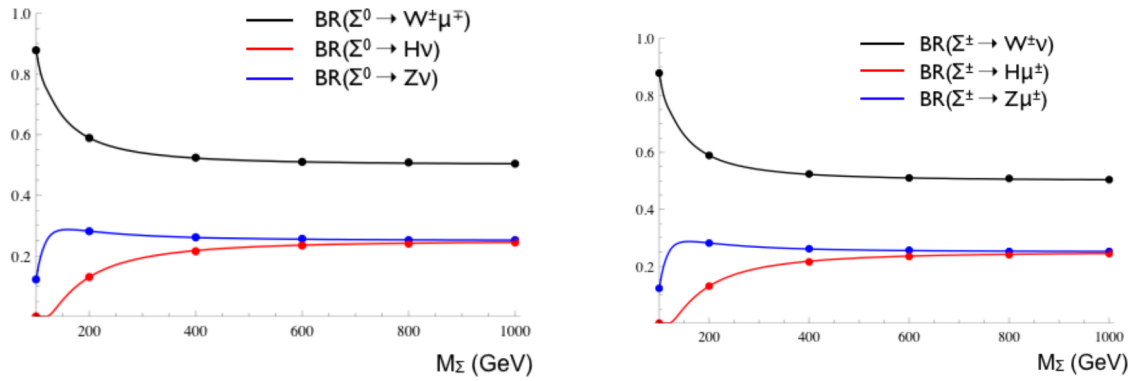

Figure 7.28: Branching ratios of the neutral (left) and charged component (right) of the fermionic triplet in the case $V_e = V_\tau = 0, V_\mu = 0.063$. The dots correspond to numerically evaluated values while the lines correspond to the analytical computations [41].

The theoretical cross-sections used are on par with the reference analysis implementation of the Type-III seesaw, for which the LO and NLO values have been calculated from theory [207]. The values are given in Table 7.8. This cross-section calculation includes next-to-leading order (NLO) plus next-to-leading logarithmic (NLL) accuracy, under the assumption that the heavy leptons are $SU(2)$ triplet fermions [213, 214]. However, this initial cross-section value is ultimately an implementation detail, and is not important in the context of comparing expected upper limits.

7.5.2 Doubly-Charged Higgs

The doubly-charged Higgs model is studied through pair production resulting in a four-lepton final state. In this channel, no additional objects are produced at tree level, therefore missing energy is expected to be low.

The coupling of the doubly-charged Higgs particle to the W-boson depends on the vacuum expectation value v_Δ. For $v_\Delta = 0$, $BR(H^{\pm\pm} \to W^\pm W^\pm) = 0$, resulting in fully leptonic decay modes of the doubly-charged Higgs. This is the most optimistic scenario for an analysis using leptonic final states and thus $v_\Delta = 0$ is chosen as the value for the generation of this particular $H^{\pm\pm}$ sample. Additionally, this means that production of the doubly-charged Higgs is solely though pair-production mediated by the Drell-Yan process. Final-state signatures of the doubly-charged Higgs can in this case be expected to be captured by a four-lepton region, assuming none of its constituent objects are misidentified.

The relative strength of the Yukawa coupling, $h_{\ell\ell'}$ in Equation 1.36, must also be set to a particular set of values. This choice affects the relative leptonic branching fractions as well as the decay width. Upper limits have been set on them relative to the particle's mass [54]. For sample generation, the chosen value is $h_{\ell\ell'} = 0.02$, although with $h_{\tau\tau'} = h_{\ell\tau'} = 0$. This is a scenario where no tau leptons are created by $H^{\pm\pm}$ decays, which is another optimistic assumption for a model-independent search studying only light leptons.

Two specific mass points for the $H^{\pm\pm}$ are used. These are 300 GeV and 500 GeV, corresponding to the lowest mass probed by the reference analysis and (roughly) to the current observed limits. Cross sections for these mass points have been calculated at leading order (LO) and next-to-leading order (NLO) for Drell-Yan production. These

Model	Mass [GeV]	σ_{LO} [fb]	σ_{NLO} [fb]
Type-III Seesaw	400	137	180
	700	10.5	13.9
$H^{\pm\pm}$	300	18.6	23.3
	500	2.01	2.49

Table 7.8: Calculated cross-sections at leading order (LO) and next-to-leading order (NLO) used for sample generation for potential Type-III seesaw heavy neutrino models [207] and for Doubly-charged Higgs left-right symmetric models [51]. The Type-III seesaw cross-section σ_{NLO} includes next-to-leading logarithmic (NLL) accuracy, and the Doubly-charged Higgs cross-section σ_{NLO} is the sum of left-handed and right-handed production, $H_L^{\pm\pm}$ and $H_R^{\pm\pm}$.

cross-sections are given in table 7.8. The NLO cross-section is used. The reported value is the sum of the cross sections of the doubly-charged Higgs coupling to left-handed and right-handed leptons, respectively $H_L^{\pm\pm}$ and $H_R^{\pm\pm}$[3], the relative cross section ratio between the two being 2.3 due to different couplings to the Z-boson.

Some notable points of comparison between the model-independent search and the reference analysis are:

- The reference analysis also includes multilepton regions containing 3 and 4 lepton final states. Results are available for a 4 lepton region signal-region only fit which considers an inclusive four-lepton final state.
- The reference analysis studies multiple scenarios of relative branching fractions for the different leptonic decay modes. However, perusing the results of the reference analysis it is evident that the expected limits are insensitive to this detail. Because of this, only one branching ratio configuration is presented here, namely one of equal branching fractions for the three leptonic decay modes.
- Results are presented by the reference analysis using only 2015 and 2016 ATLAS data, for a total integrated luminosity of 36.1 fb^{-1}. For a meaningful comparison the full run 2 limits of this analysis will need to be scaled accordingly.

7.5.3 Obtaining cross-section limits

To obtain the best cross-section limits, the best signal region for measuring a particular model must first be determined. The signal contamination in the control regions must be sufficiently small so that it is negligible compared to the standard model backgrounds, and there must be at least one signal region that contains a significant abundance of predicted signal events relative to background. To verify this, the event yields of the tested models has been calculated using the cross-sections given in Table 7.8. The results of this process are given in Table 7.9 for the Type-III seesaw model, and Table 7.10 for the Doubly-charged Higgs model.

[3]Summing these cross-sections implicitly assumes the $H_L^{\pm\pm}$ and $H_R^{\pm\pm}$ to be of equal mass, which is not a requirement motivated by theory. However this detail is irrelevant when comparing cross-section limits of this analysis with other analyses.

Region	$E_{\mathrm{T}}^{\mathrm{miss}}$ (GeV)	Total Bkg.	Signal M = 400 GeV	$S/(S+B)$ (%)	Signal M = 700 GeV	$S/(S+B)$ (%)
Fakes Validation	-	1956 ± 109	5.03 ± 0.15	0.256	0.26 ± 0.01	0.0135
Off-Z Validation	-	511 ± 23	16.3 ± 0.3	3.09	1.04 ± 0.01	0.202
WZ CR	-	6759 ± 413	11.3 ± 0.2	0.167	0.57 ± 0.01	0.00844
ZZ CR	-	803 ± 62	0.92 ± 0.04	0.114	0.06 ± 0.00	0.00756
3ℓ, On-Z	< 50	2815 ± 190	4.59 ± 0.14	0.163	0.17 ± 0.01	0.00586
3ℓ, On-Z	> 50	5596 ± 723	132 ± 0	2.32	12.6 ± 0.1	0.225
3ℓ, Off-Z	< 50	1800 ± 81	25.6 ± 0.3	1.4	0.79 ± 0.01	0.0438
3ℓ, Off-Z	> 50	1973 ± 152	298 ± 1	13.2	29.4 ± 0.1	1.47
4ℓ, On-Z	< 50	194 ± 11	5.18 ± 0.07	2.6	0.16 ± 0.00	0.0834
4ℓ, On-Z	> 50	89.9 ± 9.8	41.9 ± 0.2	31.8	4.15 ± 0.01	4.41
4ℓ, Off-Z	-	39.9 ± 2.6	13.9 ± 0.1	25.8	1.40 ± 0.01	3.39

Table 7.9: Event counts for the sum of background and the Type-III seesaw samples at $M_L = 400$, 700 GeV, including all uncertainties, given for the control regions and each signal region. Event counts are given prior to the separation into mass bins and are meant to give an overview of the relative abundance of signal in each region. Also presented is the ratio of signal events over signal + background events, $S/(S+B)$, expressed as a percentage.

Region	$E_{\mathrm{T}}^{\mathrm{miss}}$ (GeV)	Total Bkg.	Signal M = 300 GeV	$S/(S+B)$ (%)	Signal M = 500 GeV	$S/(S+B)$ (%)
Fakes Validation	-	1956 ± 109	0.47 ± 0.08	0.0239	0.02 ± 0.00	0.000865
Off-Z Validation	-	512 ± 23	45.0 ± 0.7	8.09	3.09 ± 0.04	0.6
WZ CR	-	6760 ± 413	1.21 ± 0.13	0.018	0.04 ± 0.01	0.000619
ZZ CR	-	803 ± 62	0.13 ± 0.04	0.016	0.00 ± 0.00	0
3ℓ, On-Z	< 50	2815 ± 190	1.62 ± 0.15	0.0575	0.08 ± 0.01	0.00273
3ℓ, On-Z	> 50	5596 ± 723	17.7 ± 0.5	0.315	1.06 ± 0.04	0.0189
3ℓ, Off-Z	< 50	1233 ± 58	167 ± 1	11.9	9.56 ± 0.06	0.769
3ℓ, Off-Z	> 50	1745 ± 139	717 ± 2	29.1	93.3 ± 0.2	5.07
4ℓ, On-Z	< 50	194 ± 11	32.0 ± 0.5	14.1	1.21 ± 0.00	0.617
4ℓ, On-Z	> 50	90.0 ± 9.8	16.4 ± 0.3	15.4	1.20 ± 0.01	1.32
4ℓ, Off-Z	-	40.0 ± 3.5	1122 ± 2	96.6	130 ± 0	76.5

Table 7.10: Event counts for the sum of background and the Doubly-charged Higgs samples at $M_L = 300$, 500 GeV, including all uncertainties, given for the control regions and each signal region. Event counts are given prior to the separation into mass bins and are meant to give an overview of the relative abundance of signal in each region. Also presented is the ratio of signal events over signal + background events, $S/(S+B)$, expressed as a percentage.

Model	Mass [GeV]	best single SR	Used Mass Bin	σ^{95}_{exp} [fb]	σ^{95}_{obs} [fb]
Type-III Seesaw	400	3ℓ, Off-Z, $E_{\text{T}}^{\text{miss}} > 50$ GeV	> 600 GeV	41^{+17}_{-11}	28
	400	3ℓ, Off-Z, $E_{\text{T}}^{\text{miss}} > 50$ GeV	> 400 GeV	34^{+13}_{-9}	29
	700	3ℓ, Off-Z, $E_{\text{T}}^{\text{miss}} > 50$ GeV	> 600 GeV	12^{+5}_{-3}	8.8
$H^{\pm\pm}$	300	4ℓ, Off-Z	> 400 GeV	$0.18^{+0.08}_{-0.05}$	0.12
	500	4ℓ, Off-Z	> 400 GeV	$0.16^{+0.07}_{-0.05}$	0.11

Table 7.11: The best found exclusion limits, both expected and observed, for selected BSM comparison models using the single signal region with most stringent limits. Includes the selected signal region mass bin, and the expected and observed cross-section limit, for both mass points of both models. For the Type-III seesaw 400 GeV signal, it also includes a combination of two mass adjacent bins, which further improves the expected limits.

By studying these tables it can be established which of the signal regions of this analysis is most sensitive to each model. The best signal region for distinguishing the Type-III seesaw models is **3ℓ, Off-Z, $E_{\text{T}}^{\text{miss}} > 50$**. For the Doubly-charged Higgs the best signal region is **4ℓ, Off-Z**. Figures showing the pre-fit invariant mass distributions with the (scaled) signal distributions overlaid are shown for these signal regions in Figures 7.29 and 7.30. The best cross-section limits using only a single signal region mass bin of the model-independent analysis have been gathered in Table 7.11. The limits obtained in this table are compared with the Type-III seesaw search [185] and with the doubly-charged Higgs search [52].

It should be noted that for the Type-III seesaw comparison, a combination of two mass bins is used for the $M_L = 400$ GeV signal. It was noted that two adjacent mass bins (400-600 GeV and >600 GeV) of the 3ℓ, off-Z, $E_{\text{T}}^{\text{miss}} > 50$ GeV signal region both had good sensitivity to this particular signal, and that the expected limit could be improved by combining these signal regions into a single region. It should also be noted that the expected limits for the dedicated doubly-charged Higgs analysis were obtained using only the 2015 and 2016 ATLAS data, corresponding to an integrated luminosity of 36 fb^{-1}. The additional data available in the full run-2 dataset gives this analysis a relative advantage.

Overall, the precision of the model-independent analyses, while not identical, is comparable to that of a specifically designed analysis. It is to be expected that the model-independent search is less sensitive than targeted searches, but the fact that it is not much less sensitive, compounded with the advantage of rapid deployment towards arbitrary models, proves that this analysis holds promise for a quick assessment of the sensitivity to other models.

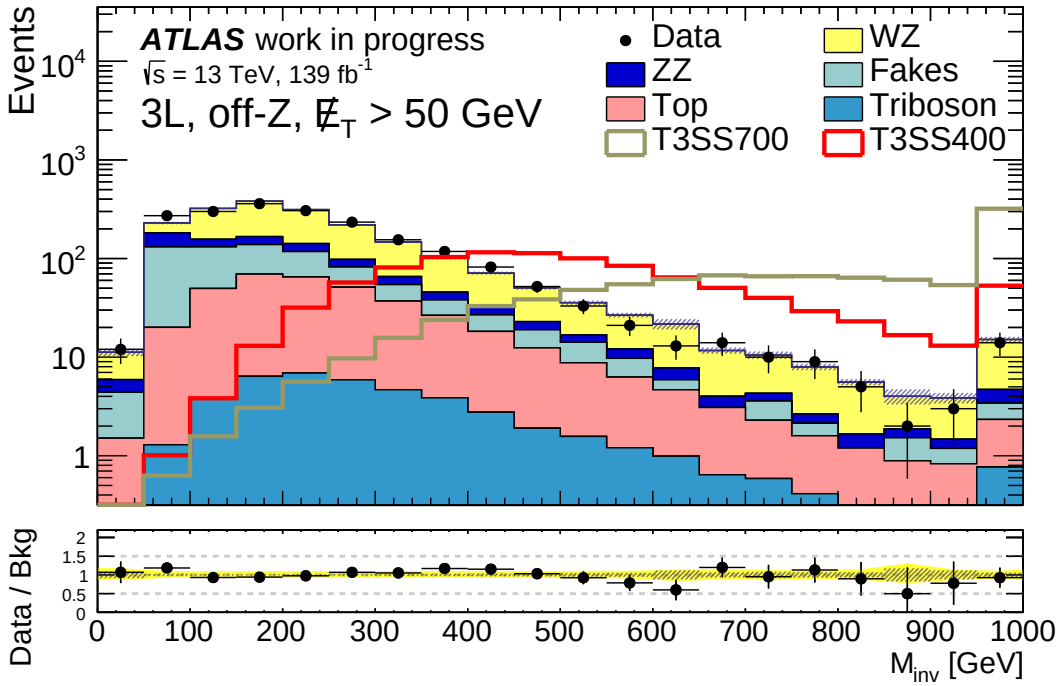

Figure 7.29: M_{inv} distribution in the 3ℓ off-Z signal region with $E_{\mathrm{T}}^{\mathrm{miss}} > 50$ GeV where the scaled distribution of Type-III seesaw models is overlaid. These signal distributions are scaled upwards to have a total contribution equal to half the total background contribution. The mass points shown are 400 GeV (T3SS400) and 700 GeV (T3SS700). Stat uncertainties are given by the gray hatched area, while the total uncertainty (stat+syst) is given as the solid yellow area.

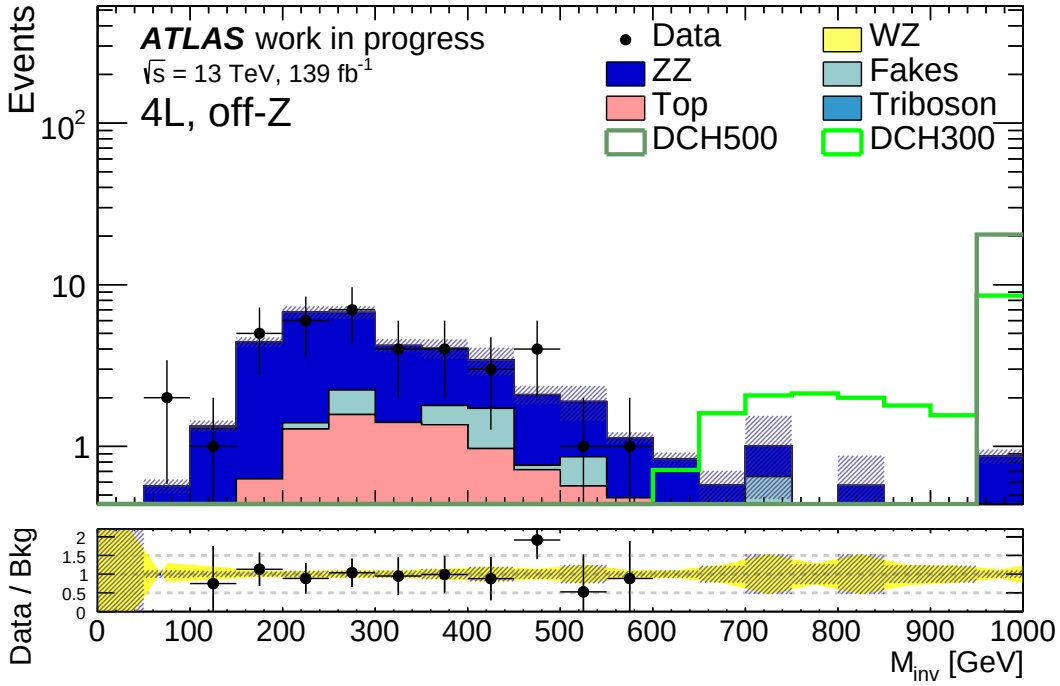

Figure 7.30: M_{inv} distribution in the 4ℓ off-Z signal region where the scaled distribution of doubly-charged Higgs models is overlaid. These signal distributions are scaled upwards to have a total contribution equal to half the total background contribution. The mass points shown are 300 GeV (DCH300) and 500 GeV (DCH500). Stat uncertainties are given by the gray hatched area, while the total uncertainty (stat+syst) is given as the solid yellow area.

Conclusion

This thesis presents a model-independent search for potential indicators of physics beyond the Standard Model. The analysis tests data collected by the ATLAS detector during run 2 of the Large Hadron Collider at CERN, consisting of 139 fb^{-1} of data at $\sqrt{s} = 13$ TeV. This analysis specifically targets final states with 3 or 4 light leptons. Multiple signal regions are considered, which separate events based on criteria such as the number of leptons in the event, the presence of a lepton pair originating from a Z-boson, the missing energy and the invariant mass (Chapter 4). Each of these signal regions is tested independently.

Monte Carlo simulation techniques are used to estimate the irreducible background originating from Standard Model processes capable of producing final states with three or more leptons. Chief among these are the production of two vector bosons, either WZ or ZZ, that decay leptonically, although processes due to top quarks with associated vector boson production and Higgs bosons decaying leptonically also contribute. Estimation of the total background due to the main Standard Model processes is facilitated by control regions. Control regions determine the normalization of the Standard Model process which they target, and furthermore impose constraints on the additional nuisance parameters that enter in the analysis.

Additional Standard Model contributions where at least one lepton is produced by detector misidentification of traversing hadrons or non-prompt semileptonic decays of heavy hadronic particles, so-called fake leptons, are also estimated using data driven techniques (Chapter 5). This is the fake factor method. The fake factor is the ratio between the efficiencies of two different selection criteria and can be used to extrapolate contributions due to fake leptons from one region to an adjacent but orthogonal one. Fake factors are estimated using dedicated single-lepton regions, then applied to the regions of interest.

In total, data for 22 signal regions have been considered and their compatibility with the Standard Model has been checked. The significance threshold was raised to account for the increased probability of statistical fluctuations due to multiple regions being probed. No major deviations were uncovered (Chapter 7). In the absence of potential signals and without a specific model to constrain, expected and observed limits were expressed as 95% CL visible cross-section limits (σ_{vis}). With these σ_{vis} values, one is able to reinterpret the results of the analysis in the context of any particular signal, assuming its efficiency and acceptance with respect to the used event selection is known.

For the purpose of comparison, the analysis is reinterpreted using simulated signal models that have been previously studied by dedicated analyses. The models tested are the Type-III seesaw mechanism, assuming an additional heavy lepton and heavy neutrino of equal mass being produced by a heavy W-boson, and a Higgs triplet model hypothesizing an additional Higgs boson with charge $q = \pm 2$ being pair produced through Drell-Yan production. Expected limits from these analyses using two possible particle masses per theory were compared with the expected limits yielded by this analysis. For the Type-III

seesaw model, expected limits of $\sigma^{95}_{exp} = 41^{+17}_{-11}$ fb for a heavy-lepton mass $M = 400$ GeV, and $\sigma^{95}_{exp} = 12^{+5}_{-3}$ fb for a heavy-lepton mass $M = 700$ GeV are found by this analysis. For the doubly-charged Higgs model, expected limits are $\sigma^{95}_{exp} = 0.18^{+0.08}_{-0.05}$ fb for a $H^{\pm\pm}$ mass of $M = 300$ GeV, and $\sigma^{95}_{exp} = 0.16^{+0.07}_{-0.05}$ fb for a $H^{\pm\pm}$ mass $M = 500$ GeV. Although the limits obtained by this analysis are not superior to the reference analyses, they are nevertheless sufficiently comparable to motivate one of the benefits of a general analysis framework such as the one shown in this thesis. Model-independent searches can be reinterpreted swiftly to set limits on a large number of different models and can reveal indications of potential new physics beyond the Standard Model in large amounts of data.

The analysis as it has been presented offers opportunities to quickly test physics models that produce final states containing three or four light leptons. Because a large amount of data can be investigated simultaneously, the development of this model-independent search can find indicators of or set limits on many regions of the phase space that may otherwise be overlooked by dedicated analyses. One hopes that future analyses looking to explore this phase space will find it beneficial as a sensitivity benchmark to help decide whether or not these final states are worth exploring for a particular exotics physics model.

There are still many avenues that can be taken that would improve and expand the distinguishing capabilities of the model-independent analyses presented here. Many additional ideas have been proposed, considered, and explored, but ultimately not included into this version of the analysis. Should statistical tools, such as the generation of many pseudo-datasets using the probability distribution function of the tested hypothesis, be added to analyze regions where the total background prediction is too small for the asymptotic assumption to be valid, additional mass bins of $M_{\text{inv}} > 800$ GeV can be added to all signal regions to test for high-mass particles with increased precision. These statistical tools would also allow for signal regions with five or more leptons to be probed. Additionally, dedicated regions with jets originating from b-hadron decays have been considered by this analysis but ultimately not included due to an inability to validate the fake prediction in these regions. Ensuring the proper functioning of the fake background in this region would enable these additional signal regions, providing increased precision to theories which include production of third generation quarks. Finally, the precision of all signal regions can be improved by additionally considering hadronically decaying τ leptons.

In conclusion, the model-independent search already offers a promising framework to rapidly test many physics models, and future developments would be sure to expand this selection, offering more detection capability for an ever-growing number of competing physical theories.

Appendices

Appendix A

Fake Composition Plots

This Appendix provides a complete overview of plots of the multiple regions from which fake factors are extracted. These regions shown in these plots are separated based on lepton flavor, pseudorapidity range, and the presence of a b-jet. The leptons are then further subdivided according to their status as an ID or Anti-ID leptons, the definitions of which are discussed in Chapter 5. The plots show a transverse momentum distribution with bins of equal size (leftmost plots) and according to the determined fake factor bins (middle plots) as well as the pseudorapidity distribution (right). Figures A.1 and A.2 show the fake factor extraction regions for electrons, while Figure A.3 shows these regions for the muons.

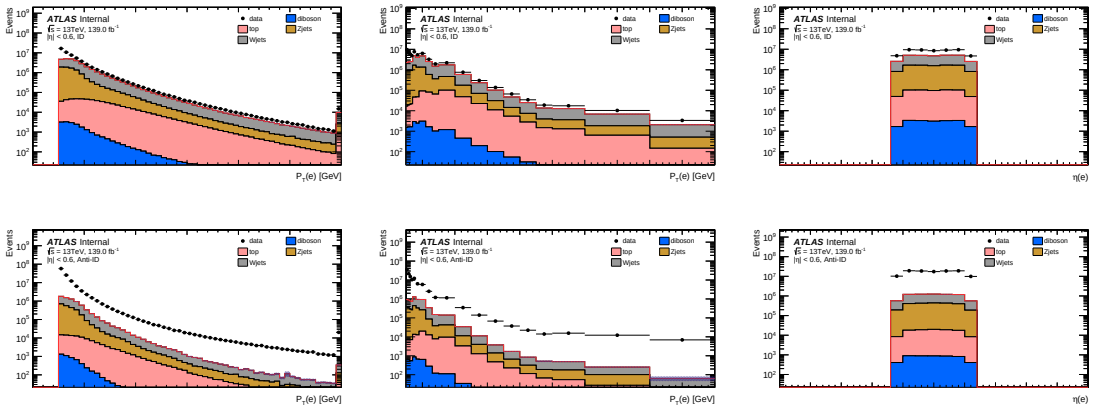

(a) $0.0 < \eta < 0.6$ electron ID (top) and anti-ID (bottom) selection

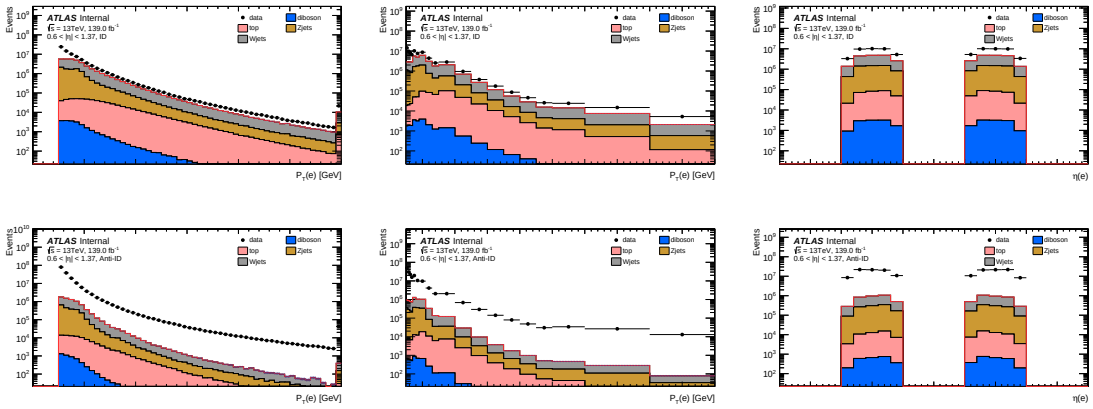

(b) $0.6 < \eta < 1.37$ electron ID (top) and anti-ID (bottom) selection

Figure A.1: All the electron fake regions according to their corresponding fake factor bins for events with $\eta < 1.37$, featuring the electron transverse momentum distributions binned evenly (left) and binned according to fake factor bins (middle) and the pseudorapidity (η) distribution (right).

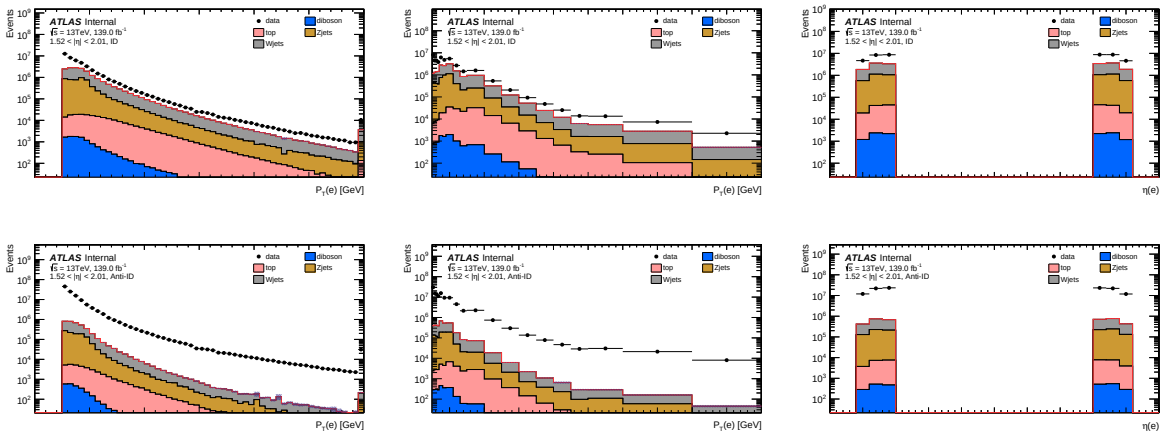

(a) $1.52 < \eta < 2.01$ electron ID (top) and anti-ID (bottom) selection

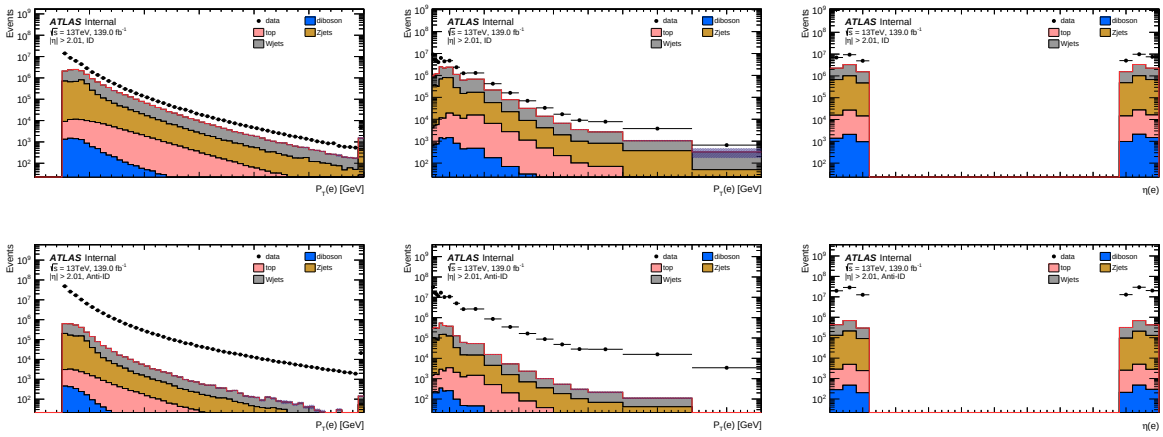

(b) $1.52 < \eta < 2.01$ electron ID (top) and anti-ID (bottom) selection

Figure A.2: All the electron fake regions according to their corresponding fake factor bins for events with $\eta > 1.52$, featuring the electron transverse momentum distributions binned evenly (left) and binned according to fake factor bins (middle) and the pseudorapidity (η) distribution (right).

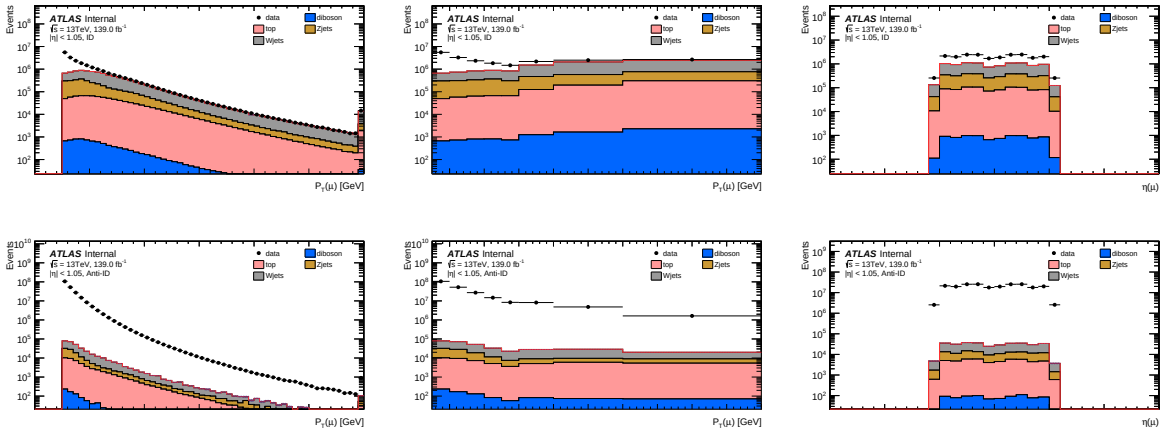

(a) $0.0 < \eta < 1.05$ muon ID (top) and anti-ID (bottom) selection

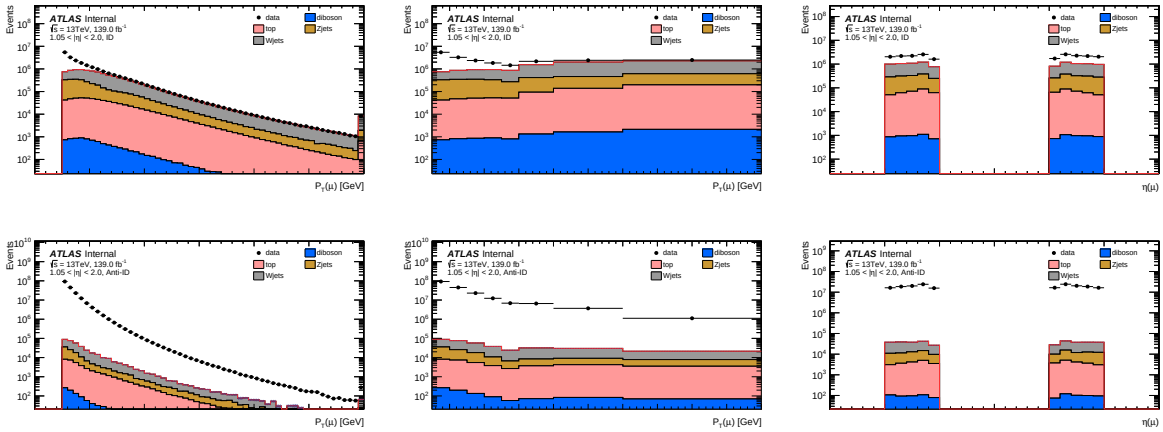

(b) $1.05 < \eta < 2.0$ muon ID (top) and anti-ID (bottom) selection

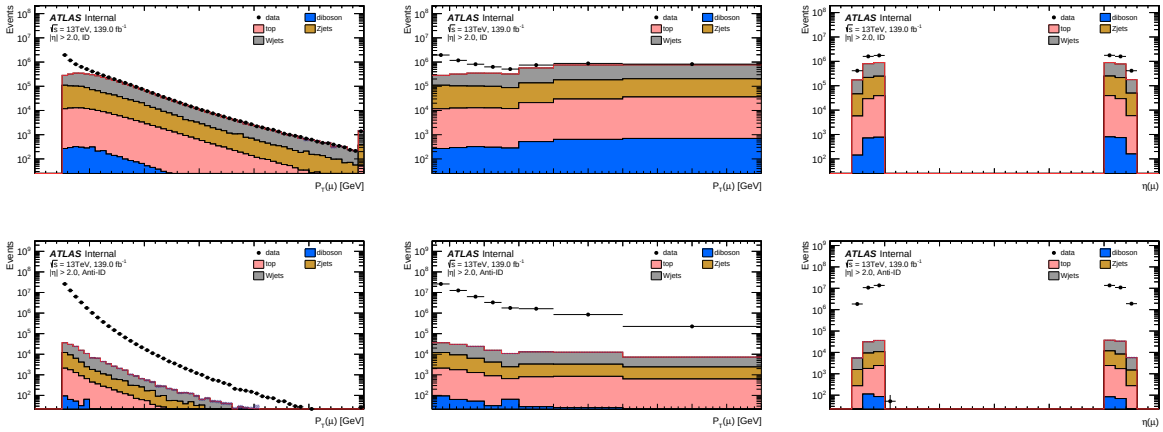

(c) $2.0 < \eta < 2.5$ muon ID (top) and anti-ID (bottom) selection

Figure A.3: All the muon fake regions for events according to their corresponding fake factor bins, featuring the muon transverse momentum distributions binned evenly (left) and binned according to fake factor bins (middle) and the pseudorapidity (η) distribution (right).

Appendix B

Four lepton, on-Z excess breakdown

Slight excesses post-fit were noticed in the 4ℓ, on-Z regions, both for $E_{\mathrm{T}}^{\mathrm{miss}} < 50$ GeV and $E_{\mathrm{T}}^{\mathrm{miss}} > 50$ GeV (see Section 7.3). These excesses are by themselves not significant (Z = 1.09 for $E_{\mathrm{T}}^{\mathrm{miss}} < 50$ GeV and Z = 1.80 for $E_{\mathrm{T}}^{\mathrm{miss}} > 50$ GeV). However, the regions were nevertheless studied more closely to ensure the proper functioning of the fitting algorithm and for the benefit of future analyses studying this region and/or using the model-independent analysis framework. The results of this breakdown are given in this appendix.

Throughout this section, the **excess region** is defined as the 4ℓ, on-Z region with any $E_{\mathrm{T}}^{\mathrm{miss}}$ value. Uncertainties given in plots are statistical only. The background contributions given here (triboson, ZZ, top, fakes) are identical to those of the nominal analysis, with one addition: the tWZ sample was added to test if this could explain the missing contribution. This sample is generated at NLO using the MadGraph5_aMC@NLO v2.3.3 [215] interfaced to Pythia8.210. The DR1 scheme was applied to veto ttZ events from this sample[216]. Select plots in this section show the top contribution broken down into its constituent processes for clarity.

Invariant mass plots of these regions are given in Figure B.1. No distinct features of the excess stand out in this plot, apart from a larger excess around $M_{\mathrm{inv}} \approx 330$ GeV when $E_{\mathrm{T}}^{\mathrm{miss}} < 50$ GeV. Figure B.2 shows the dilepton mass of the on-Z lepton pair of the event. Here a distinct asymmetry is present in the $E_{\mathrm{T}}^{\mathrm{miss}} > 50$ GeV region, with a clear excess of data for masses below the Z boson mass compared to the background, and a deficit at dilepton masses above the Z boson mass. Figure B.3 shows the dilepton mass of the **off-Z** lepton pair (the two remaining leptons of the event that are not used to form the on-Z lepton pair), which shows a similar asymmetry. Figure B.4 shows the $E_{\mathrm{T}}^{\mathrm{miss}}$ spectrum of the entire excess region. Here it can be seen that the excess is primarily visible at $E_{\mathrm{T}}^{\mathrm{miss}} > 20$ GeV.

Figures show far do not demonstrate anything that is not easily explained by statistical fluctuations. However, when the lepton flavor is considered, as is done in Figure B.5 for the excess region, showing the amount of electrons in the event. From this plot it becomes clear that the excess is especially prominent for $eee\mu$ and $e\mu\mu\mu$ events because the background prediction is low in this region.

Various processes can cause $eee\mu$ and $e\mu\mu\mu$ final states in the 4 lepton, on-Z region, such as $Z(\to \tau\tau \to \ell\ell)Z(\to \ell\ell)$, $t\bar{t}Z$, tWZ or events with three prompt and one fake leptons (such as WZ + fake). ZZ processes with leptonically decaying taus have been included in the ZZ background, as has been confirmed by the PMG Weak Boson conveners and tested by means of truth studies (looking at events with two truth ν_τ). $t\bar{t}Z$ has also been

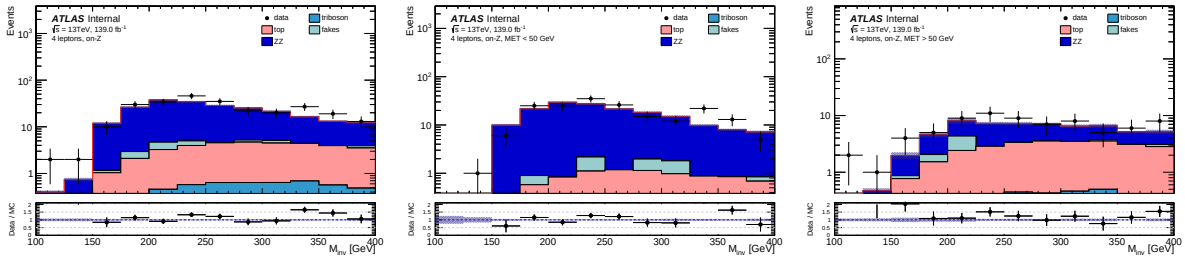

(a) All $E_{\mathrm{T}}^{\mathrm{miss}}$ **(b)** $E_{\mathrm{T}}^{\mathrm{miss}} < 50$ GeV **(c)** $E_{\mathrm{T}}^{\mathrm{miss}} > 50$ GeV

Figure B.1: Invariant Mass distributions for the 4 lepton, on-Z excess regions.

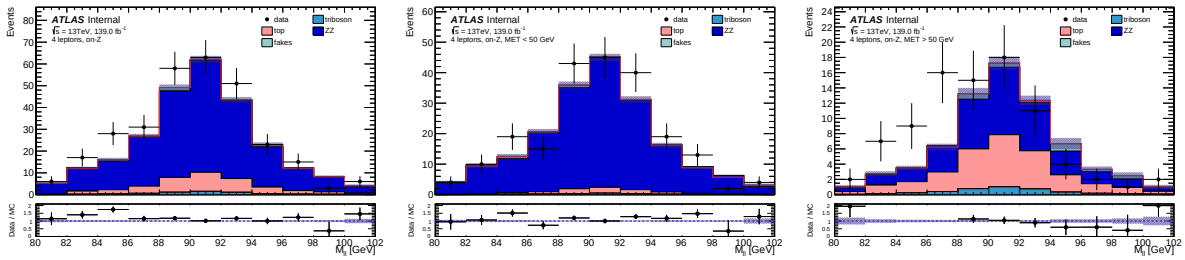

(a) All $E_{\mathrm{T}}^{\mathrm{miss}}$ **(b)** $E_{\mathrm{T}}^{\mathrm{miss}} < 50$ GeV **(c)** $E_{\mathrm{T}}^{\mathrm{miss}} > 50$ GeV

Figure B.2: Dilepton Mass distributions for the 4 lepton, on-Z excess regions.

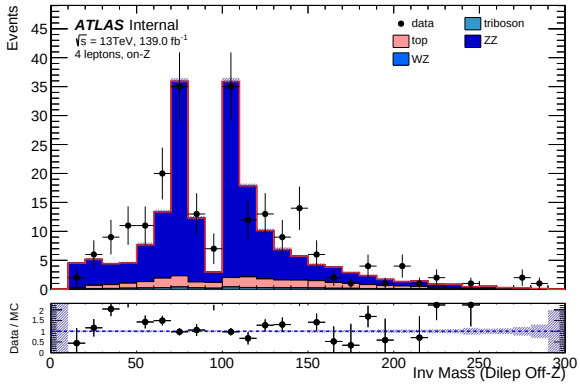

Figure B.3: Dilepton mass distribution of the *off-Z* lepton pair for the 4 lepton, on-Z excess region (any $E_{\mathrm{T}}^{\mathrm{miss}}$ value).

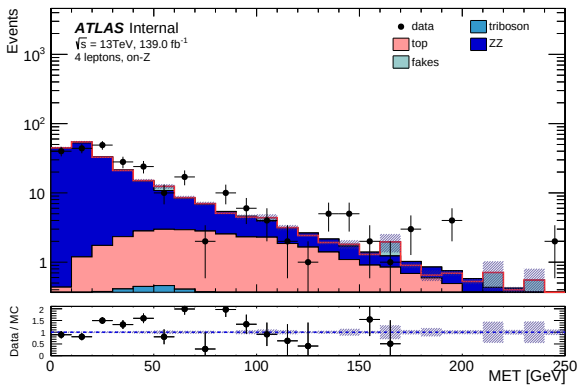

Figure B.4: Missing transverse energy distributions for the 4 lepton, on-Z excess region.

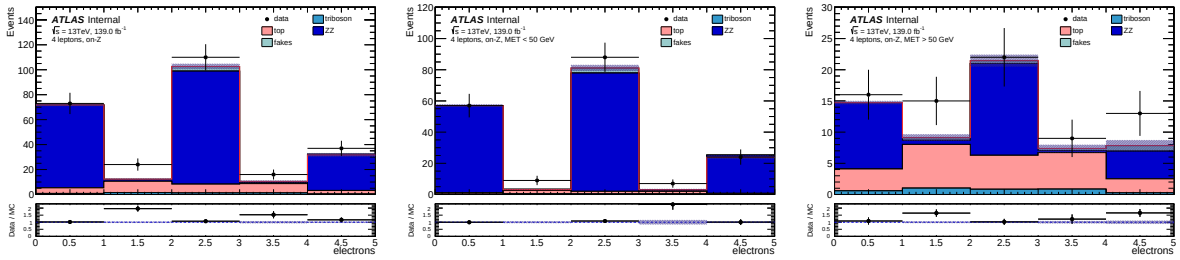

(a) All $E_{\mathrm{T}}^{\mathrm{miss}}$ **(b)** $E_{\mathrm{T}}^{\mathrm{miss}} < 50$ GeV **(c)** $E_{\mathrm{T}}^{\mathrm{miss}} > 50$ GeV

Figure B.5: Electron multiplicity distributions for the 4 lepton, on-Z excess regions.

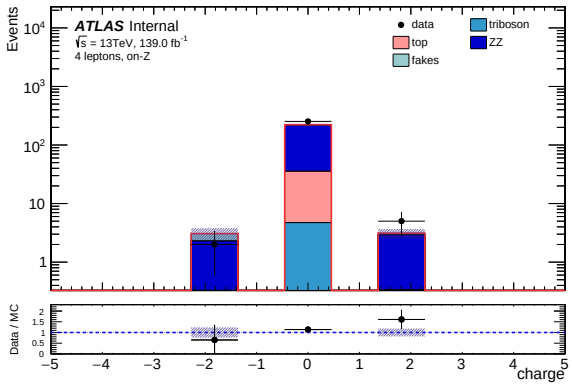

Figure B.6: Net charge distribution of all leptons in the event for the 4 lepton, on-Z excess region (when the entire $E_{\mathrm{T}}^{\mathrm{miss}}$ spectrum is considered, combining the $E_{\mathrm{T}}^{\mathrm{miss}} < 50$ GeV and $E_{\mathrm{T}}^{\mathrm{miss}} > 50$ GeV regions).

included. It is possible to exclude fake leptons as an option by looking at the net charge q of all leptons in the event. For fake events, there would be no preference for $q = 0$ over $q = \pm 2$. From the net charge distribution given in Figure B.6, we can see that this is not the case. The excess is prominent at $q = 0$.

The *mixed-flavor region* is defined as the region with either $eee\mu$ or $e\mu\mu\mu$ final states, 1 on-Z pair, and any $E_{\mathrm{T}}^{\mathrm{miss}}$ value. This region is shown with the top contributions given individually. To test if the excess is caused by tWZ events, this sample (which was not used in the nominal analysis shown in this thesis) has been added in this appendix. Figure B.7 shows the invariant mass and dilepton mass of the on-Z lepton pair. It becomes clear that the tWZ process is not sufficient to fill the gap of the excess. Figure B.8 shows the jet and b-jets (jets which originate due to the decay of hadrons containing a b-quark) multiplicity of this region. From this figure in particular it becomes clear that the excess is primarily visible in events with zero b-jets.

To further investigate the possibility of potential missing processes associated with top quarks, an additional b-tagging working point was considered[1]. The previous plots used a 77% efficiency working point. This b-jets multiplicity distribution was compared with the 85% efficiency working point. The plot showing the distribution at this efficiency is shown in Figure B.9. Using this working point, a few data events acquire an additional jet that is considered b-tagged compared to the nominal working point. However, this shift does not immediately open any other top-related processes for consideration.

[1] b-tagging working points are different algorithm configurations featuring different acceptance and rejection rates for candidate b-jets.

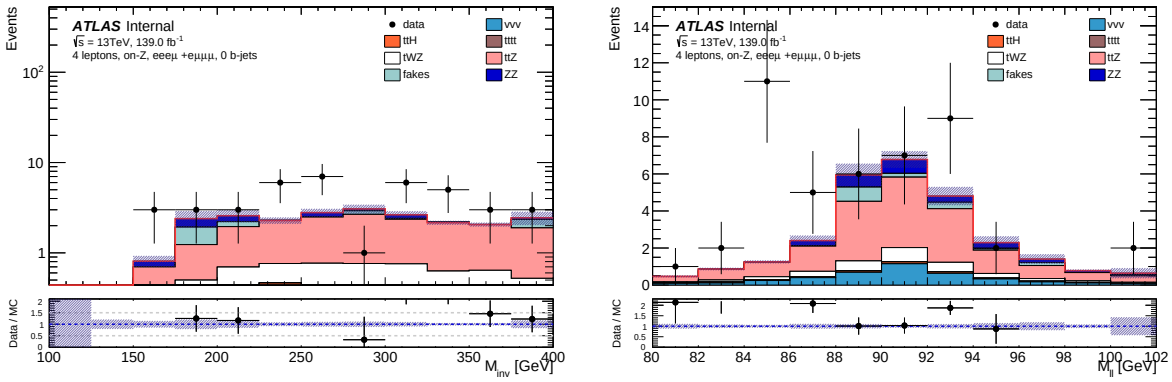

Figure B.7: Distributions of the invariant mass (left) and the dilepton mass of the on-Z lepton pair (right) for the 4 lepton, on-Z excess region considering specifically $eee\mu$ or $e\mu\mu\mu$ final states and the entire $E_{\mathrm{T}}^{\mathrm{miss}}$ spectrum.

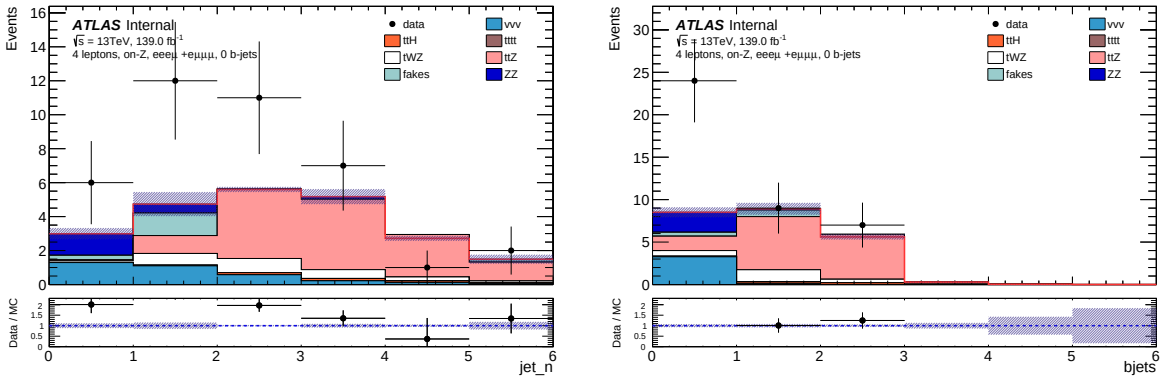

Figure B.8: Distributions of the jet multiplicity (left) and the amount of b-jets (right) for the 4 lepton, on-Z excess region considering specifically $eee\mu$ or $e\mu\mu\mu$ final states and the entire $E_{\mathrm{T}}^{\mathrm{miss}}$ spectrum.

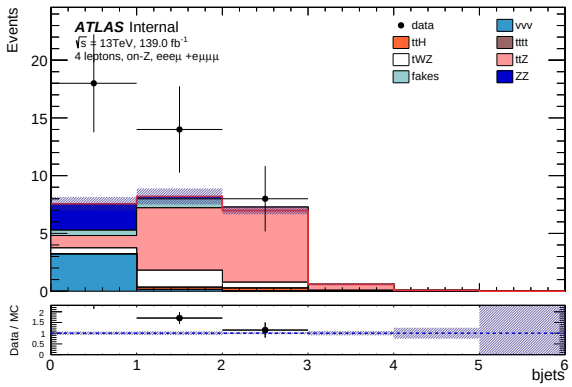

Figure B.9: Distributions of the amount of b-jets for the 4 lepton, on-Z excess region considering specifically $eee\mu$ or $e\mu\mu\mu$ final states and the entire $E_{\mathrm{T}}^{\mathrm{miss}}$ spectrum when using the 85% efficiency working point for the b-tagging algorithm.

In addition, the following tests have been performed which have been confirmed to **not** fill the excess:

- Swapping out the NLO *on-shell* triboson contributions that do *not* include fully leptonic off-shell VH processes, with the LO *on-shell + off-shell* triboson contributions that do include these processes.
- Truth studies have confirmed that the ZZ contribution *does* include the $Z(\to \tau\tau \to \ell\ell)Z(\to \ell\ell)$ contribution (where both τ leptons decay to lighter leptons. The total event yield due to these events is low because leptonically decaying taus lead to leptons that generally have $p_{\mathrm{T}} < 25$ GeV
- It was tested if some of the electrons or muons in the event were considered overlapping with a b-tagged jet. In this scenario, a jet track would be both b-tagged by the b-tagging algorithm, but ultimately removed by overlap removal in favor of the light lepton. If this could happen, it possibly indicates the presence of additional b-jets falsely identified as leptons, opening additional options of top-related processes to be considered when addressing the excess. This was tried and is **not** the case.
- A $WZ + \gamma$ sample was produced using Sherpa 2.2.5 and its event yield to the signal regions, particularly the 4ℓ, on-Z regions, was checked. It was found to be negligible (< 0.2 events predicted).
- Higgs contributions are included in the nominal backgrounds of this analysis: the $gg \to ZZ$ sample includes ggF and VBFH contributions and the triboson samples include off-shell Higgs contributions. The contributions that are missing are off-shell VH($\to ZZ$) and VH($\to \tau\tau$). Additional samples containing these contributions were produced but were found to be negligible.

The cause of the excess is currently unsolved, but may still be statistical in nature. Looking closely at $eee\mu$ or $e\mu\mu\mu$ final states which additionally have 0 b-jets leads to a large difference between data events and predicted background. The gap observed in this specific subselection may be an interesting topic for future discussion. Plots of this subregion are given in Figures B.10, B.11, B.12 and B.13.

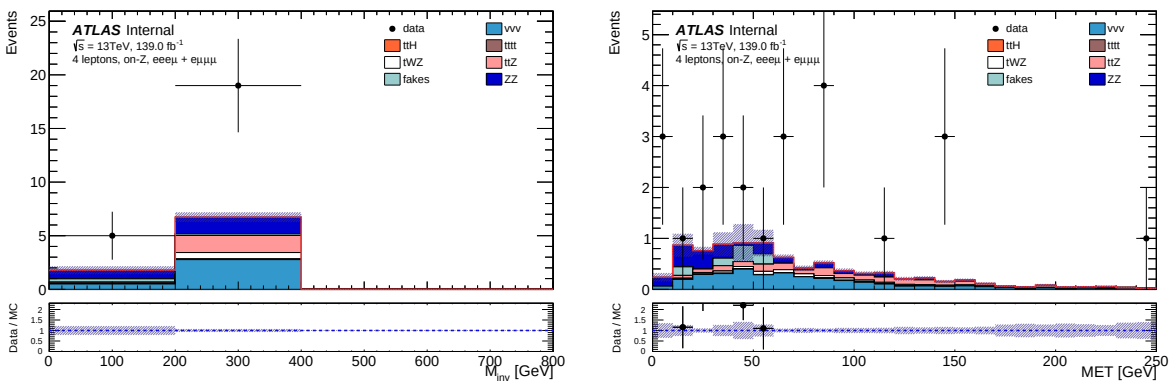

Figure B.10: Distributions of the invariant mass (left) and the missing transverse energy (right) for the 4 lepton, on-Z excess region considering specifically $eee\mu$ or $e\mu\mu\mu$ final states, the entire $E_{\mathrm{T}}^{\mathrm{miss}}$ spectrum and 0 b-jets.

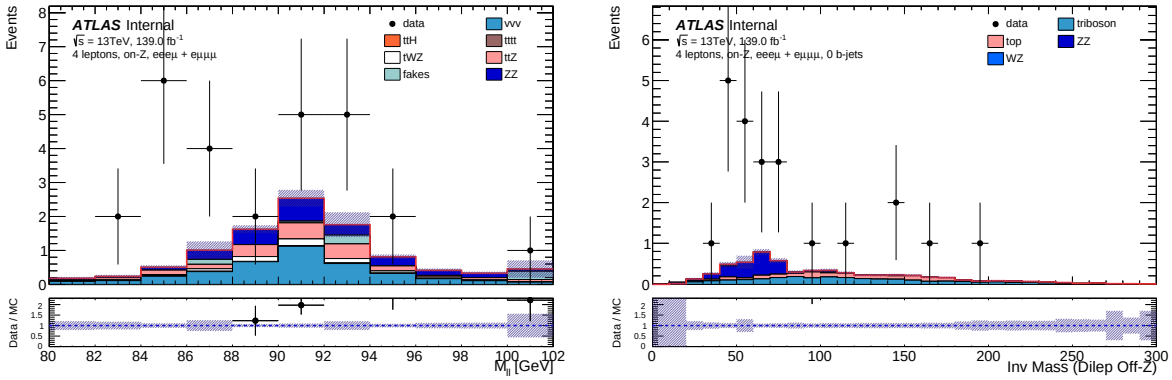

Figure B.11: Distributions of the dilepton masses for the on-Z lepton pair (left) the off-Z lepton pair (right) for the 4 lepton, on-Z excess region considering specifically $eee\mu$ or $e\mu\mu\mu$ final states, the entire $E_{\mathrm{T}}^{\mathrm{miss}}$ spectrum and 0 b-jets.

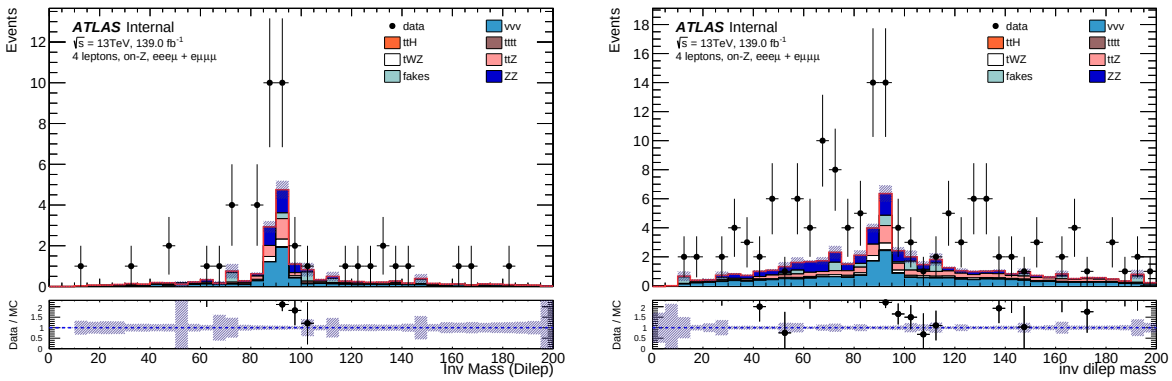

Figure B.12: Distributions of the dilepton masses for same-flavor opposite sign pairs (left) and for all possible dilepton pairs (right) for the 4 lepton, on-Z excess region considering specifically $eee\mu$ or $e\mu\mu\mu$ final states, the entire $E_{\mathrm{T}}^{\mathrm{miss}}$ spectrum and 0 b-jets.

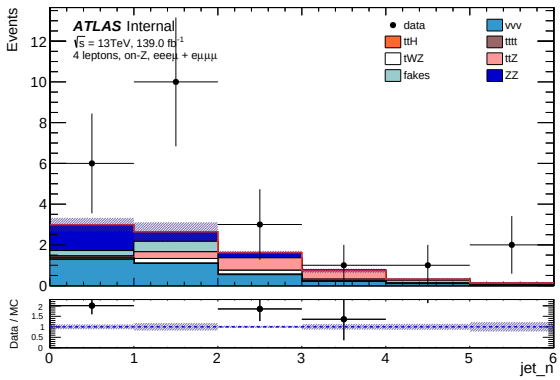

Figure B.13: Distributions of jet multiplicity for the 4 lepton, on-Z excess region considering specifically $eee\mu$ or $e\mu\mu\mu$ final states, the entire $E_{\mathrm{T}}^{\mathrm{miss}}$ spectrum and 0 b-jets.

Appendix C

Research Data Management

This thesis research has been carried out under the institute research data management policy of the Institute for Mathematics, Astrophysics and Particle Physics, as documented in `https://www.ru.nl/publish/pages/868512/imapp_rdm_policy.pdf`

- The data and the Monte Carlo simulations, using the generators described in Section 5.1, are available within the ATLAS collaboration. The full run-2 dataset will be made available under the CERN open data policy [217]; see `http://opendata.cern.ch/`
- Datasets from the data and Monte Carlo simulations are reconstructed and derived using the `athena` software framework [218]. Derived analysis object data are produced using version `21.2.77` using the exotics deviation frameworks (`EXOT12` for the nominal analysis, `EXOT19` and `EXOT22` for fake factor estimation data). Version `21.2.114` is used for the subsequent processing of the derived datasets. These datasets fall under the purview of the ATLAS collaboration.
- The `TRExFitter` [219] software package is used to perform the likelihood fit and set limits.
- *Offline* externals: ROOT Data Analysis Framework 6.16/00 [220], tabulate 0.8.3, future 0.18.2, oyaml 0.9, pathos 0.2.3, numpy 1.14.2, root-numpy 4.8.0.
- Processed datasets are stored on the Nikhef computing clusters and is available upon request. Histograms produced from processed datasets that are required to perform the statistical analysis are stored on the CERN `eos` cluster.
- Calibration and configuration code that was developed for the purpose of completing the research performed in this thesis can be obtained from `https://gitlab.cern.ch/users/pbakker/projects`.
  Docker images of the steering code are also available at `gitlab-registry.cern.ch/pbakker/multileptonanalysis`

Bibliography

[1] F. Halzen and A. Martin. *Quarks and Leptons: An Introductory Course in Modern Particle Physics*. 1984.

[2] F. Englert and R. Brout. "Broken Symmetry and the Mass of Gauge Vector Mesons". In: *Phys. Rev. Lett.* 13 (Aug. 1964), pp. 321–323.

[3] P. Higgs. "Broken Symmetries and the Masses of Gauge Bosons". In: *Phys. Rev. Lett.* 13 (Oct. 1964), pp. 508–509.

[4] J. Goldstone. "Field theories with "superconductor" solutions". In: *Nuovo Cimento* 19.CERN-TH-118 (Aug. 1960), pp. 154–164.

[5] G. 't Hooft. "Renormalizable Lagrangians for massive Yang-Mills fields". In: *Nuclear Physics B* 35.1 (1971), pp. 167–188.

[6] D. Griffiths. *Introduction to elementary particles; 2nd rev. version*. Physics textbook. New York, NY: Wiley, 2008.

[7] T. Nakano and K. Nishijima. "Charge Independence for V-particles*". In: *Progress of Theoretical Physics* 10.5 (Nov. 1953), pp. 581–582.

[8] S. Glashow. "Partial-symmetries of weak interactions". In: *Nuclear Physics* 22.4 (1961), pp. 579–588.

[9] L. Boyle. *Standard Model Of Particle Physics, Most Complete Diagram*. 2014. URL: `https://commons.wikimedia.org/wiki/File:Standard_Model_Of_Particle_Physics--Most_Complete_Diagram.png`.

[10] P. Langacker. *The standard model and beyond; 2nd ed.* High energy physics, cosmology and gravitation. CRC Press, July 2017.

[11] W. Cottingham and D. Greenwood. *An Introduction to the Standard Model of Particle Physics; 2nd ed.* Cambridge: Cambridge Univ. Press, 2007.

[12] P. D. Group. *Standard Model of Elementary Particles*. 2020. URL: `https://commons.wikimedia.org/wiki/File:Standard_Model_of_Elementary_Particles.svg`.

[13] ATLAS Collaboration. "Observation of a new particle in the search for the Standard Model Higgs boson with the ATLAS detector at the LHC". In: *Phys. Lett. B* 716 (2012), p. 1.

[14] CMS Collaboration. "Observation of a new boson at a mass of 125 GeV with the CMS experiment at the LHC". In: *Phys. Lett. B* 716 (2012), p. 30.

[15] R. Davis. "A review of the homestake solar neutrino experiment". In: *Progress in Particle and Nuclear Physics* 32 (1994), pp. 13–32.

[16] Y. Ashie et al. "Evidence for an Oscillatory Signature in Atmospheric Neutrino Oscillations". In: *Phys. Rev. Letters* 93.10 (Sept. 2004).

[17] K. Abe et al. "Evidence for the Appearance of Atmospheric Tau Neutrinos in Super-Kamiokande". In: *Phys. Rev. Letters* 110.18 (May 2013).

[18] Y. Fukuda et al. "Evidence for Oscillation of Atmospheric Neutrinos". In: *Phys. Rev. Letters* 81.8 (Aug. 1998), pp. 1562–1567.

[19] Q. Ahmad et al. “Direct Evidence for Neutrino Flavor Transformation from Neutral-Current Interactions in the Sudbury Neutrino Observatory”. In: *Phys. Rev. Letters* 89.1 (June 2002).

[20] “Review of Particle Physics”. In: *Phys. Rev. D* 98 (Oct. 2018), p. 030001.

[21] J. Valle. “Neutrino physics overview”. In: *Journal of Physics: Conference Series* 53 (2006), pp. 473–505.

[22] F. Couchot et al. “Cosmological constraints on the neutrino mass including systematic uncertainties”. In: *Astronomy & Astrophysics* 606 (Oct. 2017), A104.

[23] A. Carati and L. Galgani. “Faraway matter as a possible substitute for dark matter”. In: *Workshop Series of the Asociacion Argentina de Astronomia* (Jan. 2011), pp. 277–287.

[24] V. Trimble. “Existence and Nature of Dark Matter in the Universe”. In: *Annual Review of Astronomy and Astrophysics* 25.1 (1987), pp. 425–472.

[25] P. A. R. Ade et al. “Planck2015 results”. In: *Astronomy & Astrophysics* 594 (Sept. 2016), A13.

[26] J. Einasto. “Large-Scale Structure and Dark Matter Problem”. In: (2000).

[27] L. Canetti, M. Drewes, and M. Shaposhnikov. “Matter and antimatter in the universe”. In: *New Journal of Physics* 14.9 (Sept. 2012), p. 095012.

[28] A. D. Sakharov. “Violation of CP Invariance, C Asymmetry, and Baryon Asymmetry of the Universe”. In: *Soviet Journal of Experimental and Theoretical Physics Letters* 5 (Jan. 1967), p. 24.

[29] V. Kuzmin, V. Rubakov, and M. Shaposhnikov. “On anomalous electroweak baryon-number non-conservation in the early universe”. In: *Physics Letters B* 155.1 (1985), pp. 36–42.

[30] M. Kobayashi and T. Maskawa. “CP-Violation in the Renormalizable Theory of Weak Interaction”. In: *Progress of Theoretical Physics* 49.2 (Feb. 1973), pp. 652–657.

[31] S. Blanchet, D. Marfatia, and A. Mustafayev. “Examining leptogenesis with lepton flavor violation and the dark matter abundance”. In: *JHEP* 2010.11 (Nov. 2010).

[32] ATLAS Collaboration. “Search for chargino-neutralino production with mass splittings near the electroweak scale in three-lepton final states in $\sqrt{s} = 13$ TeV pp collisions with the ATLAS detector”. In: *Phys. Rev. D* 101 (Apr. 2020), p. 072001.

[33] P. Huang and Y. Ng. *Di-Higgs Production in SUSY models at the LHC*. 2019.

[34] F. del Aguila and J. Aguilar-Saavedra. “Distinguishing seesaw models at LHC with multi-lepton signals”. In: *Nuclear Physics B* 813.1-2 (May 2009), pp. 22–90.

[35] E. Jenkins, A. Manohar, and P. Stoffer. “Low-energy effective field theory below the electroweak scale: operators and matching”. In: *JHEP* 2018.3 (Mar. 2018).

[36] Y. Makeenko. “Brief introduction to Wilson loops and large N”. In: *Physics of Atomic Nuclei* 73.5 (May 2010), pp. 878–894.

[37] E. Ma. “Pathways to Naturally Small Neutrino Masses”. In: *Phys. Rev. Letters* 81.6 (Aug. 1998), pp. 1171–1174.

[38] V. Brdar et al. “Type I seesaw mechanism as the common origin of neutrino mass, baryon asymmetry, and the electroweak scale”. In: *Phys. Rev. D* 100.7 (Oct. 2019), p. 075029.

[39] P. Gu, H. Zhang, and S. Zhou. “Minimal type II seesaw model”. In: *Phys. Rev. D* 74.7 (Oct. 2006), p. 076002.

[40] R. Franceschini, T. Hambye, and A. Strumia. “Type-III seesaw mechanism at CERN LHC”. In: *Phys. Rev. D* 78.3 (Aug. 2008), p. 033002.

[41] C. Biggio and F. Bonnet. “Implementation of the type III seesaw model in FeynRules/MadGraph and prospects for discovery with early LHC data”. In: *The Eur. Phys. J. C* 72.2 (Feb. 2012).

[42] H. Baer et al. “Natural SUSY with a bino- or wino-like LSP”. In: *Phys. Rev. D* 91 (Jan. 2015), p. 075005.

[43] P. Dev, M. Ramsey-Musolf, and Y. Zhang. “Doubly-charged scalars in the type II seesaw mechanism: Fundamental symmetry tests and high-energy searches”. In: *Phys. Rev. D* 98.5 (Sept. 2018), p. 055013.

[44] J. F. Gunion et al. “Higgs bosons in left-right-symmetric models”. In: *Phys. Rev. D* 40 (Sept. 1989), pp. 1546–1561.

[45] N. Setzer and S. Spinner. “Running with triplets: How slepton masses change with doubly-charged Higgs bosons”. In: *Phys. Rev. D* 75.11 (June 2007), p. 117701.

[46] S. Bhattacharya, S. Jana, and S. Nandi. “Neutrino masses and scalar singlet dark matter”. In: *Phys. Rev. D* 95.5 (Mar. 2017), p. 055003.

[47] M. Nebot et al. “Prospects for the Zee-Babu model at the CERN LHC and low energy experiments”. In: *Phys. Rev. D* 77 (May 2008), p. 093013.

[48] H. Georgi and M. Machacek. “Doubly charged Higgs bosons”. In: *Nuclear Physics B* 262.3 (1985), pp. 463–477.

[49] N. G. Deshpande et al. “Left-right-symmetric electroweak models with triplet Higgs field”. In: *Phys. Rev. D* 44 (Aug. 1991).

[50] J. C. Pati and A. Salam. “Lepton number as the fourth "color"”. In: *Phys. Rev. D* 10 (July 1974), pp. 275–289.

[51] M. Muhlleitner and M. Spira. “Note on doubly charged Higgs boson pair production at hadron colliders”. In: *Phys. Rev. D* 68 (Dec. 2003), p. 117701.

[52] M. Muskinja et al. *Search for doubly-charged Higgs boson production in multi-lepton final states with the ATLAS detector using proton-proton collisions at* $\sqrt{s} = 13$ TeV. Tech. rep. ATL-COM-PHYS-2016-1415. Geneva: CERN, Sept. 2016.

[53] B. Dutta et al. “Exploring the doubly charged Higgs boson of the left-right symmetric model using vector boson fusionlike events at the LHC”. In: *Phys. Rev. D* 90.5 (Sept. 2014), p. 055015.

[54] V. Rentala, W. Shepherd, and S. Su. “Simplified model approach to same-sign dilepton resonances”. In: *Phys. Rev. D* 84.3 (Aug. 2011), p. 035004.

[55] K. Babu and S. Jana. “Probing doubly charged Higgs bosons at the LHC through photon initiated processes”. In: *Phys. Rev. D* 95.5 (Mar. 2017), p. 055020.

[56] T. Gleisberg et al. “Event generation with SHERPA 1.1”. In: *JHEP* 02 (2009), p. 007.

[57] D. E. Soper. “Parton distribution functions”. In: *Nuclear Physics B - Proceedings Supplements* 53.1-3 (Feb. 1997), pp. 69–80.

[58] J. Collins and E. Soper. “Parton distribution and decay functions”. In: *Nuclear Physics B* 194.3 (1982), pp. 445–492.

[59] F. Krauss. “Matrix Elements and Parton Showers in Hadronic Interactions”. In: *JHEP* 2002.08 (Aug. 2002), pp. 015–015.

[60] S. Catani et al. “QCD Matrix Elements + Parton Showers”. In: *JHEP* 11 (2001), p. 063.

[61] ATLAS Collaboration. *Multi-Boson Simulation for* 13 *TeV ATLAS Analyses*. ATL-PHYS-PUB-2017-005. 2017.

[62] ATLAS Collaboration. *ATLAS simulation of boson plus jets processes in Run 2*. ATL-PHYS-PUB-2017-006. 2017.
[63] ATLAS Collaboration. *Studies on top-quark Monte Carlo modelling with Sherpa and MG5_aMC@NLO*. ATL-PHYS-PUB-2017-007. 2017.
[64] ATLAS Collaboration. *A study of different colour reconnection settings for Pythia8 generator using underlying event observables*. ATL-PHYS-PUB-2017-008. 2017.
[65] L. Evans and P. Bryant. "LHC Machine". In: *JINST* 3 (2008), S08001.
[66] O. Bruning et al. "LHC Design Report Vol.1: The LHC Main Ring". In: (2004).
[67] O. Buning et al. "LHC Design Report. 2. The LHC infrastructure and general services". In: (2004).
[68] M. Benedikt et al. "LHC Design Report. 3. The LHC injector chain". In: (2004).
[69] ATLAS Collaboration. "Electron reconstruction and identification in the ATLAS experiment using the 2015 and 2016 LHC proton–proton collision data at $\sqrt{s} =$ 13 TeV". In: *Eur. Phys. J. C* 79 (2019), p. 639.
[70] W. W. Armstrong et al. "ATLAS: Technical proposal for a general-purpose p p experiment at the Large Hadron Collider at CERN". In: (1994).
[71] ATLAS Collaboration. "ATLAS: Letter of intent for a general purpose p p experiment at the large hadron collider at CERN". In: (1992).
[72] A. Hoecker. *Physics at the LHC Run-2 and Beyond*. Tech. rep. 2016.
[73] *Pulling together: Superconducting electromagnets*. 2020. URL: `https://home.cern/science/engineering/pulling-together-superconducting-electromagnets` (visited on 03/24/2020).
[74] CMS Collaboration. "CMS Physics Technical Design Report, Volume II: Physics Performance". In: *J. Phys G* 34 (2007), p. 995.
[75] LHCb Collaboration. "The LHCb Detector at the LHC". In: *Journal of Instrumentation* 3.08 (Aug. 2008), S08005–S08005.
[76] ALICE collaboration. "The ALICE experiment at the CERN LHC". In: *JINST* 3 (2008), S08002.
[77] *Luminosity determination in pp collisions at $\sqrt{s} = 13$ TeV using the ATLAS detector at the LHC*. Tech. rep. ATLAS-CONF-2019-021. Geneva: CERN, June 2019.
[78] ATLAS Collaboration. "Luminosity determination in pp collisions at $\sqrt{s} = 8$ TeV using the ATLAS detector at the LHC". In: *The Eur. Phys. J. C* 76 (Dec. 2016).
[79] G. Avoni et al. "The new LUCID-2 detector for luminosity measurement and monitoring in ATLAS". In: *Journal of Instrumentation* 13.07 (July 2018), P07017–P07017.
[80] W. Herr and B. Muratori. "Concept of luminosity". In: (2006).
[81] ATLAS Collaboration. *Luminosity Public Results Run 2*. 2019. URL: `https://twiki.cern.ch/twiki/bin/view/AtlasPublic/LuminosityPublicResultsRun2` (visited on 03/24/2020).
[82] M. Medrano et al. *Effective pile-up density as a measure of the experimental data quality for High-Luminosity LHC operational scenarios.* Tech. rep. CERN-ACC-2018-0003. Geneva: CERN, Jan. 2018.
[83] ATLAS Collaboration. "Measurement of the Inelastic Proton–Proton Cross Section at $\sqrt{s} = 13$ TeV with the ATLAS Detector at the LHC". In: *Phys. Rev. Lett.* 117 (2016), p. 182002.

[84] W. Buttinger. *Using Event Weights to account for differences in Instantaneous Luminosity and Trigger Prescale in Monte Carlo and Data*. Tech. rep. ATL-COM-SOFT-2015-119. Geneva: CERN, May 2015.

[85] ATLAS Collaboration. *ATLAS Data Summary*. 2018. URL: `https://atlas.web.cern.ch/Atlas/GROUPS/DATAPREPARATION/DataSummary` (visited on 03/24/2020).

[86] J. Pequenao. "Computer generated image of the whole ATLAS detector". Mar. 2008.

[87] J. Pequenao and P. Schaffner. "How ATLAS detects particles: diagram of particle paths in the detector". Jan. 2013.

[88] ATLAS Collaboration. *ATLAS Magnet System: Technical Design Report, 1*. ATLAS-TDR-6. 1997.

[89] ATLAS Collaboration. *ATLAS Central Solenoid: Technical Design Report*. ATLAS-TDR-9. 1997.

[90] ATLAS Collaboration. *ATLAS Barrel Toroid: Technical Design Report*. ATLAS-TDR-7. 1997.

[91] ATLAS Collaboration. *ATLAS End-Cap Toroids: Technical Design Report*. ATLAS-TDR-8. 1997.

[92] ATLAS Collaboration. *ATLAS Inner Detector: Technical Design Report, 1*. ATLAS-TDR-4. 1997.

[93] ATLAS Collaboration. *ATLAS Inner Detector: Technical Design Report, 2*. ATLAS-TDR-5. 1997.

[94] ATLAS Collaboration. "The ATLAS Experiment at the CERN Large Hadron Collider". In: *JINST* 3 (2008), S08003.

[95] ATLAS Collaboration. *ATLAS Insertable B-Layer Technical Design Report*. ATLAS-TDR-19. 2010. Addendum: ATLAS-TDR-19-ADD-1. 2012.

[96] ATLAS Collaboration. ATLAS-TDR-19-ADD-1. 2012.

[97] A. La Rosa. *The ATLAS Insertable B-Layer: from construction to operation*. 2016.

[98] B. Mandelli. "The Pixel Detector of the ATLAS Experiment for the Run 2 at the Large Hadron Collider". In: *Nuclear and Particle Physics Proceedings* 273-275 (2016). 37th International Conference on High Energy Physics (ICHEP), pp. 1166–1172.

[99] G. Ripellino. *The alignment of the ATLAS Inner Detector in Run-2*. 2016.

[100] M. S. Alam et al. "ATLAS pixel detector: Technical design report". In: (1998).

[101] ATLAS collaboration. "Operation and performance of the ATLAS semiconductor tracker". In: *Journal of Instrumentation* 9.08 (Aug. 2014), P08009–P08009.

[102] ATLAS collaboration. "Performance of the ATLAS Transition Radiation Tracker in Run 1 of the LHC: tracker properties". In: *Journal of Instrumentation* 12.05 (May 2017), P05002–P05002.

[103] ATLAS Collaboration. *ATLAS Calorimeter Performance: Technical Design Report*. ATLAS-TDR-1. 1996.

[104] ATLAS Collaboration. *ATLAS Liquid-Argon Calorimeter: Technical Design Report*. ATLAS-TDR-2. 1996.

[105] ATLAS Collaboration. *ATLAS Tile Calorimeter: Technical Design Report*. ATLAS-TDR-3. 1996.

[106] ATLAS Collaboration. *ATLAS Muon Spectrometer: Technical Design Report*. ATLAS-TDR-10. 1997.

[107] S. Palestini. "The muon spectrometer of the ATLAS experiment". In: *Nucl. Phys. Proc. Suppl.* 125 (2003). [,337(2003)], pp. 337–345.

[108] A. Theodoros et al. "Cathode strip chambers in ATLAS: Installation, commissioning and in situ performance". In: *IEEE Trans. Nucl. Sci.* 56 (2009), pp. 1568–1574.

[109] D. Levin et al. *Streamlined Calibration of the ATLAS Muon Spectrometer Precision Chambers*. Tech. rep. ATL-MUON-PROC-2009-010. IEEE Nuclear Science Symposium Conference, Nov. 2009.

[110] *ATLAS Approved Data Acquisitions Public Plots*. URL: `https://twiki.cern.ch/twiki/bin/view/AtlasPublic/ApprovedPlotsDAQ` (visited on 03/27/2020).

[111] ATLAS Collaboration. *The Run-2 ATLAS Trigger System*. Tech. rep. ATL-DAQ-PROC-2016-003. Geneva: CERN, Feb. 2016.

[112] ATLAS Collaboration. "Performance of the ATLAS Trigger System in 2010". In: *Eur. Phys. J. C* 72 (2012), p. 1849.

[113] ATLAS Collaboration. "Performance of the ATLAS trigger system in 2015". In: *Eur. Phys. J. C* 77 (2017), p. 317.

[114] E. Simioni. *The Topological Processor for the future ATLAS Level-1 Trigger: from design to commissioning*. 2014.

[115] S. Agostinelli et al. "GEANT4 – a simulation toolkit". In: *Nucl. Instrum. Meth. A* 506 (2003), p. 250.

[116] ATLAS Collaboration. "The ATLAS Simulation Infrastructure". In: *Eur. Phys. J. C* 70 (2010), p. 823.

[117] ATLAS Collaboration. *Track Reconstruction Performance of the ATLAS Inner Detector at $\sqrt{s} = 13$ TeV*. ATL-PHYS-PUB-2015-018. 2015.

[118] ATLAS collaboration. "Performance of the ATLAS Inner Detector Track and Vertex Reconstruction in the High Pile-Up LHC Environment". In: (Mar. 2012).

[119] T. Cornelissen et al. "Concepts, Design and Implementation of the ATLAS New Tracking (NEWT)". In: (Mar. 2007). Ed. by A. Salzburger.

[120] R. Frühwirth. "Application of Kalman filtering to track and vertex fitting". In: *Nucl. Instrum. Methods Phys. Res., A* 262.HEPHY-PUB-503 (June 1987), 444. 19 p.

[121] ATLAS collaboration. "Performance of the ATLAS track reconstruction algorithms in dense environments in LHC Run 2". In: *The Eur. Phys. J. C* 77.10 (Oct. 2017).

[122] ATLAS Collaboration. *Early Inner Detector Tracking Performance in the 2015 Data at $\sqrt{s} = 13$ TeV*. ATL-PHYS-PUB-2015-051. 2015.

[123] A. Salzburger. *The new ATLAS Track Extrapolation In a case study of a future high precision W mass measurement*. 2005. URL: `https://slideplayer.com/slide/5109805/`.

[124] G. Piacquadio, K. Prokofiev, and A. Wildauer. "Primary vertex reconstruction in the ATLAS experiment at LHC". In: *Journal of Physics: Conference Series* 119.3 (July 2008), p. 032033.

[125] ATLAS Collaboration. *Vertex Reconstruction Performance of the ATLAS Detector at $\sqrt{s} = 13$ TeV*. ATL-PHYS-PUB-2015-026. 2015.

[126] G. Borissov et al. "ATLAS strategy for primary vertex reconstruction during Run-2 of the LHC". In: *Journal of Physics: Conference Series* 664 (Dec. 2015), p. 072041.

[127] W. Waltenberger and R. Frühwirth. "Adaptive Vertex Fitting". In: *Journal of Physics G: Nuclear and Particle Physics* 34 (Nov. 2007), N343.

[128] I. Sanderswood. *Development of ATLAS Primary Vertex Reconstruction for LHC Run 3*. 2019.

[129] *Performance of primary vertex reconstruction in proton-proton collisions at $\sqrt{s}$ =7 TeV in the ATLAS experiment*. Tech. rep. ATLAS-CONF-2010-069. Geneva: CERN, July 2010.

[130] S. Pagan Griso et al. *Vertex reconstruction plots*. Apr. 2012. URL: https://atlas.web.cern.ch/Atlas/GROUPS/PHYSICS/IDTRACKING/PublicPlots/ATL-COM-PHYS-2012-474/.

[131] ATLAS Collaboration. "Electron reconstruction and identification in the ATLAS experiment using the 2015 and 2016 LHC proton–proton collision data at $\sqrt{s} = 13$ TeV". In: *The Eur. Phys. J. C* 79.8 (Aug. 2019).

[132] *Electron efficiency measurements with the ATLAS detector using the 2015 LHC proton-proton collision data*. Tech. rep. ATLAS-CONF-2016-024. Geneva: CERN, June 2016.

[133] ATLAS collaboration. "Electron efficiency measurements with the ATLAS detector using 2012 LHC proton–proton collision data". In: *The Eur. Phys. J. C* 77.3 (Mar. 2017).

[134] W. Lampl et al. *Calorimeter Clustering Algorithms: Description and Performance*. Tech. rep. ATL-LARG-PUB-2008-002. ATL-COM-LARG-2008-003. Geneva: CERN, Apr. 2008.

[135] A. Collaboration. *Improved electron reconstruction in ATLAS using the Gaussian Sum Filter-based model for bremsstrahlung*. Tech. rep. ATLAS-CONF-2012-047. Geneva: CERN, May 2012.

[136] ATLAS Collaboration. *Electron Gamma Public Collision Results*. 2020. URL: https://twiki.cern.ch/twiki/bin/view/AtlasPublic/ElectronGammaPublicCollisionResults (visited on 10/08/2020).

[137] ATLAS Collaboration. *ATLAS ElectronGamma Group*. 2019. URL: https://twiki.cern.ch/twiki/bin/view/AtlasProtected/ElectronGamma (visited on 09/26/2019).

[138] ATLAS Collaboration. "Muon reconstruction performance of the ATLAS detector in proton–proton collision data at $\sqrt{s}$ =13 TeV". In: *The Eur. Phys. J. C* 76.5 (May 2016).

[139] J. Illingworth and J. Kittler. "A survey of the hough transform". In: *Computer Vision, Graphics, and Image Processing* 44.1 (1988), pp. 87–116.

[140] Hassanein et al. *A Survey on Hough Transform, Theory, Techniques and Applications*. 2015.

[141] ATLAS Collaboration. *ATLAS Muon Selection Tool*. 2020. URL: https://twiki.cern.ch/twiki/bin/view/Atlas/MuonSelectionToolR21 (visited on 09/03/2020).

[142] ATLAS Collaboration. *Muon Performance Public Plots*. 2020. URL: https://twiki.cern.ch/twiki/bin/view/AtlasPublic/MuonPerformancePublicPlots (visited on 10/08/2020).

[143] ATLAS Collaboration. *Muon Trigger Public Results*. 2020. URL: https://twiki.cern.ch/twiki/bin/view/AtlasPublic/MuonTriggerPublicResults (visited on 10/29/2020).

[144] ATLAS Collaboration. *Public Egamma Trigger Plots for Collision Data*. 2020. URL: https://twiki.cern.ch/twiki/bin/view/AtlasPublic/EgammaTriggerPublicResults (visited on 10/29/2020).

[145] ATLAS Collaboration. *Electron Efficiency Correlation Model*. 2020. URL: https://twiki.cern.ch/twiki/bin/view/AtlasProtected/ElectronEfficiencyCorrelationModel (visited on 10/08/2020).

[146] ATLAS Collaboration. *Muon Combined Performance Analasys Guidelines*. 2020. URL: https://twiki.cern.ch/twiki/bin/view/AtlasProtected/MCPAnalysisGuidelinesMC16 (visited on 10/08/2020).

[147] ATLAS Collaboration. "Jet energy measurement with the ATLAS detector in proton–proton collisions at $\sqrt{s} = 7\,\text{TeV}$". In: *Eur. Phys. J. C* 73 (2013), p. 2304.

[148] ATLAS Collaboration. "Topological cell clustering in the ATLAS calorimeters and its performance in LHC Run 1". In: *Eur. Phys. J. C* 77 (2017), p. 490.

[149] M. Cacciari, G. P. Salam, and G. Soyez. "The anti-k_t jet clustering algorithm". In: *JHEP* 04 (2008), p. 063.

[150] M. Cacciari, G. P. Salam, and G. Soyez. "FastJet user manual". In: *Eur. Phys. J. C* 72 (2012), p. 1896.

[151] ATLAS Collaboration. "Jet reconstruction and performance using particle flow with the ATLAS Detector". In: *Eur. Phys. J. C* 77 (2017), p. 466.

[152] A. Collaboration. *Tagging and suppression of pileup jets with the ATLAS detector*. Tech. rep. ATLAS-CONF-2014-018. Geneva: CERN, May 2014.

[153] ATLAS Collaboration. *Forward jet vertex tagging using the particle flow algorithm*. ATL-PHYS-PUB-2019-026. 2019.

[154] A. Collaboration. *Pile-up subtraction and suppression for jets in ATLAS*. Tech. rep. ATLAS-CONF-2013-083. Geneva: CERN, Aug. 2013.

[155] ATLAS Collaboration. "Jet energy scale measurements and their systematic uncertainties in proton–proton collisions at $\sqrt{s} = 13\,\text{TeV}$ with the ATLAS detector". In: *Phys. Rev. D* 96 (2017), p. 072002.

[156] ATLAS collaboration. "Performance of missing transverse momentum reconstruction in proton-proton collisions at $\sqrt{s} = 7$ TeV with ATLAS". In: *The Eur. Phys. J. C* 72.1 (Jan. 2012).

[157] ATLAS collaboration. "Performance of algorithms that reconstruct missing transverse momentum in $\sqrt{s} = 8$ TeV proton–proton collisions in the ATLAS detector". In: *The Eur. Phys. J. C* 77.4 (Apr. 2017).

[158] ATLAS collaboration. "Performance of missing transverse momentum reconstruction with the ATLAS detector using proton–proton collisions at $\sqrt{s} = 13$ TeV". In: *The Eur. Phys. J. C* 78.11 (Nov. 2018).

[159] E. T. et al. *E_T^{miss} performance in the ATLAS detector using 2015-2016 LHC p-p collisions*. Tech. rep. ATL-COM-PHYS-2017-1732. Geneva: CERN, Dec. 2017.

[160] ATLAS Collaboration. *Data Preparation Checklist For Physics Analysis*. 2018. URL: https://twiki.cern.ch/twiki/bin/viewauth/Atlas/DataPreparationCheckListForPhysicsAnalysis (visited on 09/27/2019).

[161] ATLAS Collaboration. *Good Run Lists For Analysis Run 2*. 2019. URL: https://twiki.cern.ch/twiki/bin/viewauth/AtlasProtected/GoodRunListsForAnalysisRun2#Where_to_find_the_Good_Run_Lists (visited on 09/26/2019).

[162] ATLAS Collaboration. "Identification and rejection of pile-up jets at high pseudorapidity with the ATLAS detector". In: *Eur. Phys. J. C* 77 (2017), p. 580. Erratum: in: *Eur. Phys. J. C* 77 (2017), p. 712.

[163] S. Farrell. *AssociationUtils - Overlap removal tools*. 2019. URL: `https://gitlab.cern.ch/atlas/athena/blob/21.2/PhysicsAnalysis/AnalysisCommon/AssociationUtils/README.rst` (visited on 09/26/2019).

[164] ATLAS Collaboration. "Performance of electron and photon triggers in ATLAS during LHC Run 2". In: *The Eur. Phys. J. C* 80.1 (Jan. 2020).

[165] S. R. et al. *$ZZ \to \ell^+\ell^-\ell'^+\ell'^-$ cross-section measurements and aTGC search in 13 TeV pp collisions with the ATLAS detector*. Tech. rep. ATLAS-COM-CONF-2017-042. Geneva: CERN, May 2017.

[166] Z. Grout et al. *Unfolded four lepton mass and angular distributions*. Tech. rep. ATL-COM-PHYS-2019-1465. Geneva: CERN, Dec. 2019.

[167] E. Bothmann et al. "Event Generation with Sherpa 2.2". In: (2019).

[168] T. Gleisberg and S. Höche. "Comix, a new matrix element generator". In: *JHEP* 12 (2008), p. 039.

[169] S. Schumann and F. Krauss. "A parton shower algorithm based on Catani–Seymour dipole factorisation". In: *JHEP* 03 (2008), p. 038.

[170] S. Höche et al. "A critical appraisal of NLO+PS matching methods". In: *JHEP* 09 (2012), p. 049.

[171] S. Höche et al. "QCD matrix elements and truncated showers". In: *JHEP* 05 (2009), p. 053.

[172] S. Höche et al. "QCD matrix elements + parton showers: The NLO case". In: *JHEP* 04 (2013), p. 027.

[173] R. D. Ball et al. "Parton distributions for the LHC Run II". In: *JHEP* 04 (2015), p. 040.

[174] T. Sjöstrand, S. Mrenna, and P. Skands. "A brief introduction to PYTHIA 8.1". In: *Comput. Phys. Commun.* 178 (2008), pp. 852–867.

[175] L. Lönnblad. "Correcting the Colour-Dipole Cascade Model with Fixed Order Matrix Elements". In: *JHEP* 05 (2002), p. 046.

[176] L. Lönnblad and S. Prestel. "Matching tree-level matrix elements with interleaved showers". In: *JHEP* 03 (2012), p. 019.

[177] ATLAS Collaboration. *ATLAS Pythia 8 tunes to 7 TeV data*. ATL-PHYS-PUB-2014-021. 2014.

[178] R. D. Ball et al. "Parton distributions with LHC data". In: *Nucl. Phys. B* 867 (2013), p. 244.

[179] D. J. Lange. "The EvtGen particle decay simulation package". In: *Nucl. Instrum. Meth. A* 462 (2001), p. 152.

[180] P. Nason. "A new method for combining NLO QCD with shower Monte Carlo algorithms". In: *JHEP* 11 (2004), p. 040.

[181] S. Frixione, P. Nason, and C. Oleari. "Matching NLO QCD computations with parton shower simulations: the POWHEG method". In: *JHEP* 11 (2007), p. 070.

[182] S. Alioli et al. "A general framework for implementing NLO calculations in shower Monte Carlo programs: the POWHEG BOX". In: *JHEP* 06 (2010), p. 043.

[183] T. Sjöstrand et al. "An introduction to PYTHIA 8.2". In: *Comput. Phys. Commun.* 191 (2015), p. 159.

[184] F. Buccioni et al. "OpenLoops 2". In: *The Eur. Phys. J. C* 79.10 (Oct. 2019).

[185] *Search for type-III seesaw heavy leptons in proton-proton collisions at $\sqrt{s} = 13$ TeV with the ATLAS detector*. Tech. rep. ATLAS-CONF-2018-020. Geneva: CERN, June 2018.

[186] S. Wilks. "The Large-Sample Distribution of the Likelihood Ratio for Testing Composite Hypotheses". In: *Annals Math. Statist.* 9.1 (1938), pp. 60–62.

[187] A. Wald. "Tests of Statistical Hypotheses Concerning Several Parameters When the Number of Observations is Large". In: *Transactions of the American Mathematical Society* 54.3 (1943), pp. 426–482.

[188] A. Buse. "The Likelihood Ratio, Wald, and Lagrange Multiplier Tests: An Expository Note". In: *The American Statistician* 36.3a (1982), pp. 153–157.

[189] J. Neyman and E. S. Pearson. "On the Problem of the Most Efficient Tests of Statistical Hypotheses". In: *Philosophical Transactions of the Royal Society of London. Series A, Containing Papers of a Mathematical or Physical Character* 231 (1933), pp. 289–337.

[190] G. Cowan et al. "Asymptotic formulae for likelihood-based tests of new physics". In: *Eur. Phys. J. C* 71 (2011), p. 1554. Erratum: "Asymptotic formulae for likelihood-based tests of new physics - errata". In: *Eur. Phys. J. C* 73 (2013), p. 2501.

[191] G. Cowan et al. "Asymptotic formulae for likelihood-based tests of new physics - errata". In: *Eur. Phys. J. C* 73 (2013), p. 2501.

[192] A. L. Read. "Presentation of search results: the CL_S technique". In: *J. Phys. G* 28 (2002), p. 2693.

[193] ATLAS Collaboration. *Recipes for Systematic Uncertainties*. 2020. URL: `https://twiki.cern.ch/twiki/bin/view/AtlasProtected/PmgSystematicUncertaintyRecipes` (visited on 02/28/2020).

[194] E. Bothmann, M. Schönherr, and S. Schumann. "Reweighting QCD matrix-element and parton-shower calculations". In: *Eur. Phys. J. C* 76.11 (2016), p. 590.

[195] J. Butterworth et al. "PDF4LHC recommendations for LHC Run II". In: *J. Phys. G* 43 (2016), p. 023001.

[196] S. Dulat et al. "New parton distribution functions from a global analysis of quantum chromodynamics". In: *Phys. Rev. D* 93.3 (2016), p. 033006.

[197] L. Harland-Lang et al. "Parton distributions in the LHC era: MMHT 2014 PDFs". In: *Eur. Phys. J. C* 75.5 (2015), p. 204.

[198] ATLAS Collaboration. *ATLAS-CMS recommended predictions for single-top cross sections using the Hathor v2.1 program*. 2020. URL: `https://twiki.cern.ch/twiki/bin/view/LHCPhysics/SingleTopRefXsec` (visited on 06/09/2020).

[199] ATLAS Collaboration. *ATLAS-CMS recommended predictions for top cross sections using the Hathor v2.1 program*. 2020. URL: `https://twiki.cern.ch/twiki/bin/view/AtlasProtected/CrossSectionNLOttV` (visited on 06/09/2020).

[200] M. Aliev et al. "HATHOR – HAdronic Top and Heavy quarks crOss section calculatoR". In: *Computer Physics Communications* 182.4 (Apr. 2011), pp. 1034–1046.

[201] P. Kant et al. "HatHor for single top-quark production: Updated predictions and uncertainty estimates for single top-quark production in hadronic collisions". In: *Computer Physics Communications* 191 (June 2015), pp. 74–89.

[202] ATLAS Collaboration. *Luminosity determination in pp collisions at $\sqrt{s} = 13$ TeV using the ATLAS detector at the LHC*. Tech. rep. ATLAS-CONF-2019-021. Geneva: CERN, June 2019.

[203] ATLAS Collaboration. *Jet Uncertainties*. 2020. URL: `https://twiki.cern.ch/twiki/bin/view/AtlasProtected/JetUncertainties` (visited on 05/29/2020).

[204] ATLAS collaboration. *Jet energy scale and resolution measured in proton-proton collisions at $\sqrt{s} = 13$ TeV with the ATLAS detector*. 2020.

[205] ATLAS Collaboration. *Measurement of W and Z Boson Production Cross Sections in pp Collisions at $\sqrt{s} = 13$ TeV in the ATLAS Detector*. Tech. rep. ATLAS-CONF-2015-039. Geneva: CERN, Aug. 2015.

[206] J. Butterworth et al. *Single Boson and Diboson Production Cross Sections in pp Collisions at $\sqrt{s} = 7$ TeV*. Tech. rep. ATL-COM-PHYS-2010-695. Geneva: CERN, Aug. 2010.

[207] G. Carratta et al. *Search for type-III seesaw heavy leptons in dilepton final states using 139 fb^{-1} of pp collisions at $\sqrt{(s)} = 13$ TeV with the ATLAS detector*. Tech. rep. ATL-COM-PHYS-2019-659. Geneva: CERN, June 2019.

[208] ATLAS Collaboration. *Search for type-III seesaw heavy leptons in dilepton final states in pp collisions at $\sqrt{s} = 13$ TeV with the ATLAS detector*. 2020.

[209] ATLAS Collaboration. "Search for doubly charged Higgs boson production in multi-lepton final states with the ATLAS detector using proton–proton collisions at $\sqrt{s} = 13\,\text{TeV}$". In: *The Eur. Phys. J. C* 78.3 (Mar. 2018).

[210] F. del Aguila, J. de Blas, and M. Pérez-Victoria. "Effects of new leptons in electroweak precision data". In: *Phys. Rev. D* 78.1 (July 2008), p. 013010.

[211] A. Abada et al. "$\mu \to e\gamma$ and $\tau \to \ell\gamma$ decays in the fermion triplet seesaw model". In: *Phys. Rev. D* 78.3 (Aug. 2008), p. 033007.

[212] A. Abada et al. "Low energy effects of neutrino masses". In: *JHEP* 2007.12 (Dec. 2007), pp. 061–061.

[213] B. Fuks et al. "Gaugino production in proton-proton collisions at a center-of-mass energy of 8 TeV". In: *JHEP* 2012.10 (Oct. 2012), pp. 1–28.

[214] B. e. a. Fuks. "Precision predictions for electroweak superpartner production at hadron colliders with Resummino". In: *The Eur. Phys. J. C* 73.7 (July 2013), p. 2480.

[215] J. Alwall et al. "The automated computation of tree-level and next-to-leading order differential cross sections, and their matching to parton shower simulations". In: *JHEP* 07 (2014), p. 079.

[216] O. B. Bylund. *Modelling Wt and tWZ production at NLO for ATLAS analyses*. 2016.

[217] *CERN Open Data Policy for the LHC Experiments*. Tech. rep. CERN-OPEN-2020-013. Geneva: CERN, Nov. 2020.

[218] ATLAS Collaboration. *athena - The ATLAS Experiment's main offline software repository*. 2021. URL: `https://gitlab.cern.ch/atlas/athena/`.

[219] ATLAS Collaboration. *TRExFitter - a framework for binned template profile likelihood fits*. 2021. URL: `https://gitlab.cern.ch/TRExStats/TRExFitter`.

[220] R. Brun and F. Rademakers. "ROOT — An object oriented data analysis framework". In: *Nucl. Instrum. Meth. A* 389.1 (1997), pp. 81–86.

Summary

Particle physics is the study of the smallest, indivisible building blocks from which our universe is built. Its central framework is the Standard Model (SM), a highly successful theory encompassing all fundamental particles confirmed to exist so far. The SM has been robust in the face of scrutiny and has had its validity confirmed by many experiments in particle physics to date. Its latest triumph came in 2012, when the ATLAS and CMS collaborations published the discovery of a new particle with properties consistent with a Higgs boson. With the discovery of this particle, the Standard Model would be considered complete.

Yet, the work is not done. Three of the four fundamental forces of nature have been incorporated into the SM: the weak nuclear force, the strong nuclear force and the electromagnetic force. In unifying these forces with the gravitational force, however, the Standard Model is found wanting. In addition, there are certain phenomena that have been observed that are as of yet unexplained by the SM alone, including, but not limited to:

- Neutrino masses: long assumed to be massless, the small but non-zero mass of these ghostly particles came as a surprise to physicists, as did the apparent ability of any of the three generation of neutrinos to shapeshift into its differently-flavored counterparts.
- Dark Matter: a hypothesized substance that makes up as much as 85% of all matter in the universe today. Its eponymous darkness refers to it being seemingly impervious to the electromagnetic force.
- Matter-antimatter asymmetry in the early universe: antimatter in many ways is a mirror image of ordinary matter. As a rule, matter can be created from energy only in proportion to an equal amount of antimatter. Yet the universe we live in seems to exist out of ordinary matter only.

Nevertheless, the Standard Model is the bedrock on which contemporary particle physics experiments are built. The frontier of these experiments is the high-energy regime, which potentially hides a sector of heavy but elusive new particles. Many in the community hope for the SM to be the progenitor of a much grander, much more unified theory. However, until irrefutable evidence is found for physics Beyond the Standard Model(BSM)[1], a definitive formulation of such a Grand Unified Theory seems to be a distant dream.

The proverbial hunt is on: the ATLAS collaboration at the CERN facility hosts many analyses intent on finding evidence of potential BSM signals. Searches are conducted on the shrapnel that is produced as a result of particle collisions. Bunches of protons, squeezed together and bent by the powerful magnets of the Large Hadron Collider (LHC),

[1] alternatively *exotic physics*

are accelerated to nearly the speed of light and made to collide with each other. These particle collisions are sufficiently powerful to make available a large amount of energy for the production of heavy particles. Such particles quickly collapse into lighter particles, however, and therefore cannot be detected directly. Instead, the lighter decay products interacting with the detector are reconstructed to derive the properties of a single event. The kinematic properties of objects in an event can then be combined to point towards the existence of a BSM parent particle, very briefly called into existence before falling apart.

Model-independent multilepton searches

Leptons are a class of particles in the Standard Model. There are six of them, sorted into three generations, with each generation featuring one charged lepton and one neutrino. Our focus is on *light leptons*: the two charged leptons with the lightest mass. These are the *electron* and the *muon*. These particles are of particular interest because many promising theories of BSM physics are expected to couple to leptons[2]. Furthermore, heavier particles have a possibility of decaying into light leptons. Because of this, a study of light leptons is a study that covers a large number of possibilities[3].

This analysis in particular focuses on events where exactly three or four light leptons have been detected. This is a promising region for a model-independent search, which seeks to be sensitive to a multitude of BSM models. Indeed, datasets of three and four lepton events are exposed to multiple potential theories of exotic physics. Examples of these theories include the *Type-III seesaw mechanism*, which can be probed by studying three-lepton events, and the *Doubly-charged Higgs production*, whose pair production can be studied through four-lepton events. The former of these theories would offer potential solutions to each of the three shortcomings mentioned above, while the latter would provide new information on the Higgs sector and provide invaluable insight on the nature of lepton flavor. Feynman diagrams demonstrating how these final states are effected by the aforementioned theories are shown in Figure S.1

Because this is a model-independent search, it is imperative to keep an open mind about the exact model parameters of this and other potentially interesting theories. Nevertheless, it is important to understand what the potential for discovery might be compared to a specialized analysis dedicated to one specific model. To this end, this analysis is also performed using an iteration of each of the above theories. The results of the latter are compared to that of dedicated analyses in order to gauge the relative sensitivity of our search.

In order to determine the presence of additional BSM contributions in the dataset of interest, it must first be divided into smaller signal regions. This division is done using criteria focused on isolating potentially interesting signals from the SM processes also permeating the data. The amount of background events and our ability to accurately predict the background contributions can both be bottlenecks to the precision of the analysis. A large amount of background compared to the signal strength makes it easy for

[2]This includes neutrinos. However, neutrinos only interact weakly and are therefore invisible to the ATLAS detector.

[3]The heavy τ lepton would be an interesting additional particle to study, but this comes with significant difficulties due to its short lifetime. Nevertheless, some sensitivity to τ leptons is obtained due to its ability to decay to light leptons.

this signal to become lost in the noise. This effect can only be counteracted by procuring more data. Furthermore, our ability to estimate with precision the Standard Model contributions may be hindered by uncertainties, limiting the distinguishing power of the analysis.

An additional difficulty of background estimation is that certain Standard Model processes do not promptly produce an event with three or more light leptons, but the recorded event nevertheless has such a topology. This might happen when non-leptonic particles undergo secondary decays which lead to the production of additional leptons, which are then recorded. Measurements from the detector from other particles may also be wrongfully identified as leptons during reconstruction. In either case we have an additional background contribution to contend with. This is referred to as the *fake background*. Dedicated, data-driven techniques are required in order to estimate this additional background. Specifically, the total background contribution due to these fake events is estimated from a region where such events are plentiful. This rate of events is then extrapolated to the regions of interest (the three or four light lepton regions) using a set of reweighting techniques based on the observed efficiencies of the reconstruction algorithms.

Once the SM background is estimated and the signal regions, 22 of them in total, have been defined, the data are revealed. Deviations between the data and the SM expectation are judged based on the degree of this deviation. Significant deviations are of great interest and warrant further investigation. For regions in which no deviation is found, an upper limit is produced instead. This upper limit is what allows future analyzers to exclude with 95% confidence the presence of a contribution in the data of a particular size (or greater). Reporting these upper limit in a model-independent fashion is expedient, as future analyses may quickly process them to draw conclusions on the implications for their BSM theory of choice.

Results

A histogram showing the measured data and the expected background from various sources for all of the considered signal regions is shown in Figure S.2. The slight excesses and deficits that have been seen when comparing these two have been studied and found to be

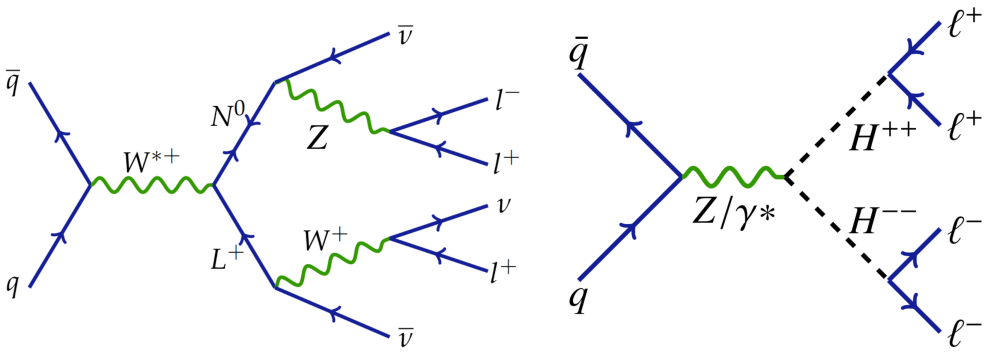

Figure S.1: Left: Feynman diagram demonstrating how the Type-III seesaw mechanism can lead to final states containing three charged leptons through the heavy W-like boson production process $W^{\pm} \to L^{\pm}N^0$. Right: Feynman diagram of a four charged lepton final state through the production of a doubly-charged Higgs pair accommodated by the Drell-Yan process.

compatible with a reasonable expectation of statistical fluctuations that might occur when a limited amount of data are observed. In the absence of a discovery, upper limits have been produced for each of the signal regions instead. These upper limits have furthermore been reinterpreted for the Type-III seesaw and doubly-charged Higgs models for the most sensitive signal regions for both of these models. For the Type-III seesaw model, expected limits of $\sigma^{95}_{exp} = 41^{+17}_{-11}$ fb for a heavy-lepton mass $M = 400$ GeV, and $\sigma^{95}_{exp} = 12^{+5}_{-3}$ fb for a heavy-lepton mass $M = 700$ GeV are found by this analysis. For the doubly-charged Higgs model, expected limits are $\sigma^{95}_{exp} = 0.18^{+0.08}_{-0.05}$ fb for a $H^{\pm\pm}$ mass of $M = 300$ GeV, and $\sigma^{95}_{exp} = 0.16^{+0.07}_{-0.05}$ fb for a $H^{\pm\pm}$ mass of $M = 500$ GeV. These limits were compared with those found by dedicated analyses studying the same model. It is found that these limits are comparable, even though the dedicated analysis ultimately produce superior results.

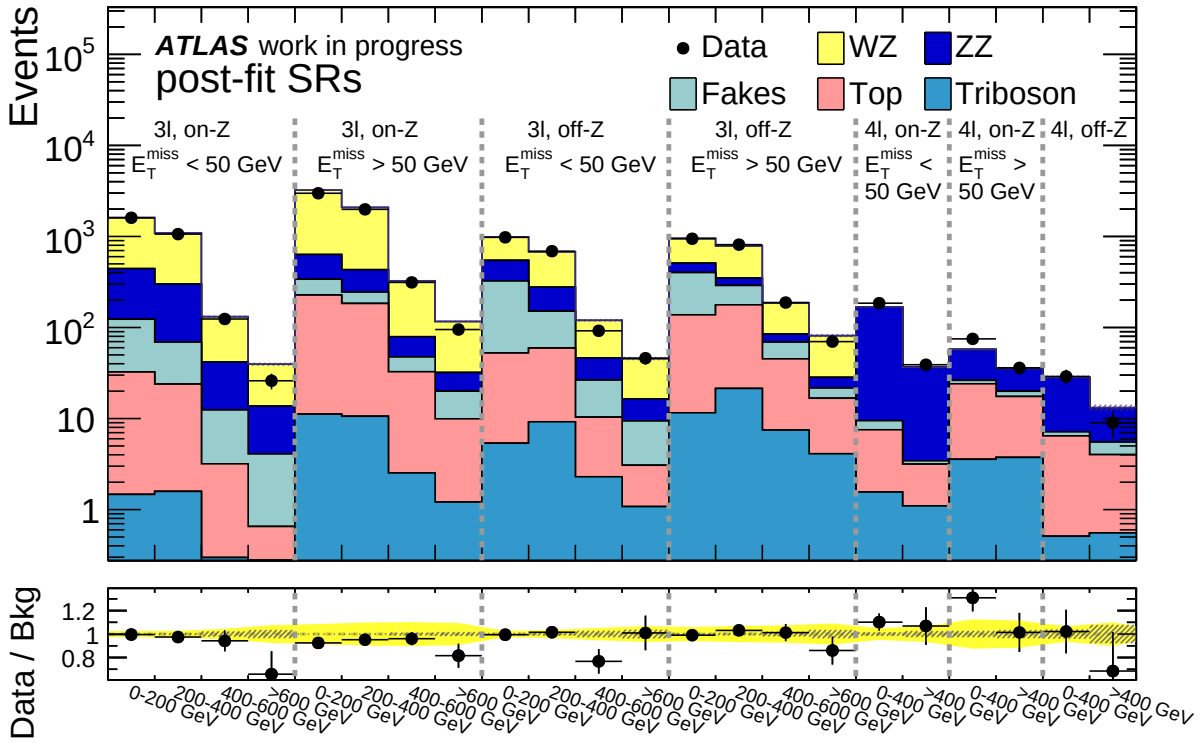

Figure S.2: Fits comparing background expectation to measured data in the 22 signal regions of this analysis. The bottom pannel shows the ratio between the data divided by the total background expectation for each signal region. Stat. uncertainties are given by the gray hatched area, while the total uncertainty (stat+syst) is given as the solid yellow area

The Model-independent multilepton search offers a promising avenue in the current landscape of particle physics research. A large number of competing BSM models can currently be investigated, lending credence to conducting a search that probes a large amount of data in many signal regions simultaneously. While the precision of this analysis is not as good as a dedicated analysis, the benefits of studying a larger phase space give model-independent searches an edge when one is unsure of where to look.

There are still many ways that this analysis can be improved, both to increase the sensitivity of the analysis and increasing the number of signal regions that are investigated in order to become sensitive to a greater range of BSM models. Currently, the precision with which the cross section of certain SM processes are computed proves to be a bottleneck

for large fractions of the dataset. Higher-order computation of these cross-sections and improved techniques for estimating related uncertainties would prove beneficial to analysis sensitivity. Furthermore, this analysis only studies light leptons; additional sensitivity is attainable by fully incorporating τ leptons into the study. Improvements can also be made to enable more freedom in the analysis' choice of signal regions: Applying additional limit-setting techniques enables more granular signal region divisions in phase space where expected background is low. Improved fake background estimation would improve regions with insufficient statistics for data-driven techniques to function aptly.

Model-independent multilepton searches, like the one conducted in this thesis, offer the discovery possibility of physics beyond the Standard Model. In a time where the next avenue for discovery is not so obvious, the indiscriminate, wide-net approach offers an important flexibility in its potential. Further development of this class of analysis promises to yield exciting opportunities in the near future.

Samenvatting

Deeltjesfysica bestudeert de kleinst mogelijke bouwstenen waaruit ons universum is opgebouwd. Het centrale model is het Standaardmodel (SM): een zeer succesvolle theorie die alle fundamentele deeltjes bevat waarvan we kunnen bevestigen dat ze bestaan. Het SM heeft zich staande gehouden tegen nauwkeurig onderzoek en de geldigheid ervan is bevestigd door een groot aantal uitgevoerde experimenten. De laatste triomf voor de theorie kwam in 2012, toen de ATLAS en CMS collaboraties zeer sterk bewijs publiceerden voor het bestaan van een Higgs boson. Met de ontdekking van dit deeltje zou het SM als compleet kunnen worden beschouwd.

Maar het werk is nog niet af. Drie van de vier fundamentele krachten van de natuur zijn verwerkt in het SM: de zwakke kernkracht, de sterke kernkracht en de elektromagnetische kracht. Het SM is echter nog niet in staat om deze krachten te verenigen met de zwaartekracht. Verder zijn er zekere fenomenen die geobserveerd zijn maar niet kunnen worden verklaard met alleen het SM, inclusief, maar niet gelimiteerd tot:

- Neutrinomassa's: lange tijd is aangenomen dat deze schimmige deeltjes massaloos zijn. Toen het tegendeel werd aangetoond kwam dit als een verassing voor natuurkundigen. Dit geldt ook voor de mogelijkheid van ieder van deze drie deeltjes om zich te kunnen veranderen in de andere twee smaken van het trio.
- Donkere materie: bijna 85% van alle materie in het huidige universum lijkt gemaakt van een hypothetische substantie die nog nooit direct is geobserveerd. Deze wordt 'donker' genoemd omdat zij geen interactie aangaat met de elektromagnetische kracht.
- Materie-antimaterie asymmetrie in het vroege universum: antimaterie is op veel manieren een spiegelbeeld van normale materie. In het algemeen geldt dat energie alleen in materie kan worden omgezet als tegelijkertijd een gelijke proportie aan antimaterie wordt gecreëerd. Toch lijkt het universum waarin we leven alleen uit normale materie te bestaan.

Desondanks is het Standaardmodel de basis waarop moderne experimenten in de deeltjesfysica worden opgesteld. De interesse van deze experimenten ligt veelal op het hogeenergie regime, waar zich potentieel een nieuwe sector van zware maar kortlevende nieuwe deeltjes verbergt. Wetenschappers hopen dat het Standaardmodel de voorvader zal blijken te zijn van een meer complete theorie. Helaas zal een formulering van een dergelijke verenigde theorie uitblijven totdat er onbetwistbaar bewijs is gevonden voor fysica buiten het Standaardmodel (BSM)[4].

De ATLAS collaboratie bij het CERN laboratorium heeft meerdere analyses met als doel het vinden van potentiële signalen van BSM fysica. Onderzocht worden de brokstukken die zijn geproduceerd als een resultaat van deeltjesbotsingen. Bundels van protonen, dicht op

[4]alternatief: *exotische natuurkunde*.

elkaar gefocusseerd en gestuurd door de krachtige magneten van de Large Hadron Collider (LHC), worden versneld tot bijna de lichtsnelheid om vervolgens op elkaar te botsen. Deze botsingen zijn dermate krachtig dat een grote hoeveelheid energie beschikbaar komt voor de productie van zware deeltjes. Zulke deeltjes vervallen echter snel weer naar lichtere deeltjes, en kunnen daarom niet direct gedetecteerd worden. Daarom worden de lichtere deeltjes die door de detector vliegen gedetecteerd, waaruit vervolgens de deelnemende deeltjes aan de initiële botsing en opeenvolgende vervallen kunnen worden herleid. Deze groep interacties en resulterende deeltjes samen heet een evenement. De kinetische eigenschappen van objecten in een evenement kunnen door experimenteerders worden bestudeert om te wijzen naar het kortdurente bestaan van een BSM moederdeeltje.

Model-onafhankelijke multilepton zoektochten

Leptonen zijn een klasse van deeltjes in het Standaardmodel. In totaal zijn er zes leptonen, verdeeld over drie generaties, waar elke generatie een geladen lepton en een neutrino bevat. Onze focus is op de *lichte leptonen*: de twee geladen leptonen met de laagste massa, het electron en het muon[5]. Deze deeltjes zijn interessant omdat meerdere veelbelovende BSM theorieën naar verwachting koppelen aan leptonen[6]. Veel zwaardere deeltjes in het SM kunnen bovendien vervallen in lichte leptonen. Vanwege deze redenen zal het bestuderen van lichte leptonen gevoelig zijn voor een enorme hoeveelheid mogelijkheden.

Deze analyse in het bijzonder is gericht op evenementen waar precies drie of vier lichte leptonen gedetecteerd zijn. Datasets met dergelijke evenementen zijn gevoelig voor allerlei potentiële BSM-modellen. Voorbeelden van dit soort theorieën zijn het *Type-III seesaw-mechanisme*, wat goed bestudeerd kan worden in evenementen met drie leptonen, en de *Dubbel-geladen Higgs productie*, waar een dataset met vier-lepton evenementen gevoelig voor is. De eerste van deze theorieën zou een potentiële oplossing bieden voor elk van de drie gebreken die eerder zijn genoemd, terwijl de tweede nieuwe informatie zou verschaffen over de Higgs-sector en waardevolle inzichten zal geven over de onschendbaarheid van leptonsmaak. Feynman-diagrammmen die aantonen hoe deze theorieën kunnen leiden tot eindtoestanden met drie en vier leptonen zijn gegeven in figuur S.1.

Omdat dit een model-onafhankelijke zoektocht betreft, is het van belang dat we ons niet blind staren op de exacte model-parameters van deze en andere theorieën. Toch is het belangrijk om te begrijpen wat voor potentie ter ontdekking een model-onafhankelijke zoektocht te bieden heeft in vergelijking met een analyse die zich in een specifiek model specialiseert. Hierom wordt deze analyse ook uitgevoerd met voorbeeldmodellen van de twee bovengenoemde theorieën. Deze specifieke resultaten kunnen namelijk vergeleken worden met de resultaten van specifieke analyses om een beeld te schetsen van de relatieve gevoeligheid van deze zoektocht.

Om de aanwezigheid van BSM contributies in de dataset te bepalen, wordt ze verdeeld in kleinere signaalgebieden. Deze scheiding is gebaseerd op criteria die het onderscheiden van potentiële signalen van de SM-achtergrond voorop stellen. De hoeveelheid achtergrond-evenementen en het vermogen om de hoeveelheid achtergrond nauwkeurig te schatten zijn de limiterende factoren voor de precisie van deze analyse. Een grote hoeveelheid

[5] en hun antideeltjes, het positron en antimuon

[6] Inclusief neutrino's. Neutrino's zijn echter onzichtbaar voor de ATLAS detector.

achtergrond in vergelijking tot de hoeveelheid signaal-evenementen zal het waarschijnlijk maken dat het signaal verloren gaat in de ruis. Dit kan alleen verholpen worden door meer data te verzamelen. Verder kan ons vermogen om de hoeveelheid achtergrond precies te voorspellen gelimiteerd zijn, wat een onzekerheid oplevert in de schattingen op deze achtergronden.

Een bijkomende hindernis in de achtergrondvoorspelling is dat er SM-processen bestaan die op zichzelf niet drie leptonen kunnen produceren, maar door omstandigheden toch evenementen leveren met drie of meer lichte leptonen. Dit kan gebeuren als niet-leptonische deeltjes interacties ondergaan die uiteindelijk een extra lepton opleveren. Ook incorrecte reconstructies van metingen in de detector kunnen foutief leiden tot een extra lepton. In beide gevallen kan dit leiden tot een extra imitatie-achtergrond. Speciale data-gedreven technieken zijn nodig om deze achtergrond af te schatten. Voor deze analyse wordt de contributie van deze evenementen eerst gemeten in een dataset waar dergelijke evenementen in veelvoudig aanwezig zijn. Deze meting kan vervolgens geëxtrapoleerd worden naar de signaalgebieden (de drie- en vier-lepton gebieden) met behulp van een set herwegingen die afhangen van de relatieve efficiëntie van de reconstructie-algoritmes.

Als de SM-achtergrond bepaald is en de signaalgebieden, in totaal 22, gedefinieerd zijn, kan de data bestudeerd worden. Afwijkingen van de data en de SM-verwachting worden beoordeeld gebaseerd op de mate van deze afwijking. Significante afwijkingen zijn bijzonder interessant en zullen vervolgonderzoek vereisen. Voor signaalgebieden waar geen afwijking is gevonden kunnen echter bovenlimieten worden gesteld. Deze limieten stellen toekomstige analyses in staat om met 95% zekerheid de aanwezigheid van een signaal met een zekere minimale kracht uit te sluiten. Deze bovenlimieten zijn op een model-onafhankelijke wijze geformuleerd zodat ze snel geherinterpreteerd kunnen worden om conclusies te trekken over elke willekeurige BSM-theorie.

Resultaten

Een histogram waar de gemeten data en de verwachte achtergronden getoond is van de verscheidene signaalgebieden is gegeven in figuur S.2. Kleine afwijkingen zijn te zien in

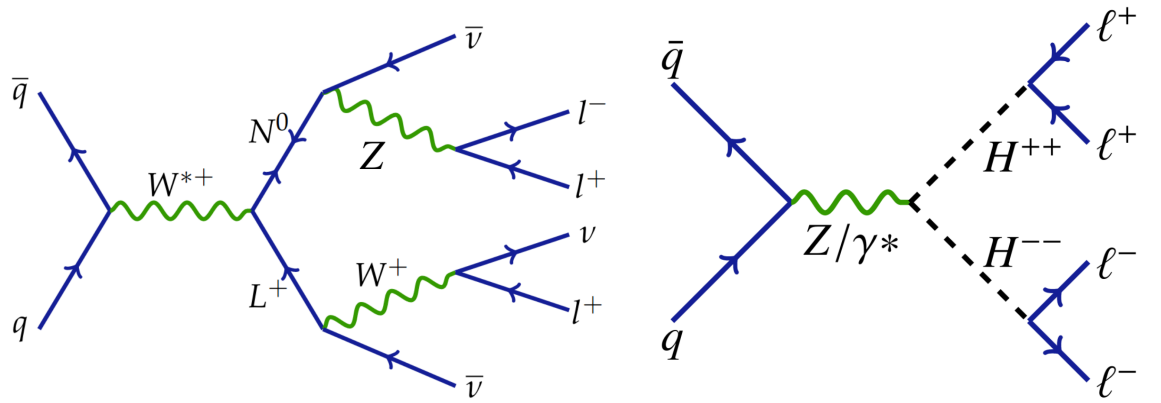

Figure S.1: Links: Feynman-diagram dat demonstreert hoe het Type-III seesaw-mechanisme kan leiden tot een evenement met drie geladen leptonen middels de productie van een zwaar W-achtig boson. Rechts: Feynman-diagram van de paarproductie van dubbel-geladen Higgs boson middels het Drell-Yan process, wat vervolgens leidt tot een evenement met vier geladen leptonen.

enkele signaalgebieden. Deze afwijkingen zijn bestudeerd en de conclusie is getrokken dat ze compatibel zijn met het Standaardmodel. Omdat geen ontdekking is gedaan, zijn bovenlimieten geproduceerd voor elk van de signaalgebieden. Deze bovenlimieten zijn vervolgens geherinterpreteerd voor een specifieke theorieën van Type-III seesaw-mechanisme en Dubbel-geladen Higgs productie. Voor het Type-III seesaw-mechanisme zijn verwachte limieten $\sigma^{95}_{exp} = 41^{+17}_{-11}$ fb voor een zwaar-lepton massa $M = 400$ GeV, en $\sigma^{95}_{exp} = 12^{+5}_{-3}$ fb voor een zwaar-lepton massa $M = 700$ GeV gevonden door deze analyse. Voor Dubbel-geladen Higgs productie zijn verwachte limieten van $\sigma^{95}_{exp} = 0.18^{+0.08}_{-0.05}$ fb voor een $H^{\pm\pm}$ massa van $M = 300$ GeV, en $\sigma^{95}_{exp} = 0.16^{+0.07}_{-0.05}$ fb voor een $H^{\pm\pm}$ massa van $M = 500$ GeV. Deze limieten zijn vergeleken met specifieke analyses die dezelfde modellen hebben bestudeerd. Uit deze vergelijking blijkt dat vergelijkbare limieten gevonden kunnen worden door de model-onafhankelijke zoektocht, alhoewel de specifieke analyses uiteindelijk toch superieure resultaten konden leveren.

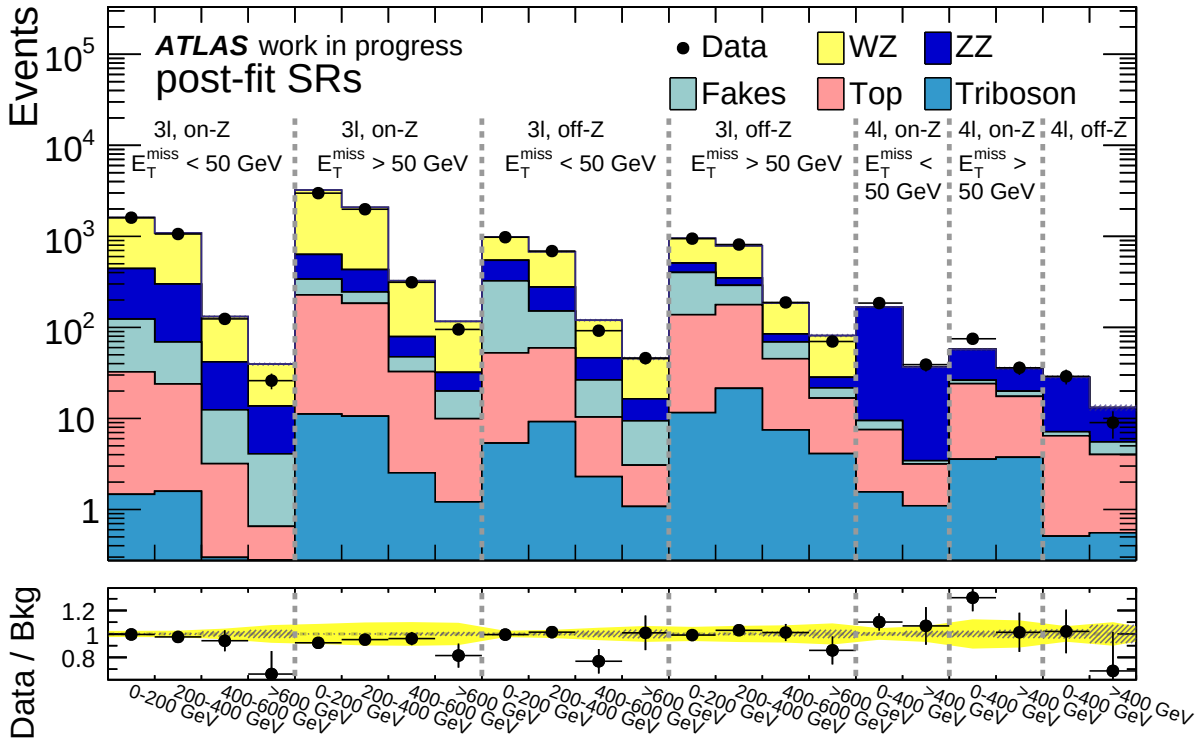

Figure S.2: Fits die de verwachte achtergrond vergelijken met de gemeten data in alle signaalgebieden van de analyse. 22 signaalgebiden zijn hier getoond, verdeeld middels criteria zoals het aantal leptonen, de aanwezigheid van 2 leptonen afkomstig van een Z-boson, de missende transversale energie van het evenement, en de invariante massa van alle leptonen. Het onderste paneel toont de verhouding tussen de data en de achtergrondsverwachting.

De model-onafhankelijke multilepton zoektocht biedt een veelbelovende methode in het huidige landschap van deeltjesfysica in de ATLAS detector. Met een grote hoeveelheid BSM-modellen die onderzocht kunnen worden, is het profijtelijk om een zoektocht te lanceren die in staat is om een grote hoeveelheid data in meerdere signaalgebieden tegelijk kan bestuderen. Hoewel de precisie iets slechter is dan dat van een specifieke analyse, zijn er desondanks voordelen te zien in het bestuderen van een grotere hoeveelheid data als men niet zeker is waar het best gezocht kan worden.

Er zijn nog vele manieren waarop deze analyse verder ontwikkeld kan worden, zowel om de gevoeligheid van de analyse te verbeteren als om de hoeveelheid signaalgebieden dat kan worden bestudeerd te verbreden. Momenteel is de precisie waarmee de cross-secties van zekere SM-processen bepaald zijn een limiterende factor voor zekere signaalgebieden. Hogere-orde berekeningen van deze cross-secties en nauwkeurige methodes om de onzekerheid te bepalen zullen veel opleveren voor deze analyse. Verder worden door deze analyse alleen de lichte leptonen onderzocht; de gevoeligheid zou toenemen als het τ-lepton volledig in deze analyse wordt meegenomen. Verbeteringen kunnen ook worden gemaakt om meer vrijheid te bieden in het opstellen van de signaalgebieden: Extra statistisch gereedschap om limieten op te stellen zou een fijnere verdeling van signaalgebieden toelaten in gebieden waar de verwachte achtergrond laag is. Verbeterde schatting van de imitatie-achtergrond laat ons verdere gebieden definiëren waar een tekort aan statistiek een data-gedreven bepaling van achtergrond nu nog verhindert.

Model-onafhankelijke multilepton zoektochten, zoals besproken in dit proefschrift, leveren de mogelijkheid tot ontdekking van fysica buiten het Standaardmodel. In een tijd waar het pad naar de volgende ontdekking niet geheel helder is, kunnen dergelijke analyses met een breed bereik de belangrijke flexibiliteit leveren die nodig zal blijken. Toekomstige ontwikkeling van dit type analyse belooft veel interessante mogelijkheden te bieden in de nabije toekomst.

Acknowledgments

The end of a thesis offers a good opportunity for a moment of reflection. It is the boundary between the completion of one great challenge and the start of the next. And so when one journey comes to an end it comes with the realization that without the help of many amazing people it either wouldn't have been possible, or it wouldn't have been worthwhile. With that realization, it is only fitting that I would end this journey by extending a note of gratitude.

A massive thank you to Olya Igonkina, for giving me the opportunity to start at Nikhef as a master student, and later on to continue as a PhD researcher. Your passion for particle physics has inspired many more than just myself. Thank you for showing me what commitment to one's work looks like, and thank you for teaching me to focus on opportunities, not on problems. The work I've presented here would not have been possible without you. I wish you could've seen it.

I'd also like to extend my heartfelt gratitude towards Frank Filthaut, who took on the task of being my promoter when the need arose, and provided invaluable guidance during the final year of my analysis. I'd furthermore like to thank my copromoter, Sascha Caron, and his zealous devotion to general searches, as well as my manuscript committee: prof. Sijbrand de Jong, prof. Robert Fleischer, prof. Ronald Kleiss, dr. Flavia Dias and dr. Mengquing Wu. Thank your for taking the time to give my thesis a critical read-through, and for providing corrections where needed.

Marcus, thank you for your invaluable assistance throughout my PhD and your around-the-clock availability that seemed to know no bounds. Your knowledge of the inner workings of the ATLAS collaboration, your technical expertise regarding its software frameworks, and your uncanny expertise in digging up and deciphering the arcane lore from so many twiki pages were the critical ingredients that were required for me to set up my analysis. I couldn't have done it without your help. I wouldn't have even gotten started.

There are many people at Nikhef I would like to thank. First of all Hartger, who helped me hit the ground running when I first arrived as a green Master student. Then there are my fellow PhD researchers in our little corner of exotics physics: thank you to Matteo, for reminding me to take tea breaks every now and then; it was a privilege to listen to you solve your own problems. Thank you to Terry, for all the good times during our outings and conferences, and for always going along with my sometimes chaotic energy; I am glad you are staying in the Netherlands, although I wish it was under better circumstances. And good luck to Edwin, best of luck to you in continuing the LFV legacy. I hope you enjoy the office, if you manage to still get some use out of it.

My deepest gratitude also to the entire Nikhef-ATLAS group: Marc, Broos, Ann-Kathrin, Michiel, Marko, Alice, Federica, Hannah, Jordy, Rahul, Ashley, Anamika, Alessio, Jeroen, Sara, Brian and Bryan. Your contributions to our lunches and coffee breaks where

refreshing and invaluable. A special thanks to honorary Nikhef-ATLAS member Kees, for always being up for some verbal sparring no matter the topic, and for your company during the last months of the final sprint of the PhD. Also a thank you to Tim for setting me on the road to the perfect .vimrc, although it cost me more time than it likely ever will gain. And a special thank you to Birgit and Jasper, for taking upon themselves the task of hosting our gatherings, be it for Sinterklaas or otherwise. I enjoyed them immensely.

My thanks to all friends and former Aikers, among others Daniel, Rutger, Mick en Bastiaan. Thanks to you and others I've had an such an excellent time at university that I needed an extra year just to enjoy it fully. Thank you to all smashers, karters, bestuurders en borrelaars that made the mice-infested basement of a run-down faculty building such a wonderful place.

Thank you to Gabriel, for the guidance I needed to get me through the last phase of my PhD. You helped me focus on what is important and to get my priorities in order. My academic career has occasionally proven to be beset by challenges, but if there ever was a turnaround point for me, it was your wisdom that allowed it to happen.

Maxim, thank you for your bottomless optimism and cheer. Thank you for always seeing the best in me. It's been quite an adventure, and I should think great things are coming for both of us. Similarly, I'd like to thank Sean, George, Nick and Karl for being my soundboard, and for tolerating my sometimes flippant and prideful personality.

Sjanine, mahal na mahal kita. You inspire me every day. Thank you for your patience with me in those seemingly endless final months of writing my manuscript, and for tolerating my absence during all those nights and weekends that we missed. I cannot imagine a future that doesn't have you in it.

Perhaps most importantly, I'd like to express my gratitude towards my family. To my mom, for encouraging me to be a lifelong learner. Thank you for taking such pride in me so that I could stay humble. To my dad, thank you for showing me the way. Even now you are the person that I seek to emulate and impress. And of course thank you to my sisters, Aislinn, Megan and Bronwyn. Every day I come to value each of you more and more.

Lastly, I wish to thank God, for creating this universe and allowing me to witness it.